Rational Catalyst Design for Selective Hydrogenations: Nitroarenes and Alkynes as case studies.

THÈSE N^{O} 6553 (2015)

PRÉSENTÉE LE 27 MARS 2015
À LA FACULTÉ DES SCIENCES DE BASE
LABORATOIRE DE GÉNIE DE LA RÉACTION CHIMIQUE
PROGRAMME DOCTORAL EN CHIMIE ET GÉNIE CHIMIQUE

ÉCOLE POLYTECHNIQUE FÉDÉRALE DE LAUSANNE

POUR L'OBTENTION DU GRADE DE DOCTEUR ÈS SCIENCES

PAR

Daniel André Samuel LAMEY

acceptée sur proposition du jury:

Prof. K. Sivula, président du jury
Prof. L. Kiwi, directrice de thèse
Dr F. Cardenas Lizana, rapporteur
Dr S. Gomez-Quero, rapporteur
Prof. G. Laurenczy, rapporteur

ÉCOLE POLYTECHNIQUE
FÉDÉRALE DE LAUSANNE
Suisse
2015

“The greatest enemy of knowledge is not ignorance, it is the illusion of knowledge”.

-Stephen Hawking-

Remerciements

En premier lieu, je remercie tout particulièrement le Professeur Lioubov Kiwi-Minsker de m'avoir accueilli dans son groupe pour la réalisation de ce travail de thèse, consécutif à mon travail de master. Ce fut quatre années d'un riche apprentissage et je suis reconnaissant pour son soutien, ses conseils mais aussi pour sa confiance et la grande liberté de travail qui m'ont été accordés. Merci également pour les excellentes conférences auxquelles j'ai eu le grand plaisir de participer.

Le soutien financier assuré par le Fonds National Suisse de la Recherche Scientifique (subsides n° 200020-132522 et 200020_149869) qui a permis la réalisation de cette thèse a été grandement apprécié.

Mes remerciements s'adressent également aux membres du jury de cette thèse, Dr. Santiago Gómez-Quero, Dr. Fernando Cárdenas-Lizana et Prof. Gabor Laurenczy pour avoir examiné mon travail ainsi qu'au Prof. Kevin Sivula pour la présidence du jury. Merci d'avoir aimablement accepté d'être les rapporteurs de cette thèse, pour vos remarques pertinentes et d'avoir fait de ma défense un moment profitable d'échanges.

Je tiens également à remercier le Prof. Albert Renken pour sa disponibilité et ses conseils avisés.

J'exprime toute ma reconnaissance à Fernando qui a supervisé mon travail dès mon arrivée au GGRC, pour sa grande disponibilité et nos longues et fructueuses discussions. Il a suivi ce travail avec toute l'expertise que les personnes qui le côtoient lui reconnaissent et je lui dois une grande partie de cette thèse. Ça a été un plaisir de collaborer et de pouvoir ainsi profiter de ton expérience des plus enrichissantes.

C'est une chance d'avoir un atelier de mécanique et d'électronique expert à disposition. Un grand merci à vous tous pour les constructions sur-mesure, fort utiles à la conception des installations, pour les réparations mieux que d'origine mais aussi pour vos bonnes idées. Je remercie également la sympathique et serviable équipe du magasin de chimie, ainsi que nos secrétaires pour leur aide précieuse. Merci aussi à PAP et Yoann pour leur aide dans la gestion du parc informatique du groupe, j'ai toujours apprécié de passer vous voir.

Je remercie également Duncan Alexander, Danièle Laub et Colette Vallotton de l'équipe du CIME pour les préparations d'échantillons et les images de microscopie. Un grand merci à Nicolas Xanthopoulos pour les nombreuses analyses XPS réalisées pour mes études.

J'aimerais remercier mes amis et collègues qui ont fait de ces années de thèse une expérience mémorable. Artur, pour tous les bons moments passés depuis les débuts en travail de master jusqu'aux soirées fondues, séries et kozeling. Merci aussi pour les leçons de russe, les sorties en vélo et pour ton auto. Charline, avec qui on a partagé le bureau tout du long, merci pour les gâteaux, fruits et confitures. Je te l'accorde, ce n'est pas si souvent que tu ronchonnais et un grand merci pour les nombreux services rendus. Julien, pour les moments de franche rigolade que tu avais pour habitude d'initier à la cafétéria, pour les soirées que tu as organisées et pour ton bon coup de pouce à Bâle. Micaela, pour nos échanges scientifiques, informatiques, cinématographiques, geek... aussi de m'avoir spoilé les 5 tomes de GoT même au-delà de ce qui a déjà été écrit. Oliver et Guillaume, pour tous les points marqués lors du rangement des labs et l'organisation des raclettes. Anne-Laure pour ton amour du Valais, Madhav pour nos discussions. Igor, pour tes conseils et ton expérience dans la préparation des catalyseurs ainsi que Tatiana pour notre sécurité. Une pensée s'envole également pour Edi, qui dans son surplus d'énergie, était toujours prêt à apporter un coup de main.

Je remercie également mes deux étudiantes de Master, Irina et Sara pour leur travail assidu et leur contribution à ma thèse de par leurs nombreux résultats. Irina, ce fut par ailleurs un plaisir de découvrir le Bortch, la vraie salade Olivier et le Napoléon. Et Sasha, je te remercie de m'avoir finalement rendu les clefs de la voiture d'Artur! Je n'oublie pas les stagiaires et apprentis qui ont travaillé dans le laboratoire, merci pour les coups de main.

Finalement je tiens à remercier ceux qui me sont chers. Une tendre pensée s'adresse à Caroline. Tu as enduré mes horaires extrêmes et mes absences, aussi je te dis un grand merci pour tout ton soutien et d'avoir été là quand c'était nécessaire.

Merci à ma famille, mon frère et ma sœur pour leur présence et encouragements. Je veux en particulier remercier mes parents, de m'avoir toujours apporté ce dont j'avais besoin. Par leurs encouragements et leur soutien indéfectible, ils ont largement contribué à la réalisation de cette thèse que je leur dédie.

Abstract

Catalyst design for selective hydrogenations is of major importance for the manufacturing of fine chemicals. This is based on industry demands in terms of high selectivity for the implementation of sustainable processes. Traditional synthetic routes cannot be considered viable any longer due to low overall product yields and associated environmental issues. Besides, the cleaner catalytic procedure which uses scarce and expensive noble metals (such as Pd, Pt, Ru) is very challenging in terms of exclusive attack of a single functionality or substituent. The approach taken in this thesis is based on rational catalyst design that calls on a combination of catalyst synthesis and characterization. The role of each component, from nano- to macroscale (active site to structured support) of the catalyst is precisely identified allowing an increased catalytic performance. This has been applied for the design of catalysts suitable for industrially relevant reactions, *i.e.* the partial catalytic reduction of substituted nitroaromatic compounds and alkynes.

Molybdenum nitrides, which have received great attention for hydrotreatment activities were selected as they represent a more sustainable alternative to noble metals, less expensive and easy to prepare. Temperature programmed treatment was proved to be an effective preparation method of tetragonal β– and cubic γ–Mo_2N, associated with significant hydrogen uptake ability. First, β–Mo_2N was used to catalyze the liquid phase selective hydrogenation of a series of *para*-substituted nitroarenes to give the corresponding aromatic amine. The presence of electron-withdrawing substituents on the aromatic ring served to increase the reaction rates, consistent with a nucleophilic mechanism. Numerous instances reported gold as a metal well-suited for highly selective hydrogenation reactions of nitroaromatic compounds. Incorporation of low amounts (0.25% wt.) of Au nanoparticles on β–Mo_2N enhanced hydrogen uptake and catalytic activity while delivering an ultraselective response in the batch liquid phase hydrogenation of *p*-chloronitrobenzene (*p*-CNB) to *p*-chloroaniline (*p*-CAN), selected as a model reaction where C-

Cl bond cleavage can readily occur. A synergetic effect involving Au and Mo_2N was demonstrated by an appreciably greater activity exhibited by Au/Mo_2N relative to Au/Al_2O_3. In contrast, reaction over Pd/Al_2O_3 used as a benchmark resulted in combined hydrogenation and hydrodechlorination.

In a second step, the influence on the catalytic response of nitride crystallographic phase (β- *vs.* γ-Mo_2N) and surface area (7-66 m^2 g^{-1}) was examined. Both β-Mo_2N and γ-Mo_2N promoted the exclusive hydrogenation of *p*-CNB to *p*-CAN where the β-form delivered a higher specific (per m^2) rate; the specific rate for γ-Mo_2N was independent of surface area. The inclusion of Au on both nitrides served to enhance *p*-CAN production.

Finally, the catalytic effect of nitrogen incorporation into Mo has been evaluated by preparing samples with different degree of nitridation. It was demonstrated that incorporation of N did not affect morphology and each sample exhibited aggregates of crystals with similar BET surface area. However, hydrogen chemisorption and release (by temperature programmed desorption) increased with decreasing Mo/N ratio. By running catalytic tests for the nitrobenzene hydrogenation, increased hydrogenation rates were observed on Mo_2N samples with higher nitrogen content, attributed to higher availability of surface heterolytic hydrogen on Mo-N. In contrast, -C=O hydrogenolysis was favored with benzaldehyde by homolytic hydrogen chemisorption on Mo, as a result of lower N content. These results demonstrate that N incorporation in Mo structure can control the performance of catalytic hydrogenation or hydrogenolysis.

As a powerful tool for tailoring metal nanoparticle morphology, a colloidal method has been used to design structured catalysts effective for the selective alkyne and $–NO_2$ group reduction. The surface properties of Pd NPs were fine-tuned by (i) changing the nature of stabilizing agent (electrostatic *vs.* steric), (ii) controlling Pd NPs size (2-10 nm) and (iii) grafting N-containing ligands onto the structured carbon nanofibers/sintered metal fibers (CNF/SMF) surface. In the *semi*-hydrogenation of acetylene, the catalytic response was insensitive to the nature of the reducing agent. Nevertheless, a strong inhibiting effect on hydrogenation rate was found when using an electrostatic stabilizer (*vs.* steric) explained on the basis of combined geometric and electronic effects. Decreasing (from 8 → 2 nm) Pd nanoparticle size resulted in a concomitant decrease in activity, but a higher selectivity to target ethylene product was observed. Grafting of nitrogen-containing modifiers (polyvinylpyridine or polyethylenimine) on the CNF/SMF support resulted in a significant increase in olefin selectivity (up to 93%) where the catalyst showed remarkable stability during 120 h on-stream. This was attributed to the electronic modifications (charge-transfer) promoted by interactions between the Pd nanocrystals and the grafted ligands as confirmed by X-ray photospectroscopy (XPS) analysis. In comparison, stabilizer-free Pd/CNF/SMF delivered low selectivity to ethylene (65%).

However, depending on the catalytic system, the organic ligand shell can be detrimental to the activity/selectivity response. Monodispersed Ni nanocrystals (from 2 → 14 nm) were prepared *via* colloidal method, stabilized using poly-N-vinyl-2-pyrrolidone (PVP) and tested in the *m*-dinitrobenzene (*m*-DNB) hydrogenation. A 6-fold higher turnover frequency was recorded for reaction over larger Ni ensembles. The influence of PVP was established where the initial TOF and selectivity to *m*-nitroaniline (*m*-NAN) exhibited a marked dependency on the presence this polymer. This response was attributed to preferential adsorption of PVP on selective edge and vertex atoms, leaving the plane atoms free. Supporting the monodispersed (2 nm) Ni NPs on activated carbon fibers (ACF) and removing traces of PVP by a UV-ozone treatment resulted in an overall increase in selectivity to target m-NAN even at high conversions (up to 95% yield) . Two-sites Langmuir-Hinshelwood kinetic model has been applied to rationalize the results and found to be consistent with the experimental data. This work demonstrate the potential of ACF-supported Ni as an effective catalyst formulation for the clean production of functionalized anilines.

In summary, this thesis demonstrates the feasibility of industrially important hydrogenation processes in both batch liquid and continuous gas phase operation. The product distribution can be controlled on a nano-level by tuning the properties of the active phase through modifications of

the structural parameters (allotropic form, composition), modifications on the NP microenvironment (organic ligand shell) and optimization of particle size.

Keywords: Selective hydrogenation, rational catalyst design, molybdenum nitrides, Pd, Ni, structured carbon-based supports, nitroarenes, alkynes.

Version abrégée

Le design de catalyseur pour les hydrogénations sélectives est d'une importance capitale pour la confection de produits de chimie fine. Ceci est dû à aux demandes industrielles en matière de haute sélectivité pour la mise en place de procédés durables. En raison de faibles rendements globaux et des problèmes environnementaux qui en découlent, les voies de synthèse traditionnelles ne peuvent plus être considérées comme viables. Par ailleurs, les procédés catalytiques plus propres, qui utilisent des ressources peu abondantes et couteuses en métaux nobles (tels que le Pd, Pt, Ru) représentent un défi particulier vis-à-vis d'une attaque exclusive d'une seule fonctionnalité ou substituent. L'approche adoptée dans cette thèse se base sur une conception rationnelle du catalyseur qui fait appel à une combinaison multidisciplinaire de synthèse et caractérisation de catalyseurs. Le rôle de chaque composant, de l'échelle nano- à macro (du site actif au support structuré) du catalyseur est précisément identifié, permettant une performance catalytique accrue. Ceci a été mis en œuvre pour la conception de catalyseurs appropriés à des réactions industrielles pertinentes, telles que la réduction catalytique partielle de composés nitroaromatiques substitués ainsi que d'alcynes.

Les nitrures de molybdène, qui ont reçu par le passé une grande attention pour les processus d'hydrotraitement en raison de leur activité et sélectivité, ont été choisis étant donné qu'ils représentent une alternative plus durable que les métaux nobles. Les méthodes de traitement thermique programmé ont été reconnues comme étant une méthode de préparation efficace du β-Mo_2N tétragonal et du γ-Mo_2N cubique, associés à une capacité d'absorption significative. Tout d'abord, le β-Mo_2N a été employé en phase liquide pour catalyser l'hydrogénation sélective d'une

série de nitroarenes *para*-substitués et former l'amine aromatique correspondante. La présence de groupes électroattracteurs sur le noyau aromatique a permis d'augmenter les vitesses de réaction, en adéquation avec un mécanisme de réaction nucléophile. Il a été observé que l'or est un métal convenant particulièrement bien pour des réactions d'hydrogénation hautement sélectives de composés nitroaromatiques. L'incorporation de faibles quantités de nanoparticules d'or (0.25% m/m) sur le β-Mo_2N a augmenté l'adsorption d'hydrogène de même que l'activité catalytique et ce, tout en affichant une sélectivité complète pour l'hydrogénation en phase liquide du *p*-chloronitrobenzene (*p*-CNB) en *p*-chloroaniline (*p*-CAN), choisi comme réaction modèle en raison du clivage facile de la liaison C-Cl. Un effet synergétique impliquant l'or et le Mo_2N a été démontré par une activité sensiblement accrue de l'Au/Mo_2N vis-à-vis de Au/Al_2O_3. En revanche, la réaction avec du Pd/Al_2O_3 (servant de référence) a donné lieu à la réaction d'hydrogénation couplée à de l'hydrodéchlorination.

Dans un second temps, l'influence de la phase cristallographique (β- *vs.* γ-Mo_2N) et de la surface spécifique (7-66 m^2 g^{-1}) sur le comportement catalytique ont été examinées. Le β-Mo_2N tout comme le γ-Mo_2N ont permis d'hydrogéner sélectivement le *p*-CNB en *p*-CAN, et la structure β- a fourni une vitesse de réaction (par m^2) accrue; la vitesse de réaction pour le γ-Mo_2N est restée indépendante de la surface spécifique. L'inclusion d'or sur chacun des deux nitrures a permis d'améliorer la production de *p*-CAN.

Finalement, l'effet de l'incorporation d'azote dans le molybdène a été évalué en préparant divers échantillons avec des degrés variés de nitridation. Il a été démontré que l'incorporation d'azote n'a pas eu d'effet significatif sur la morphologie et chaque échantillon a révélé des agrégats cristallographiques avec des surfaces spécifiques similaires. Cependant, les quantités d'hydrogène chemisorbé et désorbé (par désorption à température programmée) ont augmenté pour des ratios Mo/N décroissants. En procédant aux tests catalytiques sur l'hydrogénation du nitrobenzene, des vitesses supérieures d'hydrogénation ont été observées avec les échantillons de Mo_2N ayant une teneur plus élevée en azote, ce qui a été attribué à une plus grande disponibilité d'hydrogène dissocié hétérolytiquement sur les paires de Mo-N. A contrario, l'hydrogénolyse du groupement –C=O a été favorisé avec le benzaldéhyde par chemisorption homolytique de l'hydrogène sur le molybdène, résultant d'une plus faible teneur en azote. Ces résultats ont clairement démontré que l'incorporation d'azote dans la structure du Mo permet de contrôler la performance de l'hydrogénation ou de l'hydrogénolyse.

Étant un outil performant pour le façonnage de la morphologie des nanoparticules métalliques, la méthode colloïdale a été employée pour concevoir des catalyseurs structurés se révélant efficaces pour la réduction sélective des groupes alcyne et $–NO_2$. Les propriétés de surface des NPs de Pd ont été affinées en (i) changeant la nature de l'agent de stabilisation (électronique *vs.* stérique), (ii) contrôlant la taille des NPs de Pd (2-10 nm) et (iii) greffant les ligands, renfermant des atomes d'azote, sur la surface de nanofibres de carbone/fibres métalliques fritées (CNF/SMF). Dans la semi-hydrogénation de l'acétylène, le résultat catalytique est resté inchangé quant à la nature de l'agent réducteur. Toutefois, un fort effet inhibiteur sur la vitesse d'hydrogénation a été observé en employant un stabilisateur électrostatique (en comparaison des stabilisateurs stériques), ceci étant attribué à des effets géométriques et stériques conjugués. Une diminution de la taille des nanoparticules de Pd (de $8 \rightarrow 2$ nm) a été accompagnée d'une diminution de l'activité mais une plus haute sélectivité pour l'éthylène a été observée. Le greffage d'agents modificateurs renfermant des atomes d'azote dans leur structure (polyvinylpyridine ou polyethylenimine) sur les supports composites de CNF/SMF a conduit à une augmentation significative de la sélectivité pour l'oléfine (jusqu'à 93%) et ce, en ayant une stabilité remarquable durant 120 h en continu. Ceci est attribué à des modifications électroniques (transfert de charge) provenant des interactions entre les nano-cristaux de Pd et le ligand greffé, ce qui est confirmé par des analyses de photospectroscopie de rayons X (XPS). A titre de comparaison, un catalyseur exempt d'agents de stabilisation a fourni une faible sélectivité pour l'éthylène (65%).

Cependant, dépendant du système catalytique, l'enveloppe de ligand organique peut être néfaste pour l'activité et/ou sélectivité. Des particules monodispersées de Ni (de 2 → 14 nm) ont été préparées par le biais de méthodes colloidales, stabilisées par du poly-N-vinyl-2-pyrrolidone (PVP) et testées pour l'hydrogénation du *m*-dinitrobenzene (*m*-DNB). Une activité spécifique (normalisée par les sites actifs, TOF) 6 fois plus grande a été obtenue sur les nanoparticules de Ni les plus grandes. L'influence du PVP a été établi, à savoir que le TOF initial et la sélectivité pour la *m*-nitroaniline (*m*-NAN) ont montré une dépendance marquée vis-à-vis de la présence de ce polymère. Ce résultat a été attribué à l'adsorption préférentielle du PVP sur les atomes de crête et de sommet, laissant les atomes des plans libres. Une augmentation globale de la sélectivité pour la *m*-NAN désiré, y compris à de hautes conversions, a pu être obtenue en déposant les naoparticules monodispersées de 2 nm de Ni sur des fibres de carbone activées (ACF) et en enlevant les traces de PVP par un traitement UV-ozone. Un modèle cinétique selon Langmuir-Hinshelwood comportant deux sites actifs a été employé pour justifier les résultats et s'est révélé cohérent en regard des résultats cinétiques expérimentaux. Ce travail démontre le potentiel du Ni supporté sur des ACF comme étant une formulation catalytique appropriée pour la une production propre et efficace d'anilines fonctionnalisées.

En résumé, cette thèse démontre la possibilité d'effectuer des réactions d'hydrogénation importantes au niveau industriel aussi bien en batch (phase liquide) qu'en continu (phase gazeuse). La distribution des produits de la réaction peut être contrôlée à un niveau nanométrique en ajustant les propriétés de la phase active au moyen de modifications de paramètres structurels (forme allotropique, composition), de modifications du microenvironnement des NP (enveloppe de ligand organique) et par l'optimisation de la taille des particules.

Mots clés: Hydrogénation sélective, conception rationnelle de catalyseurs, nitrures de molybdène, Pd, Ni, supports carbonés structurés, nitroarenes, alkynes.

Table of Contents

List of symbols

Abbreviations

AA	Ascorbic acid
AAS	Absorption atomic spectroscopy
AC	Activated carbon
ACF	Activated carbon fibers
ACN	Acetonitrile
ACS	American Chemical Society
AN	Aniline
AOT	Sodium di-2-ethylhexylsulfosuccinate
a.u.	Arbitrary units
BE	Binding energy (eV)
BET	Brunauer–Emmett–Teller
Bipy	Bipyridine
But	n-bButanol
ACN	Acetonitrile
CNF	Carbon nanofibers
CVD	Carbon vapor deposition
Et	Ethanol

fcc	Face-centered cubic
FEG	Field emission gun
FID	Flame ionization detector
GCI	Green Chemistry Institute
GHSV	Gas hourly space velocity
hcp	Hexagonal close packed
hex	Hexagonal
HexOH	Hexanol
HH	Hydrazine hydrate
HRSEM	High resolution scanning electron microscopy
HRTEM	High resolution transmission electron microscopy
i.d.	Internal diameter
IR	Infrared spectroscopy
JCPDS-ICDD	Joint Committee on Powder Diffraction Standards - International Center for Diffraction Data
m-DNB	*meta*-Dinitrobenzene.
Me	Metal
Met	Methanol
m-NAN	*meta*-Nitroaniline
MO	Molecular orbital
m-PDA	*meta*-Phenylenediamine
NB	Nitrobenzene
NMR	Nuclear magnetic resonance
NPs	Nanoparticles

p-CNB	*para*-Chloronitrobenzene
p-CAN	*para*-Chloroaniline
PEI	Polyethylenimine
PZC	Point of zero charge
PrOH	Propanol
PVA	Polyvinylalcohol
PVP	Polyvinylpyrrolidone.
PVPy	Polyvinylpyridine
RDS	Rate determining step
SE	Secondary-electron
SEM	Scanning electron microscopy
SMF	Sintered metal fibers
STEM	Scanning transmission electron microscopy
SSA	Specific surface area (m^2 g^{-1})
TCD	Thermal conductivity detector
TEM	Transmission electron microscopy
TPA	Temperature programmed adsorption
TOF	Turnover frequency (s^{-1})
TPD	Temperature programmed desorption
TPR	Temperature programmed reduction
TTAB	Tetradecyltrimethylammonium.
UV	Ultra-violet
UVO	UV-ozone

% wt.	Percentage by weight
v/v	Volume/volume
w/w	Weight/weight
XPS	X-Ray photoelectron spectroscopy
XRD	X-Ray diffractometry
ZSM	Zeolite Socony Mobil

Roman symbols

C_i	Concentration of compound *i* in bulk liquid (mol dm^{-3})
d	Diameter of the metal particle (nm)
d_{chem}	Particle size from hydrogen chemisorption measurements (nm)
d_{TEM}	Mean Pd particle size from TEM analysis (nm)
$\mathrm{d_{hkl}}$	Diameter of the metal particle using the Scherrer equation (nm)
D	Dispersion
D-P	Deposition-precipitation
F	Inlet reactant molar flow (mol min^{-1})
k_i	Rate constant of reaction i (µmol g^{-1} h^{-1})
k_j	Kinetic constant of reaction step j (mol mol^{-1} min^{-1})
K_i	Adsorption constant of compound i (l mol^{-1})
K	Dimensionless crystallite shape factor in the Scherrer equation
M_{i}	Molar mass of compound i (g mol^{-1})
m	Mass (g)
n	Amount of compound i (mol)

n_i	Number of metal particles of diameter d_i
P_i	Pressure of gas i (bar)
P_0	Initial pressure (bar)
R	Transformation rate of compound i (mol mol^{-1} min^{-1})
r	Reaction rate (mol mol^{-1} min^{-1})
R_i	Initial hydrogenation rate of the *para*-substituted nitroarene (mol dm^{-3} min^{-1})
R_0	Initial hydrogenation rate of reference benzene derivate (mol dm^{-3} min^{-1})
S_i	Selectivity with respect to compound *i*
S_i	Specific surface area of compound *i* ($\mathrm{m_i^2\ g_i^{-1}}$)
T	Temperature (K)
t	Time (min)
$\mathrm{t_R}$	Reaction time (s)
V	Volume (dm^3)
W	Weight (g)
X	Conversion (%)
X_i	Fractional conversion of reactant *i*
X_0	Fractional initial conversion
x_i	Molar fraction of compound *i*

Greek letters

ρ	Hammett reaction constant
ρ_i	Density of compound i (g cm^{-3})
σ	Sigma bond

σ_i	Hammett substituent constant
σ_p	Hammett substituent constant relative to *para*-substituted nitroarenes
λ	Incident radiation wavelength (Å)
θ_i	Surface coverage of compound i

Subscripts

Edge	Edge atoms
F	Fermi level
i	Generic compound
imp.	Impregration
max	Maximum
Plane	Plane atoms
tot	Total
Vertex	Vertex atoms

Chapter 1

Introduction

The subject and objectives of the work are presented in this chapter and the structure of the thesis is outlined.

1.1 Motivation and Objectives

Catalytic hydrogenation is one of the key processes in the manufacturing of pharmaceuticals and fine chemicals, involved in approximately 30-40% of these chemical processes [1]. In the last decades, the nanosciences have consolidated as a major direction in chemical research due to the unique properties of nanoparticles (NPs). The conventional methodology applied for catalyst development and optimization has been a "trial and error" approach. With the advancement of physico-chemical methods for characterization of solid materials, especially under working conditions ("in situ" or "operando"), the identification of the active component is becoming a reality. Indeed, the understanding of the interplay between catalytically active species and the surrounding environment is decisive to design catalysts in a more rational approach, which is based on a multidisciplinary combination of new advances in catalyst synthesis and characterization.

"Rational Catalyst Design" has been applied in this thesis to develop new effective materials for selective multiphase hydrogenations. Since the catalyst performance depends on the contribution of various components (chemical compositions, structures of the bulk and the surface, morphologies, but also conditions to which it is exposed in the reaction), rational catalyst design has to cover multiple levels at scale from the nano-design of the active sites to the macroscale of the reactor design (**Figure 1.1.**).

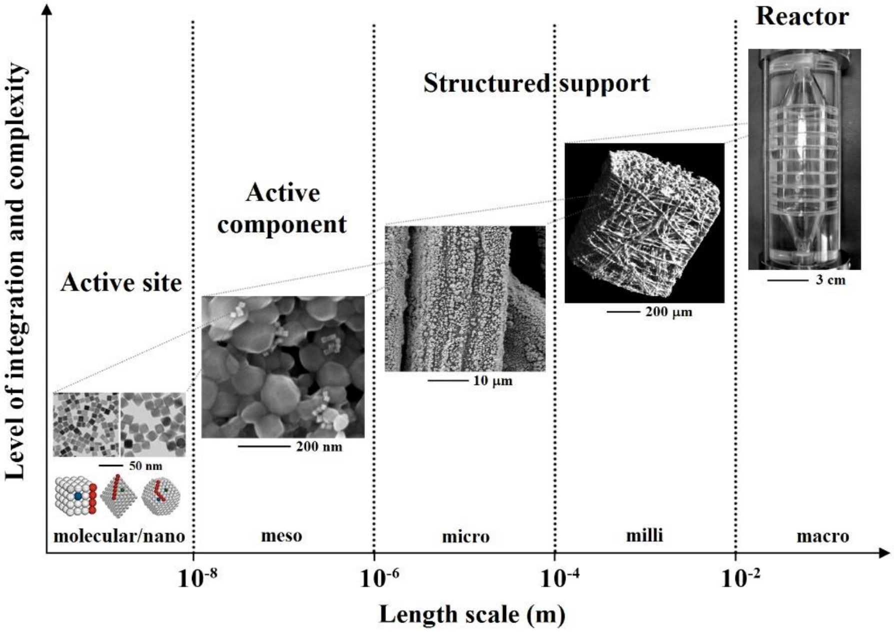

Figure 1.1. Extent of the rational catalyst design over several scales. Adapted from Ref [2].

The ultimate goal of any catalyst design process is to optimize catalytic performance *via* modifications of the chemical composition and morphology of the catalyst [3]. The strategy applied in this work is based on the selection of an active component, optimization of its intrinsic properties and its deposition on a structured support.

The thesis deals with several key issues encountered in the partial catalytic reduction of substituted nitroaromatic compounds and alkynes, two classes of industrially relevant reactions. In the selective catalytic hydrogenation of polyfunctional molecules, the exclusive attack of a single substituent in the presence of other functional groups is particularly challenging since the reduction of these groups may be easier than the target group. Conventional processes based on large amounts of metal oxide in acid media can no longer be considered sustainable due to low overall product yield and the environmental issues associated with the formation of toxic by-products. Moreover, in the cleaner catalytic alternative over conventional noble metals (such as Pd, Ru), over-hydrogenation is difficult to avoid. Besides, alkynes can be fully hydrogenated to alkanes and the use of scarce noble metals is expensive. Therefore, our efforts were first concentrated on the choice of the active phase that could replace the noble metals, such is the case of molybdenum nitride. The catalytic use of molybdenum nitrides has received great attention for hydrogen mediated reactions and in particular, for selective hydrogenations [4] with promising results in the production of functionalized anilines. A systematical study of the parameters affecting the catalytic response was carried out to design a catalyst highly selective to the target products. To boost the activity of Mo-nitrides, low contents (≤ 0.25% wt.) of noble metals can be incorporated.

Another aspect associated with most of catalytic hydrogenations is their structure sensitivity. In this kind of reactions, the metal nanoparticle size has a significant impact on the catalyst activity and selectivity. Colloidal methods provide a good control of the nanoparticle size, which allows setting out a relation between the catalytic performance and the properties of the active phase. A large number of variables are involved in the preparation of metal NPs like the reducing and stabilization agents. Rational catalyst design identifies precisely the role of each component allowing an increased catalyst performance (high product selectivity at high conversions).

1.2 Structure of the Work

The thesis focuses on catalyst design and optimization for selective hydrogenation reactions. In **Chapter 2**, the current state of the art in the field of heterogeneous catalysis relevant to this work is reviewed. In **Chapter 3** is proposed a new catalyst formulation based on Mo-nitrides for hydrogenation of nitroaromatic compounds. It is subdivided in four sub-chapters:

In **sub-chapter 3.1**, a tetragonal molybdenum nitride (β-Mo_2N) has been prepared and tested in liquid phase hydrogenation of a series of para-substituted nitrobenzenes to give the corresponding aromatic amine. The catalytic results were compared with those obtained over Pd/Al_2O_3, used as a benchmark. The effect of electron-donating and electron-withdrawing groups was evaluated and a reaction mechanism has been established through a Hammett relationship. In **sub-chapter 3.2**, the remarkable properties of β-Mo_2N were combined with the use of Au in $Au/Mo_2N$and tested in both liquid and gas phase selective hydrogenation of *p*-chloronitrobenzene. The catalytic action of Au/Mo_2N was also compared with Au/Al_2O_3 (as benchmark) to probe a possible support effect. **Sub-chapter 3.3** analyzes the independent effect of the Mo-nitride crystallographic phase (tetragonal β-Mo_2N *vs.* cubic γ-Mo_2N) and surface area in the *p*-chloronitrobenzene gas phase hydrogenation. A series of relevant characterization techniques were used (BET, TPD, XRD, SEM, XPS) to link catalytic response with structural properties and hydrogen uptake abilities of the catalyst. Gold was incorporated on both nitrides to enhance the corresponding amine production rates. The approach of active phase design by modification of structural parameters was taken further to study the catalytic effect of systematic increased nitrogen incorporation in Mo structure on hydrogenation and hydrogenolysis **(sub-chapter 3.4)**. A series of characterization measurements were carried out (XRD, XPS) to quantify the Mo/N ratio.

A move from powders to structured systems can result in morphological changes (see **Figure 1.1**). Different carbon-based supports were used for monodispersed metal NPs in the hydrogenation of alkynes and nitroarenes. **(Chapter 4).** Thus, Pd NPs have been deposited on carbon nanofibers (CNF) grown on structured sintered metal fibers (SMF) (**sub-chapter 4.1**). It was demonstrated that the surface properties of Pd NPs could be finely tuned by an organic ligand shell and precise control of the NPs size. Bearing this in mind, Ni NPs were supported on activated carbon fibers (ACF) for the design of a highly selective catalyst for 1,3-dinitrobenzene (*m*-DNB) hydrogenation (**sub-chapter 4.2**).

Finally, the findings of the study are summarized in **Chapter 5** and general conclusions along an outlook are given.

Chapter 2

State of the Art

This chapter presents the current state of research in the field of catalyst design for hydrogenations. A first part discusses molybdenum nitrides systems, regarding their structure, preparation, and applications for the hydrogenation of aromatic nitro-compounds and alkynes. The second part deals with the design of structured catalyst, based on carbon supports and metal NPs of controlled size prepared *via* colloidal methods. Their use for gas-phase selective hydrogenation of C≡C and for liquid phase hydrogenation of aromatic nitro-compounds is also addressed.

2.1. Molybdenum-Nitride Based Catalytic Systems

Molybdenum nitrides are compounds consisting of nitrogen atoms dissolved interstitially in the lattice of Mo. They present not only unique physical and chemical properties such as great strength and durability, hardness and superconductivity but can also adsorb and activate hydrogen [4]. The catalytic properties of this material attract a lot of attention from the 80's [5], inspired by the pioneering work of Levy and Boudart on tungsten carbides [6]. In several types of reactions such as hydrogen mediated reactions, Mo-nitrides, among group VI nitrides, demonstrate catalytic activities approaching or surpassing those of noble metals [4, 7].

In carbon monoxide hydrogenation, for instance, cubic Mo nitride demonstrates higher hydrogenation activity as compared to Ru [8]. This was ascribed to modification of electron density (direction and amount of charge transfer) due to the nitrogen incorporation and contraction of the metal d-band due to the expansion of the Mo lattice constants. This phenomenon can be explained when considering the interaction of the bonding state of the hydrogen with the metal d-band. The metal d-band hybridizes with the bonding (σ) orbital of the H_2 to form bonding (d-σ) and antibonding (d-σ)* states, as illustrated in **Figure 2.1**.

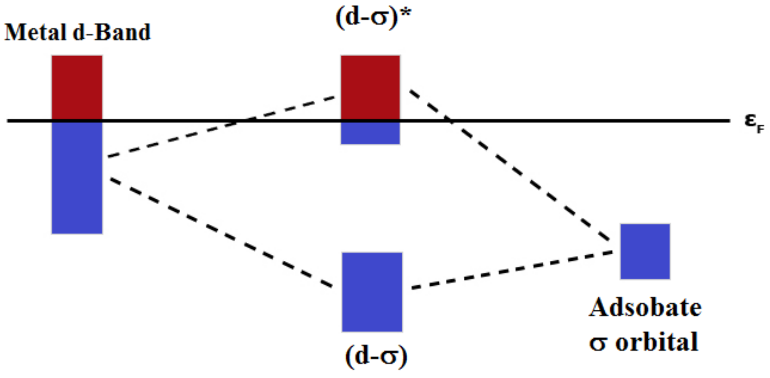

Figure 2.1. Molecular orbital model applied to the d-band theory, adapted from [9]

In the example shown above, the (d-σ) state is full, but the extent of filling of the (d-σ)* state depends on the local electronic structure of the metal at the surface, *i.e.* the surface density of states. An increased filling of the antibonding (d-σ)* state corresponds to a destabilization of the metal-adsorbate interaction and hence, weaker binding. In practice, the location of the d-band center closely correlates with the extent of filling of the (d-σ)* molecular orbital (MO) [10].

In the context of chemisorption of H_2 on Mo-nitride surface, a higher d-band center (smaller $\varepsilon_{\text{d-band center}} - \varepsilon_F$, which occurs through the incorporation of N in Mo lattice) corresponds to an increase in energy (relative to the Fermi level (ε_F), as the highest energy level occupied by electrons) and subsequent decrease in filling of the (d-σ)* state. It implies that the metal-adsorbate system is less destabilized, which translates to stronger binding between metal and adsorbate.

2.1.1. Structure

The chemistry of Mo-nitrides is similar to that of pure metals. The non-metallic nitrogen atoms occupy interstitial positions between metallic Mo atoms, hence this material is known as interstitial alloy [11]. They adopt simple metal structures with the metal atoms forming lattices of body-centered tetragonal (β-Mo_2N), face-centered cubic (fcc γ-Mo_2N) or simple hexagonal (hex δ-MoN). However, this thesis will focus on the first two allotropic forms, which have been the most commonly synthesized and used for catalytic applications (**Figure 2.2**).

The nitrogen content in beta-phase is still a matter of debate and although a Mo/N ratio of *ca.* 2.5 has been the most widely obtained [12-14], different ratios over the range 2.3-2.8 have also been reported [15, 16].

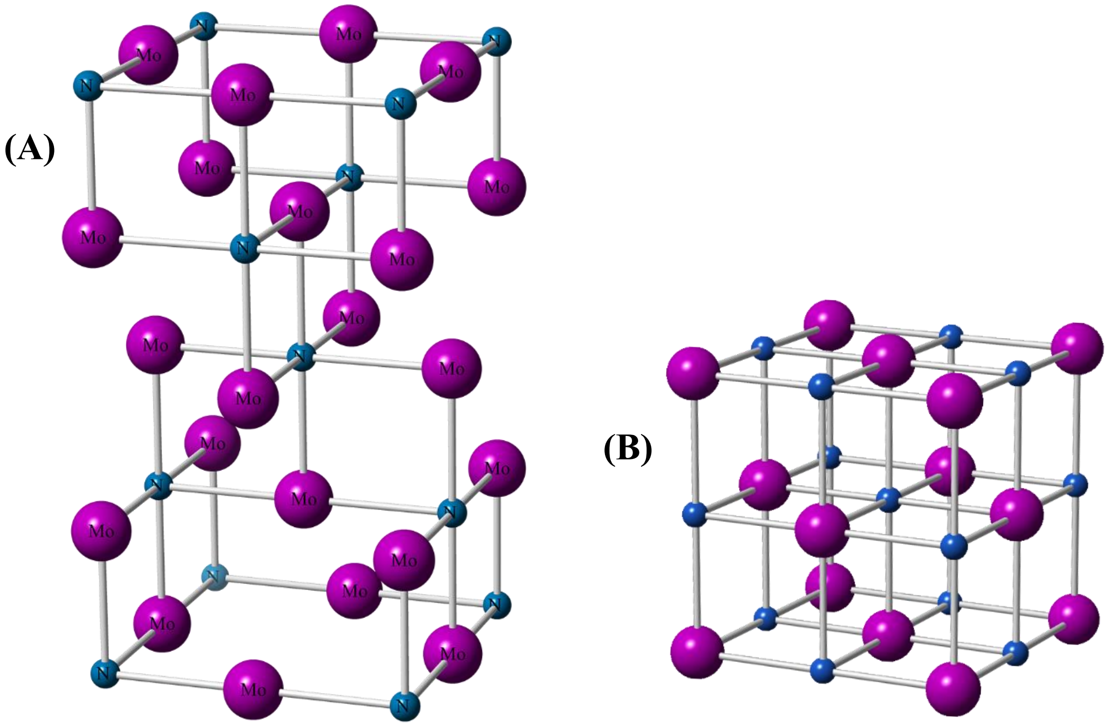

Figure 2.2. Representation of the crystallographic structure of **(A)** *β*-Mo_2N and **(B)** *γ*-Mo_2N.

Note: large purple and small blue spheres represent Mo and N atoms, respectively.

2.1.2. Mechanism of H_2 Adsorption and Activation

On the crystal structures represented in **Figure 2.2**, different active sites can be identified, such as (i) full coordinated Mo and (ii) partially coordinated Mo. The latter correspond to metallic Mo edges and nitrogen deficient sites. Few attempts have been made to propose a mechanism of the hydrogen adsorption and activation on Mo nitrides. Li *et al.* [17] suggested a mechanism of hydrogen activation involving a heterolytic dissociation on Mo-N pairs:

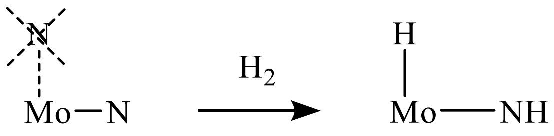

$$\overset{\cancel{\text{N}}}{\text{Mo}}\text{—N} \xrightarrow{H_2} \overset{\text{H}}{\text{Mo}}\text{—NH}$$

where the crossed N atom represents the nitrogen deficient site of Mo present on the surface. Such N-deficient sites are suggested to be suppressed during the nitride passivation and regenerated through reduction by H_2:

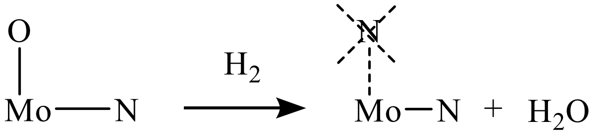

It has been shown that high concentration of nitrogen deficient Mo surface atoms are found on Mo-nitrides with low BET surface area [18]. Besides, the adsorption of hydrogen per unit of surface increases with decreasing surface area and/or increasing particle size of Mo_2N [19], attributed to the retention of hydrogen on subsurface sites [20]. It has also been proposed [4] that a high concentration of the surface Mo atoms could favor homolytic dissociation giving Mo–H moieties. This process has been depicted as:

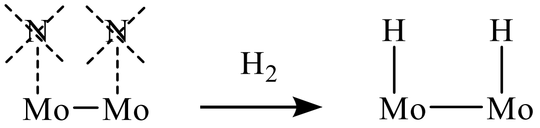

Owing to the low Mo–H bond strength, such hydrogen could be transferred from the surface to reactant molecules in the form of a hydrogen radical-like species. Yet, there is no experimental evidence to either confirm or discriminate between the heterolytic and homolytic dissociation of H_2. Moreover, hydridic hydrogen may also migrate from the surface to the sub-surface layer and/or interstices. Since sub-surface is the predominant location of the nitrogen atoms in the crystal, the much higher strength of the N–H bond than that of the Mo–H bond provides the driving force for this process [21].

Hydrogen adsorption on Mo_2N has also been studied by Haddix *et al.* [22] using NMR. Hydrogen adsorbs on the surface at room temperature in the form of localized rafts strongly bound H atoms, occupying at most 10% of the total N_2 BET surface area. Accordingly, the authors also suggested that hydrogen adsorption occurs at nitrogen-deficient sites of Mo present on the nitride surface. In an analogous way, this observation on the catalytically active sites was further corroborated by a study of the influence of N/Mo ratio on the rate of hydrodenitrogenation [23], where activity decreased as the N/Mo ratio increased. Proposal concerning "types" of hydrogen was pushed forward [24] based on temperature-programmed adsorption (TPA) and desorption (TPD) results, thus defining low and high temperature desorption sites. Depending on the temperature of desorption, three kinds of hydrogen species, *i.e.* weak, moderately strong and strong forms, were produced in the H_2-Mo_2N system. They were associated to sites located on the surface, in subsurface and bulk of the Mo-nitride, respectively.

2.1.3. Preparation

A number of procedures have been investigated for the synthesis of molybdenum nitride. Molybdenum nitride preparation methods applied to date can be divided in conventional high temperature (1400–1900 K) procedures and controlled temperature programmed techniques.

Conventional methods were reported using current arc discharge [25], pulsed laser deposition of molybdenum metal [16] and plasma spraying [26]. Developed to a lesser extent, there is also instances in the literature of the use of thermal reduction nitridation of $MoCl_5$ with either NaN_3 (at 823 K) [27, 28], or urea (at 873 K) [29], both giving nitrides with low specific surface area (SSA, m^2 g^{-1}). However, sol-gel [30] or thermal decomposition of ammonium molybdate salt under argon [31, 32] form nitride with high SSA (≈ 70 m^2 g^{-1}). For the latter one, a high ratio Mo (IV)/Mo (II), as well as the presence of C or O, have shown to raise the SSA up to 150 m^2 g^{-1}. Apart from the difficulties involved in implementing some of the preparation methods described above, the control of structural parameters is difficult and the conventional approach would not be suitable for rational catalyst design.

The use of alternative controlled temperature programmed treatments facilitates applications in catalysis due to the delivery of metal nitrides with higher SSA (up to 225 $m^2 g^{-1}$) [33]. The most commonly used temperature programmed reaction between MoO_3 and NH_3 at high final temperature (800-1000 K) produces mainly γ-Mo_2N (SSA = 100-220 $m^2 g^{-1}$) [33-36] but there is also evidence in the literature for the formation of β-Mo_2N (SSA = 10-40 $m^2 g^{-1}$) [14, 37]. A more sustainable alternative is to use H_2+N_2 mixture. With the latter treatment the formation of either β-Mo_2N (SSA < 12 $m^2 g^{-1}$) [13, 38, 39] or γ-Mo_2N (SSA = 40-120 $m^2 g^{-1}$) [36, 40] has been reported. In order to obtain high SSA (up to 170 $m^2 g^{-1}$), it has been shown that slow temperature ramping rate (≤ 1 K min^{-1}) [36] and/or high gas space velocity (typically 150000 h^{-1}) [20] are required. This has been linked to the presence of water which reduces surface area through hydrothermal sintering or/and lattice fluidization mechanisms [41]. In the particular case of preparation *via* N_2+H_2 mixtures, there is a dependency on the gas composition (lower % v/v N_2/H_2 increases SSA) where MoO_2 and Mo have been suggested as reaction intermediates for the formation of γ-Mo_2N [36]. Wise and Markel [41] have reported that the formation of an intermediate MoO_2 with a high SSA (≈ 60 $m^2 g^{-1}$) would give a γ-Mo_2N with a high SSA (≈ 130 $m^2 g^{-1}$), whereas the presence of Mo was associated with water and low surface area. However, Gong and co-workers [13] attributed the low SSA (<10 $m^2 g^{-1}$) of β-Mo_2N to the presence of the intermediate MoO_2. In the synthesis with NH_3, two others intermediates, H_xMoO_3 and γ-Mo_2ON_{1-y}, can be present and associated with the formation of (i) high surface area γ-Mo_2N and (ii) Mo with low surface area γ-Mo_2N, respectively [42]. In spite of the allotropic form synthesized, the passivation step, *i.e.* formation of an oxynitride or oxide layer slightly thicker than one monolayer [19], results in a substantial lost in surface area [43].

To sum up, previous studies have proposed the participation of MoO_2 [44], MoO_xH_y [45], Mo_4O_{11} [46] and Mo [13] as intermediates during the temperature programmed treatment of MoO_3 to form Mo nitride. Thus, Matsuda [45] and coworkers have suggested that reduction of MoO_3 at 623 K occurred through molybdenum bronze (H_xMoO_3) and MoO_2, Wise and Markel [41] reported the formation of MoO_2 and Mo intermediates at 773 K and Słoczyński [47] proposed a transition of MoO_3 to Mo_4O_{11} and MoO_2 at $T < 823$ K. More recently, Cárdenas-Lizana *et al.* explicitly identified the reaction intermediates in the beta Mo-nitride synthesis at 933 K [48]. They proposed a stepwise reduction ($MoO_3 \rightarrow MoO_2 \rightarrow Mo$) and subsequent nitridation ($Mo \rightarrow \beta\text{-}Mo_2N$). It was also the first attempt of catalytic nitroarene hydrogenation with this nitride form.

2.1.4. Molybdenum Nitrides as Catalysts in Selective Hydrogenations

High hydrogenation catalytic activity can be expected with the use of Mo-nitrides able to chemisorb and dissociate H_2 [4, 49], having a distinct activation mechanism with different surface structure. Thus, the catalytic properties are mainly affected by the SSA, which has been shown to be linked to the ratio of crystallographic planes (200)/(111) [44]. A series of Mo_2N samples prepared by Zhang et al. [50] highlighted that (111) plane atoms adsorb more hydrogen. Moreover, it has been shown that hydrogen adsorption/activation per unit of surface increases with decreasing the surface area and/or increasing the particle size of Mo_2N [19]. Surface area depends on the crystallographic phase of the molybdenum nitride: low SSA Mo-nitrides corresponds to a tetragonal β-phase, while a cubic γ-phase presents a high SSA. The use of molybdenum nitrides in hydrogen mediated reactions is limited but they have been successfully used as catalytic system in the hydrodenitrogenation of pyridine where γ-Mo_2N showed an activity superior to traditional Ni-Mo/Al_2O_3 [19] catalyst. Moreover, the activity depends on the phase used. For example, γ-Mo_2N has been shown to be more active than β-Mo_2N for hydrodenitrogenation reactions. It has been actually reported that the activity was related to the amount of NH_3 chemisorbed in NH_3-TPD, indicating that the reaction occurs on the acid sites [19]. However, γ-Mo_2N crystallite surface was associated with sites having lower activity for the hydrogenation of carbazole [14]. Mo and β-Mo_2N showed a higher activity (per surface area) than γ-Mo_2N, which was attributed to their large particles. Indeed, Nagai and co-corkers assumed that the hydrogenation was favored on the surface grain boundary of large particles and more specifically, Mo (110). Mo_2N powders have already been widely used in the ammonia synthesis [38, 51], hydrotreatment activities [50], such as hydrogenolysis of alkanes [52], dehydrogenation and isomerization [53], hydrodesulphurization [54], hydrodechlorination [55] and hydrodenitrogenation reactions [52]. It was also used in hydrogenation in liquid phase of long chain alkadienes [56], methyl benzoate [57], and in gas phase of CO [34] and crotonaldehyde [58]. Indeed, in the case of hydrogenation reactions, hydrogen adsorption microcalorimetric study has shown that Mo_2N is able to chemisorb hydrogen with various adsorption strengths depending on the SSA [59]. Moreover, no change in the surface electronic structure was noticed by X-ray photoelectron spectroscopy (XPS) after γ-Mo_2N reduction in H_2 during 3h [60]. Some studies have used a support to enhance the dispersion of the nitride, such as alumina [37, 61], zeolites [62] and carbon [58]. Finally, Cairns and co-workers [39], have added by impregnation 1% wt. Au, Pd, Ni and Cu dopants on MoO_3 and noticed some changes on the morphology of the β-Mo_2N formed after reduction and nitridation. However, they did not proceed with catalytic tests on this modified nitride.

2.1.5 Liquid and Gas Phase Hydrogenation of Aromatic Nitro-Compounds

Aromatic amino compounds are widely used in chemical industry. Halogenated anilines in particular are important intermediates for synthesis of fine chemicals such as dyes, drugs, herbicides and pesticides [63]. Their production usually involves Bechamp reaction [64] in metal–acid (Fe/HCl) reducing system or selective hydrogenation over heterogeneous catalysts. The first route leads to the production of acid effluents and toxic wastes in the form of iron oxides that have to be separated and treated before disposal. When compared to the traditional route, the selective catalytic hydrogenation appears to be a more sustainable way.

The primary challenge is to avoid cleavage or hydrogenation of other reducible groups [65]. In the hydrogenation of halonitroderivates the main problem is the cleavage of the halo group from the aromatic ring, which in most reaction systems is very difficult to avoid [66, 67]. It has been proven that this C-Cl scission can be controlled by using appropriate catalyst and depends on metal dispersion [68], the nature of support [69] and incorporation of different additives [70]. Besides, one of the most effective ways to influence the selectivity, activity and stability of the catalysts for hydrogenation reactions is the addition of a second metal to the active phase. When compared with the monometallic catalysts, this incorporation can either modify the electron properties of the individual metals [71], or alter the geometry of the metal particles placed on the support. This occurs by the migration of mobile oxidic species from the support over the metal surface (encapsulation) or by sintering of the metal particles [72]. Electronic and geometric effects usually overlap and every metal-oxide combination interacts specifically. Thus, enhancement of Mo-nitrides by a second metal seems to be an appropriate method for improved catalytic performance.

2.2 Pd and Ni Based Structured Catalysts

2.2.1 Structure Sensitivity

When a reaction is catalyzed by metal nanoparticles (NP), their morphology may or may not influence the activity and selectivity. The concept of structure sensitivity was already reported long time ago. Already before the end of the 1960s, it had become clear that the rates of some catalyzed reactions expressed per unit area (or per active site) as turnover frequency (TOF) were almost independent of metal particle size and were referred to as *facile*. On the other hand, if some form of TOF dependence on the particle size was observed, the reactions were called *demanding* [73].

The different categories of TOF dependency with NP size are represented in **Figure 2.3**. The TOF of structure-insensitive reactions is not affected by particle size (curve A). In structure-sensitive reactions, a decrease of TOF with increasing the particle size is referred to as *sympathetic* (curve B) or it may increase together with the increase of particle size (curve C) in *antipathetic* structure sensitive reactions.

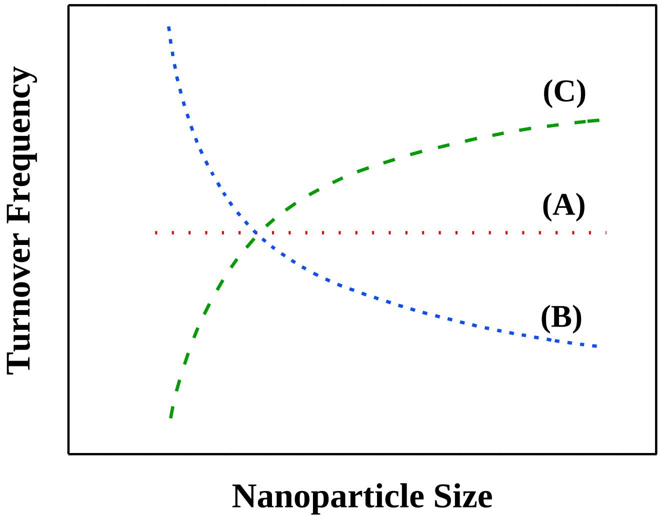

Figure 2.3. Possible TOF dependence on the metal NP size. Adapted from Bond *et al.* [73].

The relative distribution of types of active sites on a nanoparticle depends on its size. Surface atoms vary essentially in their coordination number. Accordingly, it is possible to distinguish between (i) low-coordinated atoms located on edges or vertexes and (ii) atoms with higher coordination placed on planes or directly underneath at the outermost layer by still accessible to reacting molecules, with different reactivities [74]. The ratio between surface atom types changes substantially when varying the size of a nanocrystal. As represented in **Figure 2.4** for a non-ideal cube-octahedron model, the fraction of atoms located on crystallographic planes increases with size at the expense of edge and vertex atoms.

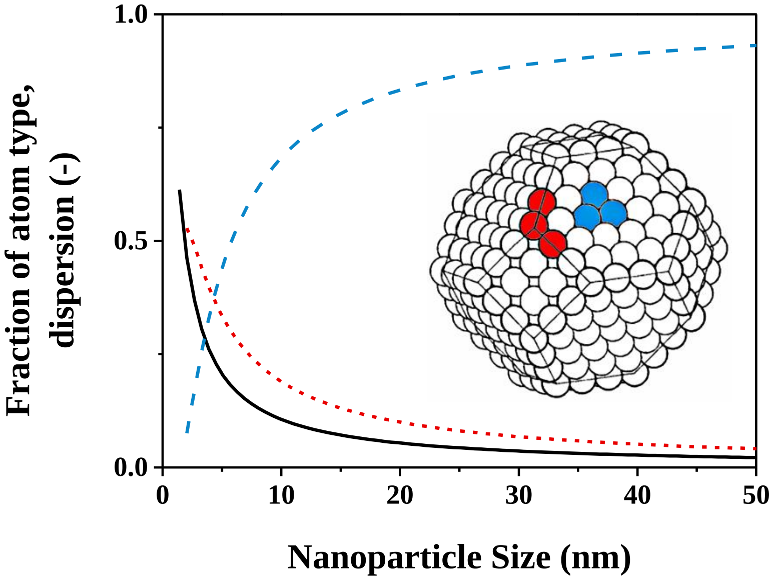

Figure 2.4. Evolution of the fraction on atom type (red: edge and vertex atoms, blue: plane atoms) and metal particle dispersion with the NP size, calculated from van Hardeveld's cubo-octahedron non-ideal model [75]. Associated crystallite representation adapted from the same reference.

A set of models was proposed by van Hardeveld and Hartog [75] in which calculations were performed on the variation in the populations of atoms of specified coordination number with crystallite size for a number of perfect and non-ideal crystal geometries (cube, octahedron, tetrahedron, cube-octahedron, etc.). From this study, it is possible to determine the relative proportion of a given type of surface atom (to the total surface atoms) with nanoparticle size, which was used to describe the structure sensitivity in various studies [76, 77]. Therefore, the catalytic performance of structure-sensitive reactions are strongly affected by both the size and shape of the nanocrystals in a catalyst [78, 79] and this could be used for rationally designing the catalyst.

In the hydrogenation of alkynes, an increasing TOF was reported for Pd NPs in the range of 4 to 10 nm [74] and invariant activity for larger particles [79]. However, higher activity was recorded for smaller crystallites in the hydrogenation of 2-butyne-1,4-diol over unsupported Pd NPs [80]. Structure sensitivity has been extensively studied in the hydrogenation of acetylene, where TOF is usually found to increase with nanoparticle size. For example, Borodzinski [76] observed antipathetic structure sensitivity over Pd/SiO_2 catalysts (4 to 26 nm) and attributed it to geometric effects that define the average surface concentration of active site. Furthermore, Tribolet *et al.* [81] reported a drop (> one order of magnitude) in TOF for Pd NPs below 3 nm which was ascribed to an increased adsorption strength of the electron-rich C≡C on electron deficient small NPs. The studies of particle size effects in hydrogenation of functionalized nitroarenes over Ni-, Ag- and Pt-based catalysts suggest both sympathetic and antipathetic structure sensitivities depending on the active metal used [82, 83]. Finally, it is worth mentioning that the support also has significant effect on the size and shape of the supported metal. An example was reported by Coq *et al.* [68] for the Pt-catalyzed *p*-chloronitrobenzene (*p*-CNB) hydrogenation.

2.2.2 Colloidal Method for Metal Nanoparticles Preparation

Control over the NP size and shape is of utmost importance for the catalysis since the catalytic activity and selectivity may be strongly affected by the nanocrystal morphology [76, 84]. In heterogeneous catalysis, colloidal methods are known to outperform the traditional approach based on impregnation of metal precursors followed by activation [74]. Indeed, the latter often leads to broad particle size distribution and makes it very difficult to control reactivity. Colloidal techniques have emerged as a powerful tool for tailoring metal nanoparticle morphology [85, 86]. Two main components can be identified in the synthesis of nanocolloids. First, the reducing agent that promotes the particles reduction to a zero-valent state, typically active for hydrogenations. The second one being the stabilizer, preventing metal NP agglomeration. Among stabilizers, two main types can be identified, namely steric stabilization through polymeric layers [87, 88] and electrostatic stabilization [89] *via* surface charges resulting in repulsion between NPs. The two aforementioned components allow size control of the NPs therefore leading to a narrow size distribution which, in turn, can affect the catalytic response of structure-sensitive reactions. Typically, stabilizing agents are linear and branched polymers, surfactants, polyelectrolytes, ionic liquids or ligands [84]. Moreover, catalytic properties of formed NPs can be controlled by using modifiers. These substances can influence catalytic response causing different effects such as active site blocking, electronic effects or site separation. Modifier can be incorporated in the support, and further interaction with NPs leads to its migration on metal surface.

Formation mechanism

During the NP formation, colloidal nucleation is the first step of the crystallization process, followed by the growth. Nucleation is expected to follow the mechanism proposed by LaMer and co-workers in the early 50's [90] and illustrated later by Xia *et al.* [85]. During the decomposition of a metal precursor in solution (see **Figure 2.5**), the atomic concentration increases steadily with time. Once the critical atom concentration is reached, *i.e.* "supersaturation" level, the atoms start to aggregate in form of small clusters in a self-nucleation process. The clusters keep growing parallel to a decrease of the concentration of metal atoms in solution. Consequently, a minimum level of supersaturation is then reached, the nuclei growth ceases and an equilibrium state is reached between the atoms in solution and the atoms on the surface of the nanocrystal. Apart from the growth *via* atomic addition, agglomeration can occur when the nuclei and nanocrystals merge into larger objects [91].

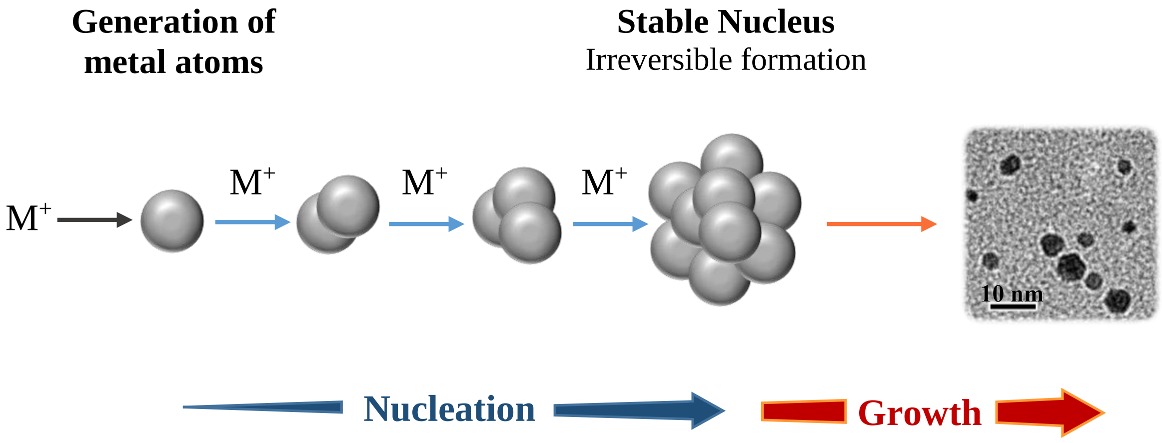

Figure 2.5. Schematic representation of NP formation, illustrating the generation of atoms, nucleation and subsequent growth.

Nucleation is the result of a complex interplay of factors such as the reaction conditions (*e.g.* concentrations, temperature, stirring rate) or the difference between the redox potentials of the metal salt and the reducing agent. In this respect, the reduction rate of the metal precursor play an important role in the nucleation process. NPs size can be controlled by varying the proportion of particle nucleation *vs.* growth. Thus, for a given concentration of metal ions, high degree of nucleation will result in abundant small particles formation whereas relatively small quantities of large particles will be formed if the growth stage dominates. To achieve a high monodispersivity of metal NPs, the nucleation must be complete for all the particle seeds before the self-sharpening growth step begins [92]. The reduction kinetics of the metal precursor can be controlled by the concentration of the metal precursor, the reaction temperature and/or pH and the strength and concentration of the reducing agent [74, 84, 93]. As for the growth, a competition occurs between a favorable decrease in bulk energy and an increase in surface energy which favors dissolution.

2.2.3 Structured Carbon Supports for Catalytic Applications (CNF, ACF)

A step further in the rational catalyst design is an incorporation of metal nanocrystals on structured supports. The use of structured carbon for supported metals is attracting the interest in general [94, 95], for alkyne to alkene hydrogenation [96, 97] and for the chemoselective hydrogenation of functionalized nitroarenes [98, 99], in particular. Being inherently made of open macrostructures, they present several advantages such as enhanced heat and mass transfer, low pressure drop and improved reactant access to the active phase. While the limitations of powder catalysts militate against the viability of these types of catalysts in terms of process scale up and industrial implementation, structured supports are easy to handle and separate from the reaction mixture.

Carbonaceous supports have been used for a long time in heterogeneous catalysis because they can satisfy most of the desirable properties required for a suitable support [100]. The high interest they raise is largely due to their higher resistance to acidic/basic media than conventional oxide supports, high surface area, modifiable surface chemistry, adjustable porosity and easy recovery of the supported metal by controlled combustion [101]. With a graphitic mesoporous nature, carbon nanofibers (CNF) have been used in several catalytic applications such as gas phase hydrogenation of cinnamaldehyde [102] or phenol [103]. As component of a novel composite support, CNF were also grown on Inconel-based sintered metal fibers (SMF) *via* carbon vapor deposition (CVD) method [104, 105]. In the *semi*-hydrogenation of acetylene, the higher (10 times) TOF recorded with Pd/CNF/SMF as compared to Pd supported on activated carbon fibers (ACF) was attributed to a strong interaction of Pd with the CNF [81]. ACF were successfully used in the selective hydrogenations of 2-butyne-1,4-diol [106], 1-hexyne [107] and nitrobenzene [108]. It is worth to note that the pronounced catalyst deactivation was observed for ACF-supported Pt and Ni in the hydrogenation of citral [109]. A problem of catalyst deactivation was solved by immobilized ionic liquid layer on ACF into which the metallic transition metal species have been incorporated [110].

In the hydrogenation of nitrobenzene, higher reaction rates were recorded with activated carbon (AC) supported Ni in comparison to Ni/CNF, both treated by a mixture of acids [111]. This was attributed to the greater surface acidity that served to enhance nitrobenzene activation. This is actually linked to the possibility of modifying the nature and concentration of surface functional groups by oxidizing carbon. By treatment with strongly oxidizing media in gas or in liquid phase, oxygen-containing groups can be introduced on the surface of CNF and ACF. They decrease the hydrophobicity of the carbon, thus, making the surface more suitable for the metal precursor or NPs present in polar solvents such as aqueous solutions [112]. Surface functionalization of the carbonaceous support is therefore necessary for catalyst preparations like incipient wetness impregnation, ion-exchange, or organometallic grafting.

Another aspect of surface functionalization is the strong influence on the distribution of the metal precursor on the support and, consequently, on the metal dispersions [113]. Stronger interaction with the precursor salt favors a higher metal dispersion that affects the catalytic behavior of structure sensitive reactions [114].

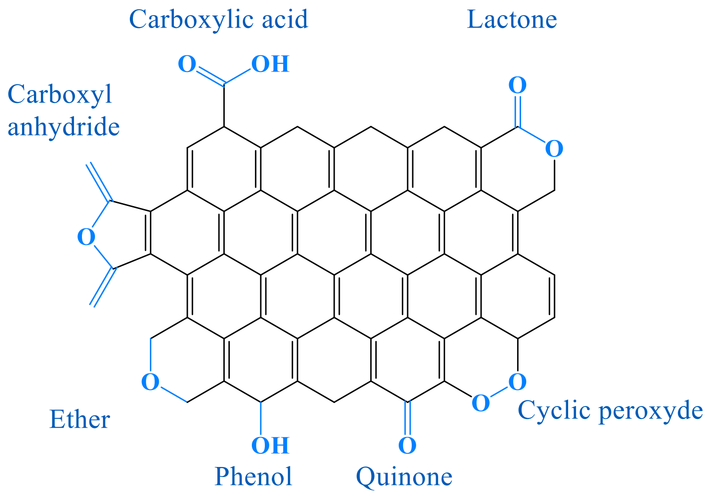

Figure 2.6. Schematic representation of the surface groups on carbon after oxidative treatment.

The oxygen containing surface groups created by oxidative treatments mainly have an acidic character [115]. Boehm and co-workers [116] categorized the surface groups as strongly acidic (carboxylic and anhydride), weakly acidic (quinone and lactone), with phenolic character (hydroxylic groups) and carbonyl groups. Their characterization was assessed by titration methods, X-Ray photoelectron spectroscopy (XPS), temperature programmed desorption spectroscopy methods (TPD) and infrared spectroscopy (IR).

2.2.4 Gas Phase C≡C Bond Hydrogenations

Selective hydrogenation of alkynes (to alkenes) is an important reaction widely employed in the preparation of fine chemicals [117]. For example, ethylene is extensively used as an intermediate in the manufacture of multiple compounds in the chemical industry such as polymers or fine chemicals. In 2008, the sales volume of ethylene reached a peak of more than 160 billion

US$ produced by at least 117 companies in 55 countries [118]. The conventional route involves thermal cracking of petroleum gas with the simultaneous formation of acetylene as reaction by-product. The presence of small amounts of acetylene in the product stream induces catalyst poisoning in the ethylene-based polymerization reactions [119]. In this context, palladium is widely used since it offers the best combined activity/selectivity for C≡C bond partial hydrogenation [120]. With the use of static constant-volume reactors, it became possible to follow the course of the reaction with time by simple manometric methods and therefore follow the reaction over a wider range of conditions [121]. The high selectivity of Pd was attributed to a thermodynamic factor, due to the preferential coverage of the surface by ethyne ascribable to its greater heat of adsorption. Higher C≡C adsorption constants (by 2 or 3 orders of magnitude) relative to C=C were reported [79, 122], even at high conversions [123] (*i.e.* low C≡C concentration). Besides, the rapid desorption of ethene which is replaced by ethyne prevents the further reduction to ethane [124].

At present, the most accepted alkyne hydrogenation mechanism follows the Langmuir-Hinshelwood model, involving associative or dissociative adsorption of alkyne and hydrogen on the catalyst surface [125, 126]. Rajaram *et al.* proposed various reaction intermediates for product formation in the case of mono- and di-substituted acetylenes [127]. The reaction proceeds through successive additions of hydrogen atoms to the carbon atoms of the unsaturated bond. In the absence of any mass-transfer limitations, the reaction rate can be limited by dissociative adsorption of hydrogen, bonding of the first hydrogen atom with the substrate molecule or by the addition of the second hydrogen to the adsorbed substrate [128]. Based on theoretical calculations, addition of the first hydrogen atom to the C≡C bond was adopted as the rate-determining step in a number of studies [129 , 130, 131]. In contrast, Bos *et al.* [132] and Borodziński and co-workers [133] identified the addition of the second hydrogen to the adsorbed alkyne as the most energy demanding step and this assumption was accordingly used to explain the experimental results in the C≡C hydrogenation [122, 126]. In the particular case of acetylene hydrogenation, a non-competitive transfer of hydrogen by carbonaceous deposits was modeled by Borodzinski and Cybulski [134] and used later in various studies [125, 135, 136]. It assumes the existence of three different types of actives sites with specific adsorption capacities. Between narrow carbonaceous deposits, acetylene was proposed to adsorb perpendicularly to the surface (as vinyldiene) where it is selectively hydrogenated to ethylene by competitively adsorbed hydrogen atoms. Another type of active site was defined on deposits where acetylene is non-competitively adsorbed and hydrogenated by hydrogen spill-over. A last site, located in larger interstices, was associated to the unwanted hydrogenation of ethylene to ethane, on which all gases (acetylene, ethylene and hydrogen) can be adsorbed. Another important aspect of the alkyne hydrogenation reactions and acetylene in particular, is the simultaneous formation of oligomers. Although Pd-containing catalysts show high activity, they promote the undesired formation of ethane that can result either from further hydrogenation of ethylene or direct attack of the C≡C bond [117]. Sheridan [137] proposed an oligomerization mechanism through a free-radical polymerization with an adjacent σ-diadsorbed ethyne molecule, induced by the sequential adsorption of hydrogen atoms to the adsorbed ethyne in a C_2H_3 "half-hydrogenated state".

High selectivity to alkene is not a feature that is unique to palladium. It has been recently shown that NiO (3 nm) can also perform well in the acetylene hydrogenation [119] as compared to Pd/Al_2O_3 (10 nm) in the phenylacetlyene hydrogenation [138], with high selectivity (>95% to ethane *vs.* 78% to styrene), albeit TOF recorded with NiO NPs was lower by one order of magnitude.

2.2.5 Liquid Phase Hydrogenations of Aromatic Nitro-compounds

With aromatic nitro-compounds bearing more than one functional group, it is difficult to avoid completely the reduction of a second functionality. In the particular case of haloaromatics, reductive dehalogenation can readily occur since the hydrogenolysis of carbon-halogen bond is promoted by the amino substitution in the aromatic ring [139]. The selectivity of nitroaromatics hydrogenation is affected by a number of factors such as the nature of the catalyst (metal, support and particle size), the additive (promoter, inhibitor and poison) and reaction conditions (solvent, temperature and pressure) [140].

A range of metals has been tested for the hydrogenation of substituted nitroaromatic compounds [108, 140]. Excellent results were recorded with supported Ru, Rh and Ir, but the most frequently used catalysts for the nitro group reduction are either the noble metals Pd and Pt supported on active carbon or aluminum oxide, or Raney Nickel [141]. Even though Ni is less active than the aforementioned noble metals, it became attractive for obvious costs reasons.

An appropriate choice of the support offered selectivities greater than 98% at full conversion for Ni-catalyzed hydrogenation of chloronitrobenzenes on TiO_2 [142] or CNF [143, 144]. Corma *et al.* [145] also reported high selectivities for nitroaromatics hydrogenation (up to 98.7% at 99.6% conversion of 4-nitrobenzaldehyde) with TiO_2-supported Ni. Nanosized nickel catalysts are reported to exhibit better catalytic performances as compared to Raney Ni [146]. Mahata *et al.* [147] observed superior activity, selectivity and stability of nanosized nickel in the hydrogenation of nitrobenzene in comparison to conventional Raney nickel catalysts.

Ni has also been successfully used in the gas phase hydrogenation of chloro- and bromonitrobenzenes, where the aromatic aniline was exclusively produced [148]. Although the selectivity was not affected, higher hydrogenation rates (up to 5 times) were observed on metal oxide than on carbonaceous supports, which was ascribed to particle size and electronic interactions. Modifications on the environment of Pd/C NPs was also assessed for halonitrobenzenes by probing the effect of solvent on the selectivity and activity [149] or replacing the organic solvent by ionic liquids [150]. In this latter case, the degree of dehalogenation at full conversion was reduced by up to one order of magnitude.

Even though Pd could be less selective than Pt [141], modifications with organic or inorganic modifiers were used to improve the catalytic performance. An improvement of chemoselectivity was demonstrated with ethylenediamine employed as a catalytic poison of Pd/C [151] and with diphenyl sulfide immobilized on Pd/C which gave yields of 91–97% aniline without affecting a Cl, methoxy, or COOBn substituent [152]. Several promoters such as Fe in Ni-P alloys [153], Mo, W and Ru in Ni-B clusters [154] and amorphous alloys [155, 156] have been quite effective to suppress undesired hydrodehalogenation side reactions. In addition, Raney Ni promoted by vanadium showed significant decrease of the accumulation of the aromatic amines intermediates [157].

2.3 Conclusions

In the class of interstitial compounds, molybdenum nitrides set themselves apart from conventional noble metal based-catalysts. Controlled temperature programmed treatments of MoO_3 precursor was shown to be the most appropriate synthesis method, allowing precise control of the Mo-nitride structural parameters. Two main crystallographic phases are identified, tetragonal β-Mo_2N and cubic γ-Mo_2N, which exhibit low and high specific surface area, respectively. The nitridation extent could also vary significantly from one nitride composition to another, which may have an impact on the catalytic response.

Across multiple catalytic applications, molybdenum nitrides have proved to be a viable alternative to noble metals. Although they are active due to a limited capacity for hydrogen activation, Mo_2N deliver high selectivities to target products. To increase the catalytic activity, a second metal (Au, Pd, *et al.*) could be added to the system to create a new metal-nitride synergy.

The performance in catalytic hydrogenations is affected by a number of parameters and one of the key factors is the interplay between the active phase properties and the reacting molecules. Mechanistic, electronic and geometric effects have been considered to tackle this complex phenomenon, and to establish a correlation between the characteristics of the active phase and the catalytic response. In terms of structural characteristics that control catalytic performance, the size and surface structure of metal NPs play a critical role on reactions denoted as structure-sensitive. Therefore, the understanding of the size-effect can be used for the rational catalyst design of structure sensitive reactions. By adjusting the preparative pathways, the great potential of colloidal methods was widely reported for the fine-tailoring of a nanostructure size and morphology. An appropriate choice of the support, with appropriate physical and chemical characteristics that prevent mass and heat transfer limitations, metal agglomeration or leaching, is necessary to design an efficient catalyst at a larger scale. In this respect, structured carbon-based supports represent a valuable alternative to conventional powdered or granulated catalysts. In summary, control of the active metal characteristics through the optimization of particle size, modification of the active site properties and choosing a suitable support represent the powerful tools of catalyst design.

Chapter 3

New Catalyst Formulations Based on Molybdenum Nitrides for $–NO_2$ Reduction

The potential of Mo-nitrides has already been demonstrated, as being able to dissociate hydrogen on their surface, and thus making them appropriate for hydrogenation reactions. However, the isolated effect of structural parameters that are varying together with modifications of the preparation method is still a subject of investigations. Applying the approach of rational catalyst design, β-Mo_2N was prepared and tested over a series of substituted nitrobenzenes in the $-NO_2$ to $-NH_2$ reduction. The independent effect of the Mo-nitride crystallographic phase (β *vs.* γ) and surface area on the catalytic response was then assessed for a model (*p*-CNB → *p*-CAN) reaction. Additionally, the promoting effect of gold NPs on both β-Mo_2N and γ-Mo_2N was evaluated in gas and/or liquid phase. The effect of the nitrogen content in Mo-Nitrides on the catalytic performance was also examined.

3.1 Selective Three-Phase Hydrogenation of Aromatic Nitro-compounds over *β*-Molybdenum Nitride

Abstract

A tetragonal molybdenum nitride (β–Mo_2N) has been prepared by temperature programmed treatment of MoO_3 in flowing N_2+H_2 and, for the first time, shown to catalyze the liquid phase selective hydrogenation (T = 423 K; P_{H_2} = 11 bar) of a series of *para*-substituted (-H, -OH, -O-CH_3, -CH_3, -Cl, -I and -NO_2) nitrobenzenes to give the corresponding aromatic amine. Reaction over Pd/Al_2O_3, as a benchmark catalyst (Pd particle size *ca.* 18 nm), resulted in a composite hydrodechlorination/hydrogenation of *p*-chloronitrobenzene (as a representative nitroarene) to generate nitrobenzene and aniline. β-Mo_2N has been characterized in terms of temperature-programmed reduction (TPR), H_2 chemisorption/temperature programmed desorption (TPD), BET surface area/pore volume, elemental analysis, powder X-ray diffraction (XRD), X-ray photoelectron spectroscopy (XPS), scanning (SEM) and transmission (TEM) electronic microscopy. Elemental analysis, XRD, SEM and TEM have confirmed the formation of tetragonal β–Mo_2N, characterized by an agglomeration of flake-like crystallites. *Post*-synthesis, the nitride was passivated by contact with 1% v/v O_2/He at ambient temperature and XPS analysis has demonstrated the formation of a superficial passivating oxide overlayer without bulk oxidation. *Pre*-reaction, activation by TPR to 673 K was necessary to remove the passivating film. Hydrogen TPD has revealed significant hydrogen uptake (0.7 μmol m^{-2}) associated with β-Mo_2N. Nitro group reduction kinetics have been subjected to a Hammett treatment where the reaction constant ($\rho = 0.4$) is diagnostic of an increase in rate due to the presence of electron-withdrawing

substituents on the aromatic ring, consistent with a nucleophilic mechanism. The results of this study establish the viability of β-Mo_2N to promote selective nitroarene hydrogenation.

3.1.1. Introduction

Aromatic amines are used extensively as intermediates in the manufacture of fine chemicals, pharmaceutical and agricultural products [63]. Standard synthesis routes based on Fe-promoted reduction in acid media (Bechamp reaction) do not meet the current requirements for sustainable process design due to low selectivity to the target amine and the production of large quantities of toxic waste [140]. The alternative catalytic approach *via* batch liquid phase hydrogenation using conventional transition metal (*e.g.* Ni and Pd) catalysts shows promise in terms of increased conversion [153, 158, 159] but the low overall reaction selectivity represents a drawback that must be addressed [141]. Taking the hydrogenation of *p*-chloronitrobenzene (*p*-CNB) to *p*-chloroaniline (*p*-CAN), undesirable C–Cl hydrogenolysis is difficult to circumvent at high conversions [140]. Indeed, Mo *et al.* [160] and Li and co-workers [161] have recently reported the formation of nitrobenzene (NB) and aniline (AN) in the hydrogenation of *p*-CNB over unsupported NiB nanotubes and nanospheres. Low selectivity with respect to $-NO_2$ group reduction also extends to gas phase operation where cyclohexylamine and NB have been identified as secondary products in the hydrotreatment of NB and *o*-CNB over polymer-supported Pt [162] and Pd/Al_2O_3 [163], respectively. Application of coupling reactions [164], support modifications (*e.g.* polymer functionalisation [165], carbon nanofibre orientation [166], magnetization of γ-Al_2O_3 [167]) and/or the use of bi- (Ni-B [159], NiPB [168] or Pt-Pd [169]) and tri- (NiCoB [170]) metallic systems have been examined as a possible means of enhancing selectivity. However, the associated complexity and costs militate against the viability of these approaches in terms of process scale up. There is now a pressing need for a more efficient catalyst system to promote the selective hydrogenation of aromatic polyfunctional nitroarenes.

The use of molybdenum nitrides in hydrogen mediated reactions is attracting increasing attention as a viable alternative to conventional transition metal catalysts. Li *et al.* [171], studying the hydrogenation of long chain alkadienes over Mo nitrides, reported an up to 54% increase in conversion (relative to Pd/Al_2O_3) and enhanced selectivity to an alkene product that was governed by the Mo^0/Mo^{m+} ($m = 2,3$) ratio. Hydrogenation activity of molybdenum nitrides can be linked to a modification of electronic density and contraction of the *d*-band due to the interstitial introduction of nitrogen in the Mo lattice [172], resulting in an increased capacity for H_2 adsorption [4]. Mo nitrides have now been successfully used to promote NO reduction [173, 174] and the hydrogenation of CO [175] and ethyne [176]. The potential for Mo_2N application in the selective hydrogenation of polyfunctional reactants has also been flagged [177]. Guerrero-Ruiz *et al.* [58] reported high selectivites to the less thermodynamically favored crotyl alcohol (from crotonaldehyde) over mesorporous carbon supported Mo nitride and correlated this to a preferential activation of the C=O group on the (200) plane. Taking the possible allotropic forms, cubic γ-Mo_2N has been the more widely studied [58, 173-177] in terms of hydrogen mediated catalytic applications. However, Mckay *et al.* [38] have reported a higher catalytic activity for (tetragonal) β-Mo_2N when compared with δ-MoN and γ-Mo_2N in ammonia synthesis. A comprehensive search through the literature failed to unearth any instance where Mo nitride has been used in the liquid phase catalytic hydrogenation of nitroarenes. Results have been recently reported [178] for the gas phase hydrogenation of *p*-CNB over β-Mo_2N, where reaction exclusivity in terms of *p*-CAN as (the only) product has been recorded. That work is extended here by considering the application of β-Mo_2N to catalyze the liquid phase hydrogenation of *p*-CNB, where catalytic performance is assessed against a standard Pd/Al_2O_3 catalyst. Furthermore, the catalytic action of β-Mo_2N to promote $-NO_2$ group reduction for a series or *para*-substituted nitroarenes has been investigated and the catalytic data have been subjected to a Hammett treatment.

3.1.2. Experimental

3.1.2.1. Materials and Analytical Methods

The reactants (NB, *p*-nitrophenol, *p*-nitroanisole, *p*-nitrotoluene, *p*-CNB, *p*-iodonitrobenzene and *p*-dinitrobenzene, Sigma Aldrich ≥ 98%) and solvent (ethanol, Sigma Aldrich ≥ 99%) were used as supplied, without further purification. All the gases used in this study (H_2, N_2, Ar, O_2 and He) were of ultra high purity (>99.99%, Carbagas). The composition of the reaction/product mixtures was determined using a Perkin-Elmer Auto System XL chromatograph equipped with a programmed split/splitless injector and a flame ionization detector, employing a Stabilwax (Cross-bond Carbowax-PEG, Restek, USA) capillary column (*i.d.* = 0.32 mm, length = 30 m, film thickness = 0.25 μm). Data acquisition and manipulation were performed using the TotalChrom Workstation (Version 6.3.2 for Windows) chromatography data system. Reactant and product molar fractions (x_i) were obtained using detailed calibration plots (not shown) where the total mass balance in the mixture (based on GC analysis) was analyzed for every extracted sample. The extent of hydrogenation can be represented by the reactant fractional conversion where, taking *p*-CNB ($X_{p\text{-CNB}}$) as representative reactant

$$X_{p-CNB} = 1 - x_{p-CNB} \tag{3.1.1}$$

and selectivity in terms of *p*-CAN (S_{p-CAN}) as target product is given by

$$S_{p-CAN} = x_{p-CAN} \Big/ \sum_{products} x_i \qquad \textbf{(3.1.2)}$$

The concentration of organic species in the bulk liquid phase (C_i, mol dm^{-3}) was determined assuming that the density was constant and equal to that of *p*-CNB ($\rho_{p\text{-}CNB}$ = 1.298 g cm^{-3}) [179]

$$C_i = x_i \times \left(\rho_{p\text{-}CNB} / M_{p\text{-}CNB}\right) \qquad \textbf{(3.1.3)}$$

and $M_{p\text{-CNB}}$ represents *p*-CNB molar mass.

3.1.2.2. Catalyst Preparation

a. *β*-Mo_2N

Mo nitride synthesis was conducted in a horizontally mounted quartz reactor *via* the temperature programmed reduction-nitridation of MoO_3 (99.9995%, Alfa Aesar) in a continuous flow of H_2+N_2 at atmospheric pressure. The precursor (*ca.* 4 g MoO_3) was loaded into the tubular reactor (30 cm × 1 cm *i.d.*) and heated in 30 cm^3 min^{-1} (Gas hourly space velocity (*GHSV*) = 460 h^{-1}, Bronkhorst mass flow controlled) 15% v/v N_2/H_2 at 5 K min^{-1} to 933 K, maintaining the final temperature for 100 h. The reaction was quenched by switching to an Ar flow (30 cm^3 min^{-1}) for 1 h and cooling to room temperature. Samples for off-line analysis were passivated (at 293 K) in 1% v/v O_2/He; there was no detectable temperature increase during sample passivation. The latter step was introduced to avoid uncontrolled sample oxidation upon exposure to air [180]. Prior to use, the nitride was activated in 60 cm^3 min^{-1} H_2 at 2 K min^{-1} to 673 K and maintained at the final isothermal hold for 1 h.

b. Pd/Al_2O_3

The Al_2O_3 support was obtained from Sigma-Aldrich and used as received. Five Pd supported samples (0.1, 0.5, 1, 2 and 4% wt.) were synthesized by deposition of *ex-situ* prepared monodispersed Pd^0 nano-particles. An aqueous solution of $PdCl_2$ (Fluka, >99%) and $Na_2MoO_4 \cdot H_2O$ (Fluka, >99%) (Pd/Mo mol ratio = 1) was heated at *ca.* 368 K (under continuous stirring) until complete evaporation. The solid residue was dissolved in water and contacted (at room temperature) with a continuous flow of H_2 (100 cm^3 min^{-1}) for 30 min. This procedure has been demonstrated [181] to result in the formation of uniform Pd^0 nano-particles stabilized by molybdate anions. Pd nano-particle deposition was achieved *via* adsorption where the Al_2O_3 support (*ca.* 2 g) was immersed in a stirred aqueous solution (*ca.* 500 cm^3) containing the target Pd loading until the solution was colorless (*ca.* 2 h), *i.e.* complete deposition. The slurry was then filtered, dried in air at room temperature and sieved into a batch of 75 μm average diameter. Prior to use, the catalyst was activated in 60 cm^3 min^{-1} H_2 at 2 K min^{-1} to 493 K and maintained at the final isothermal hold for 1 h.

3.1.2.3. Catalyst Characterization

Nitride elemental (nitrogen) analysis was determined using an Exeter CE-440 Elemental Analyzer after sample combustion at *ca.* 1873 K. The Pd content (in Pd/Al_2O_3) was measured by absorption atomic spectroscopy (AAS) using a Shimadzu AA-6650 spectrometer with an air-acetylene flame from the diluted extract in aqua regia (25% v/v HNO_3/HCl). Temperature programmed reduction (TPR), H_2 chemisorption, temperature programmed desorption (TPD) and BET surface areas were obtained using the CHEM-BET 3000 unit. The characterization measurements were carried out *in situ* following the reduction/nitridation/passivation steps. TPR analysis was conducted by heating the sample in 17 cm^3 min^{-1} 5% v/v H_2/N_2 at 2 K min^{-1} to 673

K (β-Mo_2N) or 493 K (Pd/Al_2O_3). The exit gas passed through a liquid N_2 trap and changes in H_2 consumption/release were monitored by TCD with data acquisition/manipulation using the TPR Win^{TM} software. The reduced samples were maintained at the final temperature until the signal returned to baseline. The samples were then swept with 65 cm^3 min^{-1} N_2 for 1.5 h, cooled to room temperature and subjected to H_2 chemisorption using a pulse (10 μl) titration procedure. Hydrogen TPD was conducted in a N_2 flow (65 cm^3 min^{-1}) at 50 K min^{-1} to 873 K. BET areas were recorded with a 30% v/v N_2/He flow using pure N_2 as internal standard. At least two cycles of N_2 adsorption-desorption in the flow mode were employed to determine total surface area using the standard single point method. Pore volume measurements were performed using the commercial Micromeritics Flowsorb II 2300 unit. Prior to analysis, the samples were outgassed at 423 K for 1 h and the total pore volume was obtained at a relative N_2 pressure (P/P_0) = 0.95. BET surface area, pore volume and H_2 consumption/release measurements were reproducible to within ± 5%; the values quoted represent the mean.

Powder X-ray diffractograms (XRD) were recorded on a Bruker/Siemens D500 incident X-ray diffractometer using Cu Kα radiation. The samples were scanned at a rate of 0.02° $step^{-1}$ over the range $20° \leq 2\theta \leq 90°$ (scan time = 5 s $step^{-1}$). Diffractograms were identified using the JCPDS-ICDD reference standard, *i.e.* β-Mo_2N (25-1368), Pd (46-1043) and δ-Al_2O_3 (47-1770). Lattice parameters were determined by means of the CELLREF software and used to determine the crystal structure of the β-Mo_2N using the CrystalMaker software. X-ray photoelectron spectroscopy (XPS) analyzes were conducted on an Axis Ultra instrument (Kratos) using a monochromatic Al Kα X-ray source (1486.6 eV). Prior to analysis, the nitride sample was adhered to a conducting carbon tape, mounted in the sample holder and subjected to ultra-high vacuum conditions ($<10^{-8}$ Torr). The source power was maintained at 150 W and the emitted photoelectrons were sampled from a square area of 750×350 μm^2; the photoelectron take-off angle was 90°. The analyzer pass energy was 80 eV for survey spectra (0 - 1000eV) and 40 eV for high resolution spectra (over the Mo $3d_{3/2}$ and Mo $3d_{5/2}$ binding energy (BE) range, 227-239 eV). The adventitious C 1s peak was calibrated at 284.5 eV and used as internal standard to compensate for any charging effects. Spectral curve fitting and quantification employed the CasaXPS software, using relative sensitivity factors provided by Kratos.

Analysis by scanning electron microscopy (SEM) was conducted using a Philips FEI XL30-FEG equipped with an Everhart-Thornley secondary-electron detector operated at an accelerating voltage of 10-15 kV and a NORAN System SIX (version 1.6) for data analysis. The samples were subjected to a hydrocarbon decontamination treatment using a plasma-cleaner (EVACTRON). Transmission electron microscopy measurements were performed using a JEOL JEM 2011 HRTEM unit with a UTW energy dispersive X-ray detector (Oxford Instruments) operated at an accelerating voltage of 200 kV using Gatan DigitalMicrograph 3.4 for data treatment. The specimens were prepared by dispersion in acetone and deposited on a holey carbon/Cu grid (300 Mesh). Up to 400 individual Pd metal particles were counted for each catalyst and the mean metal diameter (d_{TEM}) was calculated from:

$$d_{\text{TEM}} = \frac{\sum_i n_i d_i}{\sum_i n_i} \qquad \textbf{(3.1.4)}$$

where n_i is the number of particles of diameter d_i. The size limit for the detection of Pd particles is *ca.* 1 nm.

3.1.2.4 Catalytic System

Liquid phase hydrogenation reactions (*T* = 423 K; P_{H_2} = 11 bar) were carried out in a commercial semi-batch stirred stainless steel reactor (100 cm^3 autoclave, Büchi AG, Uster, Switzerland) equipped with a pressure controlled H_2 supply system. Madon and Boudart demonstrated [182] that, for heterogeneous catalytic systems operating with negligible mass transfer limitations, a proportional correlation between activity and the number of active sites can be established for a series of catalysts with different metal content but similar dispersion, *i.e.* invariant specific activity. Taking this approach, the (0.1-4% wt.) Pd/Al_2O_3 catalysts were used to determine working conditions where the reaction proceeded under kinetic control. The associated linear relationships (not shown) established reactor operation in the absence of mass transfer constraints for hydrogenation rates $< 72 \times 10^5$ μmol_{-NO_2} mol^{-1} min^{-1}. Detailed testing to determine the activity/selectivity response employed 1% wt. Pd/Al_2O_3 as a representative catalyst. Hydrogen consumption in the reactor vessel was monitored on-line with a press flow gas controller (BPC-6002, Büchi, Switzerland) and a stainless steel 6-blade disk turbine impeller (equipped with a self-gassing hollow shaft) provided effective agitation at 1800 rpm. A recirculator (HAAKE B-N3) was used to stabilize the reaction temperature to within ± 1 K using oil (Shell Thermia; thermal conductivity = 0.45 kJ m^{-1} h^{-1} K^{-1}; specific heat = 2.4 kJ kg^{-1} K^{-1}) as the thermal medium. At the beginning of each experiment, a 60 cm^3 ethanolic solution of the nitroarene reactant was charged and flushed three times with N_2 under constant agitation. The catalyst was activated *ex-situ* in a quartz reactor (300 mm length; *i.d.* = 10 mm; 60 cm^3 min^{-1} H_2; *GHSV* = 200 h^{-1}) to 493 K (Pd/Al_2O_3) or 673 K (β-Mo_2N) at 2 K min^{-1}, cooled to room temperature and kept in an inert (N_2) atmosphere. The catalyst was then fluidized in a flow of N_2, transferred to the reactor and the temperature was stabilized (*ca.* 45 min) under gentle stirring (*ca.* 300 rpm). Hydrogen was then introduced, the system was pressurized (to 20 ± 0.5 bar, up to 20 times in excess of the stoichiometric requirements for hydrogenation to the respective amine) and stirring (at 1800 rpm) was engaged (time $t = 0$ for reaction). In a series of blank tests, reactions carried out in the absence of catalyst did not result in any measurable conversion. The initial $–NO_2/Mo_2N$ (or Pd) molar ratio spanned the range 0.2 - 480. A *non*-invasive liquid sampling system *via* a syringe with in-line filters allowed a controlled removal of aliquots (≤ 0.5 cm^3) from the reactor. Repeated reaction runs with the same batch of catalyst delivered conversion/selectivity values that were reproducible to within ± 5%.

3.1.3. Results and Discussion

3.1.3.1 Catalyst Characterization

a. *β*-Mo_2N

BET area-pore volume/ XPS/TPR

The BET area associated with the *as prepared* nitride (7 m^2 g^{-1}, see **Table 3.1.1**) is close to that reported in the literature (9 m^2 g^{-1}) [13] for *β*-Mo_2N synthesized *via* temperature programmed treatment of MoO_3 in N_2/H_2. No published pore volume data could be found with which to compare our measurement (0.02 cm^3 g^{-1}). *β*-Mo_2N passivation was conducted in a flow of diluted (1% v/v) O_2 (see Experimental section) to generate a protective oxide film on the nitride surface and circumvent bulk oxidation [12]. This passivation layer has been characterized as chemisorbed oxygen associated with Mo surface atoms [19, 183]. XPS analysis was conducted to characterize the passivated nitride surface and the spectra over the Mo 3*d* (Mo $3d_{3/2}$ and $3d_{5/2}$) BE region for the MoO_3 precursor **(A)** and passivated *β*-Mo_2N **(B)** can be compared in **Figure 3.1.1**; the associated BE values are given in **Table 3.1.1**.

		β-Mo_2N	Pd/Al_2O_3	Error
Nitrogen content (% w/w)[a]		5	-	± 0.3
Pd loading (% w/w)[b]		-	0.92	± 0.02
BET (m^2 g^{-1})		7[c] (3)[d]	157	± 1
Pore volume (cm^3 g^{-1})		0.02	0	± 0.005
TPR	T_{max} (K)	637	332	± 1
	H_2 consumed (μmol g^{-1})	303	-	± 2
H_2 chemisorption (μmol g^{-1})		0.29	3.90	± 0.01
TPD	T_{max} (K)	750, 806, 900	-	± 1
	H_2 desorbed (μmol m^{-2})	0.7	-	± 0.05
Pd size range (nm)		-	3-30	± 0.5
d_{TEM} (nm)		-	18	± 2.3
XPS Mo $3d_{5/2}$ BE (eV)		228.5, 233.0	-	± 0.1

[a]from elemental analysis; [b]from AAS; [c]activated nitride; [d]passivated nitride

Table 3.1.1. Nitrogen content, Pd loading, BET surface area, total pore volume, characteristic temperature programmed reduction (TPR) T_{max} with associated H_2 consumption, H_2 uptake/TPD measurements, Pd particle size range and mean (d_{TEM}) and XPS binding energies associated with β-Mo_2N.

The XPS profile for MoO_3 exhibits a single spin-orbit doublet (Mo $3d_{5/2}$:$3d_{3/2}$ = 3:2, Mo atom % = 27, O atom % = 73) with a Mo $3d_{5/2}$ BE = 233.0 eV that is characteristic of Mo^{6+} [184, 185]. The XPS profile for the passivated β-Mo_2N (**Figure 3.1.1(B)**) shows a second predominant doublet at a lower binding energy (Mo $3d_{5/2}$ = 228.5 eV).

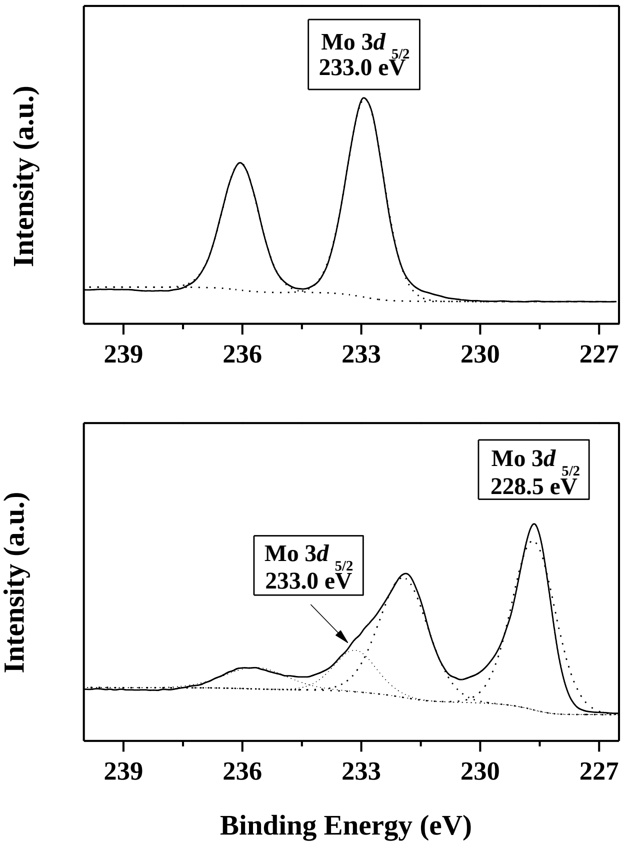

Figure 3.1.1. XPS spectra in the Mo 3*d* region of **(A)** MoO_3 and **(B)** passivated *β*-Mo_2N. *Note*: Experimental values are represented by solid lines and dotted lines illustrate peak deconvolution from curve fitting analysis.

While the XPS peaks for Mo^{6+} in MoO_3 are strong and well defined, they are noticeably less intense in the passivated *β*-Mo_2N and the strong signal at lower BE can be associated with nitride character (lower Mo oxidation state). Li *et al.* [171] using an advanced deconvolution to resolve a single Mo $3d_{5/2}$ signal for the XPS analysis of Mo nitrides and carbides reported a range of Mo^{m+} oxidation states (*m* varying from 0 to 6) assigned to BE values in the range 227.8-233.1

eV. McKay *et al.* [62], in their XPS analysis of passivated Mo_2N films on ZSM-5, also recorded a residual Mo^{6+} doublet (Mo $3d_{5/2}$ at 233.0 eV) that they attributed to the passivating oxide layer, which was readily removed by brief Ar ion etching. *Post*-passivation, there was a measurable decrease in BET (from 7 to 3 m^2 g^{-1}), as observed elsewhere [186]. Choi *et al.* [187] have suggested that a reduction in surface area is the result of O_2 dissolution in Mo_2N. The removal of the passivating layer was investigated by TPR and the result is presented in **Figure 3.1.2(A)**. The TPR profile exhibits a broad positive (hydrogen consumption) peak with T_{max} = 637 K, which can be ascribed to the reduction of the surface oxide layer with water release [183]. It should be noted that higher temperatures (by up to 673 K) are required for MoO_3 reduction [188], consistent with a more facile removal of the superficial passivating layer. Gong and co-workers [13] observed a single reduction peak (at 700 K) during the TPR of passivated β-Mo_2N while Colling *et al.* [19] reported the desorption of H_2O associated with the reduction of the passivated surface of γ-Mo_2N at T >400 K. As the TPR signal returned to baseline in the isothermal hold (see **Figure 3.1.2(A)**), a final temperature of 673 K was deemed to be sufficient for β-Mo_2N activation.

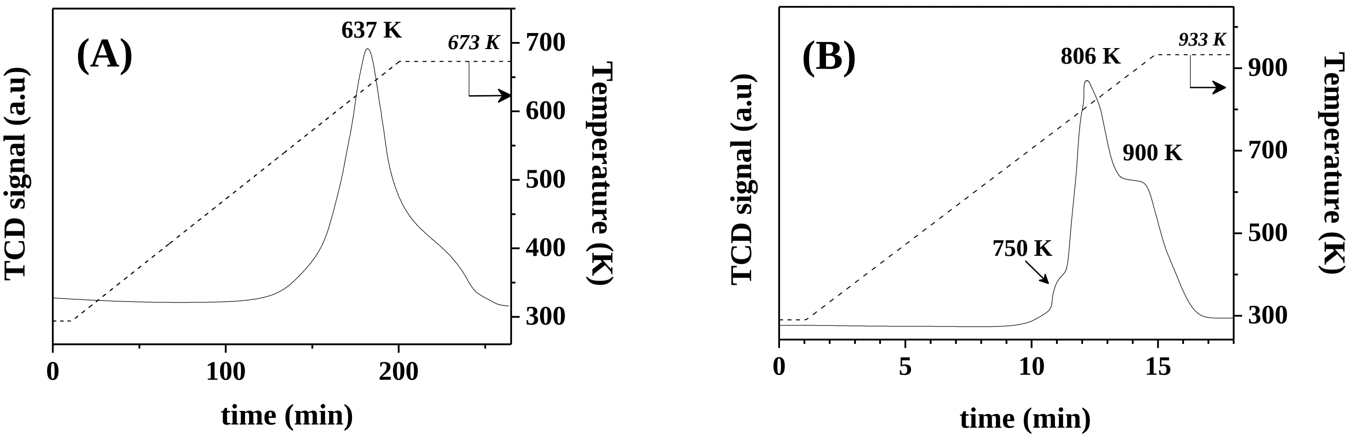

Figure 3.1.2. **(A)** TPR profile for passivated β-Mo_2N and **(B)** TPD from activated β-Mo_2N.

Elemental Analysis/XRD/TEM/SEM

The bulk nitrogen content for *β*-Mo_2N obtained from elemental analysis (5% w/w) was close to the surface content (*ca.* 8% w/w) obtained by XPS and is in accordance with reported values [12, 13]. The XRD pattern of the passivated nitride (**Figure 3.1.3(A)**) corresponds to the *β*-Mo_2N reference (JCPDS-ICDD, 25-1368) with reflections at 37.7°, 43.1°, 45.3°, 62.7°, 64.3°, 75.5°, 78.6° and 80.5° associated with the (1 1 2), (2 0 0), (0 0 4), (2 2 0), (2 0 4), (3 1 2), (1 1 6) and (2 2 4) planes. There was no evidence of any bulk oxide (MoO_3 or MoO_2), confirming that the oxide precursor had been completely converted to the nitride where the passivation procedure resulted in a superficial (as opposed to bulk) oxidation as indicated by the XPS measurements. While the XRD results are consistent with *β*-Mo_2N synthesis, the characteristic diffraction peaks for the *β*-form are very close to those of the *γ*-allotrope. In order to check for a possible *γ*-nitride content, the passivated nitride was subjected to a single crystal analysis using the CELLREF software for lattice parameter optimization. The results are given in **Table 3.1.2**, where the residual error when adjusting the *d*-spacing to tetragonal *β*-Mo_2N is up to 50 times lower than that for cubic *γ*-Mo_2N. Indeed, the results actually show a better adjustment to *β*-Mo_2N for the passivated sample relative to the JCPDS-ICDD standard (25-1368). The crystal structure of the tetragonal *β*-Mo_2N unit cell obtained from the lattice parameters extracted by simulation with CELLREF is shown as an inset in **Figure 3.1.3(A)**, where the atomic arrangement has been established following Ettmayer's approach [189]. A representative high resolution TEM image is presented in **Figure 3.1.3(B)**, where the associated diffractogram pattern has been included as an inset. The *d*-spacings (0.24, 0.21 and 0.20 nm) between the planes in the atomic lattice match, respectively, the (112), (200) and (004) planes of *β*-Mo_2N. Morphological features were assessed by SEM analysis and the results are presented in **Figure 3.1.3(C)**. The micrograph reveals an agglomeration of flake-like ensembles in the micron range (*ca.* 1-5 μm; see enlarged image in the inset). A similar structure has been reported elsewhere for *β*-Mo_2N [38, 39] and associated with water release during the reduction of MoO_3, which precedes the nitridation step. This results in a significant disruption to the platelet orthorhombic crystal structure that characterizes the starting MoO_3, *i.e.* a *non*-topotactic transformation [178]. This differs from published findings [41, 49] where the platelet morphology was maintained.

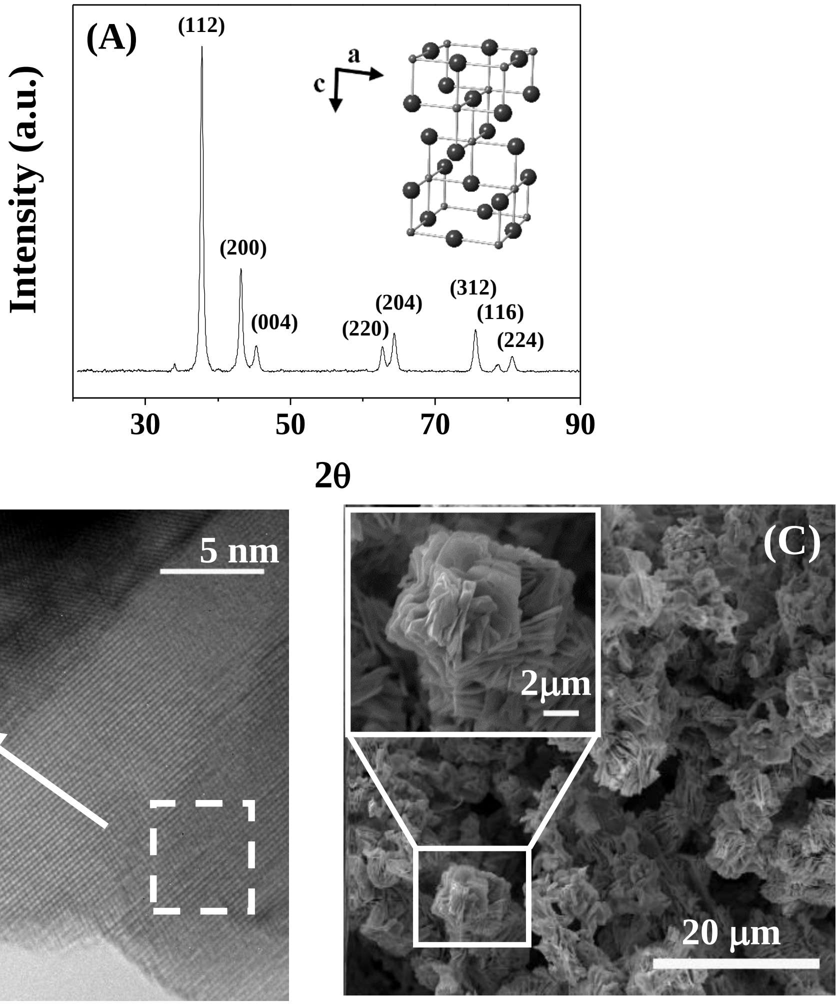

Figure 3.1.3: **(A)** XRD pattern with tetragonal crystal unit cell, **(B)** representative TEM image (with diffractogram pattern) and **(C)** SEM micrograph (with magnified image as inset) of *β*-Mo_2N. *Note*: XRD peak/plane assignments are based on JCPDS-ICDD standard for *β*-Mo_2N (25-1368).

Cubic γ-Mo_2N			Tetragonal β-Mo_2N		
h k l	Residual Error (%)		h k l	Residual Error (%)	
	25-1366[a]	This work		25-1368[a]	This work
1 1 1	0.09	0.18	1 1 2	0.13	0.01
2 0 0	0.06	0.47	2 0 0	0.10	0.02
2 2 0	0.08	0.54	0 0 4	0.05	0.02
3 1 1	0.17	0.40	2 2 0	0.03	0.04
2 2 2	0.09	0.15	2 0 4	0.02	0.03
			3 1 2	0.08	0.01
			1 1 6	0.01	0.02
			2 2 4	0.08	0.03
Lattice Parameters	a = 4.168	a = 4.144		a = 4.192 c = 8.039	a = 4.196 c = 8.008

[a] JCPDS-ICDD standard reference

Table 3.1.2: Lattice parameters and residual error associated with the main planes for γ-Mo_2N and β-Mo_2N obtained from the JCPDS-ICDD reference and the Mo nitride synthesized in this work.

Hydrogen chemisorption/TPD

Post-TPR, β-Mo_2N exhibited a measurable ambient temperature H_2 uptake (0.29 μmol g^{-1}, **Table 3.1.1**). It was not possible to find any comparable measurement of H_2 chemisorption on β-Mo_2N in the literature. We should, however, flag the work of Li. *et al.* [24] who demonstrated room temperature hydrogen adsorption on Mo_2N, although the crystallographic phase was not identified. In addition, Saito and Anderson [190] recorded an uptake of 14.3 μmol g^{-1} on γ-Mo_2N+Mo (BET = 7.3 m^2 g^{-1}). The dynamics of H_2 adsorption on group VI metal nitrides is still not well understood. Furimsky in his review [4] has considered H_2 activation on nitrogen deficient Mo-N sites, which leads to a heterolytic interaction with possible dissociative adsorption. The limited published work suggests that H_2 chemisorption capacity is dependent on temperature [191] and nitride surface area [59]. Li *et al.* [17], studying H_2 adsorption on β-Mo_2N, recorded an order of magnitude greater uptake (from 12 to 173 μmol g^{-1}) with increasing temperature (308 K → 623 K) that they attributed to the formation of a stable hydride phase in the nitride sub-surface. Temperature programmed desorption analysis, subsequent to H_2 chemisorption, demonstrated a significant quantity of H_2 associated with β-Mo_2N (see **Figure 3.1.2(B)** and **Table 3.1.1**) where the amount desorbed was appreciably greater (by up to a factor of 20) than that measured by chemisorption and must result from hydrogen uptake during TPR. The total H_2 desorbed (0.7 μmol m^{-2}) is close to that reported (0.8 μmol m^{-2}) by Li and co-workers. [17]. The TPD profile presents a broad peak, extending from *ca.* 700 K into the final isothermal hold (933 K) with a T_{max} at 806 K and two shoulders at 750 K and 900 K. This response suggests the release of a hydrogen component that interacts to varying degrees with β-Mo_2N. The possibility of strongly bound hydrogen species in the sub-layers and/or bulk Mo_2N has been proposed [24]. Choi *et al.* [20] observed a high temperature peak (at *ca.* 800 K) for H_2 TPD from a β–$Mo_{16}N_7$ thin film and associated this with hydrogen desorption from high energy sub-surface sites. Li *et al.* [24] demonstrated that hydrogen adsorbed at room temperature desorbed in the temperature range 600-773 K and suggested a surface dissociative adsorption on Mo-N pairs with migration from low to high energy sites. Moreover, Haddix and co-workers [22], using NMR to probe hydrogen interaction with Mo_2N, concluded that strongly bound hydrogen atoms can be generated at room temperature, occupying *ca.* 10% of the total (BET) surface area, suggesting adsorption at nitrogen deficient sites on the surface. A depletion in nitrogen content has been suggested for thermal treatments (T >823 K) [19, 20, 183]. There was no detectable (by XRD) alteration to nitride structure resulting from the TPD measurements in this study and no significant change in nitrogen content (from elemental analysis).

b. Pd/Al_2O_3

A 1% w/w Pd/Al_2O_3 was chosen as a reference catalyst against which the catalytic performance of β-Mo_2N was assessed; critical structural characteristics are given in **Table 3.1.1**. The BET area (157 m^2 g^{-1}) is within the range (75-178 m^2 g^{-1}) of values reported in the literature for δ-Al_2O_3 [192, 193]. The recorded TPR profile is shown in **Figure 3.1.4(A)** and presents a single sharp negative peak (H_2 release) at 332 K, which can be ascribed to the decomposition of Pd hydride formed by H_2 absorption where P_{H_2} >0.013 atm [194]. Hydride composition (H/Pd molar ratio) is dependent on Pd particle size where an increase in Pd dispersion is accompanied by a concomitant enhancement in surface-to-bulk atom ratio with a decrease in the void space available for H_2 diffusion in the metal cluster [195]. The value recorded in this study (= 0.31 μmol_H μmol_{Pd}^{-1}) is significantly lower than that reported [196, 197] for bulk Pd (0.66 - 0.73 μmol_H μmol_{Pd}^{-1}), suggesting the presence of a well dispersed Pd phase. There was no evidence of any H_2 consumption prior to hydride decomposition, confirming the presence of Pd^0 in the *as-prepared* sample (see Experimental section). Hydrogen chemisorption was an order of magnitude greater than that recorded for β-Mo_2N (see **Table 3.1.1**) and close to the value reported (0.3 mmol g_{Pd}^{-1}) elsewhere [148] for Pd/Al_2O_3 prepared by standard impregnation (d_{TEM} = 20 nm), suggesting a similar metal dispersion to the catalyst used in this study. Indeed, a Pd particle size of *ca.* 14 nm was calculated from H_2 chemisorption ($d_{chem}= 6/(S_{Pd} \times \rho_{Pd})$ where $\rho_{Pd} = 12.02$ g_{Pd} cm_{Pd}^{-3}), assuming spherical morphology [195, 198] and exclusive dissociative adsorption (H_2:Pd = 1:2) [199, 200]. XRD analysis generated the diffractogram shown in **Figure 3.1.4(B)**, which is dominated by a peak at *ca.* 67° due to the (442) plane of δ-Al_2O_3. In addition to the support peaks, there are reflections due to a Pd metal phase, *i.e.* at $2\theta = 40.1°$, 46.7° and 82.1° corresponding to (111), (200) and (311) planes, respectively. The representative TEM micrograph shown in **Figure 3.1.4(C)** demonstrates that Pd is present as discrete particles (≤ 30 nm) with a mean size of 18 nm (**Table 3.1.1**) that is consistent with the H_2 chemisorption measurement.

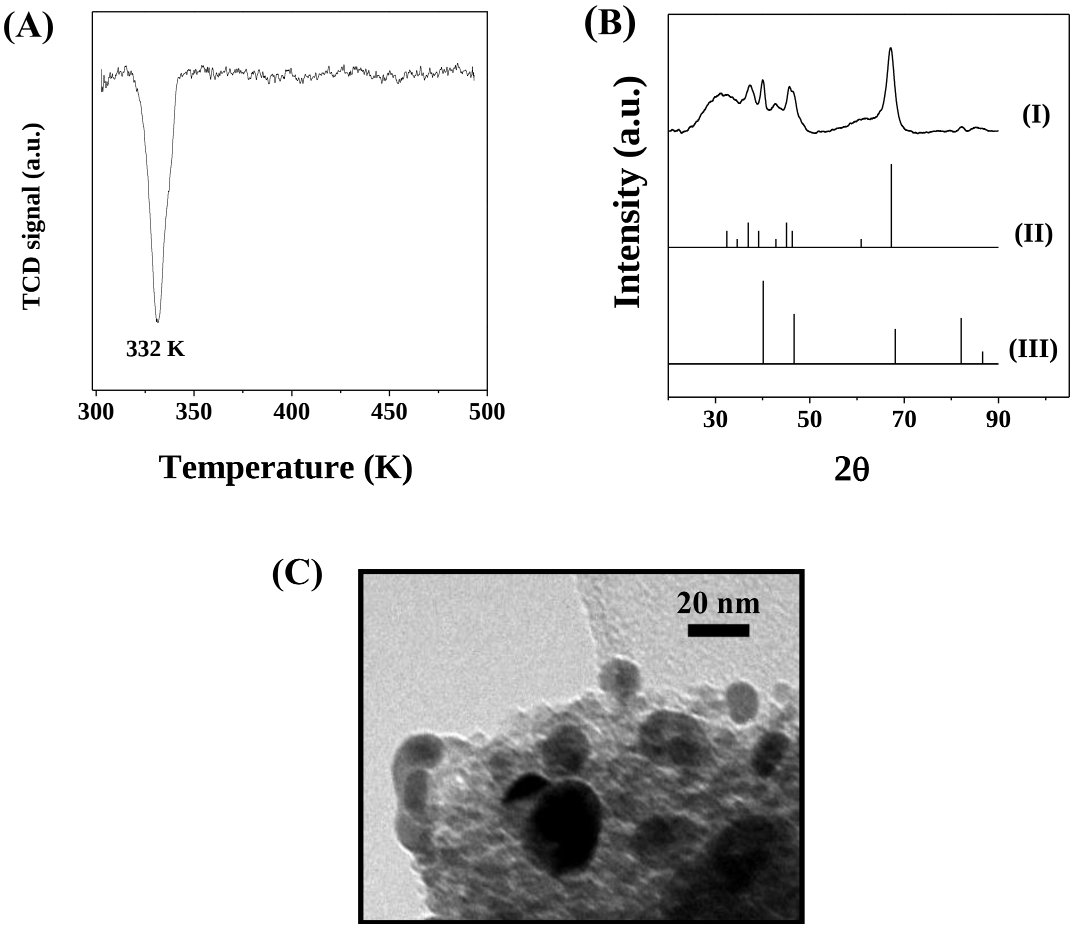

Figure 3.1.4: (A) TPR profile for Pd/Al_2O_3; **(B)** XRD diffractograms for **(I)** activated Pd/Al_2O_3 and JCPDS-ICDD reference for **(II)** δ-Al_2O_3 (47-1770) and **(III)** Pd (46-1043); **(C)** representative TEM image of Pd/Al_2O_3.

3.1.3.2 Catalyst Activity/Selectivity

a. Hydrogenation of *p*-Chloronitrobenzene

The observed capacity of β-Mo_2N for hydrogen uptake/desorption (**Table 3.1.1**) suggests a catalytic hydrogenation capability that was tested in the batch liquid phase conversion of *p*-CNB, as a model reactant; the temporal variation of *p*-CNB concentration is shown in **Figure 3.1.5(A)**. 100% *p*-CAN yield was achieved with no evidence of aromatic ring hydrogenation and/or or hydrogenolysis of the –Cl or $–NO_2$ substituents. This ultraselective response, in terms of $–NO_2$ group reduction, is a significant finding when considering the number of studies dealing with liquid phase catalytic *p*-CNB hydrogenation where C–Cl bond scission has been a feature of reaction over mono- (Ni [158], Pd [201], Pt [202] and Ru [203]) and bi- (Pt-X; X= Cr, Mn, Fe, Co, Ni and Cu [204] and LaNiB [158]) metallic catalysts. The target amine product (*p*-CAN) is a high production volume compound used in the manufacture of a range of pesticides, herbicides, pigments, pharmaceuticals and cosmetics [205]. Catalytic activity was quantified in terms of the initial *p*-CNB hydrogenation rate ($R_{p\text{-}CNB} = 3.1 \times 10^{-5}$ mol dm^{-3} min^{-1}), determined from a linear regression of the temporal *p*-CNB concentration profile (see inset to **Figure 3.1.5(A)**). In order to fully evaluate the performance of β-Mo_2N, the catalytic response was compared with that of an established hydrogenation catalyst (Pd/Al_2O_3) under the same reaction conditions. Indeed, supported Pd has been extensively used to promote the liquid phase hydrogenation of substituted nitroarenes [165, 167, 169, 206], including *p*-CNB [165, 207, 208]. The temporal concentration profiles for the conversion of *p*-CNB are shown in **Figure 3.1.5(B)**, where it can be seen that the activity in terms of *p*-CNB consumption was significantly higher for Pd/Al_2O_3. This can be linked to the greater hydrogen chemisorption capacity exhibited by Pd/Al_2O_3 (**Table 3.1.1**). However, while the nitride delivered 100% yield to the target *p*-CAN, Pd/Al_2O_3 promoted hydrodechlorination with the formation of NB and subsequent hydrogenation to AN with a 78% yield to *p*-CAN at complete *p*-CNB conversion.

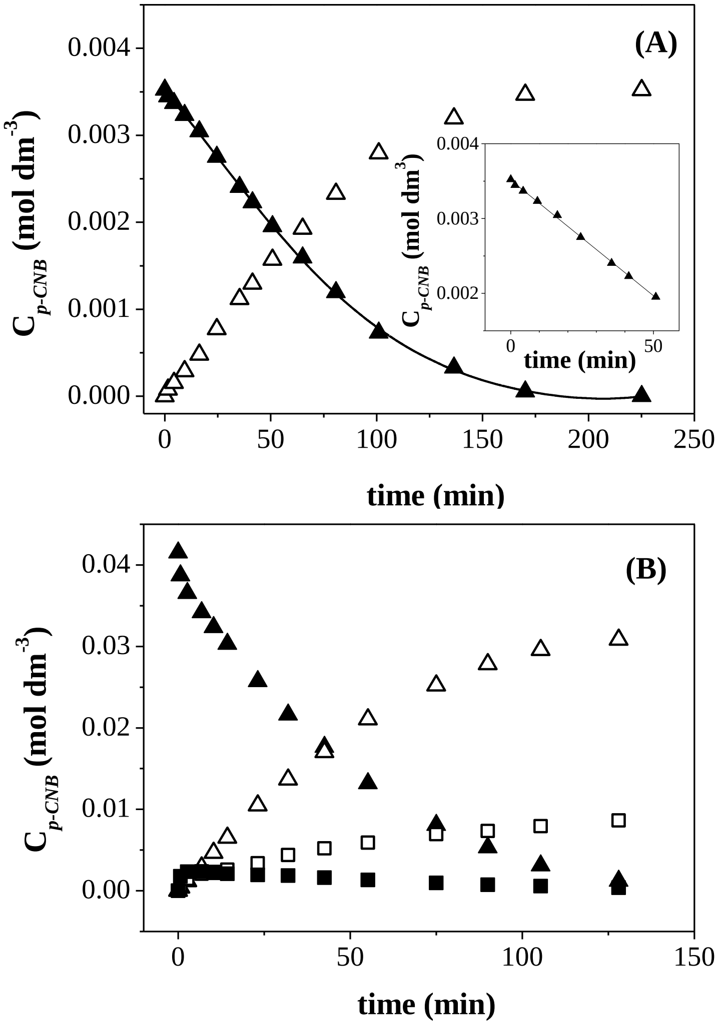

Figure 3.1.5: Temporal variation of *p*-CNB (▲), *p*-CAN (△), NB (■) and AN (□) concentration (C_i) for reaction over **(A)** β-Mo$_2$N and **(B)** Pd/Al$_2$O$_3$. Inset to **Figure 5(A)**: linear fit to temporal $C_{p\text{-CNB}}$ used to obtain initial rate ($R_{p\text{-CNB}}$); P_{H_2} = 11 bar, T = 423 K, *p*-CNB/β-Mo$_2$N = 0.2 $\mathrm{mol}_{p\text{-CNB}}\ \mathrm{mol}^{-1}_{\beta\text{-Mo}_2\text{N}}$, *p*-CNB/Pd = 480 $\mathrm{mol}_{p\text{-CNB}}\ \mathrm{mol}^{-1}_{\mathrm{Pd}}$.

As emphasized by Somorjai and Kliewer [209], maximising selectivity to high value products is the critical challenge in 21st century chemical processing. The increasing sustainability demand placed on the chemical sector is the driver for improved selectivity to avoid costly downstream separations, clean up and disposal. Any step change improvement in catalysis must address crucial selectivity issues. These results serve to demonstrate the selective catalytic hydrogenation action of β-Mo_2N and the potential for cleaner amine synthesis.

b. Hydrogenation of *para*-Substituted Nitrobenzenes: A Hammett Treatment.

In order to quantify the effect on reactivity due to the presence of a second functionality in the *para*-position, the hydrogenation of a series of *para*-substituted (-H, -OH, -O-CH_3, -CH_3, -Cl, -I and -NO_2) nitrobenzenes was investigated over β-Mo_2N and applied the Hammett relationship. The Hammett correlation is a practical tool that can be used to predict rate and equilibrium constants [210, 211] and elucidate reaction mechanisms [212] without prior experimental determination. In this approach, the initial hydrogenation rate (to the amine) for substituted nitroarene reactants (R_i) is related to that recorded for the reference benzene derivate (R_0, NB in this case) according to

$$\ln\left[\frac{R_i}{R_0}\right] = \rho \times \sigma_i \tag{3.1.5}$$

where σ_i and ρ are the substituent and reaction constants, respectively. The σ_i factor is an empirical parameter that is dependent on the substituent position on the ring and electron donating/acceptor character [213]; reference values are available in the literature [212, 213]. The ρ term, or reaction constant, is a measure of the susceptibility of the reaction to substituent electronic effects [214]. When the transition state is negatively charged, the reaction rate is accelerated by electron-withdrawing substituents and $\rho > 0$. Although initially conceived for *non*-catalytic reactions, the applicability of the Hammett approach has been demonstrated for catalyzed homogeneous [211, 215, 216] and heterogeneous [217, 218] processes in both gas [215-217] and liquid [211, 218] phase operation. Of direct relevance to this study is the work of Lopidana *et al.* [219] and Belousov *et al.* [220] who demonstrated adjustment to the Hammett equation for the liquid phase hydrogenation of polysubstituted nitroarenes over Pt/SiO_2-$AlPO_4$ and Re thiocomplexes, respectively. The applicability of the Hammett relationship to the nitroarene hydrogenation rate data generated using β-Mo_2N is demonstrated in **Figure 3.1.6**. The slope of the linear fit gives a positive value for ρ (= 0.4), which is consistent with a nucleophilic mechanism as proposed elsewhere [221], *i.e.* hydrogen acting as nucleophilic agent that attacks the activated –NO_2 group with the formation of a negatively charged intermediate.

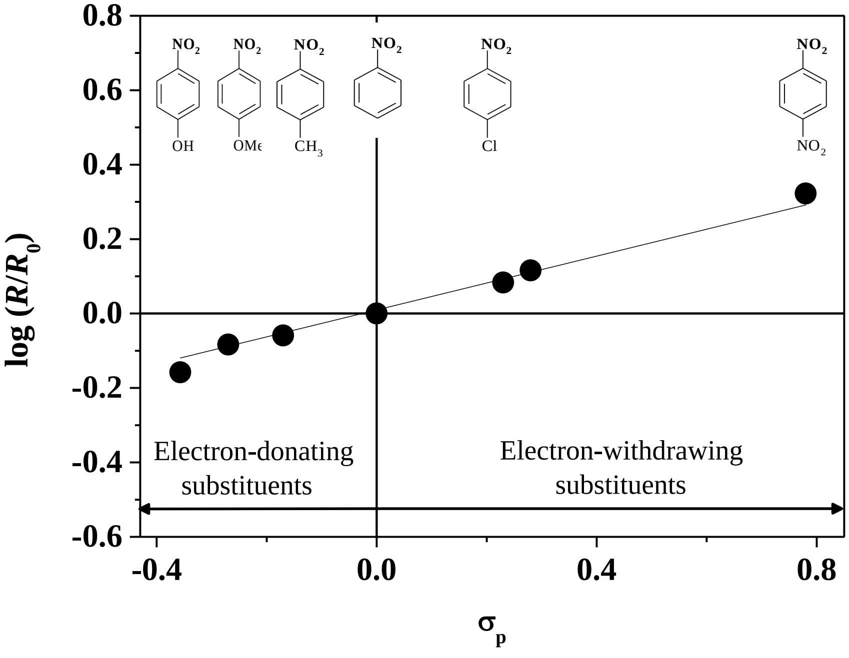

Figure 3.1.6: Hammett plot for the selective −NO2 group reduction of *para*-substituted nitroarenes over β-Mo_2N at T = 423 K.

The ρ value obtained in this study is comparable to those reported for the liquid phase hydrogenation of nitro-aromatics over unsupported iron oxide hydroxide [222] and Re thiocomplexes [220] (0.24-0.55) and Pt/SiO_2-$AlPO_4$ (0.1-2.0 [219]) and gas phase operation over

Au/TiO_2 (0.93) and Ag/TiO_2 (0.22) [223]. This suggests an analogous reaction mechanism for the formation of amines in these heterogeneous catalysts systems. A first insight into the nitroarene hydrogenation mechanism over β-Mo_2N was provided here with far ranging implications for processes in the agrochemical, fine chemical and pharmaceutical sectors.

3.1.4. Conclusions

β-Mo_2N was synthesized by the temperature programmed treatment (to 933 K) of MoO_3 in N_2/H_2 (15% v/v) to deliver a crystalline product (BET = 7 m^2 g^{-1}; pore volume = 0.02 cm^3 g^{-1}), characterized by an agglomeration of flake-like structures (1-5 μm). The passivated (in 1% v/v O_2) nitride exhibited a residual Mo^{6+} content that can be attributed to the superficial oxide layer where XPS analysis indicates a lower Mo oxidation state for β-Mo_2N. Temperature programmed reduction to 637 K was necessary to remove the passivation layer and TPD measurement has revealed a significant quantity of hydrogen (0.7 μmol m^{-2}) associated with the activated β-Mo_2N. The Mo nitride was used as a catalyst in the liquid phase hydrogenation of *p*-CNB where 100% selective with respect to –NO_2 group reduction was achieved at complete conversion of the nitroarene. In contrast, Pd/Al_2O_3 (BET area = 157 m^2 g^{-1}, total pore volume = 0.2 m^3 g^{-1}, mean Pd particle size *ca.* 18 nm), used as a benchmark catalyst, was *non*-selective and generated NB and AN (from *p*-CNB) from a combined hydrodechlorination/hydrogenation. The hydrogenation of a range of *para*-substituted (-H, -OH, -O-CH_3, -CH_3, -Cl, -I and -NO_2) nitrobenzenes over β-Mo_2N proceeded *via* a nucleophilic mechanism where the presence of electron withdrawing ring substituents served to elevate rate, as demonstrated by the linear Hammett relationship and positive reaction constant (ρ = 0.4). These results demonstrate the potential of β-Mo_2N to promote the clean production of amino-compounds with multiple industrial applications.

3.2 Au/Mo_2N as a New Catalyst Formulation for the Hydrogenation of *p*-CNB in both Liquid and Gas Phase

Abstract

The batch liquid phase hydrogenation of *p*-chloronitrobenzene over Mo_2N resulted in the sole formation of *p*-chloroaniline. Incorporation of Au nanoparticles (mean size = 8 nm) enhanced hydrogen uptake with a four-fold increase in rate, retention of ultraselectivity with stability over repeated reaction cycles. Reaction exclusivity to *p*-chloroaniline extended to continuous gas phase operation where Au/Mo_2N outperformed Au/Al_2O_3 as a benchmark. Under the same conditions, Pd/Mo_2N was *non*-selective, generating nitrobenzene and aniline *via* combined hydrodechlorination and hydrogenation. These results demonstrate the viability of Au/Mo_2N as a new catalyst formulation in selective substituted nitroarene hydrogenation.

3.2.1. Introduction

Catalysis has a crucial role to play in sustainable chemical manufacture where chemoselectivity, the ability to react one functional group while preserving other (often more reactive) functionalities, is a major challenge [209]. Indeed, the appreciable waste resulting from the conversion of nitroarenes, the focus of this study, led Sheldon [224] to introduce the concept of the E(nvironmental) Factor (kg waste/kg product), which highlighted the severe environmental impact associated with the production of substituted amines as high value chemical commodities [141]. Taking the hydrogenation of chloronitrobenzenes as an example, nitroso- and hydroxylamine- intermediates can undergo side reactions to generate toxic (dichloroazoxybenzene, dichloroazobenzene and dichlorohydrazobenzene) *by*-products [141]. Moreover, C–Cl bond scission results in the formation of nitrobenzene (NB) and aniline (AN) as principal products [225]. A critical advancement in cleaner amine synthesis in batch operation using oxide supported Au catalysts has resulted from the work of Corma *et al.* [226], who demonstrated a preferential activation of $-NO_2$ with H_2 dissociation at low coordination Au sites by *in situ* IR spectroscopy and theoretical calculations. A recent brainstorming exercise involving the American Chemical Society (ACS), Green Chemistry Institute (GCI) and global pharmaceutical corporations (the ACS GCI Pharmaceutical Roundtable) has highlighted the switch from batch to continuous processing as crucial for the sustainable manufacture of fine chemicals [227]. Adopting this imperative, $-NO_2$ hydrogenation chemoselectivity over Au in gas phase continuous operation was established in previous studies [225, 228, 229]. Studies to date have shown low hydrogenation activity for Au that can be ascribed to a restricted activation/dissociation of H_2 [230], which is dependent on Au particle size [231]. Given that hydrogen activation can be a limiting factor, the use of a support for Au that can chemisorb H_2 (increasing surface concentration) was explored as a possible route to higher hydrogenation rates.

Mo nitrides exhibit a significant hydrogen uptake capacity, which has been attributed to a contraction of the *d*-band and modification of electron density as a result of the interstitial incorporation of N in the Mo metal lattice [4]. The use of Mo nitrides in hydrogen mediated reactions has been considered to some extent with evidence of catalytic activity for gas phase NO reduction [173] and the hydrogenation of CO [175] and ethyne [176]. As Mo_2N can chemisorb hydrogen and Au is selective for nitro-group reduction, the combination of Au with Mo nitride is proposed in this study as a new catalyst formulation directed at elevating hydrogenation rate while maintaining chemo-selectivity. Taking *p*-chloronitrobenzene (*p*-CNB) as a test reactant, the catalytic action of Mo_2N and Au/Mo_2N was examined in both batch liquid and continuous gas phase operation. The catalytic action of Au/Mo_2N was also compared with Au/Al_2O_3 (as benchmark [229]) to probe a possible support effect, *i.e.* Mo_2N *vs.* Al_2O_3. Moreover, as Pd has shown enhanced activity in $–NO_2$ reduction [232], the catalytic performance of Pd/Mo_2N was also examined.

3.2.2 Experimental Section

3.2.2.1 Catalyst Preparation and Characterization

Mo_2N was prepared by heating MoO_3 (99.9995% w/w, Alfa Aesar) in 15 cm^3 min^{-1} (*GHSV* = 1500 h^{-1}) 15% v/v N_2/H_2 at 5 K min^{-1} to 933 K (18 h). Reduction/nitridation was quenched in Ar (65 cm^3 min^{-1}), the sample cooled to room temperature and passivated (in 1% v/v O_2/He) for off-line analysis. Nitride passivation *post*-synthesis served to provide a superficial oxide film and was required to avoid sample autothermal oxidation upon contact with air [233]. A suspension of

$HAuCl_4$ (300 cm^3, 3×10^{-4} M, Aldrich), aqueous urea (100 cm^3, 0.86 M) and Mo_2N was mixed (at 300 rpm) and heated (1 K min^{-1}) to 353 K (2.5 h). The solid was filtered and washed with distilled water until the wash water was Cl-free (based on the $AgNO_3$ test), dried in He (45 cm^3 min^{-1}) at 383 K for 3 h, sieved into a batch of 75 μm average particle diameter and stored at 277 K under He in the dark. Pd/Mo_2N (2.5×10^{-4} M $Pd(NO_3)_2$, Aldrich) was synthesized following the same protocol. For comparison purposes, Au supported on Al_2O_3 (Puralox, Condea Vista) was prepared by standard impregnation with $HAuCl_4$ as described previously [234], dried and stored as above.

Temperature programmed reduction (TPR) and H_2 chemisorption (at 290 K) measurements were conducted using the commercial CHEM-BET 3000 (Quantachrome) unit. Samples were activated in 17 cm^3 min^{-1} 5% v/v H_2/N_2 at 2 K min^{-1} to 493-673 ± 1 K (1 h), swept with 65 cm^3 min^{-1} N_2 (1.5 h) and cooled to room temperature. After TPR, the reduced samples were swept with a 65 cm^3 min^{-1} flow of N_2 for 1.5 h, cooled to room temperature and subjected to H_2 chemisorption using a pulse (10 μl) titration procedure. BET area was recorded in a 30% v/v N_2/He flow and pore volume determined at a relative N_2 pressure of 0.95 using a Micromeritics Flowsorb II 2300 unit. Powder X-ray diffractograms were recorded on a Bruker/Siemens D500 incident X-ray diffractometer (Cu Kα radiation) and identified against JCPDS-ICDD standards (Mo_2N (25-1368); Au (04-0784)). Analysis by scanning electron microscopy (SEM) was conducted on a Philips FEI XL30-SFEG operated at an accelerating voltage of 10-20 kV. The samples for analysis were subjected to a hydrocarbon decontamination treatment using a plasma-cleaner (EVACTRON). Analysis of nitrogen content was performed using an Exeter CE-440 Elemental Analyzer after sample combustion at *ca.* 1873 K. The Au and Pd content (supported on β-Mo_2N or Al_2O_3 and in solution during reaction) was determined by atomic absorption spectrometry (Shimadzu AA-6650 spectrometer) using an air-acetylene flame. High resolution transmission electron microscopy

(HRTEM) employed a JEOL JEM 2011 unit operated at an accelerating voltage of 200 kV using Gatan DigitalMicrograph 3.4 for data treatment. The specimens were prepared by dispersion in acetone and deposited on a holey carbon/Cu grid (300 Mesh). The mean metal (Au or Pd) particle size is given as surface area-weighted mean (*d*) [228] where over 200 individual metal particles were counted for each catalyst.

3.2.2.2 Catalysis Procedures

Liquid phase reactions ($P_{H_2} = 11\ bar; T = 423 K$) were carried out in a commercial batch stirred stainless steel reactor (100 cm^3 autoclave, Büchi AG, Uster, Switzerland). Operation under negligible mass transfer resistance was established using the Madon and Boudart approach [182]. A stainless steel 6-blade disk turbine impeller equipped with a self-gassing hollow shaft provided effective agitation at a stirring speed of 1800 rpm. A recirculator (HAAKE B-N3) was used to stabilize the reaction temperature at T = 423 ± 1 K. The initial catalyst/*p*-CNB ratio spanned the range 320-1078 g mol^{-1}. Hydrogenation performance was assessed over three reaction cycles. In the first cycle, the catalyst was activated *ex-situ* in a quartz tube (60 cm^3 min^{-1} H_2; *GHSV* = 200 h^{-1}) at 673 K, cooled to room temperature and transferred to the reactor in a flow of N_2. Hydrogen consumption during reaction was monitored on-line with a press flow gas controller (BPC-6002, Büchi, Switzerland). In a series of blank tests, reactions carried out in the absence of catalyst did not result in any measurable conversion. A *non*-invasive liquid sampling system *via* a syringe with in-line filters allowed a controlled removal of aliquots ($\leq$ 0.5 cm^3) from the reactor. After reaction, the catalyst was filtered, reactivated as above and subjected to a second and a third reaction cycle.

Gas phase *p*-CNB hydrogenation was carried out ($P_{H_2} = 1\ bar; T = 493 K$) in a fixed bed vertical glass reactor (i.d. = 15 mm), operated under conditions of negligible heat/mass transport limitations. A layer of borosilicate glass beads served as preheating zone, ensuring that the organic reactant was vaporized and reached reaction temperature before contacting the catalyst. Isothermal conditions (± 1 K) were maintained by diluting the catalyst bed with ground glass (75 µm); the ground glass was mixed thoroughly with catalyst before insertion in the reactor. The reaction temperature was continuously monitored using a thermocouple inserted in a thermowell within the catalyst bed. *p*-CNB (Sigma-Aldrich, ≥ 99%) in ethanol (Sigma Aldrich, ≥ 99.8%) was delivered at a fixed calibrated flow rate *via* a glass/teflon air-tight syringe and teflon line using a microprocessor controlled infusion pump (Model 100 kd Scientific). A co-current flow of *p*-CNB and ultra pure H_2 (<1% v/v organic in H_2) was maintained at $GHSV = 330\ \text{min}^{-1}$ with a catalyst mass to inlet *p*-CNB molar rate (W/F) in the range 8×10^3-8×10^4 g mol^{-1} min. Product composition was determined using a Perkin-Elmer Auto System XL chromatograph equipped with a programmed split/splitless injector and a flame ionization detector, employing a DB-1 capillary column. Repeated reactions with the same batch of catalyst delivered conversion/selectivity values that were reproducibility to within ± 7%.

3.2.3. Results and Discussion

3.2.3.1 Catalyst Characterization

The formation of Mo_2N was confirmed by XRD (see **Figure 3.2.1(AI)**) where signals over the range $2\theta = 38°$-$81°$ can be assigned to the eight principal planes of β-nitride (JCPDS-ICDD 25-1368). The representative TEM image in **Figure 3.2.1(AII)** coupled with diffraction analysis **(IIa)** establish a spacing of 0.24 nm between the planes in the atomic lattice that is characteristic of the β-Mo_2N (112) plane. Moreover, nitrogen content (5.4% wt.), BET surface area (7 m^2 g^{-1}) and pore volume (0.02 cm^3 g^{-1}) are close to those quoted in the literature for molybdenum nitride

[39]. The SEM micrograph of the *as*-prepared sample is presented in **Figure 3.2.1(A)III** and shows an agglomeration of crystallites < 5 μm (see **IIIa**). As the starting MoO_3 is characterized by a platelet morphology [11], the reduction/nitridation process ($MoO_3 \rightarrow MoO_2 \rightarrow Mo \rightarrow Mo_2N$) resulted in a *non*-topotactic transformation where the precursor orthorombic crystal structure was not maintained [178]. Temperature programmed reduction (TPR) of Mo_2N (**Figure 3.2.2**, profile **I**) generated a single peak at T_{max} = 637 K that can be associated with hydrogen consumption for the removal of the passivation overlayer [19]. It has been proposed [23] that passivation of Mo_2N results in the formation of one or two chemisorbed oxygen monolayers. The incorporation of Au (0.25% w/w, see **Table 3.2.1**) with Mo_2N induced a shift in the main hydrogen consumption peak (by 34 K) to a lower temperature, demonstrating a more facile removal of the passivating oxygen due to the presence of Au (**Figure 3.2.2**, profile **II**). Although no directly comparable TPR analysis could be found in the open literature, these results are in line with the work of Wang *et al.* [235] who recorded a decrease in the reduction temperature (up to 150 K) of the passivation layer due to the inclusion of Ni. Chemisorption measurements have revealed a measurable increase in the amount of hydrogen uptake due to the inclusion of Au (**Table 3.2.1**), a result that suggests the presence of well dispersed Au nanoparticles (<10 nm) where dissociative adsorption can occur at low coordination sites, notably at steps, edges and corners [231]. The TEM image provided in **Figure 3.2.1(B)I** serves to illustrate the nature of Au dispersion and morphology. The diffractogram pattern for an isolated Au particle (**Figure 3.2.1(B)IIa**) confirms the presence of metallic Au with associated *d*-spacings = 0.20/0.23 nm consistent with the (200) and (111) planes of Au^0 (JCPDS-ICDD 04-0784). The intensity profile across the support shown in **Figure 3.2.1(B)IIb** delivered an average *d*-spacing = 0.24 nm, consistent with β-Mo_2N. The Au particles exhibit a *pseudo*-spherical morphology and a size distribution in the 2-14 nm range, as illustrated

in the histogram given in **Figure 3.2.1(B)III**, with a mean particle size of (*d* =) 8 nm (**Table 3.2.1**). It should be noted that there is an appreciable component of Au particles with diameters ≤ 10 nm, *i.e.* the proposed critical Au size range for catalytic activity in hydrogen mediated reactions [236].

As the aim of this work is to explore the possibility of an enhanced selective hydrogenation rate over Mo nitride supported Au, Au/Al_2O_3 was taken as a benchmark catalysts that has exhibited ultra-selectivity in –NO_2 group reduction [225]. It was established previously [234] that the reference Au/Al_2O_3 shows the same mean Au particle size (8 nm) as Au/Mo_2N. Given that nitroarene hydrogenation rate over supported Au is sensitive to dispersion [228], an explicit comparison of performance in terms of a support effect necessitates equivalence in terms of Au size. The synthesized Au/Mo_2N demonstrated an appreciably higher (by a factor of 8) level of hydrogen chemisorption relative to Au/Al_2O_3 (mmol mol_{Au}^{-1}, see **Table 3.2.1**), which must be due to a contribution from both Au and Mo_2N components. As both samples exhibit the same mean Au size, differences in uptake can be attributed to the Au/support interface where electronic interactions have been proposed to impact on hydrogen chemisorption capacity [26]. Since the catalytic action of Pd in −NO_2 reduction is well established [237], reaction over Pd/Mo_2N was also considered in order to evaluate the effect of incorporating a different metal with Mo_2N. Pd/Mo_2N presented a uniform distribution of Pd nanoparticles (size range = 1-7 nm, mean = 2 nm) and exhibited increased H_2 chemisorption (see **Table 3.2.1**) compared with the supported Au systems, as has been noted elsewhere [225].

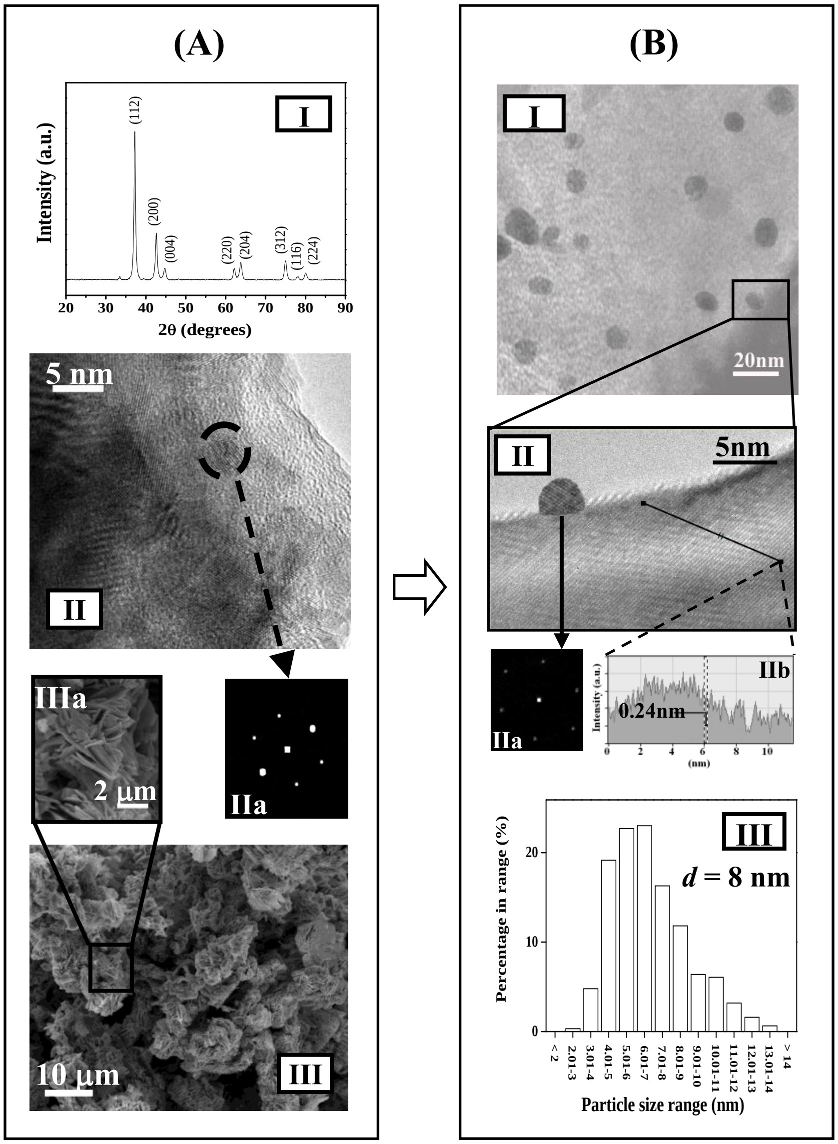

Figure 3.2.1: **(A)** Mo_2N: XRD pattern **(I,** including peak assignments based on JCPDS-ICDD 25-1368**)**, representative TEM image **(II)** with diffractogram pattern **(IIa)** and SEM micrograph **(III)** with higher magnification image **(IIIa)** illustrating crystal morphology. **(B)** Au/Mo_2N: representative medium **(I)** and high **(II)** resolution TEM images and metal particle size distribution **(III)**. *Note:* diffractogram pattern of isolated Au particle **(IIa)** and intensity profile revealing distance between planes of the atomic lattice in the 12 nm segment marked on the nitride support **(IIb)**.

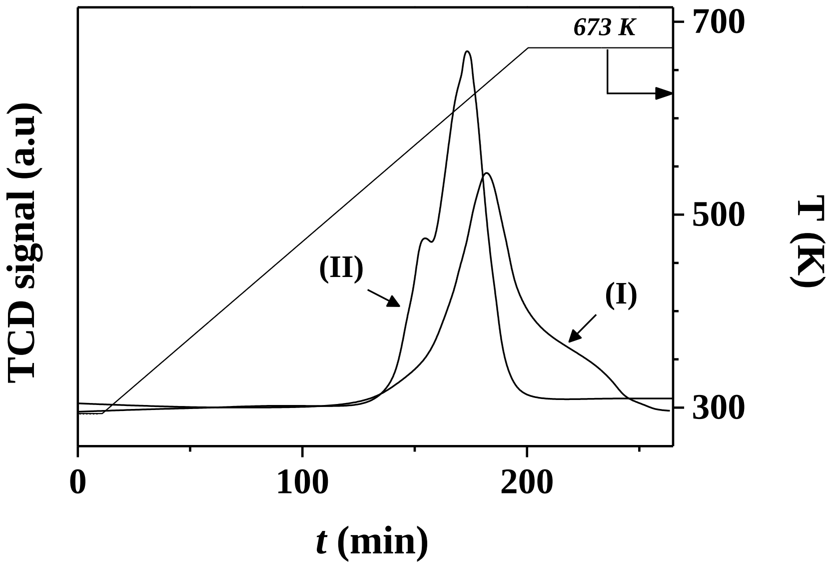

Figure 3.2.2: TPR profiles for **(I)** Mo_2N and **(II)** Au/Mo_2N.

Catalyst		Mo_2N	Au/Mo_2N	Au/Al_2O_3	Pd/Mo_2N	Error
Metal loading	(%w/w)	-	0.25	1	0.32	± 0.02
H_2 chemisorption	(μmol g^{-1})	0.29	0.42	0.21	0.51	± 0.01
	(mmol mol_{Au}^{-1})	-	32	4	-	± 1
Metal size range	(nm)	-	2-14	1-20	1-7	± 0.5
d	(nm)	-	8 ± 1.7	8 ± 1.4	2 ± 1.5	

Table 3.2.1: Hydrogen chemisorptions, metal (Au or Pd) loading and particle size range and mean value (*d*).

3.2.3.2 Catalysis Results

a. Batch Liquid Phase Operation

100% selectivity to the target *p*-chloroaniline (*p*-CAN) was achieved for reaction over Mo_2N in batch liquid phase operation at 100% conversion of *p*-CNB. There was no detectable hydrogenolytic activity to produce chlorobenzene, NB, AN or benzene. This is an important finding in the light of previous studies where C–Cl scission accompanied high CNB conversion in liquid phase reaction. Indeed, dechlorination in the hydrogenation of chloroarenes has been a feature of reactions over supported Pt, Rh, Ru, Ni and Cu [140] catalysts. Reaction kinetics exhibited *pseudo*-first order behaviour (correlation coefficient, $r^2 > 0.98$; see **Figure 3.2.3(AI)**) and catalytic activity can be quantified in terms of the initial rate of *p*-CNB consumption (157 μmol g^{-1} min^{-1}). Incorporation of Au with Mo_2N served to increase hydrogenation rate (by a factor of 4) with *p*-CAN again as the sole product (**Figure 3.2.3(A)II**). Furthermore, 100% selectivity to *p*-CAN was retained at extended reaction times (up to 27 h, not shown). Catalyst stability was considered and the feasibility of reuse can be assessed from the entries in **Figure 3.2.3(B)**. The reaction rate generated using Au/Mo_2N after three consecutive runs was equivalent to that obtained in the first reaction cycle (632 *vs.* 639 μmol g^{-1} min^{-1}) and reaction exclusivity to *p*-CAN was maintained in each cycle. Moreover, there was no evidence of Au leaching during reaction. This is an important consideration that has been emphasized by Arens and Sheldon [238]: supported metal catalysts must be resistant to metal leaching into solution under operation conditions in order to have a real synthetic utility. While this feature has not been examined in any great detail for supported Au systems, there is evidence of significant Au leaching from TiO_2 and Al_2O_3 for reactions in liquid phase [239].

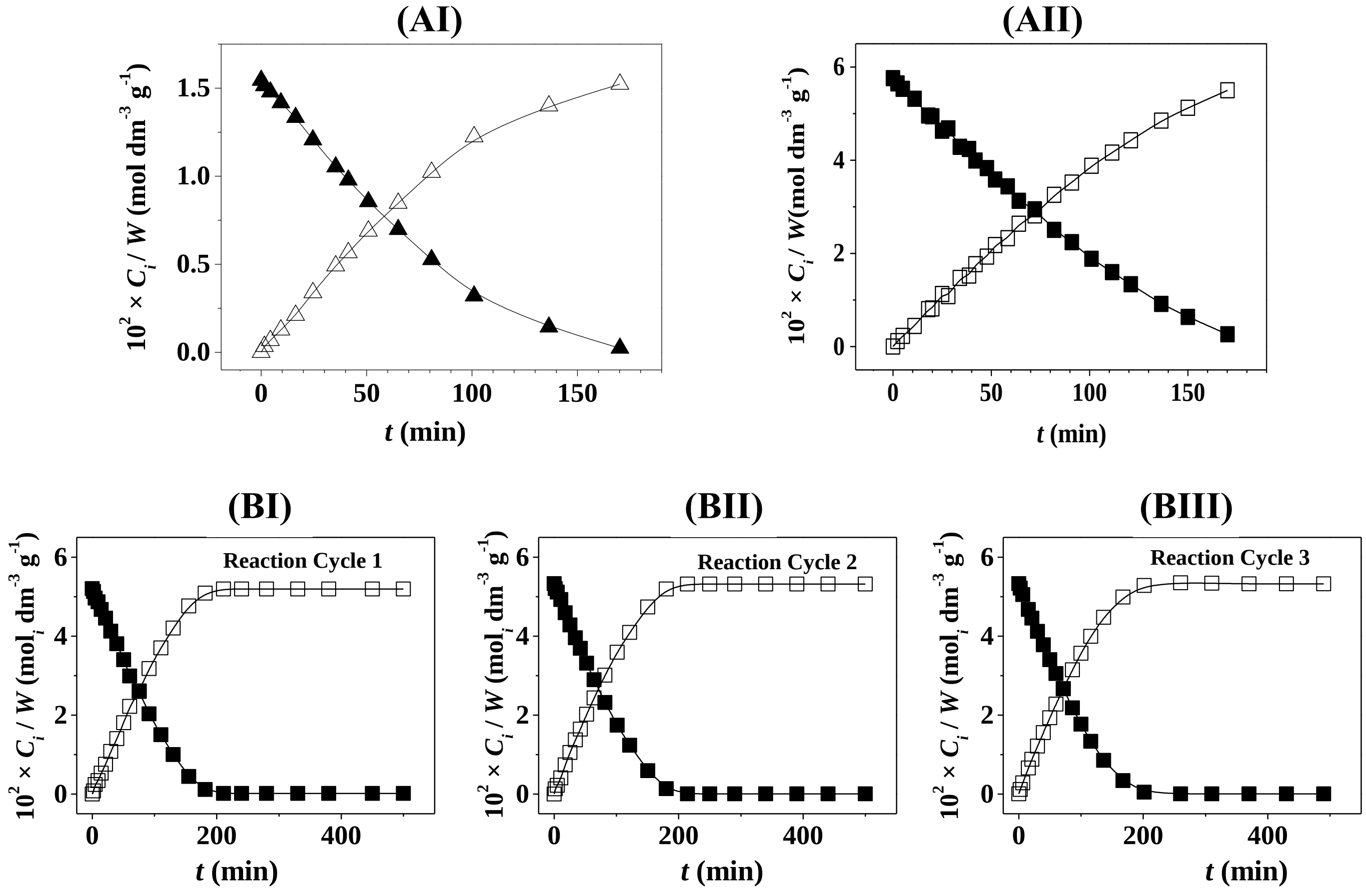

Figure 3.2.3: Catalytic response in batch liquid phase operation: **(A)** temporal variation of *p*-CNB (solid symbols) and *p*-CAN (open symbols) concentration (per g of catalyst, C_i/W) for reaction over **(I)** Mo_2N (▲,△) and **(II)** Au/Mo_2N (■,□); **(B)** temporal variation of *p*-CNB (■) and *p*-CAN (□) concentration (per g of catalyst, C_i/W) for reaction over Au/Mo_2N in three consecutive reactions **(I-III)**; *Reaction conditions*: P_{H_2} = 11 bar, T = 423 K.

b. Continuous Gas Phase Operation

Following on from the recommendations of the ACS GCI Pharmaceutical Roundtable [227], the potential of the Au/Mo_2N catalyst formulation was further tested in gas phase continuous operation. It must be stressed from the very outset that nitroarene hydrogenations to date have focused on batch liquid phase processing and this study represents the first instance where the feasibility of both operational modes is demonstrated. 100% selectivity to *p*-CAN extended to gas phase operation with increased *p*-CAN production over Au/Mo_2N relative to Mo_2N as a function of time on-stream (see **Figure 3.2.4(AI)**). The improved catalytic performance resulting from the combination of Au with Mo_2N is further demonstrated in the *pseudo*-first order kinetic plots presented in **Figure 3.2.4(AII)**. This response then holds in both liquid and gas phase reactions and can be linked to the increased hydrogen uptake on Au/Mo_2N (**Table 3.2.1**). Variations in hydrogen surface concentration are known to influence the catalytic response where a concomitant increase in activity and surface hydrogen for molybdenum nitrides has also been reported elsewhere [187]. Zhang *et al.* [240], studying the hydrogenation of cyclohexene and the hydrodesulphurisation of thiophene over Mo_2N, associated the higher activity with the incorporation of Zr to an increase in weakly bound hydrogen.

A major finding in this work is the appreciably greater activity exhibited by Au/Mo_2N relative to Au/Al_2O_3 (at a common mean Au particle size), which is demonstrated in **Figure 3.2.4(B)**. We take this as a demonstration of a surface cooperative effect involving Au and Mo_2N that results in a concomitant enhanced hydrogen uptake (**Table 3.2.1**) and catalytic efficiency. This effect can be tentatively attributed to electronic interactions at the Au/support interface. Blaser *et al.* [141] concluded that reaction at the gold-support interface can contribute to overall hydrogenation rate acceleration. Shimizu *et al.* [83] studied the effect of the carrier for supported Ag catalysts in nitroarene reduction and reported a synergy between Ag and Al_2O_3 that governed the rate-limiting H_2 dissociation to generate a H^+/H^- pair at the metal/support interface. The hydrogenation rate can also be influenced by differences in *p*-CNB/surface interaction ($–NO_2$ activation) where the Au-Mo_2N interface may play a critical role. Corma and *co*-workers [241] have differentiated between $–NO_2$ group adsorption on the support and Au-support interface in terms of reactant activation, notably for Au/TiO_2.

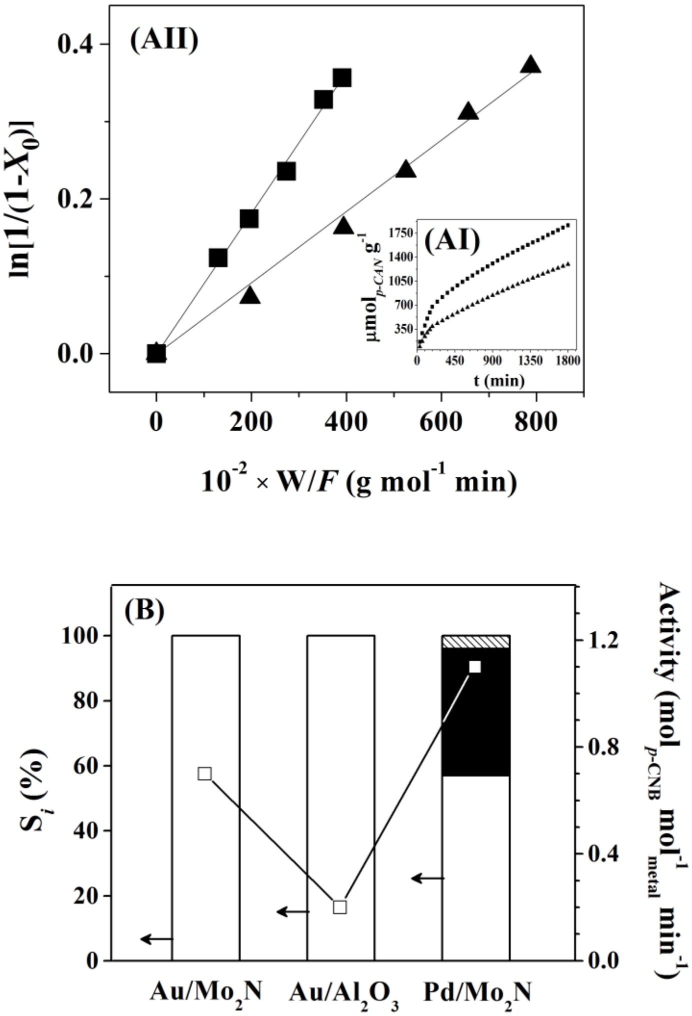

Figure 3.2.4: Catalytic response in continuous gas phase operation: **(AI)** time on-stream p-CAN production over Mo_2N (▲) and Au/Mo_2N (■); **(AII)** fractional initial conversion of p-CNB (X_0) as a function of W/F over Mo_2N (▲) and Au/Mo_2N (■) where the lines represent fit to pseudo-first order kinetics; **(B)** specific activity with selectivity to p-CAN (open bars), AN (hatched bars) and NB (solid bars) under conditions of equal fractional p-CNB conversion (X_0 ~ 0.2) over Au/Mo_2N, Au/Al_2O_3 and Pd/Mo_2N; *Reaction conditions*: P_{H_2} = 1 bar, T = 493 K.

This effect was indirectly probed by examining the catalytic action of Pd/Mo_2N where a higher *p*-CNB hydrogenation rate (**Figure 3.2.4(B)**) relative to Au/Mo_2N was recorded. These results are consistent with published literature where increased hydrogen uptake/activity over supported Pd (relative to Au) has been reported [225]. In marked contrast to Au/Mo_2N and Au/Al_2O_3, at a common *p*-CNB conversion Pd/Mo_2N promoted the formation of NB and AN as products of hydrodechlorination and hydrogenation (**Figure 3.2.4(B)**). Interaction with Pd/Mo_2N serves to activate the C−Cl bond, which is then susceptible to hydrogenolytic cleavage. This catalytic response is consistent with the literature where hydrodechlorination has been shown to predominate in the hydrotreatment of chloronitrobenzenes over Pd/Al_2O_3 [225]. Use of Pd/Mo_2N in practical (industrial) application would require the incorporation of downstream separation units in order to extract the target *p*-CAN. This is circumvented in the case of Au/Mo_2N, which delivered the best performance in this study. Process efficiency can be further improved by operating multiple passes through the catalyst bed where the ultra-selectivity imposed by Au/Mo_2N can deliver complete conversion of the inlet *p*-CNB to *p*-CAN.

The results presented in this study provide the first evidence of the combined catalytic action of Au and Mo_2N that serves to elevate surface hydrogen, resulting in an increased hydrogenation rate of *p*-CNB to the target *p*-CAN in both liquid and gas phase operation. Future work will focus on structural modification of molybdenum nitride (*e.g.* crystallographic phase and/or surface area) and control over Au particle size to increase activity while retaining selectivity. Catalytic applications will consider hydrogenation of polyfunctional nitroarenes where chemoselectivity is extremely challenging.

3.2.4. Conclusions

Au/Mo$_2$N as a new catalyst formulation promotes the (batch) liquid and (continuous) gas phase hydrogenation of *p*-CNB with 100% selectivity to *p*-CAN where the yield was maintained in repeated reaction cycles. Incorporation of Au with Mo$_2$N served to increase H$_2$ uptake with a four-fold higher hydrogenation rate relative to Mo$_2$N. Moreover, Au/Mo$_2$N outperformed a benchmark Au/Al$_2$O$_3$ catalyst that exhibited an equivalent mean Au particle size. Under the same reaction conditions, Pd/Mo$_2$N was *non*-selective and promoted a combined hydrodechlorination/ hydrogenation to give NB and AN. The viability of Au/Mo$_2$N in the selective reduction of nitroarenes was demonstrated here, for the first time, with versatility in gas and liquid phase operation.

3.3

Effect of Crystallographic Phase (*β vs. γ*) and Surface Area on Gas Phase Nitroarene Hydrogenation over Mo_2N and Au/Mo_2N

Abstract

In this chapter, the catalytic action of Mo_2N and Au/Mo_2N has been assessed in the selective gas phase hydrogenation of *p*-chloronitrobenzene (*p*-CNB) to *p*-chloroaniline (*p*-CAN). The nitrides were synthesized *via* temperature-programmed treatment of MoO_3 in H_2+N_2 and Au introduced by deposition-precipitation with urea. The influence of nitride crystallographic phase (tetragonal *β*-Mo_2N *vs.* cubic *γ*-Mo_2N) and surface area (7-66 m^2 g^{-1}) on the catalytic response was examined. Catalyst activation by temperature programmed reduction (TPR) has been monitored and the reduced catalysts characterized in terms of BET area/pore volume, H_2 chemisorption/temperature programmed desorption (TPD), powder X-ray diffraction (XRD), elemental analysis, scanning (SEM) and transmission (TEM) electron microscopy and X-ray photoelectron spectroscopy (XPS) measurements. The formation of *β*- and *γ*-Mo_2N was confirmed by XRD and TEM. *γ*-Mo_2N exhibits a platelet morphology whereas *β*-Mo_2N is characterized by an aggregation of small crystallites. Hydrogen chemisorption and TPD analysis have established a greater hydrogen uptake capacity (per unit area) for *β*-Mo_2N relative to *γ*-Mo_2N, which is associated with surface nitrogen deficiency, *i.e.* higher surface Mo/N for *β*-Mo_2N. Incorporation of Au on both nitrides resulted in an increase in surface hydrogen. The Au phase takes the form of *nano*-scale particles with a mean size of 7 and 4 nm on *β*-Mo_2N and *γ*-Mo_2N, respectively. Both *β*-Mo_2N and *γ*-Mo_2N promoted the exclusive hydrogenation of *p*-CNB to *p*-CAN where the *β*-form

delivered a higher specific (per m^2) rate; the specific rate for γ-Mo_2N was independent of surface area. The inclusion of Au on both nitrides served to enhance *p*-CAN production.

3.3.1 Introduction

The application of transition metal nitrides as hydrotreating catalysts is now established [4, 33, 242]. The use of molybdenum nitrides to promote hydrogen mediated reactions has been considered to a limited extent with evidence of significant hydrogenation activity [52, 58, 171, 176, 178, 243]. This has been ascribed to a contraction of the *d*-band and modification of electron density due to the interstitial incorporation of N in the metal lattice, which facilitates hydrogen adsorption/activation [244]. A distinct selectivity response has been observed for Mo nitride when compared with conventional supported metal (*e.g.* Pd or Pt) catalysts [58, 176, 178]. Indeed, the preferential formation of crotyl alcohol (from crotonaldehyde) [58] and ethene (from ethyne) [176] has been reported for reaction over Mo_2N with enhanced selectivities relative to Pd/Al_2O_3. The synthesis of *β*-phase molybdenum nitride (*β*-Mo_2N) was recently established [178], with application in the selective hydrogenation of *p*-chloronitrobenzene (*p*-CNB) to *p*-chloroaniline (*p*-CAN) in both continuous gas [245] and batch liquid [245, 246] operation. *p*-CAN is a high value chemical extensively used in the manufacture of fine chemicals but existing production routes exhibit serious drawbacks in terms of low selectivity and the generation of toxic waste [247]. The earlier work is now extended to consider the role of nitride crystallographic phase and surface area in gas phase hydrogenation.

In the synthesis of nitrides *via* temperature programmed reduction-nitridation, a number of factors have been proposed to influence the MoN_x phase, including the nature of the precursor [248] and preparation conditions [18, 36, 249], *i.e.* gas composition/space velocity, heating rate and final temperature. Cubic γ-Mo_2N has been the most common crystallographic form obtained *via* thermal treatment of MoO_3 in NH_3 [18, 248]. The use of H_2+N_2 mixtures can generate either (tetragonal) β-Mo_2N [13, 38, 39] or γ-Mo_2N [36, 40, 41]. Moreover, the formation of (hexagonal) δ-MoN from MoS_2+NH_3 has also been reported [250]. The synthesis of high surface area (up to 225 m^2 g^{-1}) Mo nitrides requires a low temperature ramp rate ($\leq$ 1 K min^{-1}) [36] and/or high gas space velocity (up to 150000 h^{-1}) [49] to circumvent hydrothermal sintering resulting from water released [41]. β-Mo_2N typically exhibits low surface areas (2-17 m^2 g^{-1}) [13, 39, 178] whereas higher values are characteristic of γ-Mo_2N (5-225 m^2 g^{-1}) [43, 251, 252]. The effect of the Mo nitride crystallographic phase in terms of hydrogenation applications has not been studied in a systematic manner. It is, however, worth noting that, in the case of ammonia synthesis [38] and carbazole hydrodenitrogenation [18], β-Mo_2N delivered a higher surface area normalized activity when compared with γ-Mo_2N and δ-MoN. A definitive correlation between catalytic activity and nitride area, irrespective of phase, has yet to be established. Hydrogen uptake, which is dependent on surface area and crystallographic phase [20, 24, 183], can play a critical role in determining hydrogenation rate. McKay and co-workers [38] have shown that specific activity (per m^2) for ammonia synthesis over β-Mo nitride was independent of surface area. In contrast, specific activities for thiophene desulfurisation [36] and pyridine hydrodenitrogenation [19] were found to decrease with increasing γ-Mo nitride area (from 4 to 193 m^2 g^{-1}).

The aim of the study presented in this chapter is to consider for the first time the independent effect(s) of varying surface area (7-66 m^2 g^{-1}) and Mo_2N crystallographic phase (β- and γ-) on *p*-CNB hydrogenation performance. Moreover, with a view to enhancing overall catalyst performance, the role of Au as promoter is assessed. The use of promoters with Mo nitrides catalysts has not been addressed to any significant extent. It should be noted that an increase in activity has been demonstrated for methanol steam reforming (with lower CO_2 production) over Mo nitride with the addition of Pd, Pt and Ni [253] and thiophene hydrodesulfurisation due to the inclusion of Co [254].

3.3.2 Experimental

3.3.2.1 Mo Nitride Synthesis

The MoO_3 (99.9995% w/w) precursor was obtained from Alfa Aesar. Mo nitride synthesis was conducted *via* temperature programmed treatment in H_2/N_2 or $H_2/N_2/Ar$ continuous flow at atmospheric pressure. *β*-Mo_2N synthesis was carried out in a commercial CHEM-BET 3000 (Quantachrome) unit. *γ*-Mo_2N preparation employed a fixed bed reactor. As Mo nitride powders produced in reducing gases are subject to self-ignition on contact with air [255], the samples were passivated at 293 K in 1% v/v O_2/He for *ex situ* analysis; there was no detectable temperature increase during passivation.

a. *β*-Mo_2N

The MoO_3 precursor was loaded in a quartz cell (3.76 mm i.d.) and contacted with 15 cm^3 min^{-1} (Brooks mass flow controlled; $GHSV$ = 1500 h^{-1}) H_2/N_2, kept at 293 K for 1 h and then heated at 5 K min^{-1} to 933 K, maintaining the final temperature for 18 h. The reaction was quenched by switching to an Ar flow (65 cm^3 min^{-1}) and the sample was cooled to ambient temperature.

b. *γ*-Mo_2N

The MoO_3 precursor was placed in a horizontally mounted quartz reactor (i.d. = 10 mm), flushed with dry high purity Ar (99.9% v/v) at 400 cm^3 min^{-1} ($GHSV$ = 24000 h^{-1}) for 4 h and heated to 623 K (at 5 K min^{-1}), which was maintained for 4 h. A 400 cm^3 min^{-1} flow of

8%/42%/50% v/v $N_2/H_2/Ar$ was then introduced and the temperature held constant for 2 h. Two γ-Mo_2N samples were prepared using different temperature ramping rates. The synthesis conditions were selected based on published literature [36] that has established a dependence of nitride surface area (34-101 $m^2\ g^{-1}$) on heating rate (0.2-20 K min^{-1}). The temperature was raised from 623 K to 933 K at 0.3 K min^{-1} (sample denoted as **γ-Mo_2N-a)** or 0.1 K min^{-1} (**γ-Mo_2N-b)**, maintaining the final isothermal hold for 2-13 h. The sample was quenched in Ar and rapidly (<30 min) cooled to ambient temperature; the latter step was facilitated by contacting the reactor with an external high velocity air flow.

3.3.2.2. Au/Mo_2N Preparation and Activation

Au/β-Mo_2N, Au/γ-Mo_2N-a and Au/γ-Mo_2N-b (with a nominal Au loading = 1 mol%) were prepared by deposition-precipitation (D-P). A suspension of $HAuCl_4$ (300 cm^3, 3.32×10^{-4} M), aqueous urea (100 cm^3, 0.86 M) and the nitride support (2 g), were stirred (300 rpm) and heated (1 K min^{-1}) to 353 K, maintaining the final temperature for 2.5 h. The D-P process was performed in the dark in order to avoid formation of metallic colloids in solution by photoreduction of Au(III) [256]. It has been reported that a high residual chloride content (>300 ppm) can induce the formation of large (>20 nm) Au particles [257] while the chloride can poison the catalytically active sites [258]. In order to circumvent these negative effects, the catalyst precursor was filtered, washed with distilled water until the wash water was Cl-free (based on the $AgNO_3$ test), dried in He (45 $cm^3\ min^{-1}$) at 383 K for 3 h and sieved into a batch of 75 μm average particle diameter. The samples were kept at 277 K under He in the dark in order to prevent Au agglomeration, which has been reported for storage in air and in the light [259].

3.3.2.3. Characterization

The pH values associated with the point of zero charge (pH_{PZC}) of the nitrides were determined using the potentiometric mass titration technique. In each case, three different masses (0.025, 0.050 and 0.075 g) were immersed in 50 cm^3 0.1 M NaCl to which a known amount of NaOH (0.1 M) was added to adjust the pH to *ca.* 11. After stabilisation of the pH (*ca.* 1 h), titration of the samples was performed under continuous agitation in a He atmosphere with HCl (0.1 M). Temporal changes to pH were measured using a crystal-body electrode coupled to a data logging and collection system (Pico Technology Ltd.); calibration was performed with standard buffer solutions (pH 4 and 7). Temperature programmed reduction (TPR), BET surface area, total pore volume, H_2 chemisorption and temperature programmed desorption (TPD) were determined using the commercial CHEM-BET 3000 (Quantachrome) unit. The samples were loaded into a U-shaped Quartz cell (3.76 mm i.d.) and heated in 17 cm^3 min^{-1} (Brooks mass flow controlled) 5% v/v H_2/N_2 at 2 K min^{-1} to 673 ± 1 K. The effluent gas passed through a liquid N_2 trap and changes in H_2 consumption were monitored by TCD with data acquisition using the TPR Win^{TM} software. The activated samples were maintained at the final temperature in a constant flow of H_2/N_2 until return of the signal to baseline, swept with 65 cm^3 min^{-1} N_2 for 1.5 h and cooled to room temperature. The samples were then subjected to H_2 chemisorption using a pulse (10 μl) titration procedure, followed by H_2-TPD in N_2 (65 cm^3 min^{-1}) at 45 K min^{-1} to 933 K with an isothermal hold until the signal returned to the baseline. BET areas and pore volumes were determined, respectively, in 30% and 95% v/v N_2/He using undiluted N_2 as internal standard. At least 3 cycles of N_2 adsorption-desorption in the flow mode were employed to determine total area and pore volume using the standard single point method. The measurements were reproducible to within ± 8% and the values quoted represent the mean.

Powder X-ray diffractograms were recorded on a Bruker/Siemens D500 incident X-ray diffractometer with Cu Kα radiation. The samples were scanned at a rate of 0.02º step^{-1} over the range 20º ≤ 2θ ≤ 90º. Diffractograms were identified using the JCPDS-ICDD reference standards, *i.e.* MoO_3 (35-609), *β*-Mo_2N (25-1368), *γ*-Mo_2N (25-1366) and Au (04-0784). Lattice parameters and residual error associated with the main planes for *β*-Mo_2N and *γ*-Mo_2N were determined using the TOPAS (version 3) software. Analysis by scanning electron microscopy (SEM) was conducted on a Philips FEI XL30-FEG equipped with an Everhart-Thornley secondary-electron (SE) detector, operated at an accelerating voltage of 10-15 kV and using NORAN System SIX (version 1.6) for data acquisition. Before analysis, the samples underwent a hydrocarbon decontamination treatment using a plasma-cleaner (EVACTRON). Elemental (nitrogen) analyzes were conducted using an Exeter CE-440 Elemental Analyzer after sample combustion at *ca.* 1873 K. The Au content was measured by atomic absorption spectroscopy (AAS, Shimadzu AA-6650 spectrometer with an air-acetylene flame) from the diluted extract in aqua regia (25% v/v HNO_3/HCl). X-ray photoelectron spectroscopy (XPS) analyzes were conducted on an Axis Ultra instrument (Kratos) using a monochromatic Al Kα X-ray source (1486.6 eV). Prior to analysis, the nitride sample was adhered to a conducting carbon tape, mounted in the sample holder and subjected to ultra-high vacuum conditions ($<10^{-8}$ Torr). The source power was maintained at 150 W and the emitted photoelectrons were sampled from a square area of 750×350 μm^2; the photoelectron take-off angle was 90°. The analyzer pass energy was 80 eV for survey spectra (0–1000 eV) and 40 eV for high resolution spectra (over the Mo $3d_{3/2}$ and Mo $3d_{5/2}$ binding energy (BE) range, 227-239 eV). Sputtering of the surface (for 1 min) with a 3 keV argon ion beam was employed to remove the passivating layer and reveal the sub-surface composition. The adventitious C 1s peak was calibrated at 284.5 eV and used as internal standard to compensate for any charging effects. The instrument work function was calibrated to give a BE of 84.00 eV for the Au 4$f_{7/2}$ line of metallic gold (Metalor) and the spectrometer dispersion was adjusted to give a BE of 932.70 eV for the Cu 2$p_{3/2}$ line of metallic copper (Metalor). Quantification of the XPS signal employed the CasaXPS software, using relative sensitivity factors provided by Kratos. High resolution transmission electron microscopy (HRTEM) analyzes were performed on a JEOL JEM 2011 unit with a UTW energy dispersive X-ray detector (Oxford Instruments) operated at an accelerating voltage of 200 kV; Gatan DigitalMicrograph 3.4 was employed for data acquisition. Samples for analysis were prepared by dispersion in acetone and deposited on a holey carbon/Cu grid (300 Mesh). Up to 320 individual Au particles were counted for each catalyst and the mean metal particle sizes are quoted as the number average (d_{TEM}).

3.3.2.4. Analytical Method and Catalytic System

a. Materials and analytical method

All the gases (H_2 and N_2, Ar, O_2 and He) employed were of ultra high purity (>99.99, BOC). *p*-CNB (Sigma-Aldrich, ≥ 99%) reactant and solvent (ethanol, Sigma Aldrich, ≥ 99.8%) were used without further purification. The composition of the reactant/product mixtures was determined using a Perkin-Elmer Auto System XL chromatograph equipped with a programmed split/splitless injector and a flame ionisation detector, employing a DB-1 capillary column (i.d. = 0.33 mm, length = 30 m, film thickness = 0.20 μm). Data acquisition/manipulation was performed using the TotalChrom Workstation (Version 6.1.2 for Windows) chromatography data system. The overall reactant/product molar fractions were obtained using detailed calibrations (not shown).

b. Catalytic System

The hydrogenation of *p*-CNB was carried out under atmospheric pressure at 493 K, *in situ* immediately after activation, in a fixed bed vertical glass reactor (i.d. = 15 mm). The catalytic reactor was operated under conditions that ensured negligible heat/mass transport limitations. A layer of borosilicate glass beads served as preheating zone where the organic reactant was vaporized and reached reaction temperature before contacting the catalyst. Isothermal conditions (± 1 K) were maintained by diluting the catalyst bed with ground glass (75 μm); the ground glass was mixed thoroughly with catalyst before insertion in the reactor. The reaction temperature was continuously monitored using a thermocouple inserted in a thermowell within the catalyst bed. The reactant (*p*-CNB as a solution in ethanol) was delivered at a fixed calibrated flow rate to the reactor *via* a glass/teflon air-tight syringe and teflon line using a microprocessor controlled infusion pump (Model 100 kd Scientific). A co-current flow of *p*-CNB and H_2 (<1% v/v *p*-CNB in H_2) was delivered at a $GHSV = 330\ \text{min}^{-1}$ with an inlet reactant molar flow (F) in the range 0.7-3.2 $\mu\text{mol min}^{-1}$. The H_2 flow rate was monitored using a Humonics (Model 520) digital flowmeter, where the H_2 content was maintained well in excess of the stoichiometric requirement. The mass of catalyst to inlet *p*-CNB molar feed rate (m/F) spanned the range 2.6×10^{-3}-7.9×10^{-2} g min μmol^{-1}. As a blank test, passage of *p*-CNB in a stream of H_2 through the empty reactor did not result in any detectable conversion. The reactor effluent was frozen in a liquid nitrogen trap for subsequent analysis. Fractional hydrogenation ($X_{p\text{-}CNB}$) was obtained from

$$X_{p-CNB} = \frac{[p-\text{CNB}]_{in} - [p-\text{CNB}]_{out}}{[p-\text{CNB}]_{in}} \tag{3.3.1}$$

and selectivity with respect to *p*-chloroaniline (*p*-CAN), as the target product, is given by

$$S_{p-CAN}\,(\%) = \frac{[p-\mathrm{CAN}]_{out}}{[p-\mathrm{CNB}]_{in}-[p-\mathrm{CNB}]_{out}} \times 100 \qquad \textbf{(3.3.2)}$$

Repeated reactions with different samples from the same batch of catalyst delivered conversion/selectivity values that were reproducible to within ± 7%.

3.3.3 Results and Discussion

3.3.3.1 Mo_2N

a. *β*-Mo_2N Characterization

The XRD pattern of the MoO_3 precursor is shown **Figure 3.3.1 (a)**. The reflections over the range 2θ = 23-49° correspond to the (110), (040), (021), (130), (101), (111), (041), (060), (150), (061) and (002) planes that are characteristic of orthorhombic *α*-MoO_3 (JCPDS-ICDD 35-609, see **Figure 3.3.1 (e)**). The diffractogram for the passivated *β*-Mo_2N (**Figure 3.3.1 (b)**) shows peaks at 2θ = 37.7°, 43.1°, 45.3°, 62.7°, 64.3°, 75.5°, 78.6° and 80.5° that can be associated, respectively, with the (112), (200), (004), (220), (204), (312), (116) and (224) planes of *β*-Mo_2N (JCPDS-ICDD 25-1368, **Figure 3.3.1 (f)**). It should be noted that there were no detectable signals due to Mo or oxide species, a result that confirms the complete transformation of MoO_3 to *β*-Mo_2N, where the passivation step served solely to provide a superficial oxide film without bulk oxidation [13].

In order to check for a possible *γ*-phase content, the sample was subjected to a single crystal analysis using the TOPAS software for lattice parameter optimisation and the results are presented in **Table 3.3.1**. The residual error obtained from adjusting the *d*-spacing to tetragonal *β*-Mo_2N was significantly lower when compared with that obtained for cubic *γ*-Mo_2N. The lattice parameters from the adjustment to the *β*-form (a = 4.205; c = 8.045) are very close to those for the JCPDS-ICDD standard (25-1368).

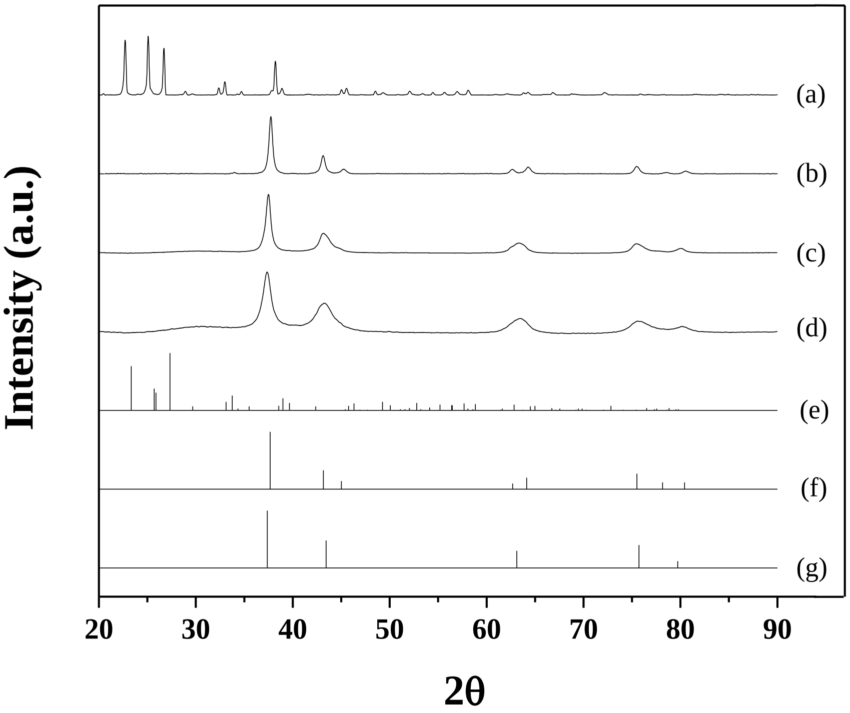

Figure 3.3.1. XRD patterns associated with **(a)** MoO_3, **(b)** β-Mo_2N, **(c)** γ-Mo_2N-a and **(d)** γ-Mo_2N-b with JCPDS-ICDD reference diffractograms for **(e)** MoO_3 (35-609), **(f)** β-Mo_2N (25-1368) and **(g)** γ-Mo_2N (25-1366).

Moreover, the nitrogen content (see **Table 3.3.2**: 5% w/w, bulk Mo/N = 2.7) is in good agreement with reported values of 2.6-2.7 [12-14, 38] for β-Mo_2N.

The synthesized β-Mo_2N was examined by TEM and a representative image is shown in **Figure 3.3.2 (1a)** where the intensity profile (see inset) yielded an average *d*-spacing of 0.24 nm, consistent with the (112) plane of β-Mo_2N. SEM analysis was also conducted to evaluate morphological features and the representative micrograph presented in **Figure 3.3.2 (2a)** shows an aggregation of small crystallites (<5 μm).

Cubic γ-Mo_2N				Tetragonal β-Mo_2N			
h k l	Residual Error (%)			h k l	Residual Error (%)		
	β-Mo_2N	γ-Mo_2N-a	γ-Mo_2N-b		β-Mo_2N	γ-Mo_2N-a	γ-Mo_2N-b
1 1 1	0.532	0.257	0.315	1 1 2	0.079	0.196	0.163
2 0 0	1.018	0.326	0.129	2 0 0	0.099	0.783	1.235
2 2 0	1.134	0.101	0.285	0 0 4	0.005	-	-
3 1 1	0.693	0.079	0.047	2 2 0	0.013	-	-
2 2 2	0.492	0.280	0.332	2 0 4	0.082	1.334	0.942
				3 1 2	0.008	0.601	0.727
				1 1 6	0.016	-	-
				2 2 4	0.035	0.171	0.793
Lattice Parameters	a = 4.198	a = 4.163	a = 4.156	Lattice Parameters	a = 4.205 c = 8.045	a = 4.172 c = 8.483	a = 4.162 c = 8.201
	a* = 4.163				a** = 4.188 c** = 8.048		

* for JCPDS-ICDD γ-Mo_2N reference (25-1366); ** for JCPDS-ICDD β-Mo_2N reference (25-1368)

Table 3.3.1: Lattice parameters and residual error associated with the main planes for γ-Mo_2N and β-Mo_2N in the analysis of Mo nitrides synthesized *via* temperature programmed treatment of MoO_3.

A β-Mo_2N crystal structure containing ensembles of varying sizes (<10 μm) has been reported elsewhere [38, 39, 248]. As the starting MoO_3 is characterized by a platelet morphology [260], the disruption of the orthorhombic precursor structure in the reduction/nitridation process ($\text{MoO}_3 \rightarrow \text{MoO}_2 \rightarrow \text{Mo} \rightarrow \text{Mo}_2\text{N}$) is the result of a *non*-topotactic transformation [13, 178, 248].

Catalyst	**β-Mo$_2$N**	**Au/ β-Mo$_2$N**	**γ-Mo$_2$N-a**	**Au/ γ-Mo$_2$N-a**	**γ-Mo$_2$N-b**	**Au/ γ-Mo$_2$N-b**	**Error**
Nitrogen content (% w/w)	5	-	6	-	6	-	± 0.4
Au loading (mol%)	-	0.26	-	0.54	-	0.59	± 0.02
Mo/N bulk ratio^a; surface ratio after Ar ion sputtering^b	2.7; 2.4	-	2.2; 1.4	-	2.2; 1.4	-	± 0.1
BET surface area (m^2 g^{-1})	7^c (3)^d	9^c (5)^d	36^c (30)^d	40^c (33)^d	66^c(60)^d	82^c (75)^d	± 1
Pore volume (cm^3 g^{-1})	0.020	0.029	0.036	0.052	0.055	0.092	± 0.005
TPR T_{max} (K)	637	603	670	610	668	607	± 1
TPR H$_2$ consumption (µmol g^{-1})	303	373	732	777	1292	1454	± 2
H$_2$ chemisorption (10^3 µmol m^{-2})	42	45	16	20	16	18	± 1
TPD T_{max} (K)	806	746	827	795, 933	823	813, 933	± 1
H$_2$ desorbed (µmol m^{-2})	0.4	1.4	0.2	0.7	0.2	0.5	± 0.05
pH$_{PZC}$	3.5	-	3.3	-	3.3	-	± 0.1
Au size range (nm)	-	2-13	-	1-8	-	1-8	± 0.5
d_{TEM} (nm)	-	7 ± 1.7	-	4 ± 1.2	-	4 ± 1.2	

Table 3.3.2: Nitrogen content, Au loading, bulk and surface atomic Mo/N ratio, BET surface area, total pore volume, characteristic temperature programmed reduction (TPR) T_{max} with associated H$_2$ consumption, H$_2$ chemisorbed/desorbed (TPD), pH of the point of zero charge (pH$_{PZC}$), Au particle size range and mean value (d_{TEM}).

Cairns and co-workers [39] attributed the formation of small β-Mo$_2$N ensembles to water release/particle expansion during precursor reduction, following the model of Sloczynski and Bobinski [261]. It has been proposed [183] that passivation of Mo$_2$N results in the formation of one or two chemisorbed oxygen layers. Surface characterization by XPS generated the spectra over the Mo 3*d* binding energy (BE) region for the MoO_3 precursor **(a)** and *β*-Mo_2N **(b)** presented in **Figure 3.3.3**. The XPS profile for MoO_3 is characterized by a sole spin-orbit doublet with a Mo $3d_{3/2}$ BE = 236.6 eV that is characteristic of Mo^{6+} [62]. Removal of the passivating oxide layer from Mo nitrides by Ar ion sputtering has been demonstrated elsewhere [62]. Sputtering was employed in this study to analyze the depth-profile composition of *β*-Mo_2N and mimic surface composition under reaction conditions. The XPS profile of the passivated sample (**Figure 3.3.3 (b1)**) shows a principal XPS peak at BE = 228.7 eV that is characteristic of $Mo^{\delta+}$ ($2 \leq \delta < 4$) in passivated *β*-Mo_2N [16, 27, 262]. The occurrence of a detectable signal at 236.4 eV is consistent with a partial oxidation to Mo^{6+} as a result of passivation [62]. While the hexavalent Mo signal in the precursor is strong and well defined, it is appreciably weaker for the Ar ion sputtered sample, demonstrating the near complete removal of the passivation layer (**Figure 3.3.3 (b2)**).

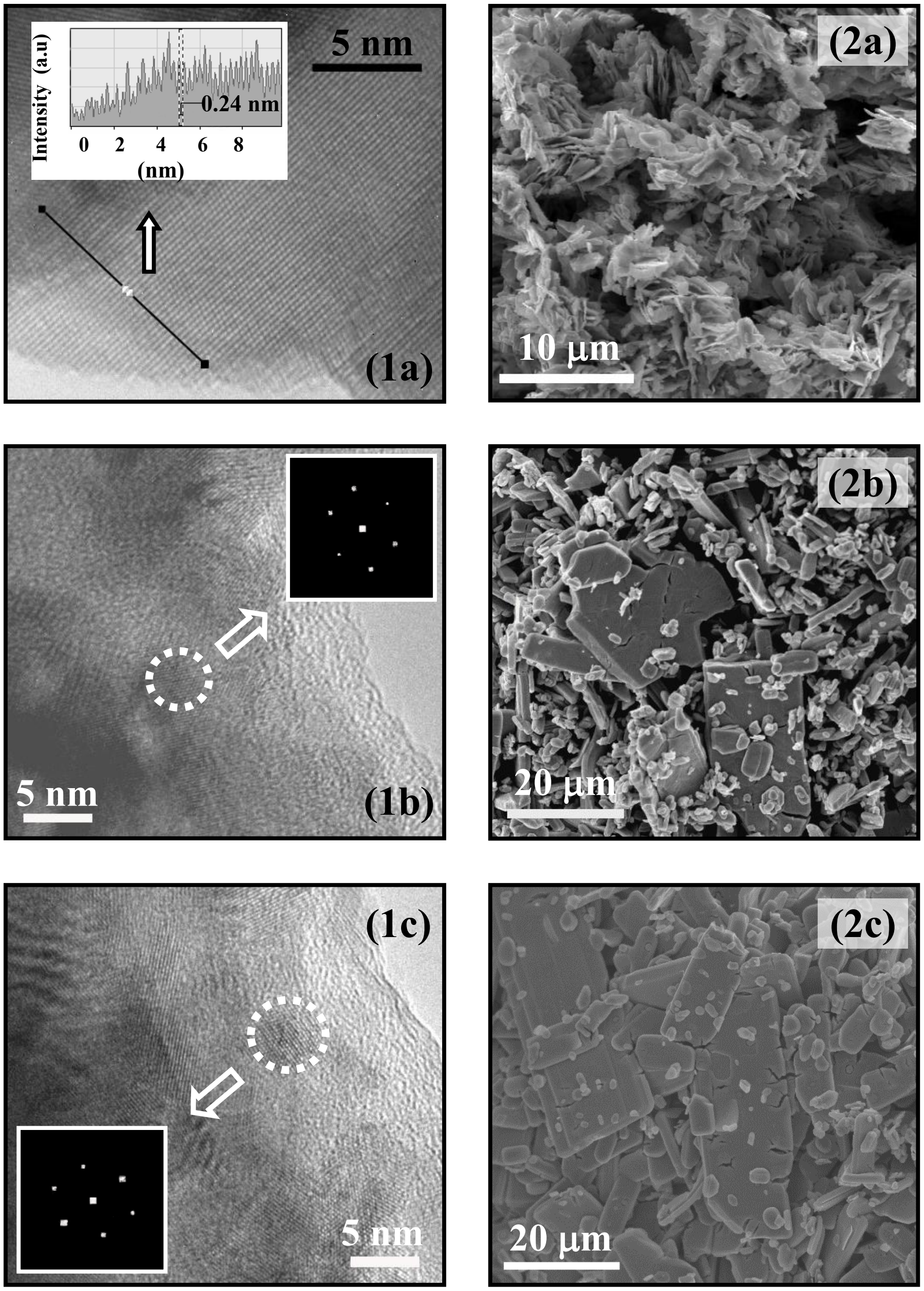

Figure 3.3.2. Representative **(1)** TEM images and **(2)** SEM micrographs of **(a)** β-Mo$_2$N, **(b)** γ-Mo$_2$N-a and **(c)** γ-Mo$_2$N-b. *Note*: Inset in **(1a)** shows the intensity profile, revealing the distance between the planes of the atomic lattice over the 10 nm segment that is marked on the TEM image; diffractogram patterns associated with the circled areas are included in **(1b)** and **(1c)**.

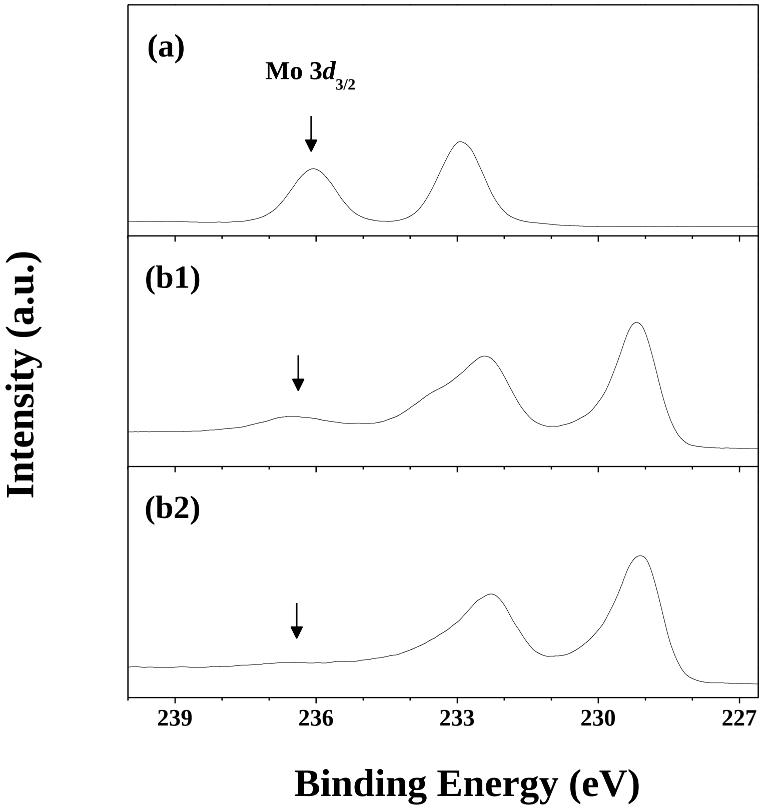

Figure 3.3.3. XPS spectra in the Mo 3*d* region of **(a)** MoO_3 and **(b)** β-Mo_2N **(1)** passivated and **(2)** after Ar ion sputtering. *Note*: Arrows illustrate the position of Mo $3d_{3/2}$ corresponding to Mo^{6+}.

The temperature requirements for the removal of this oxide overlayer were analyzed by temperature programmed reduction (TPR). The resultant profile, shown in **Figure 3.3.4 (a1)**, is characterized by a positive peak with a maximum intensity at 637 K. Hydrogen consumption at temperatures over the range 637-740 K during TPR of passivated β-Mo_2N has been reported previously [13, 183, 245, 263]. The H_2 consumed (303 μmol g^{-1}) is recorded in **Table 3.3.2** but no comparable measurement could be found in the literature. The BET surface area falls within the range of values (2-17 m^2 g^{-1}) quoted previously for β-Mo_2N synthesized by temperature programmed reaction in N_2/H_2 [13, 38, 178]. The total area after passivation decreased (from 7 to 3 m^2 g^{-1}), as has been noted elsewhere [44]. A search through the literature has failed to unearth any study where quantitative measurements of H_2 chemisorption on β-Mo_2N are recorded. However, NMR [22] and IR [243] analyzes suggest that H_2 can adsorb on Mo_2N at nitrogen deficient surface sites. Moreover, subsequent to adsorption, a heterolytic dissociation on Mo-N pairs (*via* the formation of Mo-H and N-H groups) has been proposed with migration to the sub-layers, which results in strong interactions [17, 20, 24]. A H_2 uptake of 42×10^{-3} μmol m^{-2} was recorded (**Table 3.2**) during pulse (ambient temperature) chemisorption analysis.

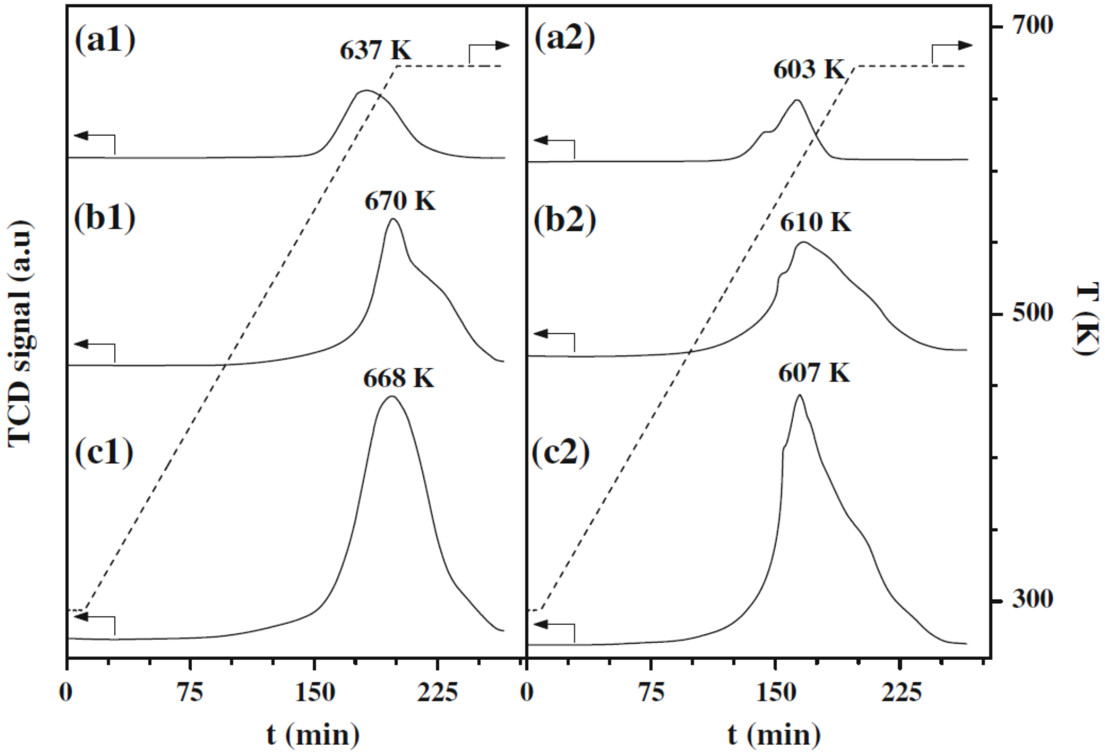

Figure 3.3.4. TPR profiles (solid line) with temperature ramp (dashed line) generated for passivated **(a)** β-Mo_2N, **(b)** γ-Mo_2N-a and **(c)** γ-Mo_2N-b **(1)** *pre-* and **(2)** *post-*Au incorporation.

Total surface hydrogen was evaluated by temperature programmed desorption (TPD) and the resultant profile is presented in **Figure 3.3.5 (a1)**. The XRD pattern (not shown) of β-Mo_2N

post-TPD was unchanged, demonstrating that the crystalline structure did not suffer any detectable alteration. Moreover, the nitrogen content (from elemental analysis) was unchanged; it has been established that loss of nitrogen from β-Mo_2N requires temperatures in excess of 1000 K [18]. The TPD profile is characterized by a broad peak (T_{max} = 806 K) where the H_2 released (0.4 μmol m^{-2}) is appreciably greater (by an order of magnitude) than that measured in the chemisorption step and must result from hydrogen uptake during TPR. Taking an overview of the limited available literature, the amount of H_2 desorbed (up to *ca.* 4 μmol m^{-2}) and associated T_{max} (370-800 K) appear to depend on nitride synthesis, *pre*-treatment and surface area [20, 183]. High temperature (700-800 K) desorption has been associated with loss of H_2 from the bulk nitride as opposed to desorption from surface sites [20].

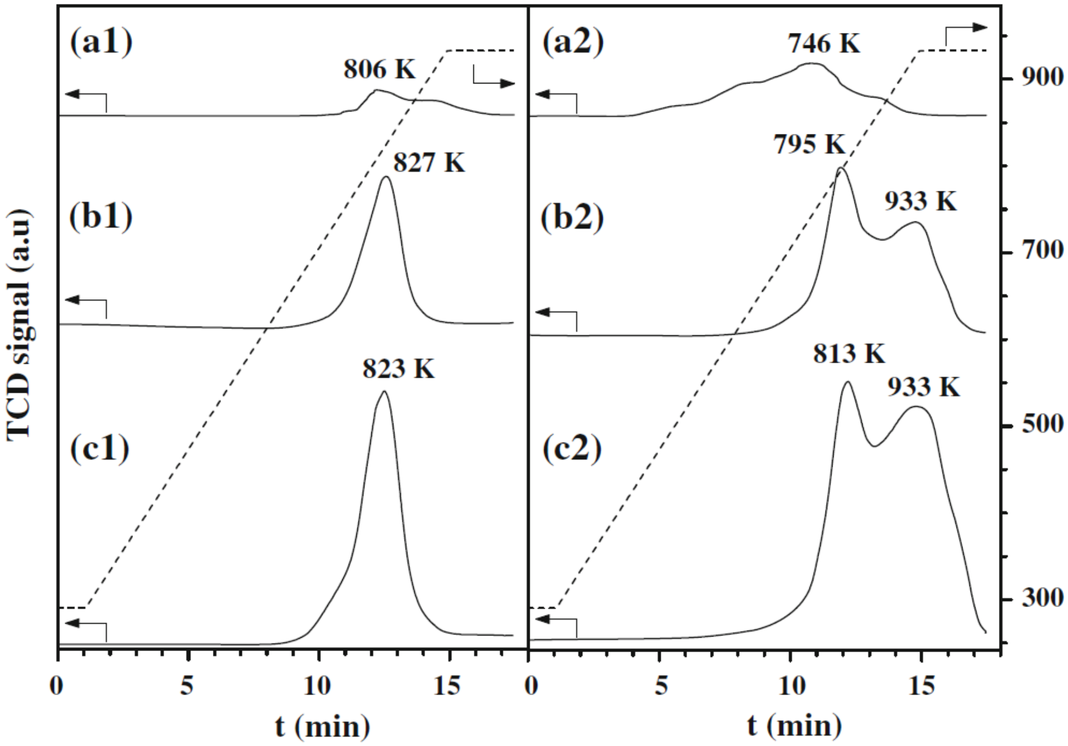

Figure 3.3.5 Hydrogen TPD response (solid line) with temperature ramp (dashed line) for **(a)** β-Mo_2N, **(b)** γ-Mo_2N-a and **(c)** γ-Mo_2N-b **(1)** *pre*- and **(2)** *post*-Au incorporation

b. *γ*-Mo_2N Characterization

Two *γ*-nitride (*γ*-Mo_2N-a and *γ*-Mo_2N-b) samples with different surface areas (**Table 3.3.2**) were synthesized by modifying the heating rate (see section 2.1.2). The total pore volumes are comparable to those quoted by Zhang and co-workers [264], *i.e.* 0.012 $cm^3\ g^{-1}$ (surface area = 17 $m^2\ g^{-1}$) and 0.060 $cm^3\ g^{-1}$ (surface area = 110 $m^2\ g^{-1}$). A reduction in surface area was observed after passivation, as noted for *β*-Mo_2N. The nitrogen content of both *γ*-Mo_2N samples (**Table 3.3.2**) was equivalent (6% w/w, bulk ratio Mo/N = 2.2) and agrees with values reported in the literature [16, 264]. The XRD patterns for *γ*-Mo_2N-a **(c)** and *γ*-Mo_2N-b **(d)** (see **Figure 3.3.1**) coincide, presenting five main peaks at $2\theta = 37.5°$, 43.6°, 63.3°, 76.0° and 80.0° that can be matched to the (111), (200), (220), (311) and (222) planes of cubic *γ*-Mo_2N (JCPDS-ICDD 25-1366, profile **(g)**). Single crystal analysis generated lattice parameters consistent with the *γ*-Mo_2N JCPDS-ICDD standard; residual error < 0.4% (**Table 3.3.1**). Representative TEM images of *γ*-Mo_2N-a and *γ*-Mo_2N-b are presented in **Figure 3.3.2 (1b)** and **Figure 3.3.2 (1c)**, respectively, where the *d*-spacings (0.20 nm and 0.24 nm) are in agreement with the (200) and (111) planes of *γ*-Mo_2N. SEM analysis (see **Figure 3.3.2 (2b)** and **2 (2c)**) has revealed the predominance of large (*ca.* 15 μm × 25 μm) platelet crystals with secondary, smaller (*ca.* 2 μm × 10 μm) rod-like formations. This suggests a retention of the platelet morphology characteristic of MoO_3 and a topotactic $MoO_3 \rightarrow Mo_xN_yO_{1-y} \rightarrow$ *γ*-Mo_2N transformation [251, 265]. The crystal size for both *γ*-Mo_2N samples is greater when compared with *β*-Mo_2N, as has been reported previously [38].

As in the case of *β*-Mo_2N, XPS analysis of *γ*-Mo_2N (not shown) confirmed a close to total removal of the passivation layer by Ar ion sputtering. A principal XPS signal at 228.3 eV was recorded that is within the range (228.2-230.0 eV) reported for passivated *γ*-Mo_2N [60, 266, 267] and attributed to $Mo^{\delta+}$ where $2 \leq \delta < 4$. In all three cases, bulk Mo/N exceeded the surface ratios

(**Table 3.3.2**). Moreover, the surface Mo/N (1.4) for both sputtered *γ*-Mo_2N samples is significantly lower than that measured for *β*-Mo_2N (2.4). The TPR profiles recorded for passivated *γ*-Mo_2N-a **(b1)** and *γ*-Mo_2N-b **(c1)** shown in **Figure 3.3.4** are characterized by a peak at 669 ± 1 K that falls within the values (590-855 K) recorded elsewhere [19, 174, 183, 235]. A comparison of the TPR profiles for both *γ*-Mo_2N samples with that of *β*-Mo_2N reveals a shift in the reduction peak to a higher temperature (by *ca.* 30 K) for *γ*-Mo_2N, suggesting differences in oxygen-nitride interactions. The hydrogen consumed during TPR can be associated with (i) removal of the passivation layer and (ii) surface adsorption of H_2, which can migrate to sub-layers. Hydrogen consumption (μmol g^{-1}, see **Table 3.3.2**) increases in the order: *β*-Mo_2N < *γ*-Mo_2N-a < *γ*-Mo_2N-b. The hydrogen required for reduction of the passivation layer should be proportional to nitride surface area and an equivalent amount of H_2 (per surface area) was recorded for the two *γ*-Mo_2N (= 20 μmol m^{-2}) samples. This value is within the range (5-20 μmol m^{-2}) reported in the literature for *γ*-Mo_2N with BET areas of 24-193 m^2 g^{-1} [19]. The significantly higher specific H_2 consumption for *β*-Mo_2N (= 43 μmol m^{-2}) relative to (both) *γ*-Mo_2N can be related to the crystallographic structure (*β*- *vs.* *γ*-) where difference in the exposed planes and surface composition can affect oxygen interaction with the nitride surface. Moreover, there is some consensus [17, 22, 24, 268] that hydrogen uptake occurs at unsaturated surface Mo sites. Higher H_2 consumption can then be related to the greater nitrogen deficient surface character (higher Mo/N) exhibited by *β*-nitride, as confirmed by XPS. Specific (per m^2) H_2 chemisorption (**Table 3.3.2**) was the same on both *γ*-Mo_2N samples but was significantly lower (by a factor of 3) than that recorded for *β*-Mo_2N. In contrast, Choi and co-workers [20] found that H_2 uptake capacity increased in the order, *β*-$Mo_{16}N_7$ < *δ*-MoN < *γ*-$Mo_{16}N_7$. They attributed this to a reduced number of Mo atoms on the surface of *β*-$Mo_{16}N_7$. The opposite effect was observed with a higher Mo/N surface ratio for *β*-Mo_2N relative to *γ*-Mo_2N. Hydrogen TPD from *γ*-Mo_2N-a **(b1)** and *γ*-Mo_2N-b **(c1)** generated the profiles presented in **Figure 3.3.5** with an equivalent H_2 release (0.2 µmol m^{-2}) at T_{max} = 825 ± 2 K, which is within the range (820-898 K) reported elsewhere [183, 269]. The shift in H_2 desorption to a higher temperature (by *ca.* 20 K) for *γ*-Mo_2N relative to *β*-Mo_2N suggests stronger interaction. Total H_2 desorbed from *γ*-Mo_2N was lower (by a factor of 2) than that recorded for *β*-Mo_2N, where the latter exhibited greater H_2 consumption (per surface area) in the TPR and chemisorption measurements. These results suggest a dependence of surface hydrogen content on crystallographic phase that might be linked to surface Mo/N.

3.3.3.2. Catalytic Results

Selectivity is the key challenge in the hydrogenation of *p*-CNB, *i.e.* exclusive $-NO_2$ group reduction without C-Cl bond scission. Dechlorination results in the formation of nitrobenzene (NB) with subsequent hydrogenation to aniline (AN) as shown in **Figure 3.3.6**. Published articles [140, 141, 270] dealing with selective nitroarene hydrogenation have identified steps employed to improve selectivity, notably use of additives/promoters (*e.g.* NaHS and KOH) [271, 272], support modifications (in terms of Lewis acid-base properties and formation of oxygen vacancies) [142, 273] and metal dispersion [145]. Hydrogenation of *p*-CNB over *β*-Mo_2N, *γ*-Mo_2N-a and *γ*-Mo_2N-b generated *p*-CAN as the sole product, with no evidence of dechlorination. This finding in itself is significant as composite hydrodechlorination/ hydrogenation (to form NB/AN) is a feature of reaction over conventional transition metal catalysts, *i.e.* Ni [274], Pt [68] and Ru [275]. Hydrogenation selectivity can be attributed to effective polarisation of the N=O group *via* surface interaction that renders the nitro function susceptible for hydrogen attack [163]. Indeed, $-NO_2$ adsorption-reduction on Mo has been demonstrated elsewhere [276, 277] and Chen [274] have shown that the addition of Mo to nickel borides promoted selective nitro-group reduction while suppressing the dehalogenation step.

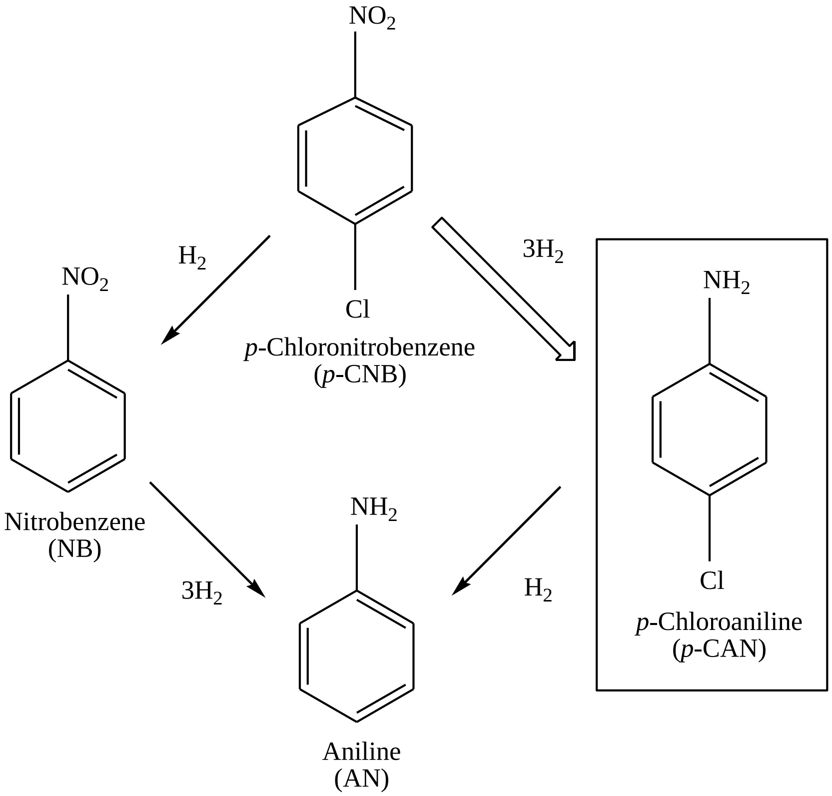

Figure 3.3.6. Main reaction pathways associated with the hydrogenation of *p*-CNB to the target (⇨) product (*p*-CAN) with non-selective (→) products resulting from hydrodechlorination/hydrogenation

A temporal decrease in fractional *p*-CNB conversion ($X_{p\text{-}CNB}$) with time on-stream was observed, which can be expressed in terms of the empirical relationship [225]

$$\frac{(X_{p-CNB} - X_0)}{(X_{30h} - X_0)} = \frac{t}{(\beta + t)} \qquad \textbf{(3.3.3)}$$

from which a value for the initial conversion (X_0) can be obtained, where X_{30h} represents fractional conversion after 30 h on-stream and β is a time scale fitting parameter. A representative (β-Mo_2N)

time on-stream response is shown in **Figure 3.3.7(a)** where it can be noted that a near steady state conversion was attained after *ca.* 15 h and maintained for 30 h of continuous operation.

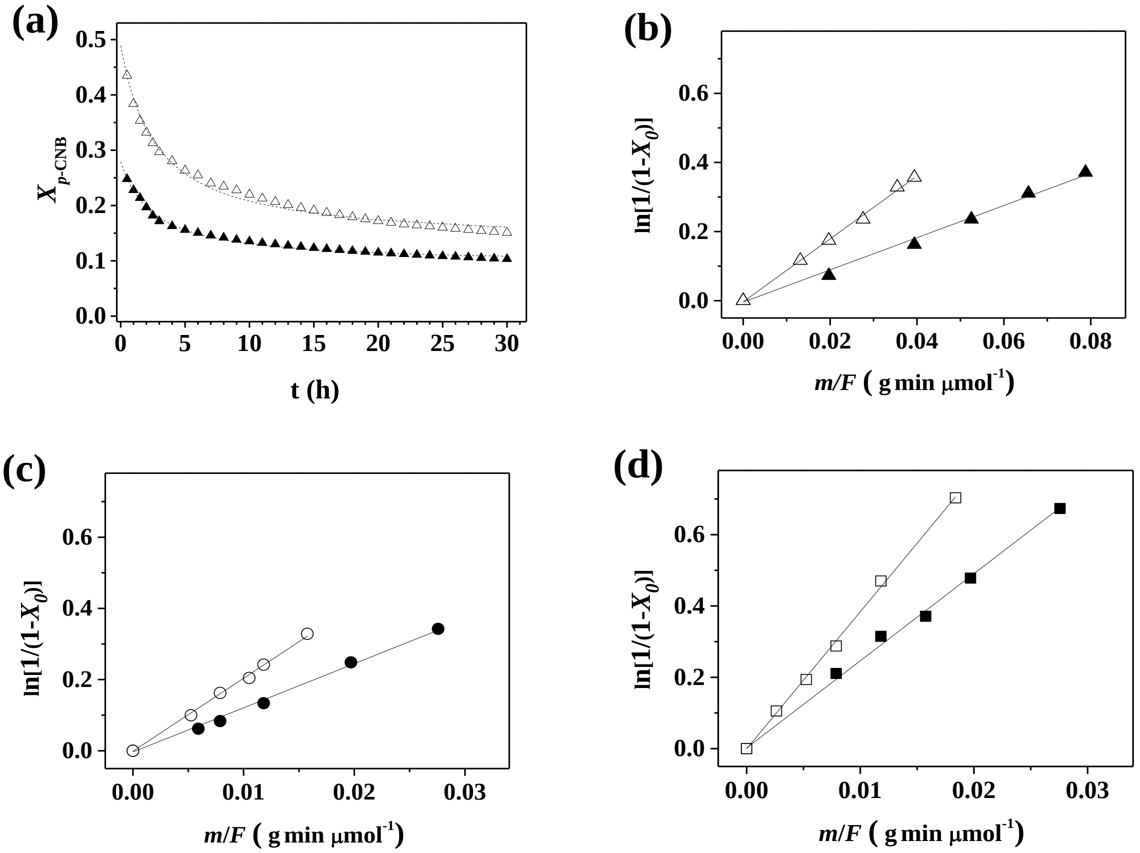

Figure 3.3.7 (a) Variation of *p*-CNB fractional conversion ($X_{p\text{-}CNB}$) with time-on-stream (m/F = 0.08 g min μmol^{-1}) for β-Mo$_2$N (▲) and Au/β-Mo$_2$N (Δ); lines represent fit to eqn. (3). Pseudo-first order kinetic plot for reaction over: **(b)** β-Mo$_2$N (▲) and Au/β-Mo$_2$N (Δ); **(c)** γ-Mo$_2$N-a (●) and Au/γ-Mo$_2$N-a (○); (**d**) γ-Mo$_2$N-b (■) and Au/γ-Mo$_2$N-b (□)

The applicability of a pseudo-first order kinetic treatment has been established for related catalyst systems [225]

$$\ln(1-X_0)^{-1} = k\left(\frac{m}{F}\right) \tag{3.3.4}$$

where *m/F* corresponds to the mass of catalyst relative to inlet *p*-CNB molar feed rate. The pseudo-first order kinetic plots for β-Mo_2N, γ-Mo_2N-a and γ-Mo_2N-b are included in **Figure 3.3.7(b)-(d)**. The linear fit (passing through the origin) confirms adherence to the kinetic model. The extracted raw rate constants (*k*, μmol g^{-1} min^{-1}, **Table 3.3.3**) follow the order, γ-Mo_2N-b > γ-Mo_2N-a > β-Mo_2N. In order to differentiate between the effect of surface area and crystal phase on the catalytic activity, the comparison must be based on specific rate (*k′*, μmol m^{-2} min^{-1}, **Table 3.3.3**).

Catalyst	Rate constant *k* (± 7%) (μmol g^{-1} min^{-1})	Specific rate constant *k′* (± 7%) ($\times 10^{-2}$ μmol m^{-2} min^{-1})
β-Mo_2N	4.6	66
γ-Mo_2N-a	12.2	34
γ-Mo_2N-b	24.5	37
Au/β-Mo_2N	9.0	100
Au/γ-Mo_2N-a	20.4	51
Au/γ-Mo_2N-b	38.4	47

Table 3.3.3. *p*-CNB hydrogenation rate constants (*k* and *k′*).

Both γ-Mo_2N-a and γ-Mo_2N-b delivered an equivalent specific activity ($35 \pm 2 \times 10^{-2}$ μmol m^{-2} min^{-1}) demonstrating that, for a given crystallographic phase, the intrinsic activity is independent of surface area. A significant finding is the appreciably higher specific rate recorded for β-Mo_2N. This can be correlated with the greater hydrogen content relative to γ-Mo_2N, which, in turn, might be related to the increased number of nitrogen deficient (higher Mo/N, see **Table 3.3.2**) surface sites. The results demonstrate that *p*-CNB hydrogenation performance is sensitive to the nitride phase where rate is proportional to surface area.

3.3.3.3. Au/Mo_2N

a. Preparation and Characterization

Catalyst supports, notably metal oxides, exhibit a characteristic pH-dependent surface charge [278]. The pH associated with the point of zero charge (pH_{PZC}) is a critical property that determines the solution pH requirements to ensure effective precursor-support interactions during catalyst preparation by D-P [279]. When pH < pH_{PZC}, the support bears a positive charge (due to protonation), favoring interaction with anionic species in solution and a pH in excess of pH_{PZC} results in a surface affinity for cationic species [280]. The pH_{PZC} depends on the chemical nature of the support rather than the crystallographic phase with equivalent values recorded for α- and γ-Al_2O_3, TiO_2-rutile and TiO_2-anastase, maghemite (γ-) and hematite (α-Fe_2O_3) [281]. The titration curves associated with pH_{PZC} measurements for β-Mo_2N **(1a)**, γ-Mo_2N-a **(1b)** and γ-Mo_2N-b **(1c)** are presented in **Figure 3.3.8**, yielding a similar value (3.4 ± 0.1) for the three nitrides. No published work that included a measurement of pH_{PZC} for Mo_2N could be found. The temporal pH variations during the preparation of Au/β-Mo_2N **(2a)**, Au/γ-Mo_2N-a **(2b)** and Au/γ-Mo_2N-b **(2c)** are also given in **Figure 3.3.8**. Initially, solution pH < pH_{PZC} and an electrostatic interaction between anionic gold species in solution ($HAuCl_4$ and/or $Au(OH)Cl_3^-$) and the positively charged support is favored [259]. The surface sites act as nucleation centers for Au deposition [282]. The progressive decomposition of urea, as a result of the increase in temperature (up to 353 K), led to a gradual increase in solution pH where pH > pH_{PZC}. The support develops a negative surface charge resulting in an electrostatic repulsion with anionic gold species. A combination of chemical and electrostatic interactions between the precipitating species and the support are required to facilitate metal deposition [279]. Moreover, supports with a greater surface area can facilitate a more homogeneous nucleation, resulting in the formation of smaller supported Au ensembles. The ultimate Au loadings (0.26–0.59 mol%, see **Table 3.3.2**) are below the nominal 1 mol%, which can be associated with the low pH_{PZC} that characterizes the three nitride supports.

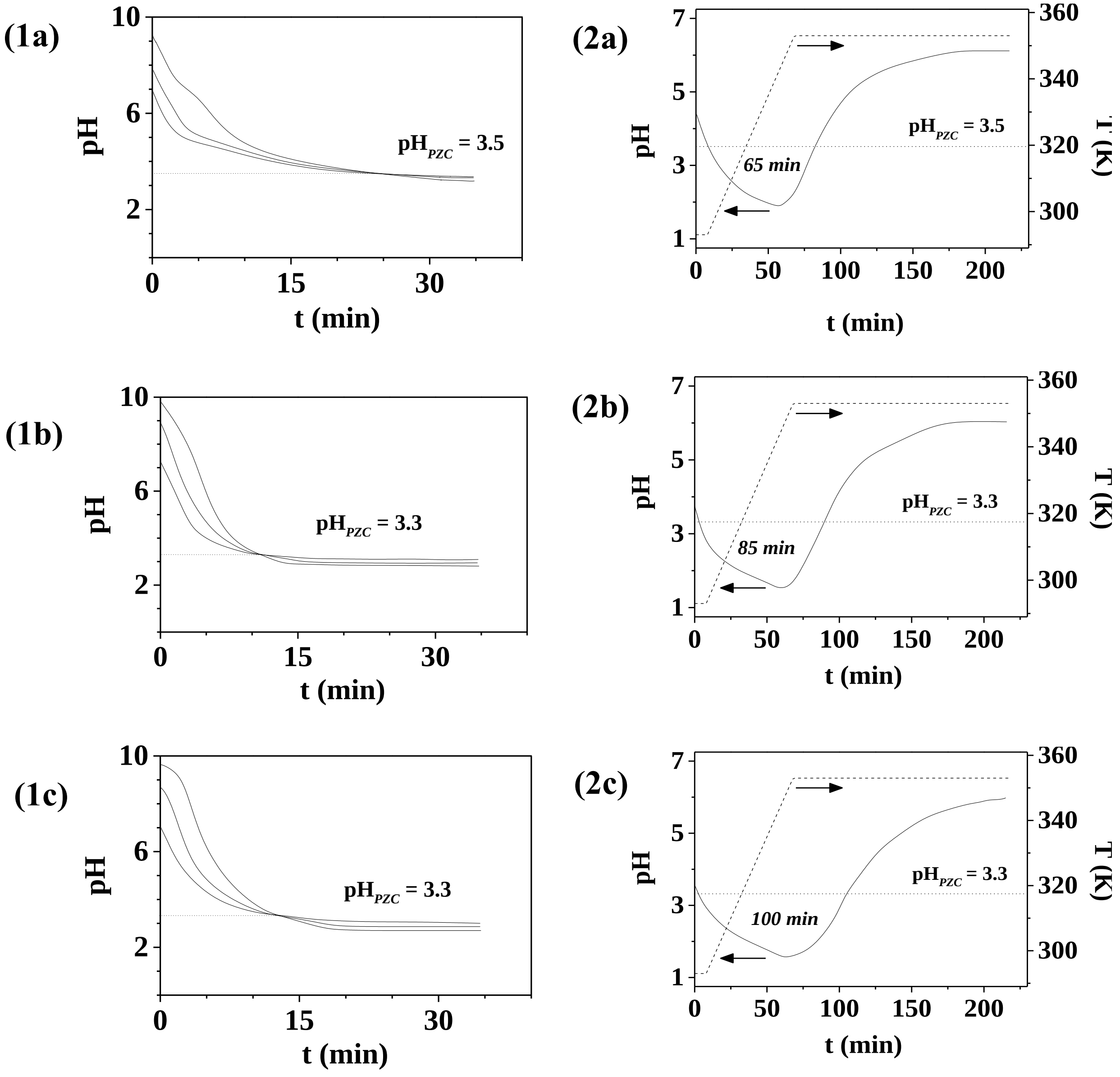

Figure 3.3.8. (1) pH profiles associated with the point of zero charge (pH_{PZC}) determination for **(a)** β-Mo_2N, **(b)** γ-Mo_2N-a and **(c)** γ-Mo_2N-b. **(2)** Temporal pH (solid line) and temperature (dashed line) variations in the preparation of **(a)** Au/β-Mo_2N, **(b)** Au/γ-Mo_2N-a and **(c)** Au/γ-Mo_2N-b. *Note*: Dotted line identifies the pH_{PZC} of the nitride; time during which pH < pH_{PZC} is given in italics.

A similar interpretation was proposed for a lower than expected Au content resulting from deposition on SiO_2 ($pH_{PZC} = 2.2$) [283]. The range of Au loadings obtained in this study can be correlated to the synthesis time where solution $pH < pH_{PZC}$, which was shortest (65 min) for β-Mo_2N, representing less favorable conditions for Au deposition resulting in the lowest metal content. The Au loading on both γ-Mo_2N supports with similar times at $pH < 3.3$ (pH_{PZC}) was essentially equivalent.

A concomitant increase in BET surface area and pore volume was observed after Au inclusion (**Table 3.3.2**). A similar phenomenon has been observed for the deposition of Pd and Au on boron nitride [284] and attributed to the development of nanopores during thermal treatment (drying and activation) with the release of water incorporated during deposition. The TPR profiles associated with Au/β-Mo_2N **(a2)**, Au/γ-Mo_2N-a **(b2)** and Au/γ-Mo_2N-b **(c2)** are presented **Figure 3.3.4**. Each is characterized by a principal H_2 consumption peak with $T_{max} = 606 \pm 4$ K ascribed to passivating layer removal where the incorporation of Au resulted in a decrease in reduction temperature (by up to 60 K, see **Figure 3.3.4(a1)-(c1)**). A similar effect has been noted elsewhere [235] for the TPR of passivated Mo_2N, *i.e.* shift to lower temperature by up to 140 K, following Ni introduction. Moreover, the incorporation of Au on reducible carriers, *e.g.* Fe_2O_3 [285] and $Ce_xZr_{1-x}O_2$ [286] has resulted in a significant decrease (by up to 400 K) in the temperature required for partial reduction of the support. Reduction of oxide supported gold ($Au^{3+} \rightarrow Au^0$) prepared by D-P has been reported to generate a TPR peak at $T < 500$ K [273]. This was not a feature of this study, suggesting a transformation of the Au precursor to metallic Au during preparation (*pre*-TPR). This has been reported previously [287], notably in the synthesis of iron oxide supported Au by *co*-precipitation. A reductive deposition of Au can occur on surface oxidized Mo species (*post*-passivation). The significantly lower standard redox potential of ionic Mo (*e.g.* E^0 for

$H_2Mo^{VI}O_4/Mo^{IV}O_2$ = +0.65 V) compared with ionic Au (E^0 for $Au^{III}(OH)_3/Au^0$ = +1.32 V, E^0 for $Au^{III}Cl_4^-/Au^0$ = +1.00 V) [288] can act to reduce the Au precursor. The incorporation of Au was accompanied by greater H_2 consumption during TPR (**Table 3.3.2**). This can be linked to (i) the increase in surface area and (ii) hydrogen spillover (from Au). It is known that H_2 chemisorption on supported Au is limited when compared with platinum group metals [289] but dissociative adsorption can proceed on low coordination Au sites, *i.e.* at edges and corners [290]. The three Au/nitride samples exhibited a measurable increase in H_2 chemisorption relative to the nitride support (**Table 3.3.2**). Hydrogen TPD generated the profiles shown in **Figure 3.3.5** for Au/*β*-Mo_2N **(a2)**, Au/*γ*-Mo_2N-a **(b2)** and Au/*γ*-Mo_2N-b **(c2)**. In each case, the incorporation of Au resulted in a significant increase in the amount of H_2 released (see **Table 3.3.2**). The TPD profiles present a principal peak (746-813 K) at a lower temperature (by up to 60 K) than that recorded for the nitride with an additional higher temperature (933 K) shoulder. These results indicate that the addition of Au results in greater capacity for hydrogen uptake (and subsequent release) with a distinct TPD response relative to the starting nitride.

Transmission electron microscopy was employed to obtain a measure of Au particle size. Representative **(1)** medium and **(2)** high magnification TEM images with particle size distributions **(3)** for **(a)** Au/*β*-Mo_2N, **(b)** Au/*γ*-Mo_2N-a and **(c)** Au/*γ*-Mo_2N-b are presented **Figure 3.3.9**. The images reveal a well dispersed Au phase in the form of *quasi*-spherical *nano*-scale particles. The diffractogram patterns for isolated Au particles are included (as insets) in the high magnification images **(2)** where the *d*-spacings (0.20/0.23) are consistent with the (111) and (200) planes of metallic gold. For the three catalysts, the Au particles (number average mean of 4-7 nm) are predominantly within the size range (≤ 10 nm) that has been deemed critical for hydrogenation activity [291]. The smaller mean Au size associated with *γ*-Mo_2N (see **Table 3.3.2**) can be ascribed to the prolonged deposition time where pH < pH_{PZC} (see **Figure 3.3.8**), resulting in stronger interactions with the support that minimize particle agglomeration.

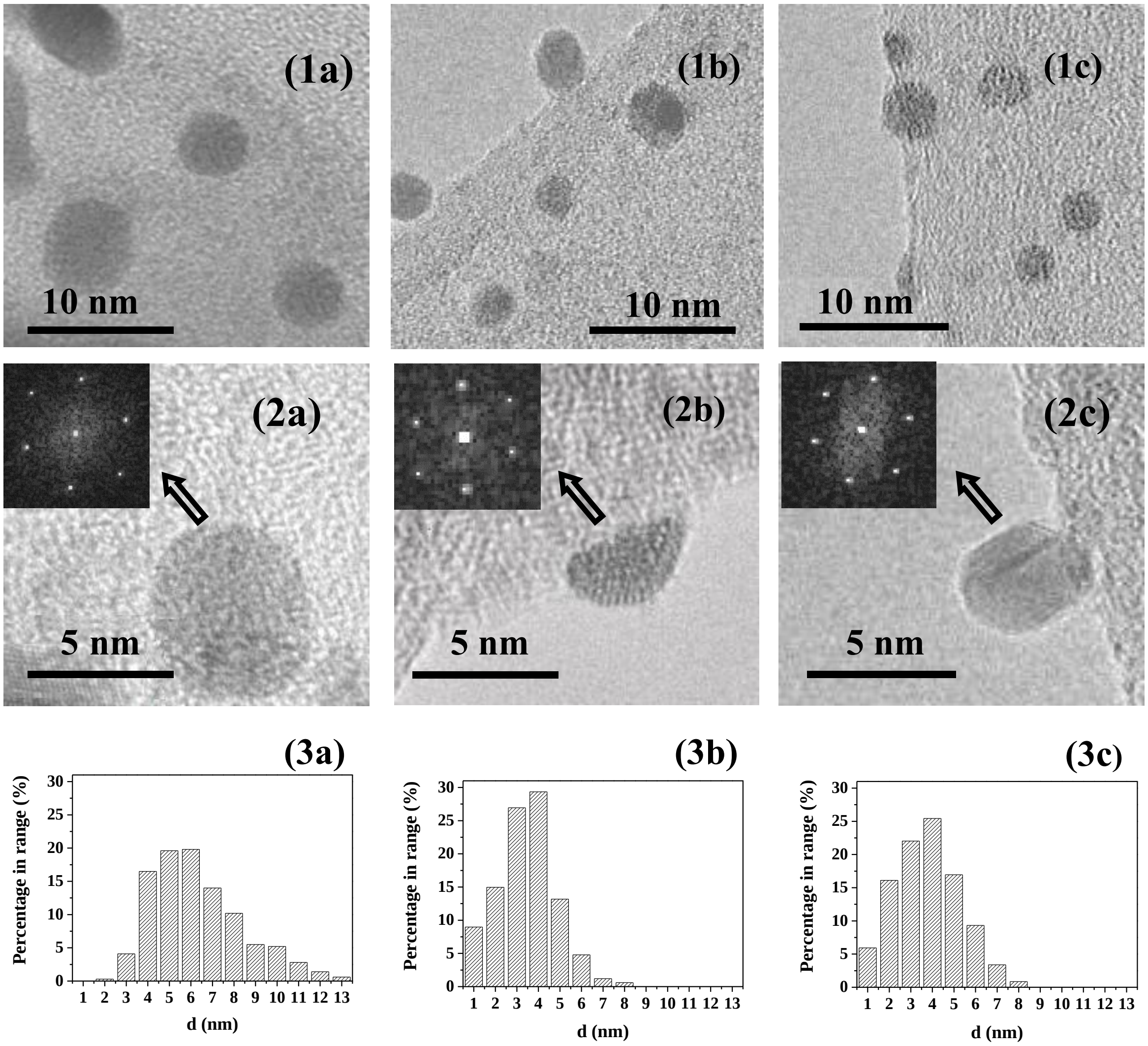

Figure 3.3.9. Representative **(1)** medium and **(2)** high magnification TEM images and **(3)** Au particle size distribution associated with **(a)** Au/β-Mo_2N, **(b)** Au/γ-Mo_2N-a and **(c)** Au/γ-Mo_2N-b. *Note:* Insets in high magnification TEM images show diffractogram patterns for single Au particles.

b. Catalytic Results

The chemoselective hydrogenation of nitro-compounds over oxide supported Au is now established [141, 270]. It has been shown that Au catalysts preferentially promote N=O reduction over other reactive functional groups, such as C≡N [292],C=O [293],C=C [270], Br [225] and Cl [294]. Activity and selectivity are dependent on Au particle size [295] and the nature of the support [141]. In the gas phase hydrogenation of *p*-CNB, the exclusive nitro-group reduction over Au supported on *non*-reducible (SiO_2, Al_2O_3) [296] and reducible (CeO_2, TiO_2, Fe_2O_3) [294] carriers has been demonstrated. The results of this study demonstrate that this chemoselective response extends to Au supported on *β*-Mo_2N and *γ*-Mo_2N where reaction exclusivity to *p*-CAN was maintained. Moreover, incorporation of Au enhanced hydrogenation performance, as shown in **Figure 3.3.7**, where the specific rate delivered by Au/*β*-Mo_2N exceeded that obtained with both Au/*γ*-Mo_2N (**Table 3.3.3**). Increased activity due to Au inclusion can be linked to an increase in reactive hydrogen as established by TPD analysis.

3.3.4 Conclusions

Temperature programmed treatment of MoO_3 in flowing N_2+H_2 was used to synthesize tetragonal *β*-Mo_2N (7 m^2 g^{-1}) and cubic *γ*-Mo_2N (36 and 66 m^2 g^{-1}). The *γ*-form exhibits a platelet (*ca.* 15 µm × 25 µm) morphology whereas *β*-Mo_2N takes the form of aggregates of small (<5 µm) crystallites. Passivation of the synthesized samples provided a protective oxide layer that prevented bulk oxidation and facilitated *ex-situ* handling. In the synthesis of Au/Mo_2N, solution pH exceeded support pH_{PZC} (3.4 ± 1) resulting in a less favorable surface interaction with the anionic Au precursor. This was particularly pronounced in the case of *β*-Mo_2N and resulted in lower Au loading and the formation of larger Au particles (mean diameter = 7 nm for Au/*β*-Mo_2N *vs.* 4 nm for Au/γ-Mo_2N) after activation. Temperature programmed reduction to 673 K was necessary to remove the passivation layer where the inclusion of Au shifted the TPR profile to lower temperatures (by up to 60 K). 100% selectivity to the target *p*-CAN product in the hydrogenation of *p*-CNB was achieved over Mo_2N, regardless of the phase. Hydrogen TPD analysis has established H_2 uptake on each nitride during TPR where β-Mo_2N exhibited a higher specific (per unit area) H_2 content relative to γ-Mo_2N. This is associated with a greater number of nitrogen deficient sites on β-Mo_2N (as established by XPS analysis), which translates into a higher specific selective hydrogenation rate. An equivalent specific rate was obtained for both γ-Mo_2N samples, indicative of invariance with respect to surface area. The addition of Au served to increase H_2 uptake capacity and elevated hydrogenation rate where *p*-CAN was again the sole product; Au/β-Mo_2N outperformed Au/γ-Mo_2N. These results demonstrate that the combination of Au with Mo_2N is a viable catalyst formulation for selective nitroarene hydrogenation.

3.4 Effect of Nitrogen Incorporation in Mo: Catalytic Hydrogenation *vs.* Hydrogenolysis

Abstract

The catalytic effect of nitrogen incorporation into Mo on hydrogenation (of -NO_2 to -NH_2 in nitrobenzene) and hydrogenolysis (of -C=O in benzaldehyde) processes is assessed in this chapter. Bulk Mo was prepared by temperature programmed reduction of MoO_3 (in H_2 to 933 K) and β-Mo_2N (confirmed by powder XRD) subsequently synthesized by Mo nitridation in N_2/H_2. Two intermediate samples (MoN-1 and MoN-2) with different Mo/N ratio were prepared by altering the duration (1 and 2 h) of the nitridation step. XPS analysis revealed a nitrogen surface enrichment (Mo/N = 2.2 → 0.9 from MoN-1 to β-Mo_2N) relative to the bulk (Mo/N = 4.9 → 2.6). Incorporation of N did not affect morphology and each sample exhibited (by SEM analysis) aggregates (<5 μm) of crystals (27-36 nm) with unchanged BET surface area (*ca.* 4 m^2 g^{-1}). Hydrogen chemisorption and release (by TPD) increased with decreasing Mo/N (Mo < MoN-1 < MoN-2 < β-Mo_2N). Gas phase hydrogenation of nitrobenzene to aniline exhibited increasing rate from Mo → β-Mo_2N, attributed to higher availability of surface heterolytic hydrogen (on Mo-N). In contrast, conversion of benzaldehyde to toluene was favored by increasing Mo/N (from β-Mo_2N → Mo) where hydrogenolytic -C=O scission is favored by homolytic hydrogen chemisorption (on Mo). These results provide the first evidence that N incorporation in Mo structure can control catalytic hydrogenation *vs.* hydrogenolysis performance.

3.4.1. Introduction

The application of Mo nitrides in catalytic hydrotreatment is now established [23, 297, 298]. Work to date has largely focused on hydrogenolysis with higher activity relative to commercial Ni-Mo/Al_2O_3 in hydrodesulfurisation [297] and hydrodenitrogenation [23]. Moreover, enhanced hydrogenation selectivity has also been reported with respect to conventional supported metal (*e.g.* Pd or Pt) catalysts [58, 176]. The two main allotropic forms (cubic γ-Mo_2N and tetragonal β-Mo_2N) have shown different catalytic properties where β-Mo_2N has delivered higher specific (*i.e.* surface area normalized) hydrogenation rates [14, 38, 299, 300]. While the catalytic application of γ-Mo_2N has been the subject of appreciable research [183, 243, 269, 301], the use of β-Mo_2N has not been considered to the same extent. Nevertheless, β-Mo_2N has been employed to promote hydrodenitrogenation of carbazole [18], hydrodesulfurisation of thiophene [13] and dibenzothiophene [302] and in ammonia synthesis [38]. The potential of β-Mo_2N in selective hydrogenation has been recently demonstrated with promising results in the production of functionalized anilines [178, 245, 246]. It is generally accepted that the adsorption and catalytic properties of transition metal nitrides in hydrogen mediated reactions are governed by both bulk structure and surface composition where (i) Mo oxidation state, (ii) degree of nitridation and (iii) Mo (nitrogen deficient Mo nitride) site density are critical parameters [303]. An explicit identification of the catalytically active site(s)/species remains challenging. In the hydrogenation of alkadiene, Mo at lower oxidation state ($Mo^{\delta+}$ where $0 \leq \delta < 4$) was proposed to exhibit higher activity, which was attributed to a more effective alkadiene activation [304]. An observed [23, 303] dependence of pyridine hydrodenitrogenation on surface Mo/N serves to illustrate the importance of the degree of nitridation. Metallic Mo edge and N deficient sites have been proposed as the principal source of hydrogenation and hydrogenolysis activity [14, 22, 243, 305, 306]. There is some evidence that H_2 adsorbs on Mo_2N at nitrogen deficient sites [22, 243] and it has been suggested that the activity response in the hydrogenation of carbazole (to perhydrocarbazole) [14, 305], indole (to indoline) [306] and butadiene (to butane) [243] is related to the action of metallic Mo. Moreover, carbazole and perhydrocarbazole C-N hydrogenolysis is thought to proceed on N deficiencies [14, 305] whereas hydrogenolysis of the indoline C-N bond occurs on Mo sites [306].

β-Mo_2N can be synthesized *via* temperature programmed reduction/nitridation of MoO_3 in N_2/H_2 [13, 38, 39]. Nitride formation follows a non-topotactic route, *i.e.* disruption of precursor morphology, with a stepwise reduction ($MoO_3 \rightarrow MoO_2 \rightarrow Mo$) and subsequent nitridation [178, 248]. The oxide precursor (MoO_3) can be reduced to Mo in H_2 at temperatures above 933 K [13, 178, 307]. Metallic Mo has exhibited catalytic activity in a range of H_2 mediated reactions, including hydrogenation of benzene [307], 1-hexene [308, 309], alkadiene [304] and hydrogenolysis of propanol [310]. A search through the literature revealed only one reported comparison of the catalytic action of β-Mo_2N with Mo where the former delivered higher carbazole hydrodenitrogenation but lower hydrogenation rates [14]. This was attributed to different active site requirements for hydrogen scission and addition steps. In this study, the catalytic effect of a systematic increased N incorporation into Mo structure on hydrogenation and hydrogenolysis was examined. The Mo/N content can be effectively controlled by varying the duration or temperature of the nitridation step [13, 249]. Drawing on previous work [178, 246, 311] that has established nitro-group hydrogenation activity and selectivity for β-Mo_2N, nitrobenzene was employed as model reactant and hydrogenolysis performance was examined in the conversion of benzaldehyde to toluene.

3.4.2. Experimental

3.4.2.1 Catalyst Preparation

Bulk Mo was prepared in a horizontally mounted quartz reactor (1 cm *i.d.*) *via* temperature programmed reduction of MoO_3 (*ca.* 4 g, 99.9995%, Alfa Aesar) in H_2 (30 cm^3 min^{-1}, *GHSV* = 460 h^{-1}) at 5 K min^{-1} to 933 K, maintaining the final temperature for 75 h then switching to an Ar flow (30 cm^3 min^{-1}) for 30 min and cooling to ambient temperature. Samples for off-line characterization were passivated at 298 K in 1% v/v O_2/He; no increase in temperature was detected during passivation. The latter step was introduced to avoid uncontrolled sample oxidation upon exposure to air [255]. The Mo powder obtained was then subjected to temperature programmed nitridation in H_2/N_2, using a commercial CHEM-BET 3000 (Quantachrome) unit. The Mo precursor was loaded in a quartz cell (0.4 cm *i.d.*) and contacted with 15 cm^3 min^{-1} (*GHSV* = 1500 h^{-1}) 15% v/v H_2/N_2 at 298 K for 1 h and heated (5 K min^{-1}) to 933 K. The effluent gas passed through a liquid N_2 trap and N_2 and H_2 consumption was monitored by a thermal conductivity detector (TCD) with data acquisition/manipulation using the TPR Win^{TM} software. The TCD response is presented **Figure 3.4.1**. The final temperature (933 K) was maintained for 5 h at which point the signal returned to baseline, *i.e.* complete nitridation. It is known [249] that altering the duration of the final isothermal hold can impact on the degree of nitridation. Two partially nitrided samples, denoted as MoN-1 and MoN-2, were accordingly generated by maintaining the final temperature for 1 h and 2 h, respectively (see **Figure 3.4.1**). The reaction was then quenched by switching to an Ar flow (65 cm^3 min^{-1}) and the samples cooled to ambient temperature with passivation, as described above.

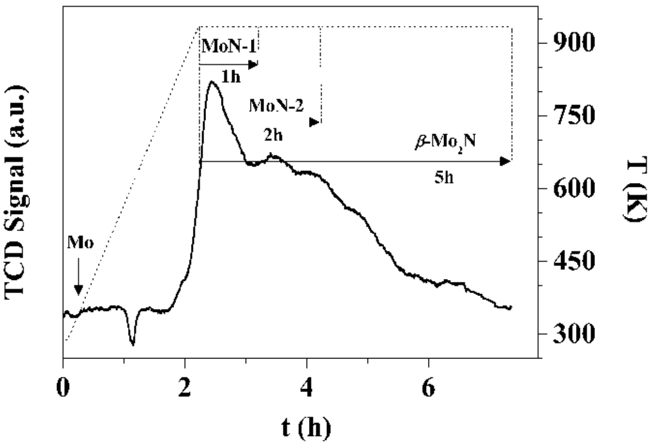

Figure 3.4.1. TCD response resulting from the temperature programmed treatment of Mo at 5 K min^{-1} to 933 K in 15% v/v N_2/H_2. The final isothermal hold was maintained for 1 h, 2 h and 5 h (see solid arrow) to generate MoN-1, MoN-2 and β-Mo_2N, respectively.

3.4.2.2 Characterization

Temperature programmed reduction (TPR)/desorption (TPD), BET surface area and H_2 chemisorption (ambient temperature) were carried out using the CHEM-BET 3000 unit. Passivated (Mo, MoN-1, MoN-2 and β-Mo_2N) samples were loaded in a quartz cell and heated in 17 cm^3 min^{-1} 5% v/v H_2/N_2 at 5 K min^{-1} to 673 K. The activated samples were maintained at the final temperature in a constant flow of H_2/N_2 until return of the signal to baseline, swept with 65 cm^3 min^{-1} N_2 for 1.5 h and cooled to ambient temperature. The samples were then subjected to H_2 chemisorption using a pulse (10 μl) titration procedure, followed by TPD in N_2 (65 cm^3 min^{-1}) at 45 K min^{-1} to 933 K. BET areas were determined in 30% v/v N_2/He using N_2 as internal standard. At least 3 cycles of N_2 adsorption-desorption in the flow mode were employed to determine total area using the standard single point method. Measurements were reproducible to within ± 6% and the values quoted represent the mean. Powder X-ray diffractograms were recorded on a

Bruker/Siemens D500 incident X-ray diffractometer using Cu Kα radiation. The samples were scanned at a rate of 0.02º step^{-1} over the range $5^\circ \leq 2\theta \leq 85^\circ$. Diffractograms were identified using the JCPDS-ICDD reference standards, i.e. Mo (42-1120) and β-Mo_2N (25-1368). Crystal particle size (d_{hkl}) was estimated using the Scherrer equation:

$$d_{\mathrm{hkl}} = \frac{K \times \lambda}{\beta \times \cos\theta} \tag{3.4.1}$$

where $K = 0.9$, λ is the incident radiation wavelength (1.5056 Å), β is the peak width at half the maximum intensity and θ represents the diffraction angle corresponding to the main plane associated with Mo ($2\theta = 40.5°$) and *β*-Mo_2N ($2\theta = 37.7°$). Elemental (bulk nitrogen) analyzes were conducted using an Exeter CE-440 Elemental Analyzer after sample combustion at *ca.* 1873 K. Analysis by scanning electron microscopy (SEM) was carried out with a Philips FEI XL30-FEG equipped with an Everhart-Thornley secondary-electron (SE) detector, operated at an accelerating voltage of 10-15 kV and using NORAN System SIX (version 1.6) for data acquisition/manipulation. Before analysis, the samples were subjected to hydrocarbon decontamination using a plasma-cleaner (EVACTRON). X-ray photoelectron spectroscopy (XPS) measurements were conducted using an Axis Ultra instrument (Kratos) with a monochromatic Al Kα X-ray source (1486.6 eV). Prior to analysis, the samples were adhered to a conducting carbon tape, mounted in the sample holder and subjected to ultra-high vacuum conditions ($<10^{-8}$ Torr). The source power was maintained at 150 W and the emitted photoelectrons were sampled from a square area of $750 \times 350\ \mu m^2$; the photoelectron take-off angle was 90°. The analyzer pass energy was 80 eV for survey spectra (0–1000 eV) and 40 eV for high resolution spectra (over the Mo $3d_{3/2}$ and Mo $3d_{5/2}$ binding energy (BE) range, 226-238 eV). The adventitious C 1*s* peak was calibrated at 284.5 eV and used as internal standard to compensate for any charging effects. The instrument work function was calibrated to give a BE of 84.00 eV for the Au $4f_{7/2}$ line for metallic gold (Metalor) and the spectrometer dispersion was adjusted to give a BE of 932.70 eV for the Cu $2p_{3/2}$ line for metallic copper (Metalor). Spectral curve analysis employed the CasaXPS software.

3.4.2.3 Catalytic runs

The catalytic conversion of nitrobenzene to aniline and benzaldehyde to toluene were carried out under atmospheric pressure at T = 493-523 K, immediately after *in situ* activation, in a fixed bed vertical glass tubular reactor (*i.d.* = 15 mm). The reactions were conducted under the operating conditions where heat/mass transport limitations were negligible. A layer of borosilicate glass beads served as preheating zone, ensuring that the organic reactant was vaporized and reached reaction temperature before contacting the catalyst. The reaction temperature was continuously monitored using a thermocouple inserted in a thermowell within the catalyst bed. Reactant (as a solution in ethanol) was delivered at a fixed calibrated flow rate (1.2 cm^3 h^{-1}) *via* a glass/Teflon air-tight syringe and Teflon line using a microprocessor controlled infusion pump (Model 100 kd Scientific). A co-current flow of the reactant and ultra pure H_2 (<1% v/v organic in H_2) was maintained at a $GHSV = 2 \times 10^4$ h^{-1} with an inlet reactant molar flow (F) of 9-38 µmol h^{-1}. The H_2 content was well in excess of the stoichiometric requirement in respect to the products generated and the flow rate was monitored using a Humonics (Model 520) digital flowmeter. The mass of catalyst to inlet reactant molar feed rate (m/F) spanned the range 266-5281 g h mol^{-1}. Reaction of benzyl alcohol was also carried out over Mo and β-Mo_2N (T = 523 K, m/F = 1250-2083 g h mol^{-1}) in order to probe the benzaldehyde conversion pathway. In a series of blank tests, passage of each reactant in a stream of H_2 through the empty reactor did not result in any detectable conversion. The reactor effluent was frozen in a liquid nitrogen trap for subsequent analysis, which was made using a Perkin-Elmer Auto System XL gas chromatograph equipped with a programmed split/splitless injector and a flame ionization detector, employing a DB-1 50 m × 0.33 mm *i.d.*, 0.20 μm film thickness capillary column (J&W Scientific). Nitrobenzene (Fluka, purity ≥ 99%), benzaldehyde (Fluka, ≥ 98%), benzyl alcohol (Riedel-de Haën, ≥ 99%) and ethanol (Sigma Aldrich, ≥ 99%) were used as supplied without further purification. All the gases (H_2, N_2, Ar, O_2 and He) employed were of ultra high purity (> 99.99%, BOC). Reactant fractional conversion (X_{NB}), taking nitrobenzene (NB) as representative, was obtained from

$$X_{\mathrm{NB}} = \frac{[\mathrm{NB}]_{\mathrm{in}} - [\mathrm{NB}]_{\mathrm{out}}}{[\mathrm{NB}]_{\mathrm{in}}} \qquad \textbf{(3.4.2)}$$

and selectivity with respect to aniline (AN), as the target product, is given by

$$S_{\mathrm{AN}}(\%) = \frac{[\mathrm{AN}]_{\mathrm{out}}}{[\mathrm{NB}]_{\mathrm{in}} - [\mathrm{NB}]_{\mathrm{out}}} \times 100 \qquad \textbf{(3.4.3)}$$

Repeated reactions with different samples from the same batch of the catalyst delivered conversion/selectivity values that were reproducibility to within ± 4%.

3.4.3. Results and Discussion

3.4.3.1. Synthesis and Characterization

Treatment of MoO_3 in H_2 to 933 K generated solely Mo, as confirmed by XRD analysis (**Figure 3.4.2(a)**) where the only peaks detected (at 40.5°, 58.6° and 73.7°) match the JCPDS-ICDD reference standard (42-1120) in terms of both position and relative peak intensity. There were no detectable signals associated with the main planes of MoO_3 (JCPDS-ICDD 35-0609) or MoO_2 (JCPDS-ICDD 32-0671). The Scherrer expression (eqn. (**3.4.1**)) was used to calculate Mo crystal size (d_{hkl} = 36 nm, **Table 3.4.1**), which falls within the range (10-100 nm) of values quoted in the literature [312].

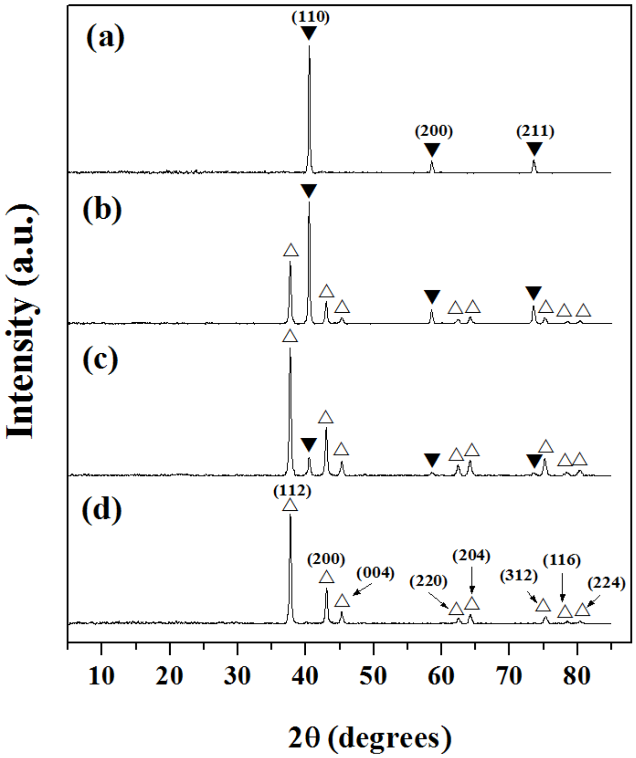

Figure 3.4.2. XRD patterns with crystallographic plane characteristic of each peak associated with **(a)** Mo, **(b)** MoN-1, **(c)** MoN-2 and **(d)** β-Mo_2N. *Note*: XRD peak assignments are based on JCPDS-ICDD reference data: (▼) Mo (42-1120) and (△) β-Mo_2N (25-1368).

SEM analysis was conducted to evaluate morphological features and a representative micrograph for Mo is shown in **Figure 3.4.3(a)**, which reveals irregularly shaped aggregates (<5 µm). The associated BET area is low (*ca.* 4 m^2 g^{-1}, **Table 3.4.1**) but comparable to that recorded for commercial and laboratory synthesized Mo samples (1-13 m^2 g^{-1}) [312]. The TCD response generated during the nitridation of Mo is shown in **Figure 3.4.1**. The negative peak, observed during the temperature ramp can be attributed to H_2 consumption due to the removal of the passivation layer (see Experimental section) before incorporation of nitrogen. Nitrogen consumption generated a broad positive signal with a return to baseline after the isothermal hold

(5 h), indicating complete sample nitridation. The bulk Mo/N ratio for β-Mo_2N determined from N_2 consumed during nitridation (2.5) matches that obtained from elemental analysis (2.6; **Table 3.4.1**) and is in good agreement with the literature (2.5-2.8) [14, 38, 39]. XRD analysis (**Figure 3.4.2(d)**) confirms full nitridation with no peak(s) due to residual Mo in evidence. The 8 peaks identified are consistent with the main reflections of β-Mo_2N (JCPDS-ICDD 25-1368). A particle size (d_{hkl}, **Table 3.4.1**) of 27 nm is in the upper range of values (3-30 nm) reported previously [14, 262, 300]. The equivalent crystal size obtained for Mo and β-Mo_2N (36 nm *vs.* 27 nm) suggests that no significant morphological modification occurred during nitridation. This also follows from the β-Mo_2N BET area that converges with the starting Mo (*ca.* 4 $m^2 g^{-1}$) and is comparable with values (2-17 $m^2 g^{-1}$) [13, 38, 178] recorded for β-Mo_2N synthesized *via* temperature programmed reaction in N_2+H_2.

Catalysts	Mo	MoN-1	MoN-2	β-Mo_2N	Error
β-Mo_2N:Mo^a	-^{b}	0.34:0.66	0.88:0.12	-^{c}	
BET ($m^2 g^{-1}$)	3.9	4.5	4.1	4.4	± 0.1
Bulk Mo/N	-	5.1^d/4.9^e	2.8^d/2.8^e	2.5^d/2.6^e	
Surface Mo/N	-	2.2	1.1	0.9	
Mo 3*d* BE (eV)	231.3 228.0	231.7 228.4	231.8 228.6	231.8 228.5	

[a] from XRD analysis
[b] d_{hkl} = 36 nm using (110) plane associated with Mo at $2\theta = 40.5^\circ$ (see eqn. (**1**))
[c] d_{hkl} = 27 nm using (112) plane associated with β-Mo_2N at $2\theta = 37.7^\circ$ (see eqn. (**1**))
[d] from N_2 consumption during nitridation
[e] from elemental analysis

Table 3.4.1. Bulk (β-Mo_2N:Mo and Mo/N) and surface (Mo/N) composition, BET surface area and XPS binding energies (BE) for Mo 3*d*.

In order to probe the correlate Mo/N with the catalytic response, two additional samples (MoN-1 and MoN-2) were generated by modifying the duration of the nitridation step, i.e. 1 and 2 h, respectively, relative to the 5 h required to generate β-Mo_2N (**Figure 3.4.1**). The XRD diffractograms shown in **Figure 3.4.2** for **(b)** MoN-1 and **(c)** MoN-2 exhibit only peaks due to Mo and β-Mo_2N. The intensity ratio of the principal plane for β-Mo_2N (at 37.7º) relative to that of Mo (40.5º) was used to estimate the β-Mo_2N:Mo ratios (see **Table 3.4.1**) where a higher Mo_2N content was established for the composite sample MoN-2 subjected to nitridation for 2 h. The bulk Mo/N measured from N_2 consumption and elemental analysis of the solid samples are again in good agreement where the ratios follow the order MoN-1 > MoN-2 > β-Mo_2N. Representative micrographs for **(b)** MoN-1, **(c)** MoN-2 and **(d)** β-Mo_2N shown **Figure 3.4.3** reveal an equivalent overall morphology that matches the starting Mo, as noted elsewhere [178, 248].

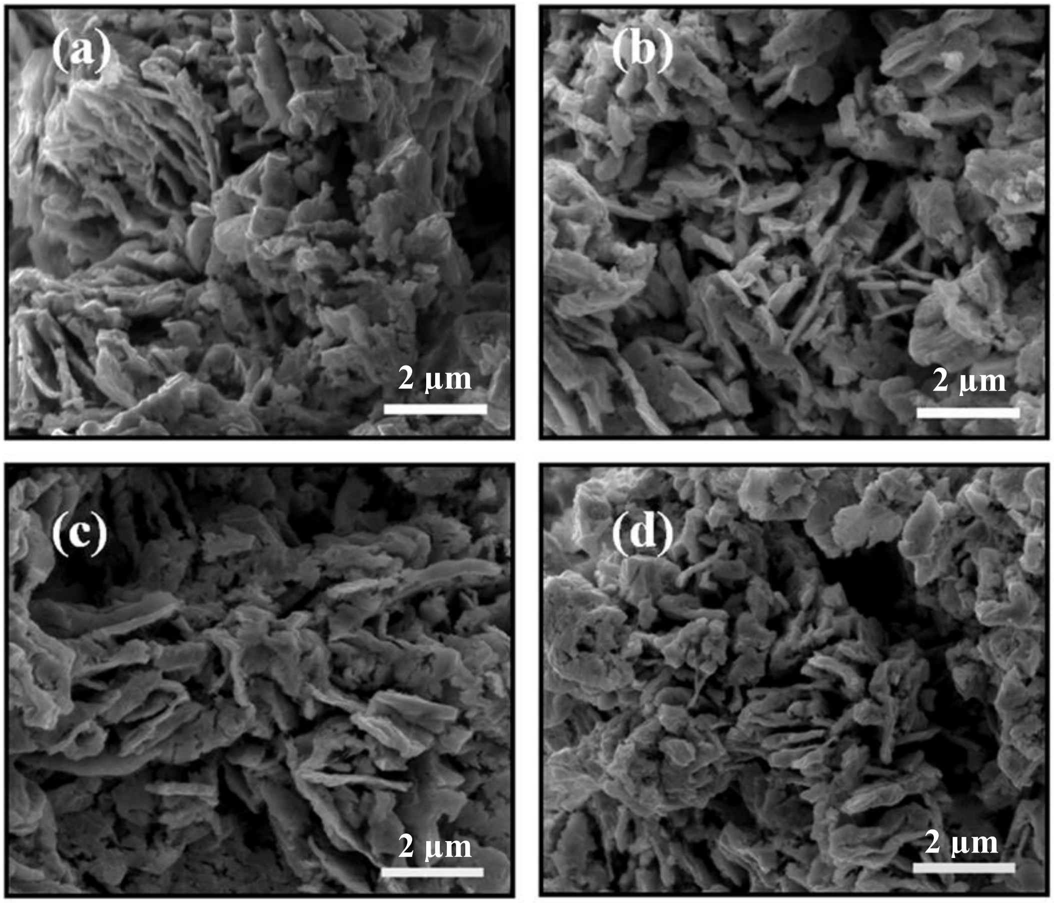

Figure 3.4.3. Representative SEM micrographs for **(a)** Mo, **(b)** MoN-1, **(c)** MoN-2 and **(d)** *β*-Mo_2N.

In previous work [178], it was proposed that a disruption of the crystal structure occurs during the $MoO_3 \rightarrow MoO_2$ reduction step and the resultant structure is retained in the subsequent steps $MoO_2 \rightarrow Mo \rightarrow \beta\text{-}Mo_2N$. This is in agreement with the results presented here where the switch from a body-centered cubic to tetragonal structure with nitrogen incorporation was not accompanied by any distinguishable variation in morphology or surface area (**Table 3.4.1**).

XRD and elemental analyzes provide information on bulk properties but these can differ significantly from surface characteristics [313]. As the catalytic step proceeds on the surface actives sites, complementary characterization of surface composition is essential. The XPS profile measured for Mo (**Figure 3.4.4(a)**) is dominated by a peak with a binding energy (BE) = 228.0 eV that can be attributed to $Mo^{\delta+}$ ($0 \leq \delta < 2$) for passivated Mo. While metallic Mo is characterized by a Mo $3d_{5/2}$ spin component at 227.8 ± 0.1 eV [308, 309, 314], the formation of a passivating oxide layer is known to shift the peak to higher BE [304, 308]. The XPS profile for β-Mo_2N (**Figure 3.4.4(d)**) exhibits a main signal at higher BE (= 228.5 eV) that is characteristic of $Mo^{\delta+}$ ($2 \leq \delta < 4$) for passivated β-Mo_2N [16, 27, 262]. The second spin component for both Mo and β-Mo_2N (BE given in **Table 3.4.1**) can be ascribed to contributions from Mo^{4+} (229.9 eV [315]) and Mo^{5+} (231.6 eV, [255, 316]) species. The Mo $3d_{5/2}$ signal for β-Mo_2N is shifted to a significantly higher BE (by 0.5 eV) relative to Mo, indicating differences in oxidation state for both samples. The XPS response for MoN-1 **(b)** and MoN-2 **(c)** largely converges with the profile for β-Mo_2N, with a main peak at 228.5 ± 0.1 eV. This suggest that there is no significant influence due to the degree of nitridation on the distribution of Mo valence states, which is in agreement with the literature [249]. The signal at higher BE (235.7-236.0 eV) for the four samples can be related to the occurrence of Mo^{6+} resulting from the passivation step [38, 316].

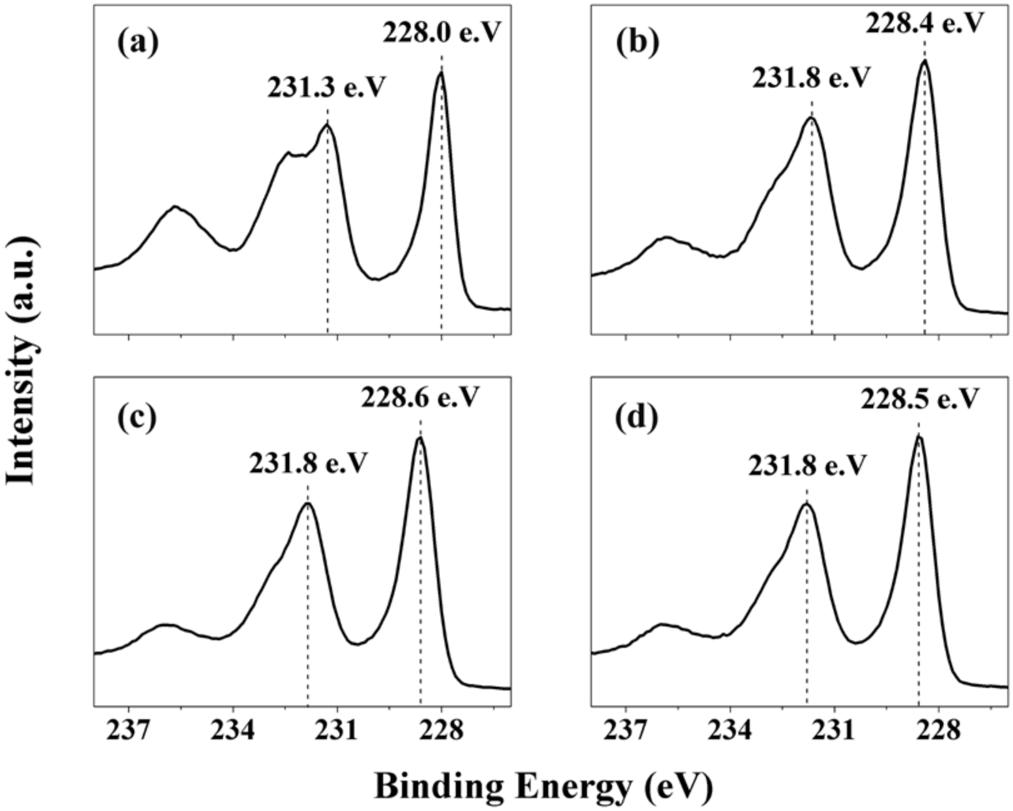

Figure 3.4.4. XPS spectra in the Mo 3*d* region for **(a)** Mo, **(b)** MoN-1, **(c)** MoN-2 and **(d)** β-Mo_2N.

The samples of surface Mo/N obtained from XPS (**Table 3.4.1**) confirm decreasing Mo/N with increasing nitridation and demonstrate a surface enrichment by nitrogen relative to bulk values. Demczyk and co-workers [313] also observed a higher surface nitrogen content and attributed this to a stoichiometry (possibly $Mo_2N_{3-x}O_x$) that differs from the bulk. Moreover, Ghampson *et al.* [300] proposed that nitrogen can be accommodated on the near surface at interstitial sites and defects, such as grain boundaries leading to lower Mo/N. The results establish four distinct samples, pure Mo and β-Mo_2N and two composites (MoN-1 and MoN-2) with (a) similar morphological characteristics (<5 μm aggregates of crystals (27-36 nm) and surface areas (*ca.* 4 $m^2\ g^{-1}$)), (b) decreasing Mo/N in the order Mo > MoN-1 > MoN-2 > β-Mo_2N with a higher surface (relative to bulk) nitrogen content and (c) $Mo^{\delta+}$ species ($0 \leq \delta \leq 6$) where increased N content resulted in higher oxidation states.

3.4.3.2. TPR, H_2 Chemisorption-TPD

Removal of the passivation layer, prior to catalysis, was achieved by TPR. The profile for the passivated Mo is presented in **Figure 3.4.5(aI)** and shows a single positive peak at 673 K. Li *et al.* [304] also applied a reductive treatment (in H_2 to 723 K) to remove the protective oxide layer from Mo but did not provide any detailed TPR analysis.

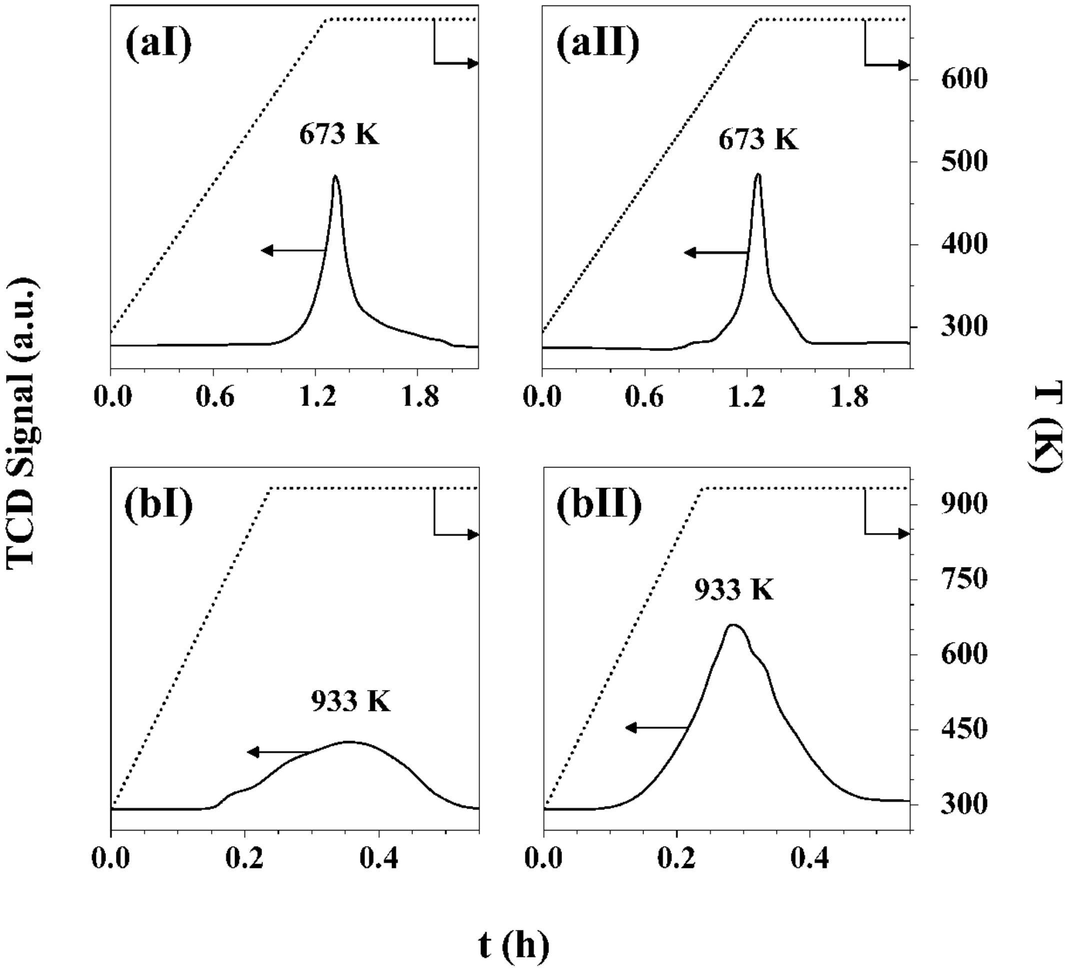

Figure 3.4.5. H_2 **(a)** TPR and **(b)** TPD profiles (solid lines) with temperature ramp (dotted lines) generated for passivated **(I)** Mo and **(II)** β-Mo_2N.

TPR of *β*-Mo_2N **Figure 3.4.5(aII)** also exhibited a similar H_2 consumption peak with a T_{max} that is within the 590-780 K range reported for passivated Mo_2N [19, 183]. The TPR profiles for MoN-1 and MoN-2 (not shown) generated an equivalent response, *i.e.* single peak at the same T_{max}. The passivation treatment can be assumed to result in a monolayer oxygen coverage and H_2 consumed during TPR should be proportional to surface area. Equivalency in H_2 consumption for the four samples (**Table 3.4.2**) is consistent with the similar total (BET) area (*ca.* 4 m^2 g^{-1}). Hydrogen uptake (by pulse titration) and release (by TPD) were measured and the results are given in **Table 3.4.2**. The available literature on the dynamics of H_2 interaction with Mo is limited [317-319]. ARPES [318] and LEED [319] analyzes have shown that H_2 can adsorb on the (110) plane of Mo although quantitative measurements were not provided in these studies. A total H_2 uptake of 0.23 µmol g^{-1} was recorded on Mo at ambient temperature but no value was found to compare this with one in the open literature. A measurably higher H_2 chemisorption capacity was observed for *β*-Mo_2N (0.35 µmol g^{-1}, **Table 3.4.2**) while adsorption on MoN-1 and MoN-2 delivered intermediate values where uptake increased with increasing degree of nitridation. This is consistent with publications [243, 320-322] indicating that the incorporation of N in Mo-phase creates supplementary sites that can modify reactant (H_2 and organic) adsorption and alter the catalytic response. Hydrogen interaction with metallic Mo leads to homolytic dissociation [4] while heterolytic dissociation on Mo-N pairs results in Mo-H and N-H formation [17, 24]. Both dissociation mechanisms are possible for Mo nitride but heterolytic interaction is favored on coordinatively unsaturated Mo sites [24]. Hydrogen TPD generated the profiles for **(I)** Mo and **(II)** *β*-Mo_2N shown in **Figure 3.4.5(b)**, which are characterized by H_2 release over a broad temperature interval with T_{max} in the final isothermal hold (933 K). Desorption at temperatures >500 K has been associated with loss of H_2 from bulk *β*-Mo_2N [20]. Hydrogen released during TPD

(**Table 3.4.2**) was up to 30 times greater than that chemisorbed, suggesting that the major uptake occurred during TPR. A migration of hydrogen to nitride sub-layers has been proposed, which results in strong interactions [17, 20, 24] and the requirement of elevated temperatures for release. The enhanced H_2 chemisorption (and total release) observed in this study can be linked to lower surface (and bulk) Mo/N ratios, where the incorporation of nitrogen serves to facilitate H_2 uptake.

Catalysts	Mo	MoN-1	MoN-2	β-Mo_2N	Error
TPR H_2 consumption (μmol g^{-1})	141	143	151	174	± 2
H_2 chemisorption (μmol g^{-1})	0.23	0.26	0.33	0.35	± 0.01
H_2 TPD (μmol g^{-1})	5.5	5.6	7.1	7.9	0.05

Table 3.4.2. Hydrogen consumed during TPR with (ambient temperature) H_2 uptake in subsequent chemisorption and release during TPD.

3.4.3.3. Hydrogenation Activity: Nitrobenzene to Aniline

The catalytic activity of Mo nitrides in nitro group reduction has been demonstrated [245, 246]. Taking nitrobenzene as a model reactant, the effect of N incorporation in Mo on hydrogenation performance was studied, taking Mo and β-Mo_2N as the two boundary systems. Hydrogenation of nitrobenzene generated aniline (**Figure 3.4.6(a)**), an important aromatic amine used as an intermediate in commercial dye, fine chemical (*e.g.* polyurethane) and pharmaceutical (*e.g.* antifebrin) manufacture [323]. This reaction has been extensively studied [223, 324, 325] and nitrobenzene is commonly used as a model reactant to test the catalytic potential of new systems for -NO_2 reduction. Nitrobenzene adsorption can proceed *via* the aromatic ring or nitro group, where the latter generates aniline [223, 225]. Strong interaction through the aromatic ring can result in the formation of cyclohexylamine (over Ni film [326]) or nitrocyclohexane (over Rh complex [327]). The four systems (Mo, MoN-1, MoN-2 and *β*-Mo_2N) considered in this study produced aniline as the sole product. No published reports of the application of Mo in the hydrogenation of nitro-compounds could be found but IR analysis [277] has shown that NO_2 can adsorb on Mo (110). It has been previously demonstrated that nitrobenzene hydrogenation to aniline proceeds over *β*-Mo_2N in liquid phase batch operation [246]. The data presented here confirm that this extends to continuous gas phase reaction where exclusivity to aniline as product suggests nitrobenzene activation on both Mo and *β*-Mo_2N *via* the nitro functionality. This is also consistent with literature that has demonstrated weak interaction of the aromatic ring with MoO_3 [260], Mo nitride [246] and carbide [260, 328].

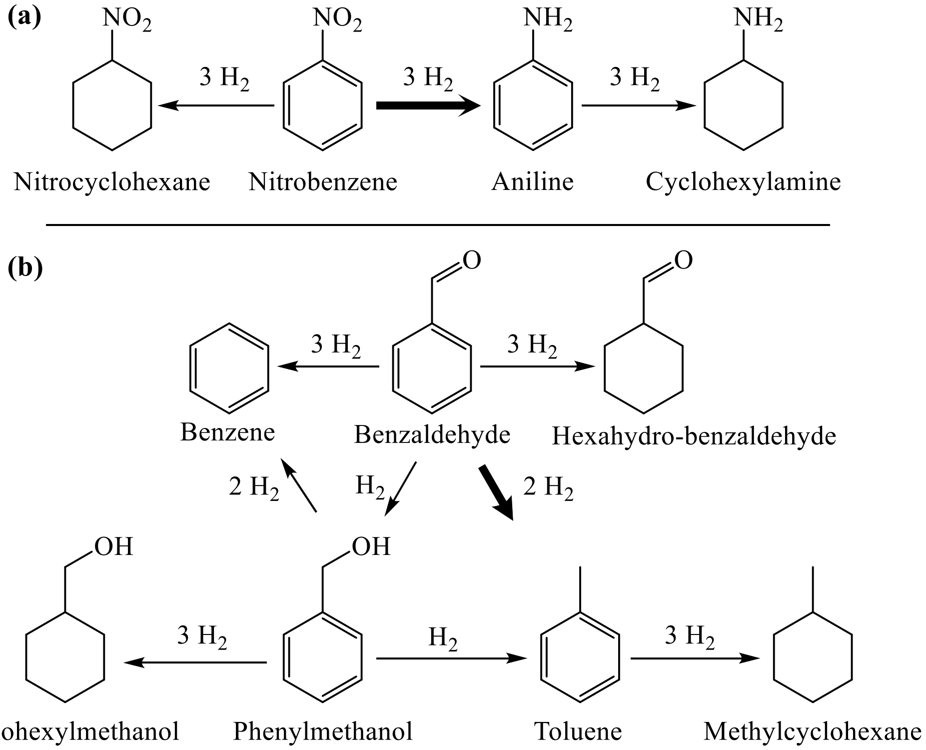

Figure 3.4.6. Reaction pathways associated with the hydrogenation of **(a)** nitrobenzene and **(b)** benzaldehyde; bold arrow identifies the step(s) observed in this study.

Representative time on-stream nitrobenzene conversion (X_{NB}) profiles are presented in **Figure 3.4.7(a)**. In each case, there is a temporal decline in conversion that can be expressed in terms of the empirical relationship [225]

$$\frac{(X_{\mathrm{NB}} - X_0)}{(X_{\mathrm{4h}} - X_0)} = \frac{t}{(\beta + t)} \tag{3.4.4}$$

where X_{4h} represents fractional conversion after 4 h on-stream and β is a time scale fitting parameter. Deactivation of Mo nitride in hydrogenation reactions has been examined by IR [177] and XPS [33] and attributed to nitrogen loss and carbon deposition during reaction. Moreover, the water generated during $-NO_2$ reduction has been proposed to have a detrimental effect on activity [329]. Values for initial conversion (X_0) were obtained from the fit to eqn. (**3.4.4**); the goodness of the fit is illustrated in **Figure 3.4.7(a)**. The applicability of pseudo-first order kinetics has been previously established [178, 299]

$$\ln(1 - X_0)^{-1} = k \cdot \left(\frac{m}{F}\right) \tag{3.4.5}$$

where *m/F* represents the ratio of mass of catalyst to inlet nitrobenzene molar feed rate. The pseudo-first order kinetic plots are given in **Figure 3.4.7(bI)** where the linear fit (passing through the origin) confirms adherence to the model. The extracted rate constants (k_1, μmol g^{-1} h^{-1}), as a measure of activity given in **Table 3.4.3** and plotted in **Figure 3.4.8**, exhibit an increase in the order: Mo < MoN-1 < MoN-2 < β-Mo_2N. This matches the observed order of increasing H_2 chemisorption and release (TPD) (**Table 3.4.2**). This in turn, can be correlated with increasing N content (decreasing Mo/N ratio, see **Table 3.4.1**). Given that an increase in surface N content (from Mo → MoN-1 → MoN-2 → β-Mo_2N) can enhance heterolytic H_2 dissociation on Mo-N pairs, *i.e.* formation of Mo-H and N-H [17, 24], this must contribute to the increase hydrogenation activity.

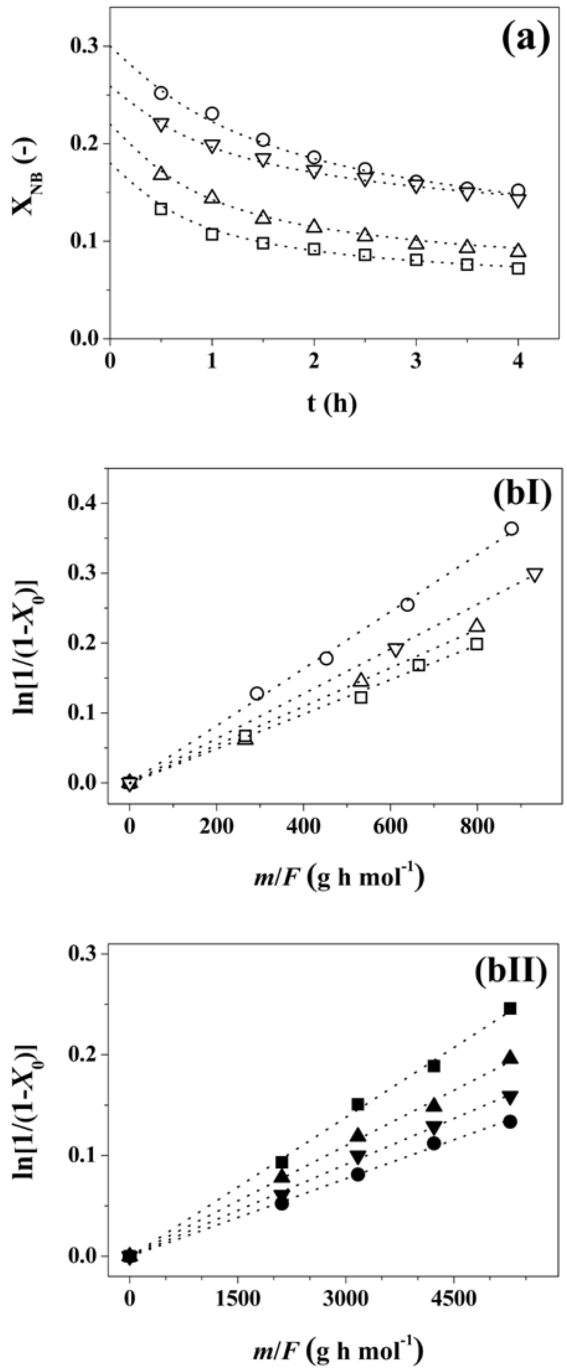

Figure 3.4.7. (a) Variation of nitrobenzene fractional conversion (X_{NB}) with time on-stream (m/F = 800-900 g h mol^{-1}); **(b)** pseudo-first order plots for hydrogenation of **(I)** nitrobenzene (open symbols) and **(II)** benzaldehyde (solid symbols); Mo (□, ■), MoN-1 (△, ▲), MoN-2 (▽, ▼) and β-Mo_2N (○, ●).

Nitrobenzene hydrogenation proceeds *via* a nucleophilic mechanism [223], where the polarized N=O function undergoes nucleophilic hydrogen attack with the formation of a negatively charged intermediate. Nitrogen inclusion in Mo modifies (from XPS analysis (**Figure 3.4.4)**) the surface oxidation state and may facilitate polarisation of the -NO_2 group leading to increased reaction rate. Indeed, HREELS analysis [322] has identified NO interaction with both Mo and N sites and -NO_2 activation may be sensitive to surface Mo/N, which influences hydrogenation rate.

3.4.3.4. Hydrogenolysis Activity: Benzaldehyde to Toluene

The catalytic hydrogenation of benzaldehyde has been promoted using transition metals (Pt, Pd, Ru, Au and Ni) supported on oxides (Al_2O_3, ZrO_2, CeO_2, TiO_2 and SiO_2) in both liquid [330-333] and gas [234, 334-336] phase operation. The reaction pathway is shown in **Figure 3.4.6(b)** where benzyl alcohol and toluene have been the principal reported products. The conversion of benzaldehyde to benzyl alcohol follows a nucleophilic mechanism [334] where -C=O polarization renders the oxygen susceptible to attack with proton transfer [337]. Toluene can result from hydrogenolysis of benzaldehyde, which is favored by a strong surface interaction with the carbonyl oxygen that undergoes hydrogenolytic cleavage [338]. Conversion of benzyl alcohol to toluene over oxide supported metals has been proposed to involve adsorption/activation of the alcohol on the support and reaction with hydrogen dissociated at the metal site [337]. When benzaldehyde is strongly held on the surface, *e.g.* in the presence of strong basic sites, benzene is formed directly from hydrogenolysis [339]. Methylcyclohexane can result from the further reduction of toluene, *e.g.* over Ni/Al_2O_3 [335]. In liquid phase operation over Ru/C, hydrogenation of the aromatic ring generated hexahydro-benzaldehyde [340] and cyclohexylmethanol [333] from benzaldehyde and benzyl alcohol, respectively.

Reaction over the four catalytic systems in this study (Mo, MoN-1, MoN-2, *β*-Mo_2N) generated toluene as the sole product, consistent with hydrogenolytic character. *β*-Mo_2N has exhibited catalytic activity in C-N [18] and C-S [13, 302] hydrogenolysis. The work of Ghampson *et al.* [300] who reported C-O hydrogenolysis in the conversion of 2-methoxyphenol to phenol over *γ*-Mo_2N can be flagged. Moreover, Guerrero-Ruiz and co-workers [58] have recorded an *γ*-Mo_2N/C promoted -C=O (crotonaldehyde) hydrogenolysis. A pseudo first order kinetic treatment was also applicable to the benzaldehyde reaction data, as demonstrated in **Figure 3.4.7(bII)**; the associated rate constants are given in **Table 3.4.3**. In order to establish if toluene is generated by direct conversion of benzaldehyde or successive (benzaldehyde → benzyl alcohol → toluene) steps, the reaction of benzyl alcohol under the same conditions was examined over Mo and *β*-Mo_2N. Benzyl alcohol was converted with 100% selectivity to benzene where the rate constant over Mo (124 μmol g^{-1} h^{-1}) and *β*-Mo_2N (49 μmol g^{-1} h^{-1}) was significantly higher than that observed for benzaldehyde as reactant (**Table 3.4.3**). These results indicate that toluene must be formed by direct hydrogenolysis of the carbonyl group. In marked contrast to nitro group reduction, the activity sequence follows the order *β*-Mo_2N < MoN-2 < MoN-1 < Mo, as depicted in **Figure 3.4.8**, suggesting that increased heterolytic hydrogen dissociation (on Mo-N) does not favor reaction and benzaldehyde hydrogenolysis must result from the reaction of homolytic surface reactive hydrogen. The catalytic response can also be influenced by benzaldehyde adsorption/activation and the results suggest enhanced -C=O activation for hydrogen scission on Mo relative to *β*-Mo_2N. No reported study of aldehyde adsorption on Mo_2N has been found but IR analysis of acetaldehyde uptake on Mo_2C [341] has revealed a chemisorptive interaction of the carbonyl oxygen with Mo that preceded C-O bond scission. It also be noted that Mo exhibits greater capacity for CO uptake than Mo_2N [243] where repulsive interaction prevails between the negatively charged nitrogen and the oxygen lone pair [342]. Moreover, a stronger interaction of organic reactants (*e.g.* alkadiene [304], benzene [315], 1-butene [321]) has been reported for Mo species at low oxidation states. The shift in the XPS response to higher BE (higher Mo oxidation state) after incorporation of nitrogen may then result in a weaker interaction of benzaldehyde with the Mo nitride surface relative to Mo.

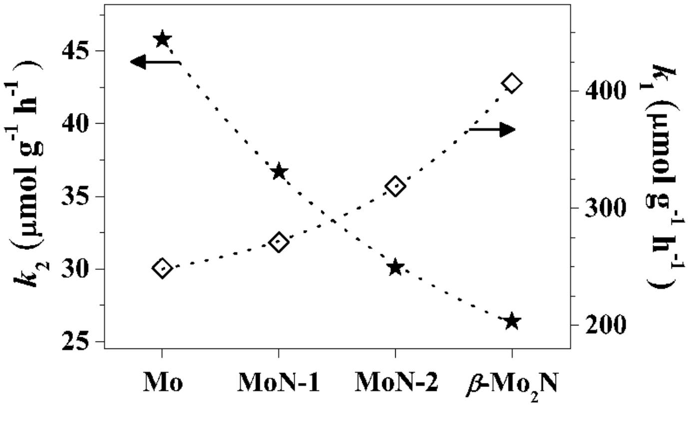

Figure 3.4.8. Rate constants associated with the hydrogenation of nitrobenzene to aniline (k_1, ◇) and benzaldehyde to toluene (k_2, ★) over Mo, MoN-1, MoN-2 and β-Mo$_2$N with 100% selectivity over all samples.

Catalysts	Mo	MoN-1	MoN-2	β-Mo$_2$N
k_1 (± 4%)	249	271	319	407
k_2 (± 4%)	46	37	30	26

Table 3.4.3. Rate constants (µmol g^{-1} h^{-1}) for the conversion of nitrobenzene (k_1), and benzaldehyde (k_2).

These results suggest the respective contribution of heterolytic (on Mo-N) chemisorbed hydrogen to catalytic hydrogenation. A decrease in Mo/N ratio lowers the available hydrogen for hydrogenolysis but enhances hydrogenation rate (**Figure 3.4.8**). It is recognized that catalyst performance may not be governed by surface hydrogen alone and the dynamics of the surface interactions by the organic (nitrobenzene and benzaldehyde) reactant can have a major bearing.

3.4.4. Conclusions

Hydrogen mediated reaction of nitro- (nitrobenzene) and carbonyl- (benzaldehyde) functions shows contrasting dependence on Mo/N ratio. Variation in Mo/N is possible by controlling the duration of Mo nitridation (in N_2/H_2) where β-Mo_2N was the product of complete nitridation. Surface area (*ca.* 4 m^2 g^{-1}) and bulk morphology (aggregates (<5 μm) of crystals (27-36 nm)) remained unchanged during nitridation. XPS measurements have revealed a surface enrichment by nitrogen (lower Mo/N) relative to the bulk where the passivated nitrided samples exhibit higher oxidation states of Mo than passivated Mo. Ambient temperature H_2 chemisorption and release (during TPD) was elevated with increasing nitridation. A higher rate of nitrobenzene hydrogenation with 100% selectivity to aniline with decreasing Mo/N is attributed to increased availability of reactive heterolytic dissociated hydrogen (on Mo-N). Reaction of benzaldehyde resulted in toluene formation where rate was enhanced with increasing Mo/N, consistent with the contribution of homolytic hydrogen (on Mo) to hydrogenolytic -C=O attack.

Chapter 4

Structured Catalysts for Selective Hydrogenations

Structured catalysts were designed for the selective C≡C → C=C and NO_2 → NH_2 transformations. Pd and Ni nanocolloids were prepared with controlled crystal sizes and deposited on a structured carbon-based support. The effect of the components involved in the preparation of metal NPs like the reducing and the stabilization agents was precisely identified to define an optimized catalyst composition for the two case studies.

4.1 Impact of Organic-Ligand Shell on Catalytic Performance of Colloidal Pd Nanoparticles for Alkyne Gas-phase Hydrogenation

Abstract

Monodispersed Pd nanoparticles (NPs) have been prepared by colloidal technique and deposited on a structured support consisting of carbon nanofibers (CNF) grown on sintered metal fibres (SMF). The surface properties of Pd NPs have been fine-tuned by (i) changing the nature of stabilizing agent (electrostatic *vs.* steric), (ii) controlling Pd NPs size (2-10 nm) and (iii) grafting N-containing ligands onto the CNF/SMF surface. In the *semi*-hydrogenation of acetylene ($T = 393$ K; $P = 1$ bar) catalytic response was insensitive to the nature of the reducing agent where equivalent activity/selectivity were obtained over Pd NPs with similar dispersion, prepared with the same stabilizer.

A similar product distribution was recorded over Pd NPs with *similar crystal size* irrespective of the colloidal stabilizer (electrostatic *vs.* steric). In contrast, a stronger inhibiting effect on hydrogenation rate has been found with electrostatic stabilizer (sodium di-2-ethylhexylsulfosuccinate) as compared to the steric ones (polyvinylpyrrolidone or polyvinylalcohol) and assigned to geometric and electronic effects. Decrease (from 8 → 2 nm) in Pd NPs size results in a concomitant decrease in activity (antipathetic size-sensitivity), but higher selectivity to target ethylene product. Grafting of nitrogen-containing modifiers (polyvinylpyridine or polyethylenimine) on the CNF/SMF support results in a significant increase in olefin selectivity (up to 93%) where the catalyst shows remarkable stability during 120 h on-stream. This is explained by the electronic modifications promoted by interactions between the Pd NPs and the

grafted ligands as confirmed by XPS analysis. In comparison, stabilizer-free Pd/CNF/SMF has low selectivity to ethylene (65%). In summary, controlled size Pd (core) nanoparticles with organic ligands (shell) demonstrated increased selectivity and remarkable stability in catalytic gas-phase alkyne *semi*-hydrogenation opening new tools for rational catalyst design.

4.1.1. Introduction

The conventional preparation methods for heterogeneous catalysts based on impregnation/deposition of metal precursors followed by drying, calcination and activation steps [343] present difficulties in terms of controlling metal nanoparticle (NP) size and shape, known to be of fundamental importance for catalysis. Colloidal techniques have emerged as a valuable alternative for tailoring metal NP morphology [79, 120]. A control in metal crystallite size allows optimizing the surface to volume ratio, maximizing the use of noble metals and allowing to control catalytic performance [344]. Organic surfactants are typically employed during the synthesis of metal nanocolloids in order to prevent undesired agglomeration. Nonetheless, the presence of these compounds, even in trace amounts, on the NP surface can have an impact on catalytic response. Up to date, the influence of metal NP size and the nature of organic shell on hydrogenations, *ca.* 20% of the reactions in the manufacture of pharmaceuticals and fine chemicals [345], has been mainly studied for liquid phase reactions [74] since ligands are more flexible in solutions (due to adsorption equilibrium) allowing the activation of adducts. For example, polymer-stabilized Pt and Pd NPs were shown to be active and highly selective in different liquid-phase reactions including hydrogenations [84].

However, these results cannot be easily extrapolated to gas-phase hydrogenations where the organic shells are believed to block the active sites with detrimental effect on catalytic activity.

Borchert *et al.* for the first time showed that supported colloidal Pt NPs can be used in gas-phase catalysis without prior ligand removal [346] offering new prospective for the design of supported catalysts. Not only small molecules, like CO, can penetrate the ligand shell, but also the adsorption of sterically more demanding molecules, like benzene [347], has been reported. However, systematic studies about the fate of organic shell under gas-phase reaction conditions are very rare. On the other hand, electronic and/or steric influences due to the partial coverage of metal NPs by ligands may cause a change in selectivity as compared to shell-free metal surface. Recently published reports [86, 348] demonstrated the influence of organic ligands on catalytic properties. However, systematic studies about a beneficial effect of different ligand shells on the identical metal core (*e.g.* metal NPs size) during gas-phase hydrogenations are still warranted.

The method of the colloidal NPs preparation and their deposition onto support is schematically depicted in **Scheme 4.1.1**. Two main variables can be identified, namely: reducing and stabilizing agents [85]. The reducing agent promotes the $M^{x+} \rightarrow M^0$ reduction step and its effect on catalytic response has been flagged elsewhere [349]. The nature of stabilizing agents can be identified as: steric, *i.e.* stabilization through polymeric layers [350], and electrostatic [84] (stabilization *via* surface charges resulting in repulsion between NPs). Preformed NPs usually undergo a cleaning step from an excess of organics with the subsequent deposition on a suitable solid support. Furthermore, the support itself can be modified by grafting of different ligands controlling the microenvironment of the metal NPs which, in turn, can impact on the catalytic response [351].

The goal of this work is to study the influence of organic shell over nanocrystal core of colloidal pre-prepared Pd^0 NPs regarding their catalytic response in selective $C{\equiv}C \rightarrow C{=}C$ hydrogenation by identifying the best stabilizer, reducing agent and the ligand grafted onto the support. The *semi*-hydrogenation of acetylene, as an important process for the removal of alkyne impurities from ethylene effluents obtained by cracking of heavy hydrocarbons [352], has been selected as a probe reaction. Palladium, known to be the best in terms of combined activity/selectivity for C≡C bond partial hydrogenation, [120] is the metal of choice. The Pd-NPs were prepared using both electrostatic (sodium di-2-ethylhexylsulfosuccinate (AOT)) and steric (polyvinylalcohol (PVA) and polyvinyl pyrrolidone (PVP)) stabilizers.

In order to clearly demonstrate the beneficial or detrimental effect of the organic shell on the catalytic properties of palladium, the identical Pd^0 NPs bearing the same size with and without ligands have been compared. The catalyst prepared *via* conventional impregnation of the same support has been used as a reference.

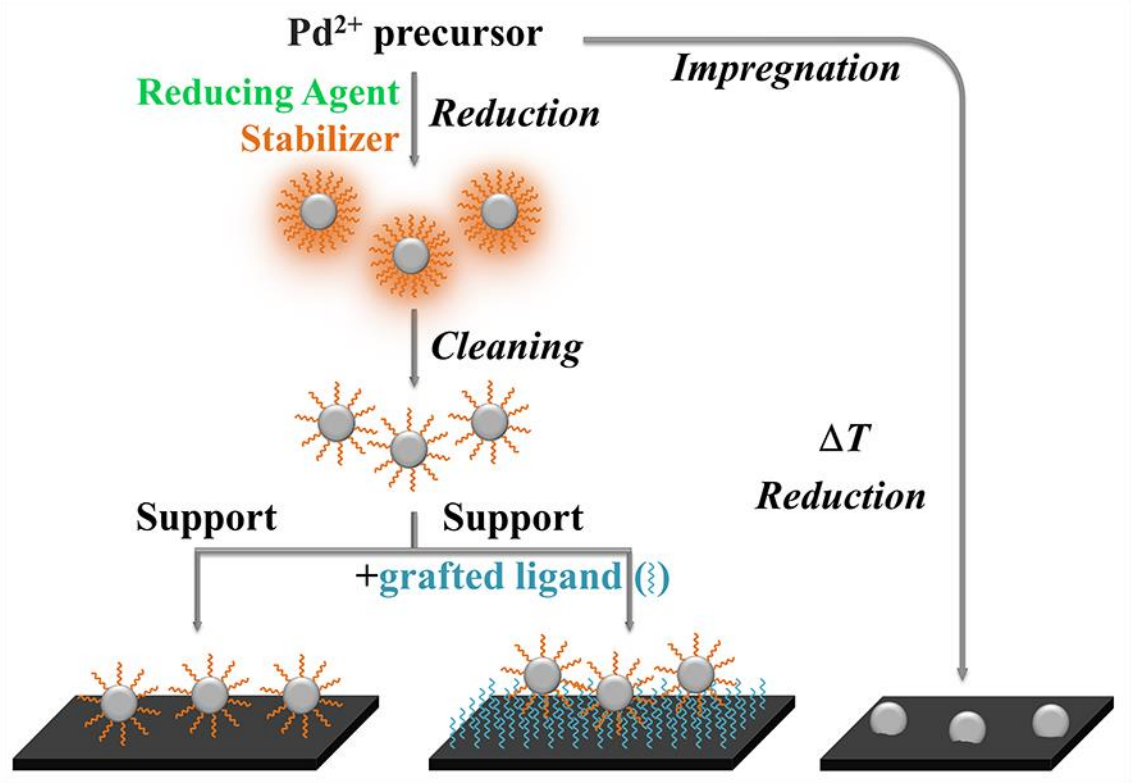

Scheme 4.1.1. Schematic representation of the method used for the preparation of supported Pd-nanoparticles: conventional impregnation versus colloidal technique.

4.1.2. Experimental

4.1.2.1. Materials and Analytical Methods

Palladium (II) chloride (Aldrich), sodium chloride (≥ 99.5%, Fluka), hydrazine monohydrate (HH, ≥ 99.0%, Fluka), L-ascorbic acid (AA, 99.0%, Sigma-Aldrich), n-butanol (But, 99.5%, Acros organics), ethanol (Et, ≥ 99.0%, Acros organics), methanol (Met, ≥ 99.8%, Sigma-Aldrich), isooctane (2,2,4-trimethylpentane, ≥ 99.5%, Sigma-Aldrich, extra-dry), polyvinylpyrrolidone (PVP, Aldrich), polyvinylalcohol (PVA, Fluka), polyvinylpyridine (PVPy , Aldrich), polyethylenimine (PEI, Aldrich), palladium (II) acetate (98%, Aldrich) and acetonitrile (ACN, ≥ 99.5%, Sigma-Aldrich) were used as received without further purification. Sodium di-2-ethylhexylsulfosuccinate (AOT, 98%, Aldrich) was firstly vacuum-dried for 24 h at 333 K prior use. Hydrogen was produced *on*-site with a hydrogen generator (NMH_2 500, Schmidlin-DBS AG) while the rest of the gases (acetylene and Ar) were of high purity (>99.7%, Carbagas).

The composition of the gas mixture was analyzed using a HP 6890 gas chromatograph equipped with an extraction valve (periodical sampling every 10 min), a programmed split/splitless injector, and two (flame ionization (FID) and thermal conductivity (TCD)) detectors employing a Carboxen 1010 (Supelco, Fluka Holding AG, Switzerland) capillary column. The concentrations of the reactant/product species were determined from the total mass balance in the reaction mixture. Hydrogenation activity is expressed in terms of the conversion of acetylene under a steady state ($X_{C_2H_2}$):

$$X_{C_2H_2}(\%) = \frac{n_{C_2H_2,in} - n_{C_2H_2,out}}{n_{C_2H_2,in}} \times 100 \qquad \textbf{(4.1.1)}$$

where $n_{C_2H_2}$ represents the number of moles of acetylene; the subscripts "in" and "out" refer to the inlet and outlet streams.

Catalyst activity is also quantified in terms of quasi-steady-state specific (per m^2 of surface Pd) reaction rate and calculated as:

$$r\,(\mathrm{mol_{C_2H_2}\ m_{Pd}^{-2}\ h^{-1}}) = \frac{\mathrm{F_{C_2H_2,in}} \times \mathrm{X_{C_2H_2}} \times \rho_{\mathrm{Pd}} \times \mathrm{d}}{6} \qquad \textbf{(4.1.2)}$$

where $F_{C_2H_2,in}$ is the inlet molar flow of acetylene (mol s^{-1}), ρ_{Pd} the Pd density (g m^{-3}) and d- the NPs mean diameter obtained from TEM/STEM analyzes. The selectivity, *e.g.* of ethylene ($S_{C_2H_4}$) as the target product is given by:

$$\mathrm{S_{C_2H_4}}(\%) = \frac{\mathrm{n_{C_2H_4,out}}}{\mathrm{n_{C_2H_2,in}} - \mathrm{n_{C_2H_2,out}}} \times 100 \qquad \textbf{(4.1.3)}$$

while the selectivity to green oil ($S_{green\ oil}$) was obtained from a mass balance: [353]

$$\mathrm{S_{green\ oil}}(\%) = 100 - (\mathrm{S_{C_2H_4}} + \mathrm{S_{C_2H_6}}) \qquad \textbf{(4.1.4)}$$

4.1.2.2. Catalyst Preparation

The Pd NPs were synthesized *via* colloidal technique using a series of reducing (HH, AA, Et, Met, and But) and stabilizing (AOT, PVP, and PVA) agents. The supported catalysts were prepared by deposition of colloidal dispersions containing the monodispersed Pd NPs were deposited *via* impregnation on a structured support consisting in carbon nanofibers (CNF) grown on sintered metal fibers (SMF) prepared following the method as described in detail elsewhere [104]. For the ligand-grafted supports, the incorporation of the co-modifiers (PVPy or PEI) was carried out by impregnation of the CNF/SMF support, followed by deposition of the Pd NPs dispersions as described above. The catalytic systems without and with co-modifier employed in this study are denoted as $Pd(d)_{R/S}$ and $Pd(d)_{R/S/M}$, respectively, where “R”, “S” and “M” refer to the reducing, stabilizing and co-modifying agents while “d” is the mean Pd NPs diameter obtained from scanning transmission electron microscopy (STEM) analyzes. More detailed information on the synthesis conditions for each individual catalyst is summarized in **Table 4.1.1**.

Colloids	**Na_2PdCl_4 (g × 10^3)**	**Reducing Agent (volume at 25°C, cm^3)**	**Stabilizer (mass, g × 10)**	**Co-modifier (50 cm^3)**	**d (nm)**
$Pd(6)_{HH/AOT}$	14	HH (1)	AOT (155)	-	6 ± 0.8
$Pd(8)_{HH/AOT}$	23	HH (2)	AOT (155)	-	8 ± 1
$Pd(9)_{HH/AOT}$	32	HH (2)	AOT (155)	-	9 ± 1
$Pd(10)_{HH/AOT}$	41	HH (3)	AOT (155)	-	10 ± 0.9
$Pd(2)_{Et/PVP}$	146	Et (600)	PVP (11)	-	2 ± 0.4
$Pd(3)_{Et/PVP}$	146	Et (600)	PVP (11)	-	3 ± 0.3
$Pd(4)_{AA/PVP}$	146	AA (30)	PVP (11)	-	4 ± 0.3
$Pd(10)_{HH/PVP}$	146	HH (3)	PVP (11)	-	10 ± 1.5
$Pd(10)_{Et/PVP}$	146	Et (30)	PVP (11)	-	10 ± 2
$Pd(5)_{AA/PVA}$	146	AA (30)	PVA (4)	-	5 ± 1.3
$Pd(5)_{Et/PVA}$	146	Et (300)	PVA (4)	-	5 ± 1.2
$Pd(6)_{But/PVA}$	146	But (300)	PVA (4)	-	6 ± 1
$Pd(7)_{HH/PVA}$	146	HH (3)	PVA (4)	-	7 ± 1.1
$Pd(10)_{Met/PVA}$	146	Met (300)	PVA (4)	-	10 ± 2.2
$Pd(2)_{Et/PVP/PVPy}$	146	Et (600)	PVP (11)	PVPy	2 ± 0.4
$Pd(2)_{Et/PVP/PEI}$	146	Et (600)	PVP (11)	PEI	2 ± 0.4
$Pd(4)_{AA/PVP/PVPy}$	146	AA (30)	PVP (11)	PVPy	4 ± 0.3
$Pd(4)_{AA/PVP/PEI}$	146	AA (30)	PVP (11)	PEI	4 ± 0.3

HH: hydrazine hydrate; AA: ascorbic acid; But: n-butanol; Et: ethanol; Met: methanol; AOT: sodium di-2-ethylhexylsulfosuccinate; PVP: polyvinyl pyrrolidone; PVA: polyvinylalcohol; PVPy: polyvinylpyridine; PEI: polyethylenimine.

Table 4.1.1. Metal precursor, reducing agents, stabilizers and ligands grafted onto the support (with specific amounts) used in the synthesis of monodispersed Pd NPs with associated crystal size (d).

a. Monodispersed Pd Nanoparticles

- **Stabilizing Agent (I): Sodium di-2-ethylhexylsulfosuccinate (AOT)**

A series of AOT-stabilized Pd NPs were synthesized according to the procedure described previously [354] but some details pertinent to this study are given below. 15.45 g of AOT were dissolved under stirring (*ca.* 500 rpm) in dried isooctane (100 cm^3) and the obtained solution was divided in two equal volumes (50 cm^3), *i.e.* solutions 1 and 2. Solution 1 was mixed with an aqueous solution of HH (3 M). Solution 2 was mixed with an aqueous solution of Na_2PdCl_4 (5 M, pH 9 adjusted with ammonia prior salt addition). Both solutions were subsequently mixed and left under vigorous stirring (*ca.* 500 rpm) for 1 h at 323 K. A change in the solution color from transparent to dark-brown at the end of the synthesis procedure confirms the formation of Pd^0 NPs [355]. Isooctane was then evaporated (323 K, 40 min) and the excess of surfactant was removed by redispersion in Et (30 cm^3) followed by centrifugation (8000 rpm, 20 min) repeated 3-times. Variations in the water/AOT molar ratios (*i.e.* 3, 5, 7, and 9) resulted in the formation of Pd NPs with various sizes (6, 8, 9, and 10 nm, respectively, denoted as **$Pd(6)_{HH/AOT}$**, **$Pd(8)_{HH/AOT}$**, **$Pd(9)_{HH/AOT}$** and **$Pd(10)_{HH/AOT}$** in this work).

- **Stabilizing Agent (II): Polyvinyl pyrrolidone (PVP)**

The methodology employed has been reported in detail elsewhere [87, 356] but the main synthesis steps are described below. For the preparation of **$Pd(2)_{Et/PVP}$** and **$Pd(10)_{Et/PVP}$** two different volumes (600 cm^3 and 30 cm^3, respectively) of an aqueous PVP solution containing Et as reducing agent (3:2 v/v water+Et) were mixed with an aqueous solution of the metal precursor (Na_2PdCl_4, 10 cm^3; PVP/Pd = 20). The reaction mixture was left at 373 K for 3 h. The **$Pd(3)_{Et/PVP}$** NPs were synthesized *via* stepwise growth using $Pd(2)_{Et/PVP}$ as seeds. A 3/2 v/v water+Et (600 cm^3) solution of PVP containing $Pd(2)_{Et/PVP}$ (2.5×10^{-4} mol) colloids was mixed with additional solution of the metal precursor (Na_2PdCl_4, 10 cm^3, PVP/Pd = 10) and left at 373 K under constant stirring (*ca.* 500 rpm) for 3 h. $\mathbf{Pd(4)_{AA/PVP}}$ and $\mathbf{Pd(10)_{HH/PVP}}$ were synthesized by mixing an AA (8.5×10^{-4} mol, PVP/Pd = 20) and HH (5.0×10^{-4} mol, PVP/Pd = 20) aqueous solution, respectively, with an aqueous solution of Pd precursor (Na_2PdCl_4, 10 cm^3, PVP/Pd = 20) containing PVP. The mixture was left under stirring at 363 K for 3 h. All the methodologies described above resulted in a dark colloidal solution, which indicates the formation of Pd^0 NPs [87]. The excess of reducing and stabilizing agents were removed by adding acetone (1/3 v/v solution/acetone) to the final mixture followed by centrifugation (repeated 3 times).

- **Stabilizing Agent III: Polyvinylalcohol (PVA)**

The PVA-stabilized Pd NPs were synthesized using a similar procedure to that described in section 2.2.1.2 where variations in the type (*i.e.* strength) of the reducing agent promotes the formation of Pd colloids with modified crystal size. $\mathbf{Pd(5)_{Et/PVA}}$, $\mathbf{Pd(6)_{But/PVA}}$, $\mathbf{Pd(10)_{Met/PVA}}$ were synthesized by mixing a 3/2 v/v water+alcohol solution (300 cm^3) containing PVA with an aqueous solution of the metal precursor (10 cm^3, PVA/Pd = 20) and left under continuous heating (363 K) and stirring (*ca.* 500 rpm) for 3 h. $\mathbf{Pd(5)_{AA/PVA}}$ and $\mathbf{Pd(7)_{HH/PVA}}$ were synthesized by mixing AA (8.5×10^{-4} mol, PVP/Pd = 20) and HH (5.0×10^{-4} mol, PVP/Pd = 20) aqueous solutions, respectively, with an aqueous solution of the Pd precursor (10 cm^3, PVA/Pd = 20) containing PVA. The solutions were maintained under constant heating (363 K) and stirring (*ca.* 500 rpm) for 3 h; the cleaning procedure was applied to remove the excess of reducing and stabilizing agents as described above.

b. Structured Carbonaceous Support

- **Carbon Nanofibers Grown on Sintered Metal Fibers (CNF/SMF)**

The CNF/SMF structured support was prepared according to the method developed in this group [104]. Shortly, the CNF (3-5% w/w) were formed on $SMF_{INCONEL}$ surface by chemical vapour deposition (CVD) of ethane in the presence of hydrogen. Before CNF growth, SMF underwent an oxidation (923 K in air for 3 h) to create active sites for CNF growth. The CNF/SMF were subsequently treated (10 min) in an ultrasonic bath to detach any amorphous carbon. CNF surface functionalization by oxigenated groups was carried out by boiling in 30% H_2O_2 aqueous solution for 2 h, then washed with water to reach pH 7.

- **CNF/SMF and co-modifier (Polyvinylpyridine (PVPy) and Polyethylenimine (PEI))**

The grafting of ligands on the support was carried out by maintaining CNF/SMF in a (5% w/w) PVPy or PEI aqueous solution (50 cm^3) for 10 h.

c. Pd/CNF/SMF Catalysts

The deposition of the Pd NPs on the CNF/SMF (with or without ligands grafted onto the CNF) was carried out by the impregnation with the colloidal dispersion of Pd-NPs after cleaning step followed by a drying in vacuum at 333 K for 2 h.

d. Benchmark Pd/CNF/SMF Catalyst

Two additional samples without stabilizer(s) or co-modifier(s) were prepared and used as benchmark in order to prove the effect of the shell surrounding the Pd NPs. A Pd/CNF/SMF (0.03% w/w Pd/CNF) was synthsized by standard wetness impregnation (denoted as $Pd_{imp.}$) using a solution of $Pd(OAc)_2$ in ACN (0.0276 g cm^{-3}), and dried under vacuum at 333 K for 2 h. Pd^0 NPs were formed by catalyst heating in 60 cm^3 min^{-1} 20% v/v H_2/Ar at 5 K min^{-1} to 573 K (1 h).

A second sample was prepared by UV-ozone treatment of Pd(4)$_{AA/PVP}$/CNF/SMF. This process was selected as it has been demonstrated that it is an effective means for PVP removal without compromising the integrity of the Pd metal NPs [357]. The Pd(4)$_{AA/PVP}$/CNF/SMF catalyst was placed under an UV lamp ($\lambda = 185$ and 257 nm) and kept under continuous radiation for 8 h. The sample was then treated in 200 cm^3 min^{-1} 20% v/v H_2/Ar at 5 K min^{-1} to 773 K (2 h) to remove any traces left of PVP.

4.1.2.3 Catalyst Characterization

The Pd content (in the synthesized colloidal solutions and the final Pd^0/CNF/SMF catalysts) was measured by atomic absorption spectroscopy (AAS) using a Shimadzu AA-6650 spectrometer with an air-acetylene flame from the diluted solutions in aqua regia (2/3 v/v HNO_3/HCl). The yield of solid carbon, *i.e.* CNF content, was obtained from a mass balance using the following expression:

$$m_{CNF}(\%) = \frac{m_{SMF,after} - m_{SMF,before}}{m_{SMF,after}} \times 100 \qquad \textbf{(4.1.5)}$$

where m_{CNF} and m_{SMF} are the mass of CNF and SMF, respectively; the subscripts “before” and “after” refer to pre- and post-CVD treatment, respectively. In order to characterize the CNF and Pd/CNF, the composites were treated for a prolonged time (30-60 min) in an ultrasonic bath to detach the carbon nanorods from the SMF surface. BET surface area was determined using an AutoChem 2910 (Micromeritics) unit with a 30% v/v N_2/He flow; pure N_2 (99.9%) served as the internal standard. At least three cycles of N_2 adsorption-desorption in the flow mode were used to determine total surface area using the standard single point method. BET surface area values were reproducible to within ± 5%; the values quoted in this report are the mean. Analysis by scanning electron microscopy (SEM) was carried out on a Carl Zeiss MERLIN FE-SEM equipped with two, annular and Everhart-Thornley secondary-electron (SE), detectors operated at an accelerating voltage of 5-30 keV with a beam current of 1.0-3.0 nA and using ZeissSmartSEM software for data acquisition/manipulation. Powder X-ray diffractograms (XRD) were recorded on a Bruker/Siemens D500 incident X-ray diffractometer with Cu Kα radiation. The samples were scanned at a 0.5° min^{-1} rate over the range $20° \leq 2\theta \leq 70°$. Diffractograms were identified using the JCPDS-ICDD reference standards, *i.e.* Pd (05-0681, [358]), graphite (56-0159, [359]) and Ni (04-0850, [359]). Nickel particle size (d_{hkl}) was estimated using the Scherrer equation [360]:

$$d_{hkl} = \frac{K \times \lambda}{\beta \times \cos\theta} \qquad \textbf{(4.1.6)}$$

where K = 0.9, λ is the incident radiation wavelength (1.5056 Å), *β* is the peak width at half the maximum intensity and θ represents the diffraction angle corresponding to the main plane associated with metallic Ni ($2\theta = 45°$). Metal (Ni and Pd) NP size was investigated by transmission (CM300 Philips/FEI) and scanning transmission electron microscopy (STEM, JEOL 2200FS field emission gun-equipped TEM unit), employing Gatan DigitalMicrograph 1.82 for data acquisition/manipulation. By using an annular dark field detector with a minimum collection semi-angle of ~100 mrad, the recorded images showed an intensity that was approximately proportional to $tZ^{1.7-2}$ (sample thickness t, average atomic number Z), facilitating a clear contrast between the heavy and lighter element components in the catalyst samples. The specimens were prepared by dispersion in Et and deposited on a holey carbon/Cu grid (300 Mesh). Up to 700 individual metal particles were counted for each catalyst and the mean metal diameter (d) was calculated from:

$$d = \frac{\sum_i n_i d_i}{\sum_i n_i} \qquad \textbf{(4.1.7)}$$

X-ray photoelectron spectroscopy (XPS) analyzes were conducted using an Axis Ultra instrument (Kratos Analytical) under ultra-high vacuum condition ($<10^{-8}$ Torr) with a monochromatic Al Kα X-ray source (1486.6 eV). The source power was maintained at 150 W and the emitted photoelectrons were sampled from a 750×350 μm^2 area at a take-off angle = 90°. The analyzer pass energy was 80 eV for survey spectra (0 – 1000 eV) and 40 eV for high resolution spectra (over the Pd $3d_{3/2}$ and $3d_{5/2}$ binding energy (BE) range, 332-345 eV). The adventitious carbon C 1s peak was calibrated at 284.5 eV and used as an internal standard to compensate for any charging effects. Spectra curve fitting and quantification were performed with the CasaXPS software. Peak deconvolution was carried out by Gaussian/Lorentzian adjustment after subtraction of a Shirley type baseline.

4.1.2.4 Catalytic Testing

Gas phase acetylene hydrogenation reaction (T = 393 K; P = 1 bar) was carried out in a jacketed tubular reactor (i.d. 12 mm) described in detail elsewhere [357]. Briefly, a 10×1 mm (*ca.* 6×10^{-2} g) disk of the structured catalyst was placed between two metal rings perpendicularly to the gas flow. A layer (*ca.* 10 cm) of borosilicate glass beads (3 mm diameter, Sartorius AG) serve to homogenize the flow of reactants and as preheating zone. Isothermal (± 1 K) conditions were ensured with a Juvo thermostat (Type 500, K.K. Juchheim Laborgeräte GmbH, Bernkastel-Kues, Germany). Reaction temperature was continuously monitored by a thermocouple inserted inside a protective quartz tube placed underneath the catalyst bed. A co-current $C_2H_2/H_2/Ar$ (1/20/79% v/v) flow was maintained at a gas hourly space velocity (*GHSV*) over the range 15×10^4 – 76×10^4 h^{-1} which was controlled using three Bronkhorst High-Tech, Ruurlo mass flow controllers. Acetylene conversion was maintained $\leq$ 20% to ensure differential operation of the reactor. Madon and Boudart have demonstrated [182] that for heterogeneous catalytic systems operating with negligible mass transfer limitations, a proportional correlation between activity and the number of active sites can be established for a group of catalysts with different metal content but similar dispersion, *i.e.* invariant specific activity. Taking this approach, a series (0.02-0.10% w/w) of Pd/CNF/SMF catalysts were used to determine working conditions where the reaction proceeded under kinetic control. The obtained linear relationship (not shown) confirmed the absence of mass transfer constraints for hydrogenation rates $< 1.95\times10^{2}$ $mol_{C_2H_2}$ mol_{Pd}^{-1} min^{-1}. In a series of blank tests, passage of the C_2H_2 reactant in a stream of H_2/Ar through the empty reactor or over the (CNF/SMF) support alone did not result in any detectable C_2H_2 conversion. Repeated reaction runs with the same batch of catalyst delivered conversion/selectivity values that were reproducible to within ± 5%.

4.1.3. Results and discussion

4.1.3.1. Catalyst Preparation and Characterization

In order to demonstrate the effect of the *reducing and stabilizing agents* in modifying the catalytic action of colloidal Pd NPs five reducing agents were considered: C_1-C_4 alcohols, HH and AA, *i.e.* variable reduction strength and three surfactants as stabilizing agents: PVA, PVP, and AOT, *i.e.* modified type and strength of stabilizer-Pd surface interaction. It is important to stress that the colloidal Pd NP size may be affected by both, the nature of the reducing [85] and stabilizing [361] agents, which in turn can influence alkyne hydrogenation performance [120]. Consequently, these three parameters, namely the size, stabilizing and reducing agent, must be taken into consideration for an accurate interpretation of the catalytic response.

Representative TEM images **(I)** and associated Pd NPs size distributions **(II)** for **(A)** $Pd(2)_{Et/PVP}$, **(B)** $Pd(3)_{Et/PVP}$, and **(C)** $Pd(4)_{AA/PVP}$, as examples, are shown in **Figure 4.1.1**. The

TEM images demonstrate the formation of spherical Pd NPs. This is consistent with a cubo-octahedral metal NP morphology, the most thermodynamically favorable crystal geometry [85, 93]. The TEM derived histograms show a narrow size distribution for the three samples demonstrating the formation of quasi-monodispersed metal colloids (standard deviation σ ≤ 0.4).

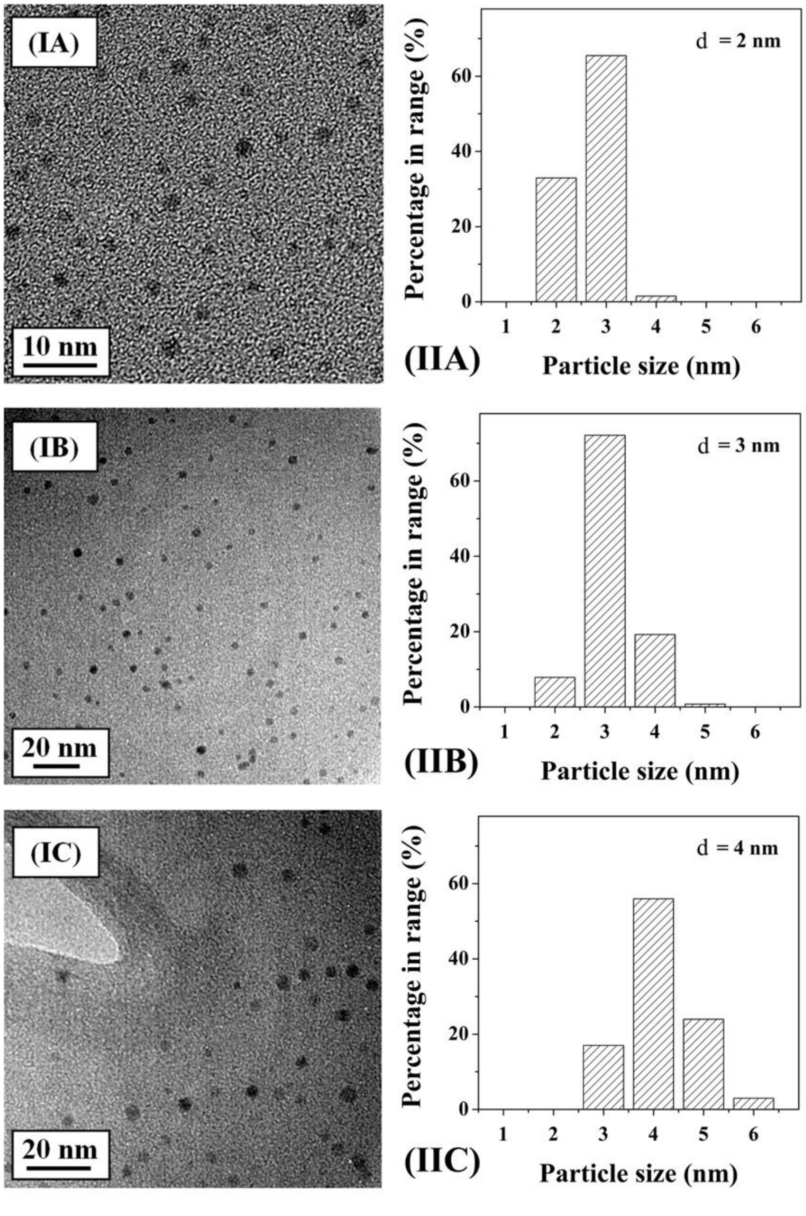

Figure 4.1.1. (I) Representative HRTEM images with **(II)** associated particle size distributions of PVP-stabilized Pd NPs for **(A)** Pd(2)$_{\mathrm{Et/PVP}}$, **(B)** Pd(3)$_{\mathrm{Et/PVP}}$, and **(C)** Pd(4)$_{\mathrm{AA/PVP}}$.

A representative high magnification micrograph of for a single Pd(2)$_{Et/PVP}$ is presented in **Figure 4.1.2** where the intensity profile across the metal crystal (see inset) yields an average *d*-spacing of 0.19 nm that matches the (200) main plane of metallic Pd^0 (JCPDS-ICDD reference standard 05-0681, [358]). The same crystal shape, narrow size distribution and the oxidation state of metallic Pd was in evidence for the all the remaining systems (not shown) indicating that the nature of the reducing and stabilizing agents do not impact significantly on either crystal geometry or mono-dispersity. Telkar and co-workers [80] have also shown that the shape of Pd NPs was not affected by variations in the type of stabilizer, *i.e.* cubic metal crystals using PVP or PVA. However, the opposite effect has also been reported where Lim *et al.* [93] in giving an overview of the available literature have identified instances of modifications in the shape of Pd nanocrystals linked to changes in the reduction kinetics for water-based systems prepared with reducing agents of variable strength.

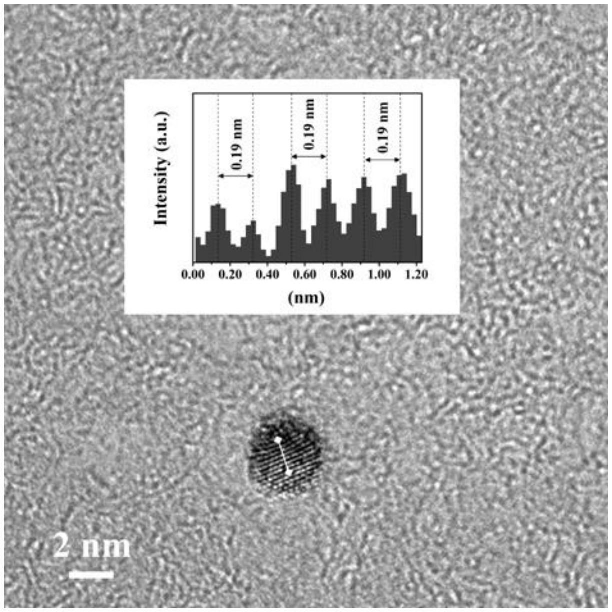

Figure 4.1.2. Representative high magnification image of Pd(2)$_{Et/PVP}$ with (inset) intensity profile revealing the distances between the planes of the atomic lattice in the 1.25 nm segment marked on the isolated Pd NP.

The micrograph presented in **Figure 4.1.3(I)** provides an overview of the overall carbon formation showing the uniform growth of CNF on the surface of the SMF. In the decomposition of ethane to carbon the principal reaction is the carbon-carbon cleavage to methane. Carbon deposition/nanorod growth requires a destructive chemisorption of ethane, *i.e.* C-C bond breakage and loss of H atoms, that is favored by a thermodynamically driven multiple bonding of the chemisorbed hydrocarbon with the metal surface that lowers the surface energy [362]. In the hydrocarbon-metal surface interaction, leading to carbon deposition, two different mechanisms for carbon growth have been described in the literature; (i) strong metal-support interactions result in the formation of carbon nanorods devoid of any metal particles at the exposed tips where the metal NPs remained firmly anchored to the support, *i.e.* "extrusion or base-growth model" [363, 364]; (ii) if the interactions between the metal and the support are weak the pressure exerted at the metal/support interface (as a result of graphitic formation) is of sufficient magnitude to extract the metal particle from the support, *i.e.* tip-growth model [364, 365]. In this work, CNF grown from SMF invariably possessed Ni particles at the nanorod tips (see inset in **Figure 4.1.3(I)**) diagnostic of a weak interaction between Ni and the SMF. The CNF (3.4% wt.) grown on the SMF support exhibited a BET surface area of 200 m^2 g^{-1} that is within the values quoted in the literature (10-391 m^2 g^{-1}) for graphitic nanotubes [101, 366], *i.e.* intermediate in magnitude relative to standard amorphous (625 m^2 g^{-1}) and graphitic carbon (10 m^2 g^{-1}) [365]. The structural properties of the CNF support were further assessed by XRD analysis and the results are presented in **Figure 4.1.3(II)**. The XRD profile of the CNF (detached from the SMF) **(A)** is characterized by a main peak at *ca.* 26°, characteristic of the (002) main plane of graphite (**(B)**, JCPDS-ICDD reference standard 56-0159, [359]) where the broadness of the peak is indicative of a morphological amorphous carbon component. In addition to this, the peaks at *ca.* $2\theta = 45°$ and 52° correspond, respectively, to (111) and (200) planes of metallic Ni (**(C)**, JCPDS-ICDD 04-0850, [359, 367]). Standard X-ray line broadening analysis based on the Scherrer formula (**eqn. 4.1.6**) yields a mean Ni NP size of 66 nm. A representative STEM micrograph of the detached CNF is given in **Figure 4.1.3(III)** and serves to illustrate the nature of the metal dispersion; associated Ni NP size distribution is presented in the histogram in **Figure 4.1.3(IV)**. STEM analysis demonstrate that Ni is present as pseudo-spherical NPs with a broad size distribution (5-125 nm; mean Ni diameter = 58 nm). There is reasonable agreement between the mean sizes obtained from both techniques (XRD and STEM). The discrepancy can be attributed to limitations associated with NP size estimation using the Scherrer formula (*e.g.* modifications in the metal NP shape and/or size distribution can result in local variations in the number of parallel lattice planes responsible for the line broadening [368]) leading to an over-estimation of metal particle size. It is established that the size of the seed metal NPs determines the ultimate width of the catalytically obtained carbon rods [369, 370]. Indeed, the representative SEM image in **Figure 4.1.3(V)** confirms the formation of CNF with a broad size distribution (see arrows) and dimensions similar to those of the Ni seeds (see **Figure 4.1.3(III-IV)**).

Although colloidal techniques allow the synthesis of monodispersed metal NPs with tailored morphology, modifications in Pd crystal size can occur during the deposition on the support [371] or as a result of heating treatment [228], an effect that it is more pronounced for smaller (<5 nm) metal NPs. In this work, Pd NPs over the 2-10 nm size range (see **Table 4.1.1**) were synthesized. Giving that 2 nm represents the smallest Pd NPs among the colloids prepared, the Pd NP size of $\mathrm{Pd(2)_{Et/PVP}}$ were analyzed (by means of STEM analysis) after deposition (on the CNF/SMF) and heating treatment (to reaction temperature = 393 K; see **Figure 4.1.3(II)**).

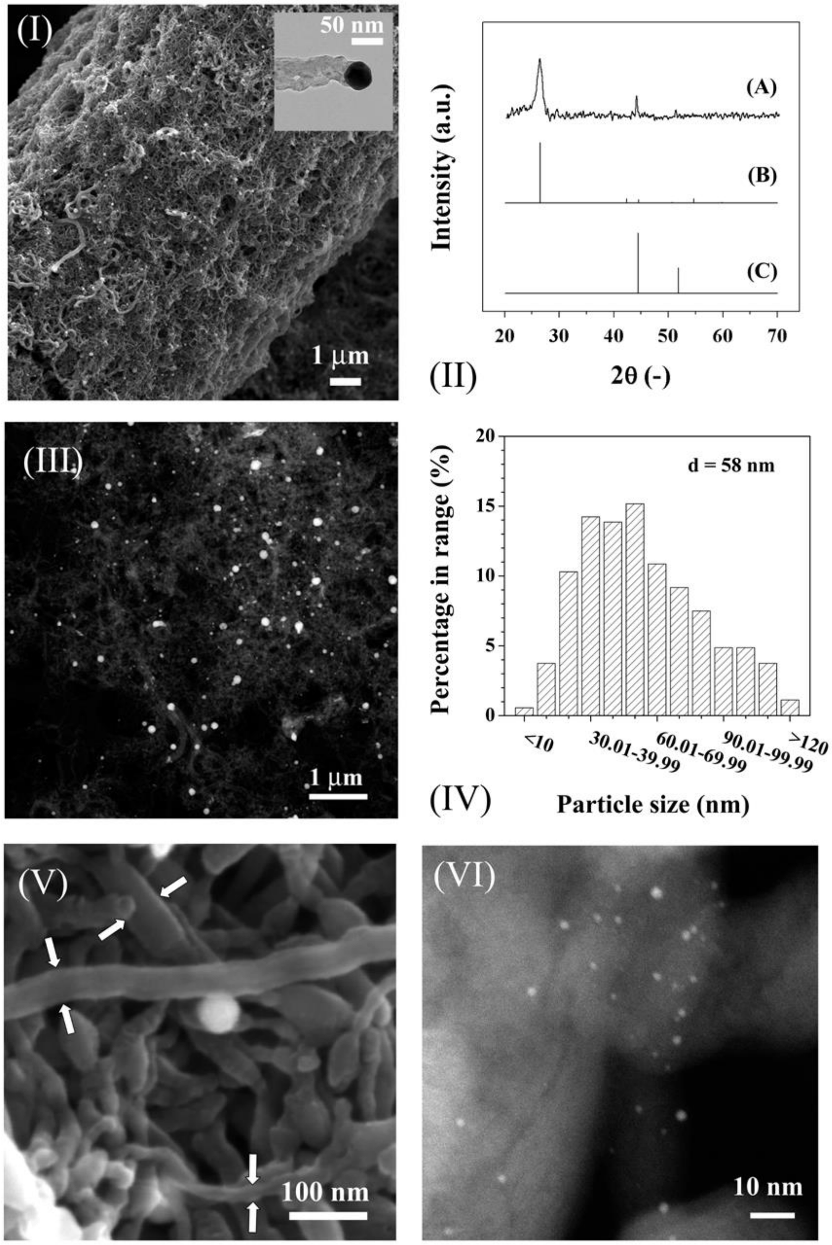

Figure 4.1.3: (I) Representative SEM image of CNF/SMF illustrating the overall carbon growth (*Inset*: TEM image of carbon nanorod tip grown on CNF/SMF); **(II)** XRD pattern for **(A)** CNF detached from SMF (peak assignment based on JCPDS-ICDD for **(B)** graphite (56-0159, [359]) and **(C)** Ni (04-0850, [359, 367]); **(III)** representative STEM image showing nickel particles on CNF/SMF with **(IV)** associated Ni NP size distribution; **(V)** SEM micrograph CNF/SMF illustrating CNF thickness (see arrows) and **(VI)** representative HRSTEM image of $Pd(2)_{Et/PVP}$/CNF/SMF activated at 393 K.

The representative HRSTEM image is consistent with the presence of homogeneously distributed and highly dispersed (*ca.* 2 nm) Pd NPs. This result demonstrates that the integrity of the metal colloids was preserved during the deposition and heating steps. Giving that for the smallest metal NPs used in this study (2 nm; see **Table 4.1.1**) the Pd crystal size was not compromised during deposition/heating, it can be concluded that the Pd size in the rest of the systems (bearing larger metal crystals) is also maintained.

The total area of the CNF decreased after grafting the PVPy (200 → 124 m^2 g^{-1}) and PEI (200 → 127 m^2 g^{-1}) co-modifiers. This result is in agreement with the reported literature dealing with polymer-modified CNF [372] and can be attributed to partial pore blockage [373]. On the other hand, STEM analysis (not shown) confirmed the preservation of Pd crystal morphology after deposition/heating to reaction temperature in the (PVPy or PEI) co-modified CNF/SMF catalysts.

The electronic character of the Pd NPs was investigated by XPS analysis; results obtained over the Pd 3d binding energy (BE) region are presented in **Figure 4.1.4**. Taking $Pd_{imp.}$ as a benchmark (**Figure 4.1.4(I)**), the core level Pd $3d_{5/2}$ shows a main signal in the 335.5 ± 0.1 eV range that is characteristic of Pd^0 [374]. A measurable decrease in the Pd $3d_{5/2}$ BE is following the sequence: Pd_{imp} > $Pd(4)_{AA/PVP}$ > $Pd(4)_{AA/PVP/PVPy}$ > $Pd(4)_{AA/PVP/PEI}$. In addition to this, the (PVP) stabilized and (PVPy and PEI) co-modified Pd NPs shown in **Figure 4.1.4(II), (III) and (IV)** exhibit an additional signal that is characteristic of oxide Pd species. A BE difference of 1.19 and 1.56 eV in $Pd(4)_{AA/PVP}$, $Pd(4)_{AA/PVP/PVPy}$ and of 2.8 eV in the PEI-containing can be ascribed to Pd species with a higher oxidation state [375]. The BE values of the $Pd^0_{5/2}$ exhibit a measurable decrease (335.4 → 334.9 eV) suggesting electron transfer from the stabilizer to the Pd resulting in a partial negatively charged metal phase ($Pd^{\delta-}$). Evangelisti and co-workers [376] observed a negative displacement (respectively 0.2 and 0.3 eV) for PVPy and PVP-stabilized Pd when compared with bulk Pd ascribed to metal–polymer interactions.

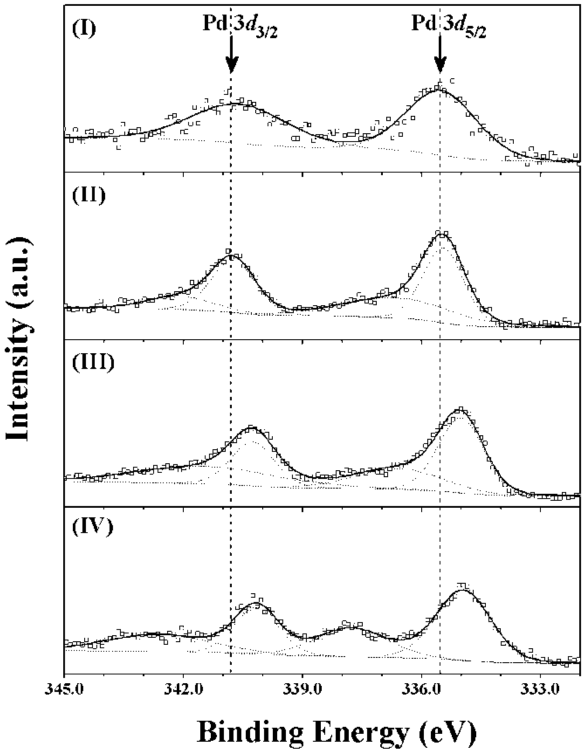

Figure 4.1.4. XPS spectra in the Pd $3d$ region of **(A)** $Pd_{imp.}$, **(B)** $Pd(4)_{AA/PVP}$, (C) $Pd(4)_{AA/PVP/PVPy}$ and **(D)** $Pd(4)_{AA/PVP/PEI}$. *Note*: Arrows illustrate the position of Pd $3d_{5/2}$ and Pd $3d_{3/2}$; experimental data is represented by open symbols while lines identify result from spectra curve fitting.

4.1.3.2. Hydrogenation of Acetylene

The reaction network showing the hydrogenation pathways associated with the conversion of acetylene is presented in **Scheme 4.1.2**, where ethylene (path **(I)**) is the target product. Typical catalysts for this reaction are based on Pd-NPs supported on metal oxides (Al_2O_3 [377], SiO_2 [378] or TiO_2 [379]). Although these catalysts show high activity, they promote the undesired formation of ethane that can result either from further hydrogenation of ethylene (path **(II)**) or direct attack of the C≡C bond (path **(III)**). In addition to this, it is well known [117, 380] that in alkyne hydrogenations Pd catalysts suffer from loss of activity with time on-stream as a result of polycondensation of unsaturated compounds, commonly known as *green oil*. Therefore, minimizing green oil formation can be identified as one of the main challenges in catalytic alkyne hydrogenation. A number of factors have been reported to inhibit green oil formation such as reaction conditions (elevated temperatures (>360 K) and/or low pressures [121]) or through catalyst modifications, *e.g.* variations in the acidity of the support [117], use of ionic liquids [381] or incorporation of IB group metals, *e.g.* Ag [377].

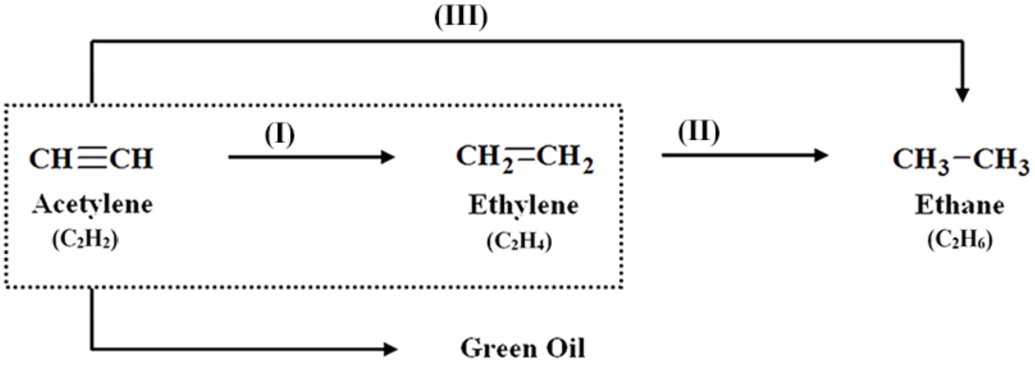

Scheme 4.1.2. Schematic reaction network associated with the hydrogenation of acetylene. *Note*: reaction pathway to target ethylene product has been framed.

The gas phase hydrogenation of acetylene over all the Pd nanocatalysts in this work show the predominant formation (up to 93%) of the target ethylene product. Green oil was generated as secondary product while only small amounts (<5%) of ethane were detected. This high selectivity with respect to the C≡C → C=C hydrogenation step is a significant result as compared to benchmark catalyst accompanied by substantial green oil formation ($S_{\text{green oil}}$ ~25 ± 5% [121]).

a. Effect of Reducing Agent

There are literature reports where an increase in the strength of the reducing agent favors the formation of smaller metal NPs [93, 382]. Nonetheless, although there are instances in the literature where modifications in hydrogenation rate have been associated to variations in the nature of the reducing agent [383], the authors have failed to unearth any study that has compared the catalytic hydrogenation response over NPs stabilized with the same surfactant, bearing a similar metal dispersion but prepared with different reducing agents.

Dependence of Pd-NPs activity/selectivity on the nature of the reducing agent used during the preparation can only be correctly evaluated testing the Pd colloids with similar size, stabilized with the same surfactant but synthesized using different reducing agents; the correspondent data of specific (per m_{Pd}^2) activity (*r*) as a function of NP size (d) is presented in **Figure 4.1.5**. At a similar Pd size (d = 5 nm) for NPs stabilized with the same surfactant (PVA) the activity and selectivity ($S_{C_2H_4}$ ~ 81%; $S_{\text{green oil}}$ ~ 16%) response overlapped, regardless the type of reducing agent (Et *vs.* AA). In order to confirm the result obtained in alkyne hydrogenation response, a series of additional experiments were conducted over $Pd(10)_{HH/PVP}$ and $Pd(10)_{Et/PVP}$ (*i.e.* same NP size (d = 10 nm) and stabilizer (PVP) but different reductant). Once again, activity and selectivity ($S_{C_2H_4}$ ~ 76%; $S_{\text{green oil}}$ ~ 22%) response was equivalent over both systems regardless the type of reducing agent (HH *vs.* Et).

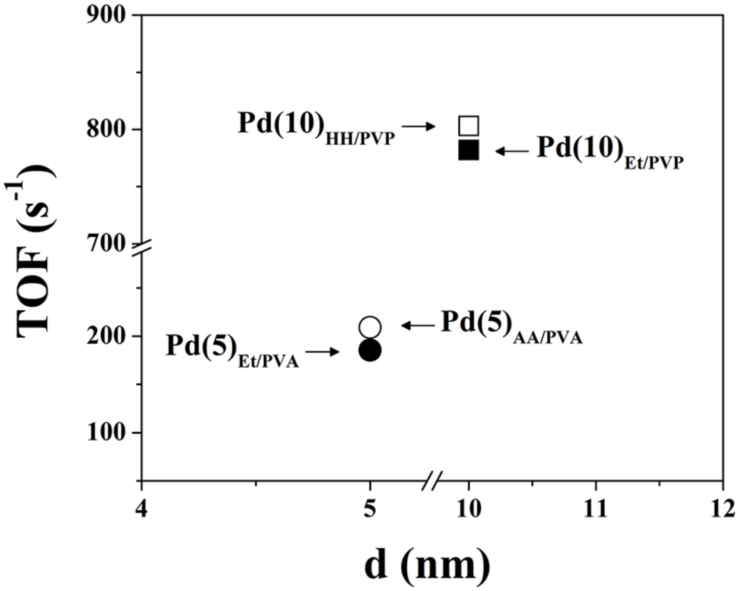

Figure 4.1.5. Variation of catalytic activity with Pd NP size for reaction over Pd(10)$_{HH/PVP}$, Pd(10)$_{Et/PVP}$, Pd(5)$_{AA/PVA}$ and Pd(5)$_{Et/PVA}$ prepared with different reducing agents (HH, AA, Et) and stabilizers (PVP (□/■) and PVA (○/●)); *Reaction conditions*: $T = 393$ K, $P = 1$ bar, Pd/C_2H_2 molar ratio = 1.4×10^{-6} - 5.0×10^{-6} h.

The results in this section show that the type of reducing agent does not influence on the catalytic response in acetylene hydrogenation; nonetheless, the catalytic differences over Pd NPs prepared with different stabilizers and bearing different NP size shall be noted. The independent impact of these two variables will be assessed in the following sections.

b. Effect of Stabilizer

In order to decouple a possible metal particle size effect from contributions of the stabilizer, experiments were carried out over Pd NPs with the same size (d = 10 nm) but stabilized with a different surfactant (PVP, PVA and AOT); the obtained data of specific (per m_{Pd}^2) activity and selectivity (S_i) as a function of metal dispersion (D) is presented in **Figure 4.1.6**. The results obtained are consistent with a similar selectivity response ($S_{C_2H_4}$ = 77 ± 1%; $S_{green\ oil}$ = 20 ± 1%); product distribution was not affected by the type (steric *vs*. electrostatic) of stabilization. In contrast to these results in gas phase, an increase in olefin selectivity in the (liquid-phase) hydrogenation of 2-methyl-3-butyn-2-ol has been recently reported [384] for PVP- (95%) relative to AOT-stabilized (90%) Pd NPs and ascribed to modifications promoted by the functionalities in the steric (PVP) stabilizer.

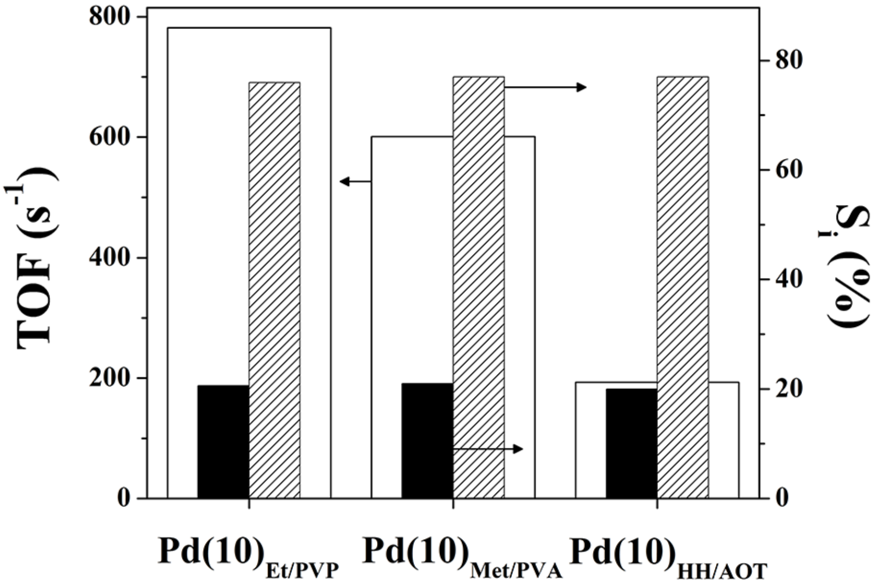

Figure 4.1.6. Variation of catalytic activity (open bars) with selectivity (S_i) to ethylene (hatched bars) and green oil (solid bars) over *steric*- (Pd(10)$_{Et/PVP}$ and Pd(10)$_{Met/PVA}$) and *electrostatic*-stabilized (Pd(10)$_{HH/AOT}$) Pd NPs with the same metal crystal size (d = 10 nm); *Reaction conditions*: T = 393 K, P = 1 bar, Pd/C_2H_2 molar ratio = $1.4\times10^{-6} - 8.6\times10^{-6}$ h. *Note:* balance to 100% selectivity corresponds to ethane.

The similar product distribution over the Pd NPs stabilized with different surfactants does not apply to the activity response where the (sterically) PVP and PVA stabilized Pd NPs delivered higher hydrogenation rate (by up to a factor of 4) at similar degree of conversion ($X_{C_2H_2}$ = 20%). Given that the Pd size was the same for all the nanocatalysts, the different activity must arise from the differences between the surfactants and, more specifically, as a result of the shell surrounding the Pd NPs that is determined by the nature of the stabilizer. These results are in line with the work of Schmidt *et al.* [385] who reported an effect in (liquid phase) cinchonidine hydrogenation rate over polyacrylic acid-stabilized Pt NPs attributed to a surface-localized acidification induced by the stabilizing agent. The presence of (electrostatic stabilizer) AOT will result in the formation of a double layer of counter ions [386]. The lower activity over $Pd(10)_{HH/AOT}$ can then be linked to repulsive forces between the Pd surface and the (electron rich) C≡C bond in the acetylene molecule [387] that diminishes acetylene adsorption on the metal surface. Such effects are not prevalent for the sterically (PVP and PVA) stabilized colloids where the open and flexible nature of the polymer chains can allow the reactant to adsorb. In contrast, a higher activity in the hydrogenation of ethylene over electrostatic (tetradecyltrimethylammonium bromide (TTAB)) compared to steric (PVP) stabilized Pt NPs has been reported elsewhere [388] and attributed to the short alkyl chain in the TTAB stabilizer that provides an increase number of available active sites.

The differences in activity between the two sterically stabilized nanocatalysts ($r_{Pd(10)_{Et/PVP}} > r_{Pd(10)_{Et/PVA}}$) can be ascribed to a combination of both "geometric" and "electronic" effects induced by the surfactant that can influence the properties of the actives sites and, in turn, the adsorption/activation of acetylene. A "geometric effect" can be expected on the basis of the different structural properties of PVA and PVP. Indeed, the linear structure of the PVA polymer will result in the formation of a "dense shield" around the Pd NPs that can hinder acetylene accessibility to the active sites. The branched (with pirrolidinyl cyclic) structure of the PVP will promote the genesis of a less dense shell around the Pd core. This conclusion is consistent with the studies using dendrimer-stabilized metal NPs where the highly-branched dendrimers bear a compact structure resulting in NP encapsulation lowing catalytic activity [389]. Nevertheless, we cannot rule out electronic effects contribution *via* charge-transfer between the amide group of the pyrrolidone ring (on PVP [390]) and –OH (on PVA [349]) to the Pd NP surface.

In order to confirm that the effect on catalytic response is solely due to the stabilizer, a series of additional experiments were conducted over Pd NPs bearing the same size (d = 10 nm) and prepared using a mixture of stabilizers; the results obtained are presented in **Figure 4.1.7**.

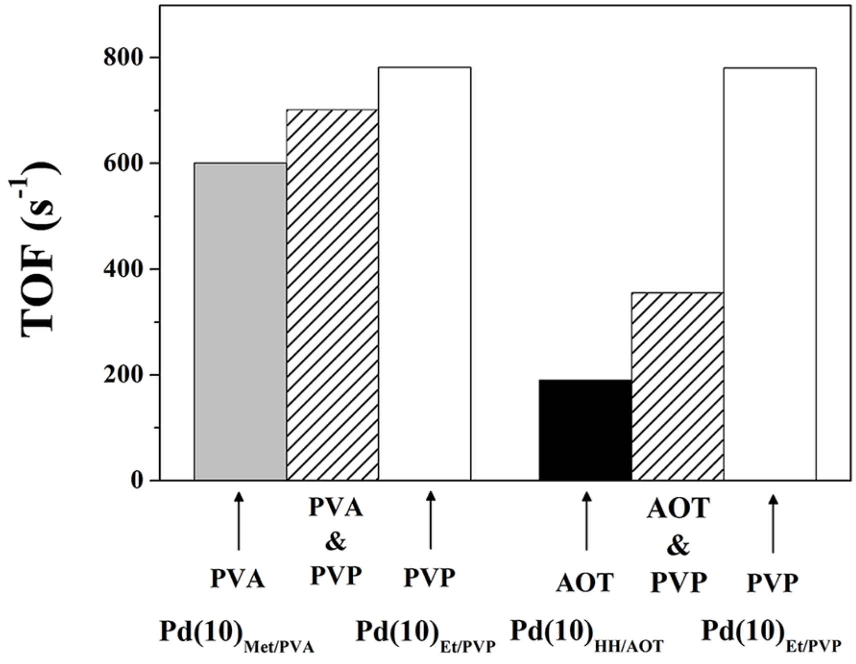

Figure 4.1.7. Variation of activity over Pd NPs with similar crystal size (d = 10 nm) stabilized with PVP (open bars; $Pd(10)_{Et/PVP}$), PVA (solid gray bar; $Pd(10)_{Met/PVA}$), AOT (solid black bar; $Pd(10)_{HH/AOT}$) and mixtures of stabilizers (hatched bars; PVA:PVP and AOT:PVP ratios = 1:1); *Reaction conditions*: T = 393 K, P = 1 bar, Pd/C_2H_2 molar ratio = $1.4\times10^{-6} – 8.6\times10^{-6}$ h. *Note:* balance to 100% selectivity corresponds to ethane.

A similar product distribution ($S_{C_2H_4}$ = 77 ± 1%; $S_{\text{green oil}}$ = 20 ± 1%) was obtained over all the systems. Moreover, the activity results for the catalysts prepared with a mixture of stabilizers fall between that obtained over the Pd NPs stabilized with the pure components. The results in this section confirm that the hydrogenation rate is controlled by the nature of the ligand shell around the Pd-core, *i.e.* enhanced hydrogenation rate over steric surfactants, while it does not impact significantly on the selectivity response.

c. Nanoparticle Size Effect

The relationship between specific (per m^2 of surface Pd) activity **(A)**/selectivity ($S_{C_2H_4}$ **(B)** and $S_{\text{green oil}}$ **(C)**) and mean Pd size (d) for all the systems considered in this work is presented in **Figure 4.1.8**. A similar trend of increased hydrogenation rate over larger Pd NPs is in evidence for all the systems regardless on the nature of the stabilizer. This response is consistent with a structure sensitive reaction where an enhanced C≡C bond hydrogenation is associated with larger particles (from 2 → < 8 nm) being insensitive for sizes ≥ 8 nm. These results are in line with published reports of *anthipathetic structure sensitivity* for gas-phase alkyne hydrogenation over Pd NPs in the size range from 4 to 10 nm [74] but it was shown herein, for the first time, that this effect extends to monodispersed Pd NPs < 4 nm.

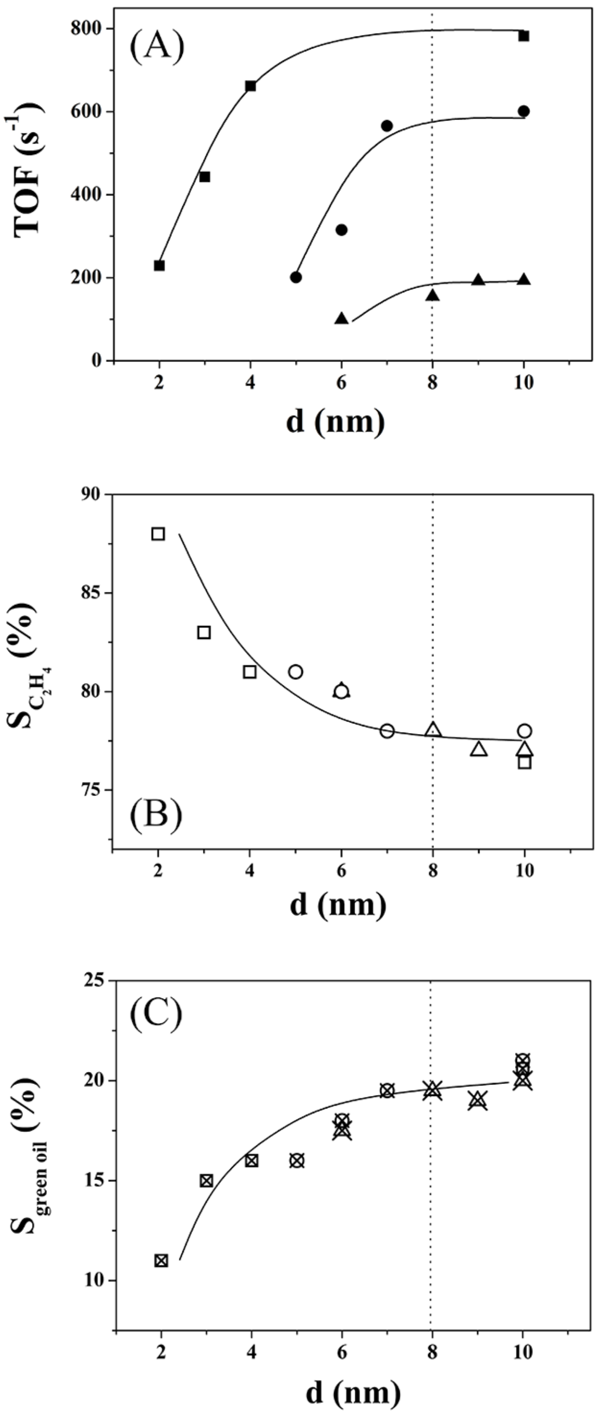

Figure 4.1.8. Variation of **(A)** activity (solid symbols) and selectivity to **(B)** ethylene ($S_{C_2H_4}$, open symbols) and **(C)** green oil (crossed symbols) with Pd NP size for reaction over PVP (■, □, ☒), PVA (●,○, ⊗) and AOT (▲, △, ⨻) stabilized Pd colloids; *Reaction conditions*: *T* = 393 K, *P* = 1 bar, Pd/C_2H_2 molar ratio = $1.4\times10^{-6} – 8.6\times10^{-6}$ h.

In terms of selectivity, the preferential partial hydrogenation ($S_{C_2H_4} \geq 73\%$) over all the Pd colloidal NPs in the range 2-10 nm is demonstrated in **Figure 4.1.8(B)**. This can be linked to an increased C≡C group (compared to C=C) adsorption strength on Pd [79], resulting in a lower adsorption equilibrium constant of the C_2H_4 which, in turn, hinders further (C=C → C-C) hydrogenation to C_2H_6. Although the formation of C_2H_4 is predominantly promoted, the results presented in **Figure 4.1.8(B-C)** demonstrate differences in product distribution over the Pd NPs with different sizes. The same $S_{C_2H_4}$ (77 ± 1%) is observed over larger (8-10 nm) Pd NPs while enhanced $S_{C_2H_4}$ (up to 87%) with a lower $S_{\text{green oil}}$ is associated for smaller Pd NPs (8 → 2 nm). A similar selectivity response in the hydrogenation of acetylene for Pd NPs in the 8-13 nm range has been reported elsewhere [353]. Moreover, Li *et al.* [391] has recently concluded (on the basis of DFT calculations) the preferential formation of ethylene (relative to ethane) on small Pd clusters (Pd_n, n = 2-8). The increased olefin selectivity over the small Pd NP size was attributed to the site isolation affecting an acetylene adsorption mode. Hartog *et al.* [392] using a series of Pd/SiO_2 with different metal dispersion (*D*) reported a measurable increase in the steady-state selectivity to ethylene for smaller metal NPs attributed also to the differences in the deposition of carbonaceous layers from acetylene leading to the sites isolation.

The results in this section demonstrate that smaller Pd NPs exhibit a lower intrinsic activity but enhanced olefin selectivity and lower green oil formation.

d. Effect of Ligand Grafted onto the CNF/SMF

Among the range of catalysts considered, $Pd(2)_{Et/PVP}$/CNF/SMF and $Pd(4)_{AA/PVP}$/CNF/SMF delivered the highest selectivity to the target product ($S_{C_2H_4}$ = 85 ± 3%) and lowest selectivity to the undesired green oil ($S_{\text{green oil}}$ = 13 ± 2%). These NPs were therefore used for further catalyst optimization.

In the liquid phase hydrogenation of alkynes, the use of 2,2'-bipyridine (bipy) and an imidazolium-functionalized bipy ligands has been shown to increase olefin selectivity, which was ascribed to a site-blocking effect by the N-containing ligands [123]. With that premise, two nitrogen-containing stabilizers (*i.e.* PVPy and PEI) were selected and grafted onto the CNF/SMF (see experimental section); the activity/selectivity results over Pd(2)/CNF/SMF **(A)** and Pd(4)/CNF/SMF **(B)** are shown in **Figure 4.1.9**. It has no significant effect on catalytic performance over the smallest (d = 2 nm) Pd NPs where an equivalent activity and selectivity response was obtained over three catalysts. In contrast, the Pd(4) catalysts demonstrated a quite distinct activity and selectivity response. The differences in catalytic performance between the 4 nm and 2 nm Pd NPs was associated to the size effect, which will determine the relative proportion of surface atoms (*i.e.* edge, plane, vertex) with different reactivity [74]. Pd_{edge} does not change significantly for Pd NPs of 2 and 4 nm, while amount of Pd_{plane} sites considerably increases. The differences in catalytic response suggest that Pd_{plane} are responsible for the catalytic response where the N-based ligands increase the selectivity *via* a permanent site-blocking effect of Pd_{edge}. The low amount of Pd_{plane} in Pd(2) catalysts can account for the similar response over the three systems. This is consistent with studies in the literature reporting low [80] or even no activity [74] of Pd_{edge} compared to Pd_{plane} surface atoms in alkyne hydrogenation. Moreover, there is also the possibility of a direct contribution due to electronic and quantum size effects. For particles sufficiently small (≤ 2 nm) a transition in the electronic state from metal to non-metal has been suggested elsewhere [393].

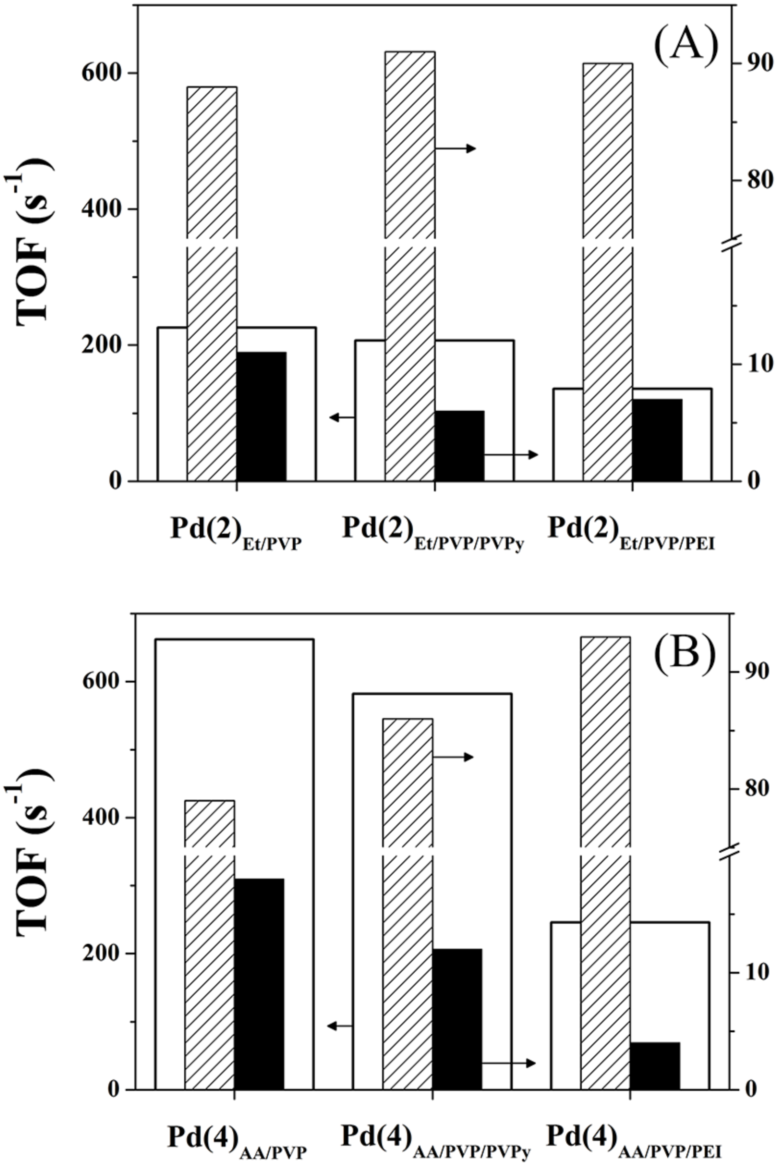

Figure 4.1.9. Variation of activity (open bars) and selectivity (S_i) to ethylene (hatched bars) and green oil (solid bars) over PVP-stabilized ($Pd(2)_{Et/PVP}$, $Pd(4)_{AA/PVP}$) and co-modified with PVPy ($Pd(2)_{Et/PVP/PVPy}$, $Pd(4)_{AA/PVP/PVPy}$) or PEI ($Pd(2)_{Et/PVP/PEI}$, $Pd(4)_{AA/PVP/PEI}$) Pd NPs of **(A)** 2 nm and **(B)** 4 nm; *Reaction conditions*: $T = 393$ K, $P = 1$ bar, Pd/C_2H_2 molar ratio = $1.4\times10^{-6} – 8.6\times10^{-6}$ h. *Note:* balance to 100% selectivity corresponds to ethane.

The distinct catalytic response over three Pd(4)-containing catalysts should arise from the differences in structural and electronic properties of the grafted ligands that will induce a modified effect on the supported Pd NPs. PVPy and PEI hold a free electron doublet on the nitrogen of the amines located in an aromatic ring (in PVPy, [394]) and an aliphatic chain (PEI, [395]). This doublet can increase the electron density of the Pd surface resulting in the formation of $Pd^{\delta-}$ NPs [376] with low affinity for the electron rich C≡C bond [387]. Taking the three systems presented in **Figure 4.1.9(B)**, the selectivity to target ethylene increased in the order: Pd(PVP) < Pd(PVPy) < Pd(PEI). This sequence mimics that of increasing the partial negative charge on the Pd NPs, shown in **Figure 4.1.4**, *i.e.* Pd(0) = 335.5 eV **(A)** < Pd(PVP) = 335.4 eV **(B)** < Pd(PVPy) = 335.0 eV **(C)** < Pd(PEI) = 334.9 eV **(D)**. Indeed, strong adsorption of acetylene leads to oligomerization [396]. Moreover, the site separation induced by carbon deposits [134] can be responsible for higher selectivity to target olefin for PEI modified Pd NPs.

In order to demonstrate the beneficial effect of the organic shell on catalytic performance, the $Pd(2)_{Et/PVP/PVPy}$ and $Pd(4)_{AA/PVP/PEI}$ with the highest selectivity to ethylene has been compared to that of ligand-free Pd(4) and impregnated benchmark Pd_{imp} (**Figure 4.1.10)**. The selectivity drops down from 93% to 60% towards ethylene over cleaned and non-stabilized Pd, while the green oil production increases up to 8 times. Although there is a contribution of different particle sizes in the impregnated system, there is clearly positive effect on the selectivity to ethylene induced by the organic-ligand shell.

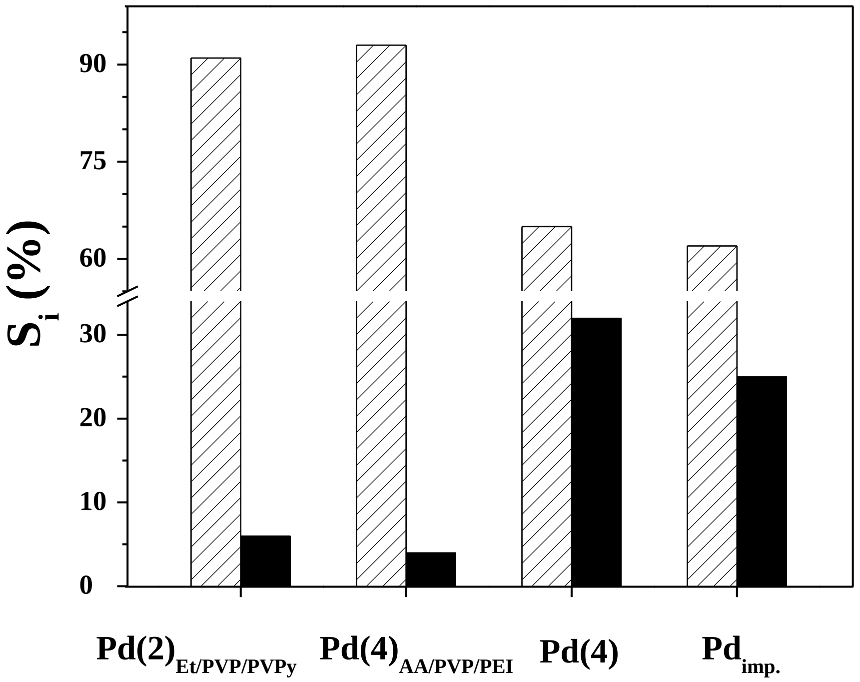

Figure 4.1.10. Variation of selectivity (S_i) to ethylene (hatched bars) and green oil (solid bars) over co-modified with PEI ($Pd(2)_{Et/PVP/PVPy}$, $Pd(4)_{AA/PVP/PEI}$ and stabilizer-free Pd NPs; *Reaction conditions*: $T = 393$ K, $P = 1$ bar, Pd/C_2H_2 molar ratio = $1.4\times10^{-6} – 8.6\times10^{-6}$ h. *Note:* balance to 100% selectivity corresponds to ethane.

In order to evaluate the catalyst stability, the reaction was carried out over a prolonged period of time (120 h). The results are presented in **Figure 4.1.11** where the activity ($X_{C_2H_2}$) and selectivity ($S_{C_2H_4}$ and $S_{green\ oil}$) are plotted as a function of time on-stream. For the best catalyst $Pd(4)_{AA/PVP/PEI}$/CNF/SMF, high selectivity ($S_{C_2H_4} \sim 93\%$) was maintained throughout this extended run with only trace amounts of undesirable green oil.

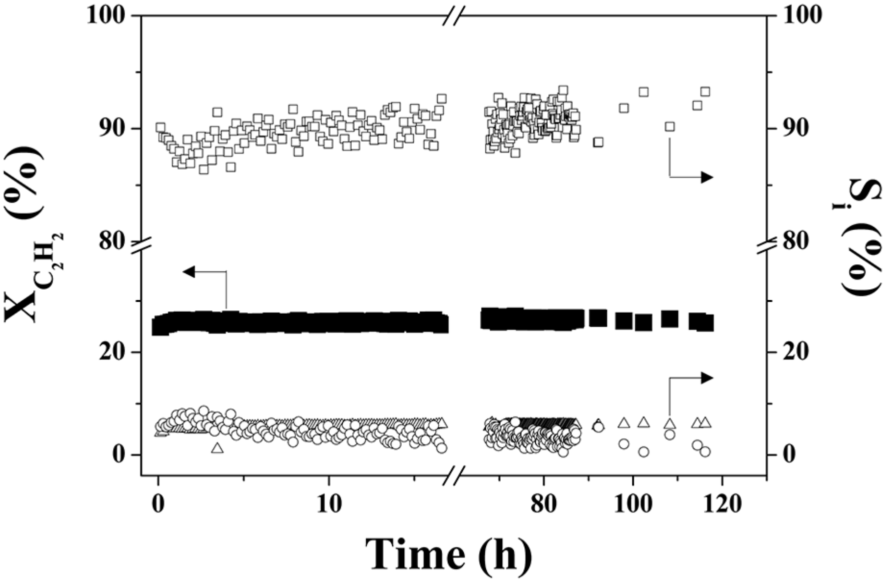

Figure 4.1.11. Variation of acetylene conversion ($X_{C_2H_2}$, solid symbols) and selectivity (S_i, open symbols) to target ethylene product ($S_{C_2H_4}$, □), green oil (○) and ethane (△) with time on-stream for Pd(4)$_{AA/PVP/PEI}$; *Reaction conditions*: *T* = 393 K, *P* = 1 bar, Pd/C_2H_2 molar ratio = 1.4×10^{-6} – 8.6×10^{-6} h.

4.1.4. Conclusions

The results presented in this study support the following conclusions:

i. Colloidal techniques with a series of reducing (HH, AA, Met, Et and But) and stabilizing (AOT, PVP and PVA) agents have been used to prepare monodispersed Pd NPs with average sizes in the range 2-10 nm as demonstrated by HRTEM. The monodispersed nanoparticles Pd with different ligand shells were deposited on a structured support (carbon nanofibers grown on sintered metal fibers, CNF/SMF) and tested in the gas phase (T = 393 K; P = 1 bar) hydrogenation of acetylene.

ii. The reducing agent used in the Pd NPs preparation did not influence the activity/selectivity in acetylene hydrogenation. In contrast, the nature of the surfactant impacts on catalytic performance with increased activity over Pd sterically (PVP and PVA) stabilized as a result of geometric and electronic effects.

iii. Catalytic performance was also affected by Pd NP size: higher specific rates for increased Pd size (from 2 → 8 nm) being insensitive to particle sizes ≥8 nm. Olefin selectivity was higher over smaller Pd NPs which can be linked to the sites isolation by carbon deposits.

iv Grafting of N-containing ligands (PVPy and PEI) onto the CNF/SMF support results in remarkable increase in selectivity to the target ethylene product (up to 93%) with only trace amounts of green oil and no detectable catalyst deactivation up to 120 h on-stream. This is explained in terms of charge-transfer induced by the grafted ligands.

v. The results of this work demonstrate that fine tailoring of colloidal Pd NPs allows tuning their catalytic response in the selective gas phase *semi*-hydrogenation of alkynes by suitable stabilizer, metal NP size optimization and ligands grafting onto the support, opening up new means for a rational catalyst design.

4.2

Colloidal Methods for Development of Ni-based Catalyst Selective in *m*-Dinitrobenzene Hydrogenation

Abstract

Monodispersed Ni NPs (from 2 to 14 nm, as confirmed by high resolution transmission electron microscopy) were prepared *via* colloidal method using poly-N-vinyl-2-pyrrolidone (PVP) as stabilizer and tested as catalysts in the *m*-dinitrobenzene multi-phase hydrogenation. Antipathetic structure sensitivity, *i.e.* a 6-fold higher turnover frequency over larger Ni NPs, has been established. The selectivity to the target *m*-nitroaniline (*m*-NAN) was size independent over Ni NPs *as per,* probably, due to the traces of PVP remaining on the Ni surface. Supporting the monodispersed (2 nm) Ni NPs on activated carbon fibers (ACF) and removing traces of PVP rendered a highly selective Ni2/ACF catalyst allowing up to 95% yield of *m*-NAN. Two-sites Langmuir-Hinshelwood kinetic model was applied to rationalize the results obtained and found to be consistent with the experimental data.

4.2.1 Introduction

Catalysts have been for a long time considered as the first examples of “nano-designed” materials since the majority of them consist of nano-sized particles (NPs) of active component supported over high-surface-area solids [84]. Very often NPs of metals (Me) are the active component responsible for the catalyst activity and selectivity [397]. This is related to the unique properties of NPs which are intermediate between those of Me atoms and Me bulk [398]. The surface structure and the electronic properties of Me NPs change strongly in the range of 1–10 nm, where electronic properties are especially altered for particles below 2 nm [399]. Therefore, the catalyst activity/selectivity may also be sensitive to the Me NPs size. This effect is known as “size-sensitivity” of catalytic reactions and is connected to the relative amount of plane, edge and vertex surface atoms which varies with the NP size [74]. The resulting variation in the surface atoms' coordination leads to an energetic inhomogeneity that is behind the structure sensitivity of hydrogenation reactions. This effect has been probed [296] and reviewed [74, 400] for a number of different reactions, where it has been rationalized on the basis of geometric and electronic factors. Advances in colloidal methods for the synthesis of Me NPs with controlled size allow nowadays an exciting opportunity of creating a catalyst “on demand” having an optimized Me NPs size.

Aromatic amines are important intermediates in the manufacture of fine chemicals [401]. Selectivity is the key issue in the reduction of polyfunctionalized arenes [345, 402]. In particular, in the hydrogenation of m-dinitrobenzene (*m*-DNB) the critical challenge is the attainment of full selectivity in terms of partial $–NO_2$ group reduction to form m-nitroaniline (*m*-NAN), a key block extensively used in the preparation of dyes and polymers [206]. There are different alternatives to overcome this challenge, like the choice of the metal [141], nanoparticle size [83, 228] or the nature of the support [148, 403]. It may be conjugated with modifications of the active sites environment such as solvents polarity [404], or the use of reaction modifiers [405]. Different metals like Pd [406], Pt [407], Ru [408] or Ni [409, 410] have been reported as an active component for the liquid phase hydrogenation of *m*-DNB. Compared to the aforementioned noble metals, Ni is inexpensive (up to 3 orders of magnitude) and has proved remarkable efficiency in a number of catalytic reductions of nitroaromatic compounds (*e.g.* nitrobenzene, [411, 412] *p*-nitrophenol [413] and nitrotoluene, nitronaphtalene, dinitroaniline [414]).

However, the size-effect for Ni-NPs has not been considered so far in the liquid phase *m*-DNB hydrogenation and therefore, the most efficient active phase in respect to the high selectivity towards the target amine could be overlooked. On the other hand, the support is known to affect the catalytic response, which can be used to fine-tune the properties of the metal active phase [415]. In order to assess solely the size effect without any influence of the carrier, the catalytic system is optimized using unsupported Ni NPs stabilized by poly-N-vinyl-2-pyrrolidone (PVP).

Along with the optimization of catalyst formulation, solvents were widely reported to have a significant effect on the rates and selectivity of catalytic hydrogenations [415]. The effect of the solvent is attributed to various factors such as their polarity, protic nature, dielectric constant and the solubility of hydrogen or the solvation of the substrate [408, 410]. A range of polar alcohols (methanol, ethanol, 1-propanol, 1-butanol, 2-hexanol) have been tested during this work as solvents.

Another issue encountered during carrying out three-phase hydrogenations is external and internal mass-transfer limitations, often responsible for a decrease of activity/selectivity. Therefore, fine powders are widely applied which minimal size is limited by separation after the reaction. Activated carbon fibers (ACF) with a filament diameter of 10–20 μm, were suggested as a suitable support for Me NPs [416]. In addition to the ease of handling, these structured supports have a high surface area allowing Me NPs stabilization within micropores.

Herein is reported the development of a Ni-based catalyst for the selective liquid phase hydrogenation of *m*-DNB to *m*-NAN. Monodispersed Ni (PVP-stabilized) NPs were prepared with the sizes between 2 to 14 nm and tested first non-supported (*as per*) to study a size-effect. The monodispersed Ni NPs were subsequently supported on ACF, where the influence of PVP on the activity and selectivity was evaluated.

4.2.2. Experimental

4.2.2.1 Materials

Nickel (II) sulfate hexahydrate (Fluka, ≥ 98.0%), polyvinylpyrrolidone (PVP, Sigma-Aldrich), ethylene glycol (Sigma-Aldrich, 99.8%), sodium hydroxide (Sigma-Aldrich, ≥ 98.0%), sodium borohydride (Sigma-Aldrich, ≥ 96.0%), tetraethylene glycol (Sigma-Aldrich, 99.0%), hydrogen peroxide (Reactolab SA, 30%), *m*-DNB, (Tokyo Chemical Industry, ≥ 99.0%) methanol (Met, Sigma-Aldrich, ≥ 99.8%), ethanol (Et, Sigma-Aldrich, 99.8%), 1-propanol (Acros Organics, 95.5%), 1-butanol (Acros Organics, 95.5%), 2-hexanol (Sigma-Aldrich, 99%) were used as received. All gases (H_2, N_2, and Ar) were of high purity (Carbagas, >99.7%).

4.2.2.2 Catalyst Preparation

a. Monodispersed Ni Nanoparticles

During the NPs formation, size can be controlled by varying the proportion of particle nucleation *vs.* growth [417] *via* the strength of the reducing agent, while the stabilizer prevents NPs agglomeration. Strong reducing agents (*e.g.* $NaBH_4$, NaOH) favor small particles through rapid nucleation and weak reducing agents (*e.g.* polyols, H_2) slow down nucleation for a particle growth dominating process. The Ni colloids of different sizes were synthesized by colloidal technique using PVP as stabilizer and a series of reducing agents. The synthesis conditions are summarized in **Table 4.2.1** and the procedure is detailed below. It is important to note that all synthesized nanoparticles were thoroughly washed to remove the PVP using a big volume (1:10) of acetone *via* decantation and re-dispersion in Et.

2 nm Ni NPs (Ni2): $NiSO_4 \cdot 6H_2O$ (0.053 g) was dissolved in ethylene glycol (100 cm^3) and PVP (0.22 g, $M = 10000$) was added. The mixture was stirred for 15 min and cooled to 273 K. The pH was adjusted to *ca.* 9 by adding NaOH (1 M, 5 cm^3) to deprotonate the reducing agent and to promote the electron transfer to the Ni cation. The solution was stirred (90 min, 413 K) and the NP colloidal suspension was purified by extraction using excess acetone (1:10) over not more than 4 h. After sedimentation of the nanocrystals, the supernatant was decanted and the remaining suspension was centrifuged. Upon removal of the solvent layer, the precipitate was redispersed in Et (15 cm^3).

4 nm Ni NPs (Ni4): $NiSO_4 \cdot 6H_2O$ (0.26 g) was dissolved in ethylene glycol (50 cm^3). To that solution PVP (2.2 g, $M = 29000$) and $NaBH_4$ (0.1 g) freshly dissolved in water (5 cm^3) were added. Particle nucleation was observed instantly and the solution was stirred during 4 h (room temperature, 500-700 rpm) up to reaction completion. The sample was purified by addition of acetone (500 cm^3) until decantation of the colloids (in which PVP is insoluble) which were redispersed in Et (15 cm^3).

11 nm Ni NPs (Ni11): $NiSO_4 \cdot 6H_2O$ (0.26 g) was dissolved in ethylene glycol (120 cm^3). PVP (2.2 g, $M = 29000$), NaOH (4 cm^3, 1 M) and hydrazine hydrate (2 cm^3, 1 M) were added. The solution was then brought to reflux for 4 h. Colloids were collected after addition of acetone (1×10^{-3} m^3) and redispersed in Et (15 cm^3).

14 nm Ni NPs (Ni14): $NiSO_4 \cdot 6H_2O$ (0.26 g) was dissolved in tetra-ethyleneglycol (120 cm^3). PVP (2.2 g, *M* = 29000) and NaOH (5 cm^3, 1 M) were added to that solution which was finally brought to reflux for 4 h. Colloids were collected after addition of acetone (1 dm^3) and redispersed in Et (15 cm^3).

Colloids	*d* (nm)	Ethylene glycol (Amount, g)	PVP 10[a] or 29[b] (Amount, g)	Base (Amount, g)
Ni2	2 ± 0.8	120	2.2[a]	NaOH, 0.2
Ni4	4 ± 0.8	50	2.2[b]	$NaBH_4$, 0.1
Ni11	11 ± 1.7	120	2.2[b]	NaOH, 0.2
Ni14	14 ± 2.1	120	2.2[b]	NaOH, 0.16; Hydrazine 0.1

Table 4.2.1. Synthesis conditions of the PVP-stabilized Ni nanoparticles.

b. Structured Supported Catalysts

The supported catalysts were prepared by deposition (*via* impregnation) of the colloidal Ni NPs on a structured support of activated carbon fibers (ACF, Kynol Europa GmbH, ~2000 m^2 g^{-1}, produced from novoloid phenolic precursor fibers by a one step process combining carbonization and chemical activation). Prior to deposition, the ACF were activated in 15% nitric acid (20 min, 363 K) to create high concentration of oxygen-containing groups on the carbon surface [115].

After deposition, Ni NPs were cleaned from PVP by UV-ozone (UVO) or thermal treatment (Δt) since both methodologies have proved effective in the removal of PVP stabilizer [357, 390]. The catalyst was placed for 4 h under an UV lamp in air (λ = 185 nm and 257 nm, where the former generates ozone upon interaction with oxygen) and afterwards was reduced in a flow reactor at 60 cm^3 min^{-1} 20% v/v H_2/N_2 at 2 K min^{-1} to 723 ± 1 K (1 h) and cooled to room temperature under N_2. PVP removal by thermal treatment involved pyrolysis in a flow of 100 cm^3 min^{-1} 20% v/v H_2/Ar at 2 K min^{-1} to 873 K (2 h). Samples were passivated at room temperature in 1% v/v O_2/Ar to prevent a strong bulk oxidation of Ni.

4.2.2.3 Catalyst Characterization

a. Unsupported Colloidal Ni Nanoparticles

Ni NPs size was determined by high resolution transmission electron microscopy (HRTEM) using a JEOL JEM-3011 unit operated using Gatan Digital Micrograph for data treatment. The specimens were prepared by Ni NPs dispersion in Et and deposited on a holey carbon/Cu grid (Agar Scientific, 300 Mesh). Up to 250 individual metal particles were counted for each catalyst and the mean diameter (d) was calculated from:

$$d=\frac{\sum_i n_i d_i}{\sum_i n_i} \qquad \textbf{(4.2.1)}$$

where n_i is the number of particles of diameter d_i.

b. Ni NPs Supported on ACF

Samples after reduction were studied by scanning transmission electron microscopy (STEM) using a FEI Tecnai Osiris microscope equipped with high brightness XFEG gun operated at 200 kV. The catalyst Ni/ACF was cut down by ultramicrotomy (Ultracut E, Reichert-Jung) to analyze the ACF cross-section. The samples were infiltrated-embedded in an EPON 812 epoxy resin and polymerized at 333 K for 24 h. Ultrathin sections (<60 nm) were obtained in a wedge configuration using a 35° angle diamond knife (Diatome).

4.2.2.4 Hydrogenation of *m*-Dinitrobenzene (*m*-DNB): Set-up and Analytics

Liquid phase hydrogenation reactions (*T* = 423 K; P_{H_2} = 6-20 bar) were carried out in a commercial batch stirred reactor (100 cm^3 stainless steel autoclave, Büchi AG, Uster, Switzerland) equipped with a pressure controlled H_2 supply system. At the beginning of each experiment, a 80 cm^3 solution of *m*-DNB ($C_{m\text{-DNB}} = 3.7 \times 10^{-3}$ mol dm^{-3}) was charged and flushed three times with N_2 under agitation. A recirculator (HAAKE B-N3) was used to stabilize the reaction temperature to within ± 1 K (*ca.* 1 h) using mineral oil (Shell Thermia; thermal conductivity = 0.45 kJ m^{-1} h^{-1} K^{-1}; specific heat = 2.4 kJ kg^{-1} K^{-1}) as the thermal medium. Hydrogen was then introduced, the system was pressurized (to 20 ± 0.2 bar, up to 11-fold excess of the stoichiometric requirements for hydrogenation to *m*-NAN) and stirring was engaged (time *t* = 0 for reaction). No measurable conversion was detected in the absence of catalyst. The initial $–NO_2$/Ni molar ratio spanned the range 28–58. A non-invasive liquid sampling system *via* a 1/8 inch stainless steel tube surrounded by two quarter turn plug valves allowed a controlled removal of aliquots (≤ 0.4 cm^3) of the reacting mixture.

Sample composition was analyzed using a Perkin-Elmer Clarus 500 chromatograph equipped with a programmed split/splitless injector and a flame ionization detector employing a Stabilwax (Cross-bond Carbowax-PEG, Restek, USA) capillary column (i.d. = 0.32 mm, length = 30 m, film thickness = 0.25 μm). Data acquisition/manipulation were performed using the TotalChrom Workstation v.6.3.2. chromatography data system and the concentration of organic species in the bulk liquid (C_i) phase were determined from the total mass balance in the reaction mixture. The conversion of *m*-DNB ($X_{m\text{-DNB}}$) is defined as:

$$X_{m\text{-DNB}}(\%) = \frac{C_{m\text{-DNB,0}} - C_{m\text{-DNB,i}}}{C_{m\text{-DNB,0}}} \times 100 \qquad \mathbf{(4.2.2)}$$

and selectivity with respect to *m*-nitroaniline ($S_{m\text{-NAN}}$) as a target product is given as:

$$S_{m-\mathrm{NAN}}(\%) = \frac{C_{m-\mathrm{NAN}}}{C_{m-\mathrm{DNB},0} - C_{m-\mathrm{DNB}}} \times 100 \tag{4.2.3}$$

Repeated reaction runs with the same batch of catalyst delivered conversion/selectivity values that were reproducible within ± 4%.

The catalyst activity was quantified in terms of the initial *m*-DNB consumption rate ($-R_{m\text{-DNB},0}$) determined from a linear regression of the temporal *m*-DNB concentration profile:

$$-R_{m\text{-DNB},0}\ (\mathrm{mol}_{m\text{-DNB}}\mathrm{mol}_{\mathrm{Ni}}^{-1}\ \mathrm{min}^{-1}) = \frac{(C_{m-\mathrm{DNB},0} - C_{m\text{-DNB}}) \cdot V}{n_{\mathrm{Ni}} \cdot t_{\mathrm{R}}} \tag{4.2.4}$$

where V is the reaction volume, n_{Ni} is the number of moles of Ni, and t_{R} the reaction time.

4.2.3. Results and Discussion

4.2.3.1 Monodispersed Ni Colloids

a. Ni Colloids Characterization

In order to confirm that the colloidal syntheses deliver the monodispersed Ni NPs, they were characterized *via* Electronic Microscopy. Representative TEM and HRSEM images **(I)** and associated Ni NPs size distributions **(II)** of Ni2 and Ni4 are shown in **Figure 4.2.1.** The results indicate spherical particle morphology, which is consistent with a thermodynamically favorable cubo-octahedral crystal shape [85]. The derived histograms show a narrow size distribution confirming the formation of monodispersed Ni colloids.

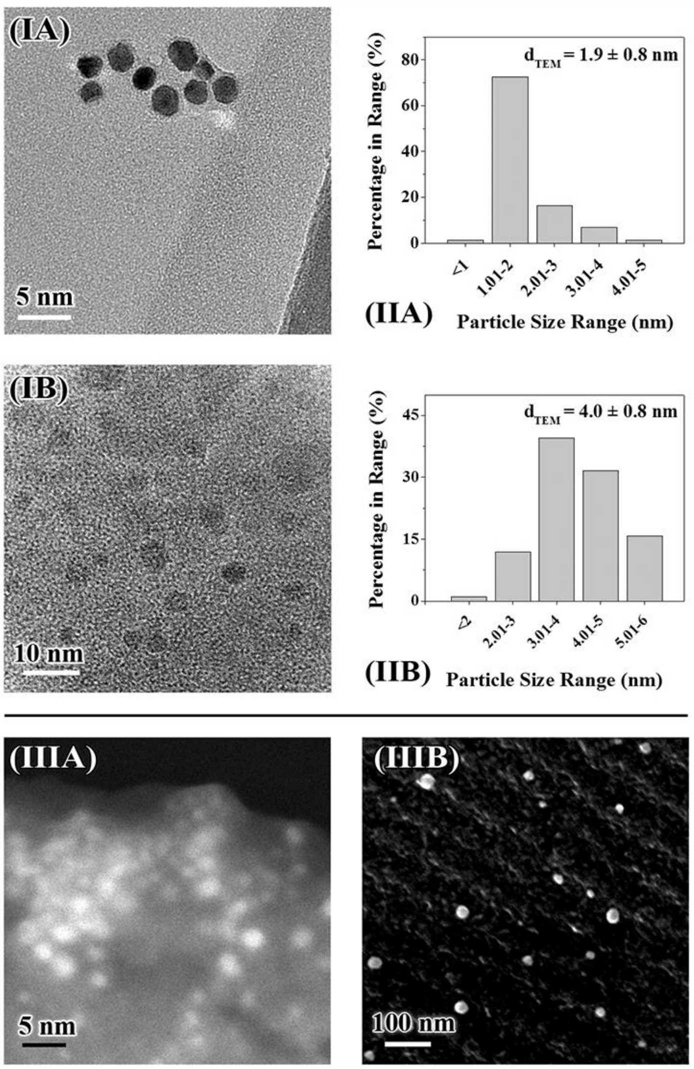

Figure 4.2.1. (I) Representative TEM images with **(II)** associated particle size distributions of PVP-stabilized nanoparticles of **(A)** Ni2 and **(B)** Ni4; **(III)** HRSEM images of Ni2 supported on ACF cleaned by **(A)** UVO or **(B)** pyrolysis.

b. Effect of the Solvent

Along with the catalyst optimization, the effect of solvent was investigated over 4 nm Ni NPs (high dispersion, while retaining a metallic character of Ni) in a series of aliphatic alcohols as reported in **Figure 4.2.2**. The activity trend shows an optimum value at 0.66 $\text{mol}_{m\text{-DNB}}\ \text{mol}^{-1}_{\text{Ni}}$

min^{-1} using 1-PrOH, while the activities measured using Met and 2-HexOH are 2- and 3-fold lower, respectively.

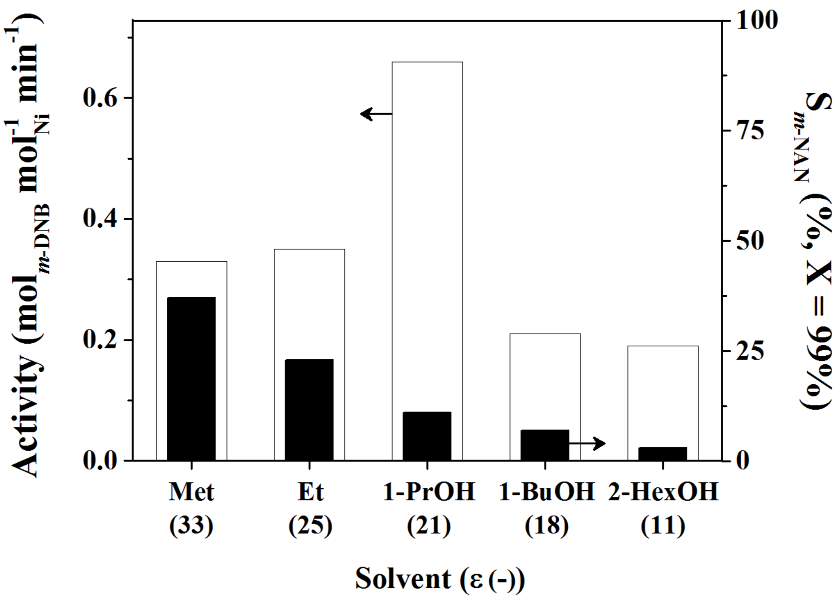

Figure 4.2.2. Variation of activity (open bars) and selectivity to *m*-NAN (solid bars) over unsupported 4 nm Ni NPs for a range of alcoholic solvents with decreasing dielectric constant. $C_{m\text{-DNB},0} = 3.7\ 10^{-3}$ mol l^{-1}, 80 cm^3 Met, $P_{H_2} = 6.1$ bar, $P_{tot} = 20$ bar, $T = 423$ K, *m*-DNB:Ni = 58.

While these observations cannot be simply correlated with solvent properties, it is worth to note that the interpretation of solvent effects in catalytic hydrogenations is often based on a combination of various parameters [418]. Berthero and co-workers [419] established solvent–catalyst interaction as the main factor influencing catalytic activity, where a strong interaction inhibits significantly the kinetics due to active site blockage. They reported higher hydrogenation rates in Et and 1-PrOH (compared to Met and toluene) due to substrate bond polarization/activation (through H-bond with the alcohol) and a subsequent low apparent activation energy. Similarly, Augustine *et. al.* [420] showed competition in the adsorption of Met and Et with H_2 on the catalytic active sites while 2-PrOH acts as a hydrogen donor. For the Pd-catalyzed acetophenone hydrogenation, Drelinkiewicza *et. al.* [421] pointed out that the catalyst activity was more influenced by the solvent polarity than H_2 solubility.

Dielectric constant is often used as a quantitative characteristic of solvent's polarity [418]. It represents well the solvent ability for charge separation and its stabilization. The selectivity trend shows a decrease following the sequence from Met ($\varepsilon = 33$) to 2-HexOH ($\varepsilon = 11$). The alcoholic solvents with high dielectric constants deliver the highest selectivity to *m*-NAN of 37 % which falls down to 3% with 2-HexOH. This effect is attributed to the higher solvation of the substrate and charges' stabilization in polar solvents such as alcohols. So, the solvents with high polarity promote the activation/polarization of the nitro group and favor its interaction with hydrogen once adsorbed on the catalyst surface [422]. Given that maximizing *m*-NAN selectivity is the critical issue in the hydrogenation of *m*-DNB, Met was the solvent of choice for the catalyst testing and optimization.

c. Structure Sensitivity

Unsupported Ni NPs of 2, 4, 11 and 14 nm (see **Table 4.2.1** for the results of TEM) were tested as catalysts for the liquid-phase hydrogenation of *m*-DNB in Met and the results are presented in **Figure 4.2.3**. The 6-fold increase of the turnover frequency (TOF) with the Ni size (**Figure 4.2.3(A)**) is consistent with an antipathetic structure sensitivity. To the best of the author's knowledge, there have been no reports demonstrating the size effect of Ni nanoparticles on liquid phase *m*-DNB hydrogenation. The size influences the TOF due to well-known electronic and geometric effects [353]. The relative ratio of the types of surface atoms (edge, vertex and plane atoms) changes substantially with varying particle size: large particles possess mainly large crystal planes with atoms of high coordination number, whereas metal atoms with low coordination numbers constitute small particles.

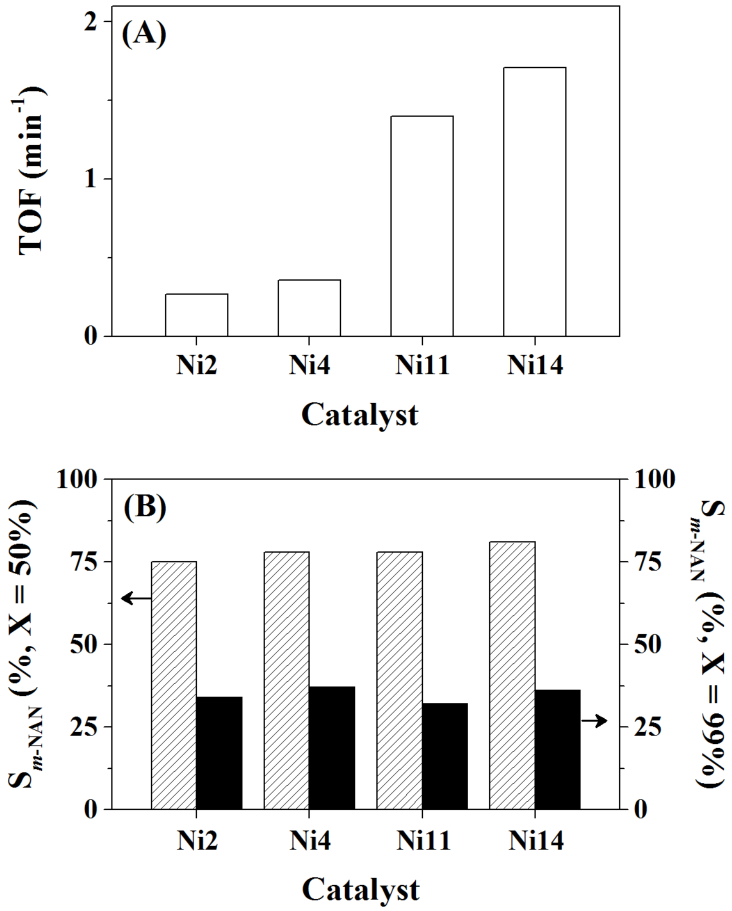

Figure 4.2.3. (A) Specific activity (TOF) and **(B)** Selectivity to *m*-NAN for unsupported Ni NPs at 50% (hatched bars) and 99% conversion (solid bars). Reaction conditions: $C_{m\text{-DNB},0} = 3.7\ 10^{-3}$ mol l^{-1}, 80 cm^3 of Met, P_{H_2} = 6.1 bar, P_{tot} = 20 bar, T = 423 K, *m*-DNB:Ni = 58.

The statistics of surface atoms [75] for non-ideal face-centered cubo-octahedron (fcc) is used herein to determine the relative amount of the different atom types on the surface for different NPs. A non-ideal model was employed and the corresponding surface atoms fractions (x_i) are reported in **Table 4.2.2**. Ni atoms with low coordination numbers, *i.e.* edge and vertex atoms, are mainly present in 2 nm NPs, whereas large particles possess mainly Ni plane atoms of higher coordination number. An increase in TOF for bigger NPs (up to 6-fold) suggests that plane Ni atoms are the active sites responsible for the *m*-DNB transformation. This is probably linked to a stronger adsorption of *m*-DNB on the plane atoms. According to the known "volcano" curve [423], an increase in the adsorption strength of aromatic compounds would result in higher activity. Indeed, the substrate adsorbs through the $-NO_2$ group, where the nitrogen holds a partial positive charge δ^+ and the plane atoms have a partial negative charge δ^-.

***d* (nm)**	***D* (%)**	**Fraction (-)**	
		Edges and vertexes – $x_{\sigma 1}$	**Planes – $x_{\sigma 2}$**
2	47.6	0.53	0.08
4	25.3	0.39	0.34
11	9.7	0.17	0.71
14	7.7	0.14	0.77

Table 4.2.2. Statistics of surface atoms for the Ni NPs used in this work.

On the contrary, the selectivity to *m*-NAN was found to be insensitive to particle size being equal to 78 ± 3% at conversion of 50% and drops to 35 ± 3% at high conversion (X = 99%, **Figure 4.2.3(B)**). This effect could be due to the influence of the PVP used as a stabilizing agent during the Ni NPs preparation. In spite of the PVP removal by thorough cleaning procedure *via* decantation and redispersion in Et (see Experimental part for details), some traces of PVP are known to remain on the metal surface [424]. These PVP traces adsorb stronger on the edges and vertexes of Ni NPs (as compared to plane atoms) since electron-rich PVP has a higher affinity to low coordinated atoms. Indeed, the partial positive charge located on NP edges and vertexes makes them a favorable anchoring point to chemisorb PVP through the free electron doublet of nitrogen or oxygen. Consequently, a low selectivity to the target product irrespective to the size of the Ni particle suggests that edge and vertex atoms are probably responsible for the reaction selectivity.

4.2.3.2 Monodispersed Ni Supported on ACF

a. Ni/ACF Characterization

In order to clean-up the PVP traces from the nickel surface, Ni NPs have been supported on ACF and treated by UV-Ozone (UVO) or pyrolysis in inert flow (see Experimental for details). The representative HRSEM image in **Figure 4.2.1(III)** provides an indication of the Ni NPs size after PVP removal, either by UVO treatment **(A)** or pyrolysis at 873 K **(B)**. The smallest (Ni2) and the biggest (Ni14) nanocrystals have been selected to provide the biggest difference in the surface atom fractions. While no significant particle growth is observed after UVO method (2.0 → 2.3 nm), Ni sintering occurs when applying thermal treatment (2.0 → 26 nm).

b. Effect of the Stabilizer Cleaning

PVP traces have a detrimental effect on selectivity. The results obtained over supported catalysts Ni/ACF are presented in **Figure 4.2.4** showing a remarkable increase in selectivity to *m*-NAN (from 35% up to 96%) upon PVP removal. Independently of the treatment type (UVO *vs.* thermal treatment), the Ni/ACF catalyst bearing the smallest (2 nm) nanoparticles were found to provide the highest selectivity. This result further suggests that low coordination Ni atoms (edges and vertexes) are responsible for the high selectivity to *m*-NAN while the plane Ni atoms contribute to the activity response. The adsorbed *m*-DNB can generate a resonance form with a positive delocalized charge in the aromatic ring, where only one $–NO_2$ is activated. As a consequence, the ring is repelled from the partially positively charged Ni atoms and adsorption occurs through the nitro group.

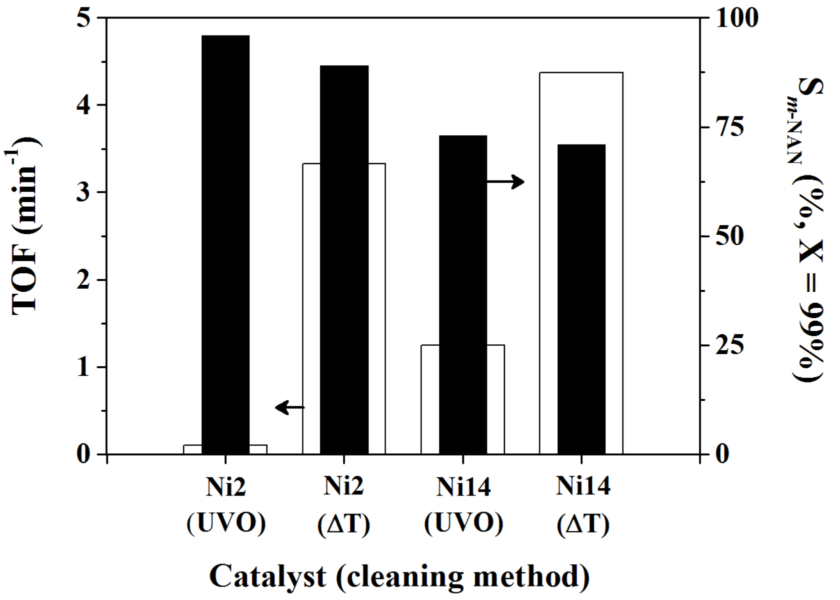

Figure 4.2.4. Variation of TOF (open bars) and selectivity to *m*-NAN (solid bars) over monodispersed (2 and 14 nm) Ni NPs/ACF treated by UV-Ozone (UVO) or pyrolysis (Δt). $C_{m\text{-DNB},0}$ = 3.7 10^{-3} mol l^{-1}, 80 cm^3 of Met, P_{H_2} = 6.1 bar, P_{tot} = 20 bar, T = 423 K, *m*-DNB:Ni = 58.

Some differences in activity/selectivity depending on the type of cleaning can be appreciated from **Figure 4.2.4**. UVO is a more suitable method as compared to thermal treatment since it delivers the smallest Ni NPS with the highest selectivity. Drop in selectivity after pyrolysis is probably due to a strong Ni NPs sintering at high temperatures [425].

The reactant and product distribution as a function of time for the (2 nm) cleaned Ni/ACF is shown on **Figure 4.2.5(A)**. *m*-DNB is converted quasi-exclusively to *m*-NAN with a zero order kinetics (linear dependence of the concentration *vs.* time) up to 75% *m*-DNB conversion with only a small production (≤ 5%) of the over-hydrogenation product, *m*-phenylenediamine (*m*-PDA). A comparison of the selectivity to *m*-NAN as a function of conversion for the unsupported PVP-stabilized Ni colloids *vs.* cleaned Ni/ACF is shown on **Figure 4.2.5(B)** (Ni2) and 5(C) (Ni14).

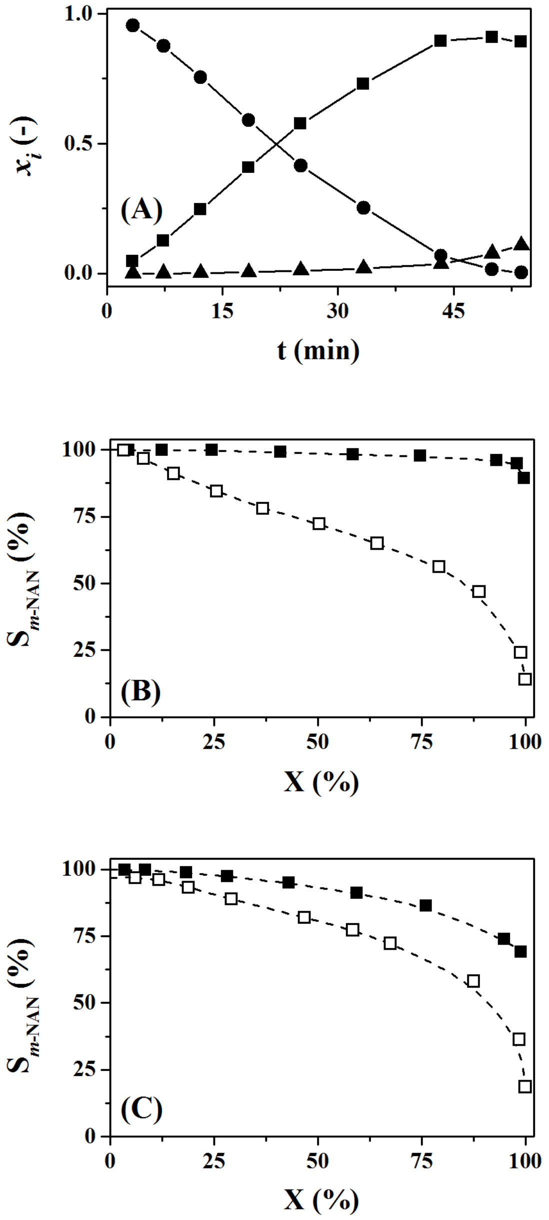

Figure 4.2.5. (A) Evolution of the molar fraction of (●) *m*-DNB, (■) *m*-NAN and (▲) *m*-PDA with time over cleaned 2 nm Ni NPs, Ni2/ACF; variation of selectivity with conversion for unsupported Ni (open symbols) and cleaned Ni NPs (solid symbols) over **(B)** Ni2/ACF and **(C)** Ni14/ACF. Reaction conditions: $C_{m\text{-DNB},0}$ = 3.7 10^{-3} mol l^{-1}, 80 cm^3 of Met, P_{H_2} = 6.1 bar, P_{tot} = 20 bar, T = 423 K, *m*-DNB:Ni = 31–68.

The highest selectivity to *m*-NAN was recorded over the Ni/ACF containing 2 nm Ni nanoparticles ($S_{m\text{-NAN}} \geq 95\%$ up to 98% conversion). In contrast, there is a continuous decrease in $S_{m\text{-NAN}}$ at high conversions for unsupported PVP-stabilized Ni colloids. This behavior suggests that the Ni surface atoms have two distinguishable active sites, denoted as (σ_1) for the plane atoms and (σ_2) for the edge and vertex atoms. The former are predominant in larger (Ni 11 and Ni 14) NPs. Consecutive/parallel reaction pathways are depicted in **Figure 4.2.6** presenting a simplified reaction scheme. In small cleaned nanoparticles both sites σ_1 and σ_2 are involved in catalysis, while only one kind of active site, (σ_1) is active in unsupported Ni NPs as the edges and vertexes are blocked by PVP. This effect could be understood supposing the preferential adsorption of PVP on low coordinated (σ_2) sites, as discussed above (see paragraph **4.2.3.1 c.**). With larger "cleaned" particles, *i.e.* Ni14/ACF sample (**Figure 4.2.5(C)**), the lower selectivity can be ascribed to the higher relative portion of plane atoms and associated (σ_1) sites if compared to the Ni2/ACF sample.

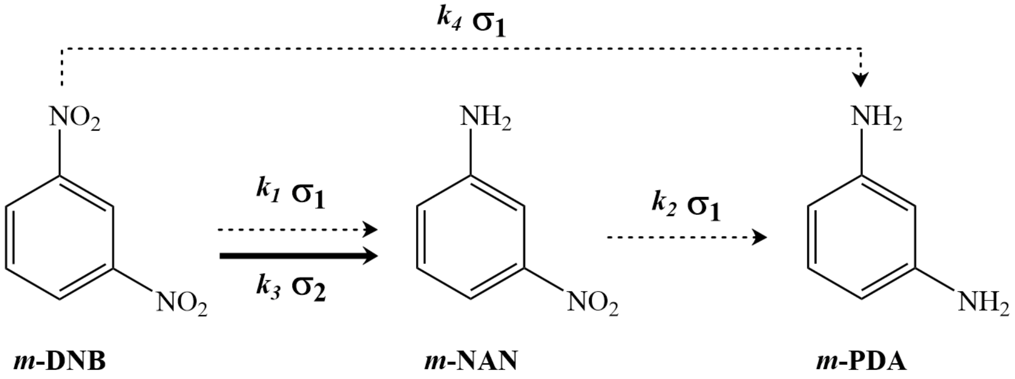

Figure 4.2.6. Reaction pathways associated with the hydrogenation of m-dinitrobenzene (*m*-DNB) to m-nitroaniline (*m*-NAN) and m-phenylenediamine (*m*-PDA). The targeted partial –NO_2 group reduction and undesired routes are represented by bold and dashed arrows, respectively.

4.2.3.3 Kinetic Modelling

The observed behavior on Ni2 and Ni14 *as per* and without PVP (Ni2/ACF and Ni14/ACF), was rationalized applying a Langmuir-Hinshelwood mechanism assuming two types of active sites, dissociative hydrogen adsorption and bimolecular reactions between the adsorbed species. The detailed derivation of the reaction rate expressions is based on a scheme presented in **Figure 4.2.6.** The rate equations are developed as follows:

m-DNB $\xrightarrow{H_2}$ m-NAN (D→N)

σ_1 sites

1	$D+\sigma_1 \xrightleftharpoons{K_{d,\sigma_1}} D\sigma_1$	$K_{D,\sigma_1}=\dfrac{\theta_{D,\sigma_1}}{C_D\cdot\theta_{\sigma_1}}$
2	$H_2+2\sigma_1 \xrightleftharpoons{K_{H_2,\sigma_1}} 2H\sigma_1$	$K_{H_2,\sigma_1}=\dfrac{\theta^2_{H,\sigma_1}}{C_{H_2}\cdot\theta^2_{\sigma_1}}$
3	$D\sigma_1+H\sigma_1 \xrightleftharpoons{K_{DH,\sigma_1}} DH\sigma_1+\sigma_1$	$K_{DH,\sigma_1}=\dfrac{\theta_{\mathrm{DH},\sigma_1}\cdot\theta_{\sigma_1}}{\theta_{\mathrm{D},\sigma_1}\cdot\theta_{H,\sigma_1}}$
4 (RDS*)	$DH\sigma_1+H\sigma_1 \xrightarrow{k_{1,\sigma_1}} N\sigma_1+\sigma_1$	$r_1=k_{1,\sigma_1}\cdot\theta_{\mathrm{DH},\sigma_1}\cdot\theta_{H,\sigma_1}$
5	$N\sigma_1 \xrightleftharpoons{K_{N,\sigma_1}} N+\sigma_1$	$K_{N,\sigma_1}=\dfrac{\theta_{N,\sigma_1}}{C_N\cdot\theta_{\sigma_1}}$

m-DNB $\xrightarrow{H_2}$ m-NAN (D→N)

σ_2 sites

1	$D+\sigma_2 \xrightleftharpoons{K_{\mathrm{D},\sigma_2}} D\sigma_2$	$K_{D,\sigma_2}=\dfrac{\theta_{D,\sigma_2}}{C_D\cdot\theta_{\sigma_2}}$
2	$H_2+2\sigma_2 \xrightleftharpoons{K_{H_2,\sigma_2}} 2H\sigma_2$	$K_{H_2,\sigma_2}=\dfrac{\theta^2_{H,\sigma_2}}{C_{H_2}\cdot\theta^2_{\sigma_2}}$
3	$D\sigma_2+H\sigma_2 \xrightleftharpoons{K_{DH,\sigma_2}} DH\sigma_2+\sigma_2$	$K_{DH,\sigma_2}=\dfrac{\theta_{\mathrm{DH},\sigma_2}\cdot\theta_{\sigma_2}}{\theta_{\mathrm{D},\sigma_2}\cdot\theta_{H,\sigma_2}}$
4 (RDS*)	$DH\sigma_2+H\sigma_2 \xrightarrow{k_{3,\sigma_2}} N\sigma_2+\sigma_2$	$r_3=k_{3,\sigma_2}\cdot\theta_{\mathrm{DH},\sigma_2}\cdot\theta_{H,\sigma_2}$
5	$N\sigma_2 \xrightleftharpoons{K_{N,\sigma_2}} N+\sigma_2$	$K_{N,\sigma_2}=\dfrac{\theta_{N,\sigma_2}}{C_N\cdot\theta_{\sigma_2}}$

m-NAN $\xrightarrow{H_2}$ *m*-PDA (N→P)

σ1 sites

1	$N + \sigma_1 \overset{K_{D,\sigma_1}}{\rightleftarrows} N\sigma_1$	$K_{N,\sigma_1} = \dfrac{\theta_{N,\sigma_1}}{C_N \cdot \theta_{\sigma_1}}$
2	$H_2 + 2\sigma_1 \overset{K_{H_2,\sigma_1}}{\rightleftarrows} 2H\sigma_1$	$K_{H_2,\sigma_1} = \dfrac{\theta^2_{H,\sigma_1}}{C_{H_2} \cdot \theta^2_{\sigma_1}}$
3	$N\sigma_1 + H\sigma_1 \overset{K_{\mathrm{N},\sigma_1}}{\rightleftarrows} NH\sigma_1 + \sigma_1$	$K_{NH,\sigma_1} = \dfrac{\theta_{NH,\sigma_1} \cdot \theta_{\sigma_1}}{\theta_{\mathrm{N},\sigma_1} \cdot \theta_{H,\sigma_1}}$
4 (RDS*)	$NH\sigma_1 + H\sigma_1 \xrightarrow{k_{2,\sigma_1}} P\sigma_1 + \sigma_1$	$r_2 = k_{2,\sigma_1} \cdot \theta_{NH,\sigma_1} \cdot \theta_{H,\sigma_1}$
5	$P\sigma_1 \overset{K_{P,\sigma_1}}{\rightleftarrows} P + \sigma_1$	$K_{P,\sigma_1} = \dfrac{\theta_{P,\sigma_1}}{C_P \cdot \theta_{\sigma_1}}$

m-DNB $\xrightarrow{2H_2}$ *m*-PDA (D→P)

σ1 sites

1	$D + \sigma_1 \overset{K_{D,\sigma_1}}{\rightleftarrows} D\sigma_1$	$K_{D,\sigma_1} = \dfrac{\theta_{D,\sigma_1}}{C_D \cdot \theta_{\sigma_1}}$
2	$H_2 + 2\sigma_1 \overset{K_{H_2,\sigma_1}}{\rightleftarrows} 2H\sigma_1$	$K_{H_2,\sigma_1} = \dfrac{\theta^2_{H,\sigma_1}}{C_{H_2} \cdot \theta^2_{\sigma_1}}$
3	$D\sigma_1 + H\sigma_1 \overset{K_{D,\sigma_1}}{\rightleftarrows} DH\sigma_1 + \sigma_1$	$K_{DH,\sigma_1} = \dfrac{\theta_{DH,\sigma_1} \cdot \theta_{\sigma_1}}{\theta_{D,\sigma_1} \cdot \theta_{H,\sigma_1}}$
4	$DH\sigma_1 + H\sigma_1 \overset{K_{DH2,\sigma_1}}{\rightleftarrows} DH2\sigma_1 + \sigma_1$	$K_{DH2,\sigma_1} = \dfrac{\theta_{DH2,\sigma_1} \cdot \theta_{\sigma_1}}{\theta_{DH,\sigma_1} \cdot \theta_{H,\sigma_1}}$
5	$DH2\sigma_1 + H\sigma_1 \overset{K_{DH3,\sigma_1}}{\rightleftarrows} DH3\sigma_1 + \sigma_1$	$K_{DH3,\sigma_1} = \dfrac{\theta_{DH3,\sigma_1} \cdot \theta_{\sigma_1}}{\theta_{DH2,\sigma_1} \cdot \theta_{H,\sigma_1}}$
6 (RDS*)	$DH3\sigma_1 + H\sigma_1 \xrightarrow{k_{4,\sigma_1}} P\sigma_1 + \sigma_1$	$r_4 = k_{4,\sigma_1} \cdot \theta_{DH3,\sigma_1} \cdot \theta_{H,\sigma_1}$
7	$P\sigma_1 \overset{K_{P,\sigma_1}}{\rightleftarrows} P + \sigma_1$	$K_{P,\sigma_1} = \dfrac{\theta_{P,\sigma_1}}{C_P \cdot \theta_{\sigma_1}}$

*RDS: Rate Determining Step

A surface balance of active sites gives coverage of vacancies for the two types of active sites. The coverage of the intermediate species was neglected:

$$1 = \theta_{\sigma_1} + \theta_{D,\sigma_1} + \theta_{N,\sigma_1} + \theta_{P,\sigma_1} + \theta_{H_2,\sigma_1} \tag{4.2.5}$$

$$1 = \theta_{\sigma_2} + \theta_{D,\sigma_2} + \theta_{N,\sigma_2} + \theta_{P,\sigma_2} + \theta_{H_2,\sigma_2} \tag{4.2.6}$$

Coverages are expressed in terms of adsorption constants and bulk concentrations:

$$\theta_{\sigma_1} = \frac{1}{1 + K_{D,\sigma_1} C_D + K_{N,\sigma_1} C_N + K_{P,\sigma_1} C_P + \sqrt{K_{H_2,\sigma_1} C_{H_2}}} \quad \textbf{(4.2.7)}$$

$$\theta_{\sigma_2} = \frac{1}{1 + K_{D,\sigma_2} C_D + K_{N,\sigma_2} C_N + K_{P,\sigma_2} C_P + \sqrt{K_{H_2,\sigma_2} C_{H_2}}} \quad \textbf{(4.2.8)}$$

The reaction rate expressions can be developed for the four paths of the reaction:

$$r_1 = \frac{k_{1,\sigma_1} K_{\mathrm{DH},\sigma_1} K_{D,\sigma_1} C_D K_{H_2,\sigma_1} C_{H_2}}{\left(1 + K_{D,\sigma_1} C_D + K_{N,\sigma_1} C_N + K_{P,\sigma_1} C_P + \sqrt{K_{H_2,\sigma_1} C_{H_2}}\right)^2} \quad \textbf{(4.2.9)}$$

$$r_3 = \frac{k_{3,\sigma_2} K_{\mathrm{DH},\sigma_2} K_{D,\sigma_2} C_D K_{H_2,\sigma_2} C_{H_2}}{\left(1 + K_{D,\sigma_2} C_D + K_{N,\sigma_2} C_N + K_{P,\sigma_2} C_P + \sqrt{K_{H_2,\sigma_2} C_{H_2}}\right)^2} \quad \textbf{(4.2.10)}$$

$$r_2 = \frac{k_{2,\sigma_1} K_{NH,\sigma_1} K_{N,\sigma_1} C_N K_{H_2,\sigma_1} C_{H_2}}{\left(1 + K_{D,\sigma_1} C_D + K_{N,\sigma_1} C_N + K_{P,\sigma_1} C_P + \sqrt{K_{H_2,\sigma_1} C_{H_2}}\right)^2} \quad \textbf{(4.2.11)}$$

$$r_4 = \frac{k_{4,\sigma_1} K_{D,\sigma_1} K_{DH,\sigma_1} K_{DH2,\sigma_1} K_{DH3,\sigma_1} C_D K_{H_2,\sigma_1}^2 C_{H_2}^2}{\left(1 + K_{D,\sigma_1} C_D + K_{N,\sigma_1} C_N + K_{P,\sigma_1} C_P + \sqrt{K_{H_2,\sigma_1} C_{H_2}}\right)^2} \quad \textbf{(4.2.12)}$$

Subscripts D, N and P refer to *m*-DNB, *m*-NAN and *m*-PDA, respectively, while DH, DH2, DH3 and NH correspond to the reaction intermediates. The rate equations can be simplified by considering the concentration of H_2 constant (large excess), by neglecting the coverage of *m*-PDA and by grouping the constants of intermediate compounds in the numerator.

This results in the following simplified rate expressions:

$$r_1 = \frac{k'_{1,\sigma_1} K_{D,\sigma_1} C_D}{\left(1 + K_{D,\sigma_1} C_D + K_{N,\sigma_1} C_N\right)^2} \quad \textbf{(4.2.13)} \qquad r_2 = \frac{k'_{2,\sigma_1} K_{N,\sigma_1} C_N}{\left(1 + K_{D,\sigma_1} C_D + K_{N,\sigma_1} C_N\right)^2} \quad \textbf{(4.2.14)}$$

$$r_3 = \frac{k'_{3,\sigma_2} K_{D,\sigma_2} C_D}{\left(1 + K_{D,\sigma_2} C_D + K_{N,\sigma_2} C_N\right)^2} \quad \textbf{(4.2.15)} \qquad r_4 = \frac{k'_{4,\sigma_1} K_{D,\sigma_1} C_D}{\left(1 + K_{D,\sigma_1} C_D + K_{N,\sigma_1} C_N\right)^2} \quad \textbf{(4.2.16)}$$

The mass balance for *m*-DNB, *m*-NAN and *m*-PDA are given by:

$$\frac{dC_D}{dt} = -r_1 - r_3 - r_4 \quad \textbf{(4.2.17)} \qquad \frac{dC_N}{dt} = r_1 + r_3 - r_2 \quad \textbf{(4.2.18)} \qquad \frac{dC_P}{dt} = r_2 + r_4 \quad \textbf{(4.2.19)}$$

The parallel *m*-DNB → *m*-PDA path was taken into consideration for Ni14, as a small amount of over-hydrogenation product occurs already at low conversion (<5%). Therefore, Equation **(4.2.12)** and r_4 contribution in the mass balance were considered for larger NPs. **Equations 4.2.13-4.2.16** were solved simultaneously using Berkeley Madonna software v.8.3.18 with Runge-Kutta's method for differential equations.

A good correlation between the model and experimental values has been obtained for all the four samples (see **Figure 4.2.7**). It is worth to note that all samples demonstrated a short (≤ 10% of the total reaction time) induction period characterized by a slower temporal decrease of the *m*-DNB concentration. It was proposed elsewhere that such induction period may be due to an activation of the catalyst in the reaction mixtures [426] or attributed to surface restructuring [427] due to the adsorption of the substrate. The catalyst activation is more likely to occur when H_2 is added to the reaction mixture due to reduction of partially passivated surface Ni layer. The induction periods were consequently not used for the kinetic curve simulations.

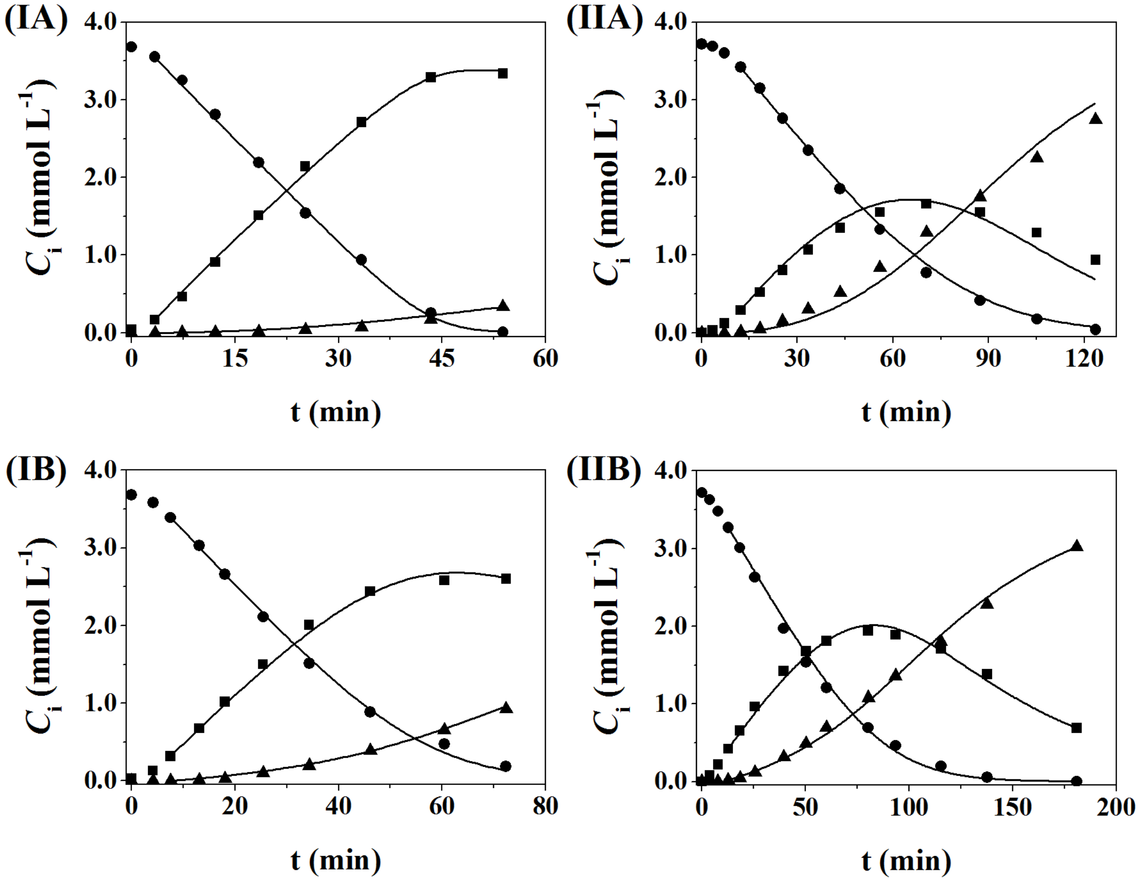

Figure 4.2.7. Experimental (●) *m*-DNB, (■) *m*-NAN and (▲) *m*-PDA and modelled (lines) concentration *vs.* time for **(I)** supported and **(II)** unsupported **(A)** Ni2 and **(B)** Ni 14 catalysts. Reaction conditions: $C_{m\text{-DNB},0}$ = 3.7 10^{-3} mol l^{-1}, 80 cm^3 of Met, P_{H_2} = 6.1 bar, P_{tot} = 20 bar, T = 423 K, *m*-DNB:Ni = 31–68.

The corresponding adsorption and kinetic constants obtained are summarized in **Table 4.2.3**. Similar values were fixed for the individual adsorption constants which are slightly higher (<2-fold) for cleaned Ni if compared to Ni colloids. As a result of adsorption through the positively charged nitrogen in the $–NO_2$ group, *m*-DNB is strongly (by two orders of magnitude) adsorbed on plane atoms (σ_1 sites) as compared to the adsorption on edge and vertex atoms (σ_2 sites). By the same logic, the partially reduced *m*-NAN exhibit 10-fold higher adsorption constant

($K_{N,\sigma 1}$) in comparison with *m*-DNB ($K_{D,\sigma 2}$). For PVP-free Ni NPs in Ni/ACF samples, the kinetic constant k_3 related to the *m*-DNB to *m*-NAN hydrogenation step on σ_2 sites is significantly higher (5- to 10-fold) than k_3 for their unsupported counterparts. It means that with unsupported Ni, the first hydrogenation step occurs essentially on σ_1 sites, where σ_2 sites play no genuine role at all. This is in good agreement with the previous assumptions (see Paragraph **4.2.3.2 b.**). High k_3/k_1 ratio and k_3/k_2 ratios, demonstrating the essential role of σ_2 sites in the first hydrogenation step with minimized over-hydrogenation accounts for the high selectivity delivered by cleaned Ni2 NPs of Ni2/ACF catalyst.

Catalyst	**Adsorption constants**			**Kinetic constants**			
	$K_{D,\sigma 1}$	$K_{D,\sigma 2}$	$K_{N,\sigma 1}$	k_1	k_2	k_3	k_4
	($\mathrm{l\ mol^{-1}}$)			($\mathrm{mmol}_{m\text{-DNB}}\ \mathrm{mol_{Ni}^{-1}}\ \mathrm{min^{-1}}$)			
Ni2	330 ± 30	4.0	43 ± 1	0.21	0.86	0.04	-
Ni14				0.15	0.40	0.05	0.03
Ni2/ACF	550 ± 50	5.9 ± 1	73 ± 3	0.37	0.12	0.75	-
Ni14/ACF				0.26	0.20	0.28	0.02

Table 4.2.3. Adsorption and kinetic constants obtained from kinetics modelling.

4.2.4 Conclusions

The results can be summarized as follows:

1. Monodispersed Ni NPs with a mean diameter between 2-14 nm were prepared *via* colloidal technique using PVP as stabilizing agent, washed from PVP and tested non-supported to study a size effect during the catalytic *semi*-hydrogenation of *m*-DNB to *m*-NAN. Colloidal Ni NPs *as per* were found to promote the formation of the over-hydrogenation product (*m*-PDA) especially at high conversion of *m*-DNB. This effect was attributed to preferential adsorption of the traces of PVP on the edge and vertex atoms responsible for the selective transformation of *m*-DNB to *m*-NAN.
2. The removal of PVP traces from Ni NPs surface *via* UV-Ozone treatment of the supported Ni/ACF samples resulted in drastic increase of selectivity to *m*-NAN at close to full conversion. The highest performance was obtained over the smallest supported 2 nm NPs (Ni2/ACF) allowing up to 96% yield of *m*-NAN.
3. Two-sites Langmuir-Hinshelwood kinetic model was applied to rationalize the results obtained and found to be consistent with the experimental kinetic data.

Chapter 5

General conclusions and Outlook

5.1 Achieved Results

The main objective of this work was to design novel catalytic formulations for industrially relevant reactions, to wit, the selective partial hydrogenation of poly-substituted nitroaromatic compounds and alkynes. To achieve this goal, a rational approach of the catalyst design was applied at different scales, from the active site to the support level.

This work focused on two different catalytic systems, starting with bulk molybdenum nitrides as an active material suitable for the $–NO_2 \rightarrow –NH_2$ reduction. A temperature programmed treatment of MoO_3 in N_2/H_2 allowed to prepare Mo-nitrides with a precise control of the crystallographic structure, nitrogen content and surface area. Subsequently, passivation by a superficial oxide layer was an effective way to prevent destructive bulk oxidation. TPD measurements revealed a significant quantity of hydrogen (0.7 μmol m^{-2}) associated with activated β-Mo_2N, which produced exclusively *p*-chloroaniline (*p*-CAN) in the batch liquid phase hydrogenation of *p*-chloronitrobenzene (*p*-CNB). In contrast, Pd/Al_2O_3 was non-selective (78% selectivity to *p*-CAN) and generated combined hydrodechlorination/hydrogenation products. By applying the Hammett relationship to the hydrogenation of a series of *para*-substituted nitroarenes, it was shown that the reaction proceeded *via* a nucleophilic mechanism where the presence of electron withdrawing substituents served to increase the reaction rate. In comparison, γ-Mo_2N showed a lower specific (per unit area) H_2 uptake as compared to β-Mo_2N, which translated into lower (approximatively 2-fold) specific hydrogenation rates. However, no variation of the specific rate was observed within γ-Mo_2N samples having different specific surface areas demonstrating that, the intrinsic activity is independent of surface area for a given crystallographic phase.

XPS measurements allowed to conclude that a greater number of nitrogen deficient sites were responsible for the higher H_2 uptake ability of β-Mo_2N. Bearing this in mind, the degree of nitridation was controlled during the catalyst preparation yielding in samples with varying Mo/N ratios. Nitrobenzene hydrogenation rate was increasing together with N content as a result of the facilitated heterolytic dissociation of H_2 on Mo-N pairs, in agreement with the mechanism of hydrogen activation proposed in the literature (see **2.1.2**). On contrary, higher N contents did not favor benzaldehyde to toluene hydrogenolysis.

In addition, low levels of supported gold has proved to further increase Mo-nitride efficiency. Au/β-Mo_2N exhibited increased hydrogenation rate (by a factor up to 4) with *p*-CAN as the sole product in both batch liquid and continuous gas phase hydrogenation of *p*-CNB, a result which was retained over consecutive runs. Furthermore, Au/Mo_2N exhibited a greater (2-fold) activity relative to a benchmark Au/Al_2O_3, demonstrating a cooperative effect of Au and Mo_2N. These findings have established the requirements for the design of Mo-nitrides catalysts suitable for the clean production of aromatic anilines.

On a different level, structured catalysts were subsequently designed using colloidal methods to tailor an active phase selective for the $C\equiv C \rightarrow C=C$ as well as $-NO_2$ group reduction. The potential of tailoring surface electronic/structural properties in Pd NPs by means of using different protective/modifying agents was demonstrated using acetylene *semi*-hydrogenation as a model reaction. This, it was established that modifications in the nature of the reducing agent do not affect significantly in catalytic response while steric (*vs.* electronic) stabilizers and larger particles were more efficient for ethylene production. Polyvinylpyrrolidone stabilized Pd (4 nm) supported on structured sintered metal fibers coated by polyvinylpyridine modified carbon nanofibers was shown to be an optimum formulation where the catalyst shows high selectivity (93%) and stability with time-on-stream. The promoting effect of selected appropriate protective and modifying agents was found to arise from two main factors, namely geometric and electronic effects induced by steric stabilizer and charge-transfer engendered by the N-containing ligands grafted on the carbonaceous support.

The development of another structured catalyst was performed for the selective m-dinitrobenzene hydrogenation, where PVP-stabilized Ni nanocolloids were optimized in terms of activity and selectivity. The TOF was found to rise with the Ni particle size, as a result of the increased number of plane atoms associated to stronger adsorption of the substrate. Colloidal Ni NPs promoted the reduction of both $–NO_2$ functionalities which was ascribed to the preferential adsorption of PVP on selective edge and vertex atoms. Once deposited on activated carbon fibers and cleaned from PVP traces by UV-Ozone treatment, Ni NPs delivered significantly increased selectivity to the partially reduced m-nitroaniline. The distinct nature of the plane and edge/vertex atoms was confirmed a kinetic modeling based on a Langmuir-Hinshelwood mechanism.

Depending on the specific reaction, the active phase can be optimized in terms of structural/electronic properties and can be tuned even further with the use of additives. N-containing ligand shell was found to confer enhanced selectivity to the tested supported Pd catalysts whereas the absence of stabilization agents translated in prominent increase of selectivity.

5.2 Further Developments

With regard to the Mo-nitrides preparation, it has been proven that the crystal phase and composition can be precisely controlled. To establish the formation mechanism involved in the preparation of different allotropic forms, the reaction mechanism and the influence of critical reaction parameters, *e.g.* heating ramp, final isothermal hold time, relative v/v N_2/H_2 and gas hourly space velocity need to be systematically studied. This work is under way and resulted in a comprehensive reaction diagram with the formation of (i) pure phases, (ii) mixtures of crystallographic phases and (iii) metallic Mo^0 in the nitride. We must now account for the disparate reactional pathways and identify the origin of the distinct catalytic response observed over the different nitride forms.

The preparation of Mo_2N with controlled structures showed a clear potential for the selective hydrogenation of substituted nitroarenes. Mo-nitrides exhibit a very high selectivity to the corresponding animes, are simple to prepare and do not suffer from noticeable deactivation. Therefore, an extension of the catalytic applications should be carried out. To date, only one study reports [176] the use of γ-Mo_2N for alkynes hydrogenation. This is the topic of an ongoing study where β- and γ-Mo_2N have been tested in the acetylene and phenylacetylene hydrogenation. The latter showed higher catalytic performance and generated very low amounts (3%) of oligomers. Doping the γ-nitride with traces (0.1% wt.) of Pd incorporated before and after the nitridation process served to increase the hydrogenation rates, however at the expense of selectivity and oligomers formation.

In addition, preliminary tests have also shown the possibility of coating SMF with a Mo_2N film by means of chemical vapor deposition methods. Whereas the use of structured Mo-nitride catalysts could be limited in terms of activity on grounds of the maximum loading on the support, the incorporation of low level of dopants (like Pd, Au, Ni, Cu) could help to address this problem.

The incorporation of traces of transition metals has been shown to exhibit pronounced effects upon the morphology of beta-phase molybdenum nitride [180] with various proportions of surface atoms of distinct coordination. It was shown [428] that the addition of a second metal component into Mo_2N increased the concentration of (111) crystal planes as compared to (200) planes, the former being more active for hydrogen adsorption [50]. In this respect, the effect of the crystal shape could be studied in the continuation of the rational catalyst design approach undertaken at the nanoscale level.

Ultimately, an exciting extension of this work on interstitial alloys would be the preparation and catalytic testing of molybdenum carbides for which the selective hydrogenation capacities were reported through various reviews [4, 11] and studies [429, 430].

Regarding the preparation of structured Ni catalysts, the removal of the stabilization agent was beneficial to achieve high selectivity. In accordance with this finding, "naked" Ni NPs were prepared by means of ion-exchange on a functionalized ACF support. Mild and strong acid treatments of the ACF resulted in the formation of quasi-monodispersed small (3 nm) and larger (10 nm) Ni NPs, respectively, and high *m*-nitroaniline yields (97%) were achieved. On the contrary, Ni/Al_2O_3 is not selective (with similar metal dispersion). To assess the possible reasons of the high selectivity (lower Ni oxidation state due to carbon), it would be necessary to characterize the active phase by means of in-situ techniques.

References

[1] R.A. Sheldon, I. Arends, U. Hanefeld, *Green Chemistry and Catalysis*, Willey-VCH, Weinheim, Germany, 2007.

[2] L. Kiwi-Minsker, M. Crespo-Quesada, *Chimia* 65 (2011) 699-703.

[3] U.S. Ozkan, *Design of Heterogeneous Catalysts*, Wiley-VCH, 2009.

[4] E. Furimsky, *Appl Catal A-Gen* 240 (2003) 1-28.

[5] S.T. Oyama, G.L. Faller, *"Catalysis, Specialist Periodical Reports"*, in: *Catalysis, Specialist Periodical Reports*, 1981, pp. 333.

[6] R.B. Levy, M. Boudart, *Science* 181 (1973) 547-549.

[7] J.G. Chen, *Chem Rev* 96 (1996) 1477-1498.

[8] G.S. Ranhotra, A.T. Bell, J.A. Reimer, *J Catal* 108 (1987) 40-49.

[9] J. Witte, in: *"ORR Catalysis with Pt-based CSNPs"*, Google Sites, URL: https://sites.google.com/site/orrcatalysiswithptbasedcsnps/home/d-band-theory, 2014.

[10] B. Hammer, J.K. Norskov, *Nature* 376 (1995) 238-240.

[11] S.T. Oyama, *The Chemistry of Transition Metal Carbides and Nitrides*, Blackie Academic, Glasgow, 1996.

[12] S.W. Gong, H.K. Chen, W. Li, B.Q. Li, *Energ Fuel* 20 (2006) 1372-1376.

[13] S. Gong, H. Chen, W. Li, B. Li, *Appl Catal A-Gen* 279 (2005) 257-261.

[14] M. Nagai, Y. Goto, A. Miyata, M. Kiyoshi, K. Hada, K. Oshikawa, S. Omi, *J Catal* 182 (1999) 292-301.

[15] H.J. Lee, J.-G. Choi, C.W. Colling, M.S. Mudholkar, L.T. Thompson, *Appl Surf Sci* 89 (1995) 121-130.

[16] K. Inumaru, K. Baba, S. Yamanaka, *Chem Mater* 17 (2005) 5935-5940.

[17] X.S. Li, K.J. Zhang, Q. Xin, C.X. Ji, Y.F. Miao, L. Wang, *React Kinet Catal L* 57 (1996) 177-182.

[18] M. Nagai, Y. Goto, O. Uchino, S. Omi, *Catal Today* 43 (1998) 249-259.

[19] C.W. Colling, J.-G. Choi, L.T. Thompson, *J Catal* 160 (1996) 35-42.

[20] J.G. Choi, H.J. Lee, L.T. Thompson, *Appl Surf Sci* 78 (1994) 299-307.

[21] M. Breysse, E. Furimsky, S. Kasztelan, M. Lacroix, G. Perot, *Catal Rev Sci Eng* 44 (2002) 651-735.

[22] G.W. Haddix, J.A. Reimer, A.T. Bell, *J Catal* 108 (1987) 50-54.

[23] C.W. Colling, L.T. Thompson, *J Catal* 146 (1994) 193-203.

[24] X.S. Li, Y.X. Chen, Y.J. Zhang, C.X. Ji, Q. Xin, *React Kinet Catal L* 58 (1996) 391-396.

[25] J. Chaudhuri, L. Nyakiti, R. Lee, Y. Ma, P. Li, Q.L. Cui, L.H. Shen, *Mater Lett* 61 (2007) 4763-4765.

[26] R. Watanabe, I. Watanabe, Y. Yazaki, N. Igarashi, K. Toyota, Noto, *J Mater Sci Lett* 5 (1986) 255-256.

[27] P.J. Cai, Z.H. Yang, C.Y. Wang, Y.L. Gu, Y.T. Qian, *Chem Lett* 34 (2005) 1360-1361.

[28] J. Ma, Y. Du, *J Alloy Compd* 463 (2008) 196-199.

[29] A. Gomathi, A. Sundaresan, C.N.R. Rao, *J Solid State Chem* 180 (2007) 291-295.

[30] B. Mazumder, A. Hector, *Top Catal* 52 (2009) 1472-1481.

[31] P. Afanasiev, *Inorg Chem* 41 (2002) 5317-5319.

[32] S. Chouzier, P. Afanasiev, M. Vrinat, T. Cseri, M. Roy-Auberger, *J Solid State Chem* 179 (2006) 3314-3323.

[33] M. Nagai, *Appl Catal A-Gen* 322 (2007) 178-190.

[34] G.S. Ranhotra, G.W. Haddix, A.T. Bell, J.A. Reimer, *J Catal* 108 (1987) 24-39.

[35] S. Li, J. Sung Lee, T. Hyeon, K.S. Suslick, *Appl Catal A-Gen* 184 (1999) 1-9.

[36] E.J. Markel, S.E. Burdick, M.E.L. II, K.L. Roberts, *J Catal* 182 (1999) 136-147.

[37] K. Hada, J. Tanabe, S. Omi, M. Nagai, *J Catal* 207 (2002) 10-22.

[38] D. Mckay, J.S.J. Hargreaves, J.L. Rico, J.L. Rivera, X.L. Sun, *J Solid State Chem* 181 (2008) 325-333.

[39] A.G. Cairns, J.G. Gallagher, J.S.J. Hargreaves, D. Mckay, E. Morrison, J.L. Rico, K. Wilson, *J Alloy Compd* 479 (2009) 851-854.

[40] K.L. Roberts, E.J. Markel, *J Phys Chem* 98 (1994) 4083-4086.

[41] R.S. Wise, E.J. Markel, *J Catal* 145 (1994) 344-355.

[42] L.T. Thompson, C.W. Colling, D. Choi, B.G. Demczyk, J.G. Choi, *Surface and Catalytic Properties of Molybdenum Nitrides*, in: F.S. L. Guczi, T. P (Eds.), *Stud Surf Sci Catal*, Elsevier, 1993, pp. 941-954.

[43] L. Volpe, M. Boudart, *J Solid State Chem* 59 (1985) 332-347.

[44] R.N. Panda, S. Kaskel, *J Mater Sci* 41 (2006) 2465-2470.

[45] T. Matsuda, Y. Hirata, H. Itoh, H. Sakagami, N. Takahashi, *Micropor Mesopor Mat* 42 (2001) 337-344.

[46] E. Lalik, W.I.F. David, P. Barnes, J.F.C. Turner, *J Phys Chem B* 105 (2001) 9153-9156.

[47] J. Słoczyński, *J Solid State Chem* 118 (1995) 84-92.

[48] F. Cardenas-Lizana, S. Gomez-Quero, N. Perret, L. Kiwi-Minsker, M.A. Keane, *Catal Sci Technol* 1 (2011) 794-801.

[49] J.G. Choi, R.L. Curl, L.T. Thompson, *J Catal* 146 (1994) 218-227.

[50] Y.-J. Zhang, Q. Xin, I. Rodriguez-Ramos, A. Guerrero-Ruiz, *Appl Catal A: Gen* 180 (1999) 237-245.

[51] L. Volpe, M. Boudart, *J Phys Chem-Us* 90 (1986) 4874-4877.

[52] M.K. Neylon, S. Choi, H. Kwon, K.E. Curry, L.T. Thompson, *Appl Catal A-Gen* 183 (1999) 253-263.

[53] G.M. Dolce, P.E. Savage, L.T. Thompson, *Energ Fuel* 11 (1997) 668-675.

[54] J. Trawczyński, *Catal Today* 65 (2001) 343-348.

[55] S. Jujjuri, F. Cárdenas-Lizana, M. Keane, *J Mater Sci* 49 (2014) 5406-5417.

[56] Y. Li, Y. Fan, J. He, B. Xu, H. Yang, J. Miao, Y. Chen, *Chem Eng J* 99 (2004) 213-218.

[57] C. Pan, G. Chen, W. Shen, H. Xu, 10 (2009) 1718-1721.

[58] A. Guerrero-Ruiz, Y. Zhang, B. Bachiller-Baeza, I. Rodriguez-Ramos, *Catal Lett* 55 (1998) 165-168.

[59] A. Guerrero-Ruiz, Q. Xin, Y.J. Zhang, A. Maroto-Valiente, I. Rodriguez-Ramos, *Langmuir* 15 (1999) 4927-4929.

[60] J.G. Choi, D. Choi, L.T. Thompson, *Appl Surf Sci* 108 (1997) 103-111.

[61] H.-M. Wang, X.-Y. Du, M.-H. Zhang, W. Li, K.-Y. Tao, *Catal Today* 131 (2008) 156-161.

[62] D. Mckay, J.S.J. Hargreaves, R.F. Howe, *Catal Lett* 112 (2006) 109-113.

[63] P.F. Vogt, J.J. Gerulis, *Ullmann's Encyclopedia of Industrial Chemistry. "Aromatic Amines"*, Wiley-VCH Verlag GmbH & Co. KGaA, Weinheim, 2005.

[64] R.A. Sheldon, H.v. Bekkum, *Fine Chemicals through Heterogeneous Catalysis."Aromatic Nitro Compounds"*, Wiley-VCH, Weinheim (Germany), 2001.

[65] P.F. Luo, K.L. Xu, R. Zhang, L. Huang, J. Wang, W.H. Xing, J. Huang, *Catal Sci Technol* 2 (2012) 301-304.

[66] B. Coq, A. Tijani, R. Dutartre, F. Figuéras, *J Mol Catal* 79 (1993) 253-264.

[67] X.X. Han, R.X. Zhou, G.H. Lai, B.H. Yue, X.M. Zheng, *J Mol Catal a-Chem* 209 (2004) 83-87.

[68] B. Coq, A. Tijani, F. Figueras, *J Mol Catal* 68 (1991) 331-345.

[69] J. Xiong, J. Chen, J. Zhang, *Catal Comm* 8 (2007) 345-350.

[70] X. Han, R. Zhou, X.M. Zheng, H. Jiang, *J Mol Catal a-Chem* 193 (2003) 103-108.

[71] B. Pawelec, A.M. Venezia, V. La Parola, E. Cano-Serrano, J.M. Campos-Martin, J.L.G. Fierro, *Appl Surf Sci* 242 (2005) 380-391.

[72] W. Unterberger, B. Jenewein, B. Klötzer, S. Penner, W. Reichl, G. Rupprechter, D. Wang, D. Wang, R. Schlögl, K. Hayek, *React Kinet Catal Lett* 87 (2006) 215-234.

[73] G.C. Bond, *Chem Soc Rev* 20 (1991) 441-475.

[74] N. Semagina, L. Kiwi-Minsker, *Catal Rev-Sci Eng* 51 (2009) 147-217.

[75] R. Van Hardeveld, F. Hartog, *Surf Sci* 15 (1969) 189-230.

[76] A. Borodziński, *Catal Lett* 71 (2001) 169-175.

[77] N. Semagina, L. Kiwi-Minsker, *Catal Lett* 127 (2009) 334-338.

[78] N. Semagina, A. Renken, L. Kiwi-Minsker, *J Phys Chem C* 111 (2007) 13933-13937.

[79] M. Crespo-Quesada, A. Yarulin, M. Jin, Y. Xia, L. Kiwi-Minsker, *JACS* 133 (2011) 12787-12794.

[80] M.M. Telkar, C.V. Rode, R.V. Chaudhari, S.S. Joshi, A.M. Nalawade, *Appl Catal A-Gen* 273 (2004) 11-19.

[81] P. Tribolet, L. Kiwi-Minsker, *Catal Today* 105 (2005) 337-343.

[82] K. Shimizu, Y. Miyamoto, T. Kawasaki, T. Tanji, Y. Tai, A. Satsuma, *J Phys Chem C* 113 (2009) 17803-17810.

[83] K. Shimizu, Y. Miyamoto, A. Satsuma, *J Catal* 270 (2010) 86-94.

[84] C.J. Jia, F. Schuth, *PCCP* 13 (2011) 2457-2487.

[85] Y. Xia, Y. Xiong, B. Lim, S.E. Skrabalak, *Angew Chem* 48 (2009) 60-103.

[86] P. Sonstrom, M. Baumer, *PCCP* 13 (2011) 19270-19284.

[87] Y. Li, E. Boone, M.A. El-Sayed, *Langmuir* 18 (2002) 4921-4925.

[88] A. Borsla, A.M. Wilhelm, H. Delmas, *Catal Today* 66 (2001) 389-395.

[89] L. Rossi, L.R. Vono, M.S. Garcia, T.T. Faria, J. Lopez-Sanchez, *Top Catal* 56 (2013) 1228-1238.

[90] V.K. LaMer, R.H. Dinegar, *JACS* 72 (1950) 4847-4854.

[91] M.A. Watzky, R.G. Finke, *JACS* 119 (1997) 10382-10400.

[92] H. Boönnemann, K.S. Nagabhushana, *Chapter 2 - Metal Nanoclusters: Synthesis and Strategies for their Size Control*, in: B.C.S. Toshima (Ed.), *Metal Nanoclusters in Catalysis and Materials Science*, Elsevier, Amsterdam, 2008, pp. 21-48.

[93] B. Lim, M. Jiang, J. Tao, P.H.C. Camargo, Y. Zhu, Y. Xia, *Adv Func Mater* 19 (2009) 189-200.

[94] T.G. Ros, D.E. Keller, A.J. van Dillen, J.W. Geus, D.C. Koningsberger, *J Catal* 211 (2002) 85-102.

[95] S. Gryglewicz, A. Sliwak, J. Cwikla, G. Gryglewicz, *Catal Lett* 144 (2014) 62-69.

[96] Y. Lee, Y. Motoyama, K. Tsuji, S.H. Yoon, I. Mochida, H. Nagashima, *Chemcatchem* 4 (2012) 778-781.

[97] E. Esmaeili, A.M. Rashidi, Y. Mortazavi, A.A. Khodadadi, M. Rashidzadeh, *J Energy Chem* 22 (2013) 717-725.

[98] M. Takasaki, Y. Motoyama, K. Higashi, S.H. Yoon, I. Mochida, H. Nagashima, *Org Lett* 10 (2008) 1601-1604.

[99] Y. Motoyama, M. Taguchi, N. Desmira, S.H. Yoon, I. Mochida, H. Nagashima, *Chemistry, an Asian journal* 9 (2014) 71-74.

[100] F. Rodríguez-Reinoso, *Carbon* 36 (1998) 159-175.

[101] P. Serp, M. Corrias, P. Kalck, *Appl Catal a-Gen* 253 (2003) 337-358.

[102] M.L. Toebes, F.F. Prinsloo, J.H. Bitter, A.J. van Dillen, K.P. de Jong, *J Catal* 214 (2003) 78-87.

[103] C. Park, M.A. Keane, *J Colloid Interf Sci* 266 (2003) 183-194.

[104] P. Tribolet, L. Kiwi-Minsker, *Catal Today* 102 (2005) 15-22.

[105] M. Ruta, N. Semagina, L. Kiwi-Minsker, *J Phys Chem C* 112 (2008) 13635-13641.

[106] L. Kiwi-Minsker, E. Joannet, A. Renken, *Ind Eng Chem Res* 44 (2005) 6148-6153.

[107] N. Semagina, A. Renken, L. Kiwi-Minsker, *Chem Eng Sci* 62 (2007) 5344-5348.

[108] M.C. Macías Pérez, C. Salinas Martínez de Lecea, A. Linares Solano, *Appl Catal A-Gen* 151 (1997) 461-475.

[109] J. Aumo, S. Oksanen, J.P. Mikkola, T. Salmi, D.Y. Murzin, *Ind Eng Chem Res* 44 (2005) 5285-5290.

[110] J.-P. Mikkola, J. Aumo, D.Y. Murzin, T. Salmi, *Catal Today* 105 (2005) 325-330.

[111] A. Nieto-Márquez, S. Gil, A. Romero, J.L. Valverde, S. Gómez-Quero, M.A. Keane, *Appl Catal A-Gen* 363 (2009) 188-198.

[112] C. Pradoburguete, *J Catal* 128 (1991) 397-404.

[113] M.C. Román-Martínez, D. Cazorla-Amorós, A. Linares-Solano, C.S.-M.n. De Lecea, H. Yamashita, M. Anpo, *Carbon* 33 (1995) 3-13.

[114] G.C. Torres, E.L. Jablonski, G.T. Baronetti, A.A. Castro, S.R. de Miguel, O.A. Scelza, M.D. Blanco, M.A. Peña Jiménez, J.L.G. Fierro, *Appl Catal A-Gen* 161 (1997) 213-226.

[115] J.L. Figueiredo, M.F.R. Pereira, M.M.A. Freitas, J.J.M. Orfao, *Carbon* 37 (1999) 1379-1389.

[116] H.P. Boehm, *Carbon* 40 (2002) 145-149.

[117] Á. Molnár, A. Sárkány, M. Varga, *J Mol Catal a-Chem* 173 (2001) 185-221.

[118] *Market Study: Ethylene*, Ceresana Research, 2010.

[119] S.A. Nikolaev, D.A. Pichugina, D.F. Mukhamedzyanova, *Gold Bull* 45 (2012) 221-231.

[120] F. Cardenas-Lizana, M. Crespo-Quesada, L. Kiwi-Minsker, *Chimia* 66 (2012) 681-686.

[121] A. Borodziński, G.C. Bond, *Catal Rev* 48 (2006) 91-144.

[122] N. Semagina, M. Grasemann, N. Xanthopoulos, A. Renken, L. Kiwi-Minsker, *J Catal* 251 (2007) 213-222.

[123] M. Crespo-Quesada, R.R. Dykeman, G. Laurenczy, P.J. Dyson, L. Kiwi-Minsker, *J Catal* 279 (2011) 66-74.

[124] G.C. Bond, G. Webb, P.B. Wells, J.M. Winterbottom, *J Catal* 1 (1962) 74-84.

[125] M.J. Vincent, R.D. Gonzalez, *Appl Catal A-Gen* 217 (2001) 143-156.

[126] E.V. Rebrov, E.A. Klinger, A. Berenguer-Murcia, E.M. Sulman, J.C. Schouten, *Org Process Res Dev* 13 (2009) 991-998.

[127] J. Rajaram, A.P.S. Narula, H.P.S. Chawla, S. Dev, *Tetrahedron* 39 (1983) 2315-2322.

[128] P. Baumeister, M. Studer, F. Roessler, *Handbook of Heterogeneous Catalysis*, VCH, Weinhem, 1997.

[129] H. Nakatsuji, M. Hada, T. Yonezawa, *Surf Sci* 185 (1987) 319-342.

[130] P.A. Sheth, M. Neurock, C.M. Smith, *J Phys Chem B* 107 (2003) 2009-2017.

[131] Y. Segura, N. Lopez, J. Perez-Ramirez, *J Catal* 247 (2007) 383-386.

[132] A.N.R. Bos, K.R. Westerterp, *Chem Eng Process* 32 (1993) 1-7.

[133] A. Borodziński, G.C. Bond, *Chem Rev* 50 (2008) 379-469.

[134] A. Borodziński, A. Cybulski, *Appl Catal A-Gen* 198 (2000) 51-66.

[135] F. Ferrante, A. Prestianni, D. Duca, *J Phys Chem C* 118 (2014) 551-558.

[136] D. Götz, M. Kuhn, P. Claus, *Chem Eng Res Des* 94, (2015) 594-604.

[137] J. Sheridan, *J Chem Soc* (1945) 470-476.

[138] G. Del Angel, J.L. Benitez, *React Kinet Catal Lett* 51 (1993) 547-553.

[139] P.N. Rylander, *19 - Phenols and Phenyl Ethers*, in: P.N. Rylander (Ed.), *Catalytic Hydrogenation Over Platinum Metals*, Academic Press, 1967, pp. 331-351.

[140] X.D. Wang, M.H. Liang, J.L. Zhang, Y. Wang, *Curr Org Chem* 11 (2007) 299-314.

[141] H.U. Blaser, H. Steiner, M. Studer, *Chemcatchem* 1 (2009) 210-221.

[142] J. Xiong, J.X. Chen, J.Y. Zhang, *Catal Commun* 8 (2007) 345-350.

[143] N. Mahata, A.F. Cunha, J.J.M. Órfão, J.L. Figueiredo, *Catal Commun* 10 (2009) 1203-1206.

[144] C. Wang, J.S. Qiu, C.H. Liang, L. Xing, X.M. Yang, *Catal Commun* 9 (2008) 1749-1753.

[145] A. Corma, P. Serna, P. Concepcion, J.J. Calvino, *JACS* 130 (2008) 8748-8753.

[146] Y. Du, H.L. Chen, R.Z. Chen, N.P. Xu, *Appl Catal A-Gen* 277 (2004) 259-264.

[147] N. Mahata, A.F. Cunha, J.J.M. Orfao, J.L. Figueiredo, *Appl Catal A-Gen* 351 (2008) 204-209.

[148] F. Cárdenas-Lizana, S. Gómez-Quero, M.A. Keane, *Appl Catal A-Gen* 334 (2008) 199-206.

[149] C.S. Lu, J.H. Lu, L. Ma, Q.F. Zhang, X.N. Li, *Adv Mater Res* 396-398 (2011) 2379-2383.

[150] D.Q. Xu, Z.Y. Hu, W.W. Li, S.P. Luo, Z.Y. Xu, *J Mol Catal A-Chem* 235 (2005) 137-142.

[151] H. Sajiki, K. Hattori, K. Hirota, *J Org Chem* 63 (1998) 7990-7992.

[152] A. Mori, T. Mizusaki, M. Kawase, T. Maegawa, Y. Monguchi, S. Takao, Y. Takagi, H. Sajiki, *Adv Synth Catal* 350 (2008) 406-410.

[153] X. Yan, J. Sun, Y. Wang, J. Yang, *J Mol Catal a-Chem* 252 (2006) 17-22.

[154] J.F. Su, B. Zhao, Y.W. Chen, *Ind Eng Chem Res* 50 (2011) 1580-1587.

[155] L.F. Chen, Y.W. Chen, *Ind Eng Chem Res* 45 (2006) 8866-8873.

[156] Y.-C. Liu, C.-Y. Huang, Y.-W. Chen, *Ind Eng Chem res* 45 (2006) 62-69.

[157] H.U. Blaser, A. Indolese, A. Schnyder, H. Steiner, M. Studer, *J Mol Catal a-Chem* 173 (2001) 3-18.

[158] Y.-C. Liu, Y.-W. Chen, *Ind Eng Chem Res* 45 (2006) 2973-2980.

[159] H. Liu, J. Deng, W. Li, *Catal Lett* 137 (2010) 261-266.

[160] M. Mo, L. Han, J. Lv, Y. Zhu, L. Peng, X. Guo, W. Ding, *Chem commun* 46 (2010) 2268-2270.

[161] H. Li, J. Zhang, H. Li, *Catal Commun* 8 (2007) 2212-2216.

[162] E. Baumgarten, A. Fiebes, A. Stumpe, *React Funct Polym* 33 (1997) 71-79.

[163] V. Vishwanathan, V. Jayasri, P.M. Basha, N. Mahata, L.M. Sikhwivhilu, N.J. Coville, *Catal Commun* 9 (2008) 453-458.

[164] P.M. Reis, B. Royo, *Tetrahedron Lett* 50 (2009) 949-952.

[165] S. Alexander, V. Udayakumar, N. Nagaraju, V. Gayathri, *Transit Met Chem* 35 (2010) 247-251.

[166] M. Takasaki, Y. Motoyama, K. Higashi, S.-H. Yoon, I. Mochida, H. Nagashima, *Org Lett* 10 (2008) 1601-1604.

[167] Y.Q. Lang, Q.Q. Wang, J.M. Xing, B. Zhang, H.Z. Liu, *Aiche J* 54 (2008) 2303-2309.

[168] H. Li, Q. Zhao, H. Li, *J Mol Catal a-Chem* 285 (2008) 29-35.

[169] C. Liu, R. Tan, N.Y. Yu, D.H. Yin, *Micropor Mesopor Mat* 131 (2010) 162-169.

[170] B. Zhao, C.J. Chou, Y.W. Chen, *Ind Eng Chem Res* 49 (2010) 1669-1676.

[171] Y. Li, Y. Fan, J. He, B. Xu, H. Yang, J. Miao, Y. Chen, *Chem Eng J* 99 (2004) 213-218.

[172] L. Volpe, M. Boudart, *J Solid State Chem* 59 (1985) 348-356.

[173] C. Shi, A.M. Zhu, X.F. Yang, C.T. Au, *Appl Catal A-Gen* 276 (2004) 223-230.

[174] H. He, H.X. Dai, K.Y. Ngan, C.T. Au, *Catal Lett* 71 (2001) 147-153.

[175] D. Liu, Y.Q. Liu, T. Zhou, C.G. Liu, G.H. Que, *Abstr Pap Am Chem S* 226 (2003) U530-U530.

[176] Z.X. Hao, Z.B. Wei, L.J. Wang, X.H. Li, C. Li, E.Z. Min, Q. Xin, *Appl Catal A-Gen* 192 (2000) 81-84.

[177] Z. Wu, Z. Hao, Z. Wei, C. Li, Q. Xin, *Stud Surf Sci Catal* 138 (2001) 445-452.

[178] F. Cárdenas-Lizana, S. Gómez-Quero, N. Perret, L. Kiwi-Minsker, M.A. Keane, *Catal Sci Technol* 1 (2011) 794-801.

[179] D.R. Lide, *Handbook of Chemistry and Physical Properties*, 88th ed., Taylor Francis Group, Boca Raton (USA), 2007-2008.

[180] A.G. Cairns, J.G. Gallagher, J.S.J. Hargreaves, D. Mckay, J.L. Rico, K. Wilson, *J Solid State Chem* 183 (2010) 613-619.

[181] G.M. Maksimova, A.L. Chuvilin, E.A. Moroz, V.A. Likholobov, K.I. Matveev, *Kinet Catal* 45 (2004) 870-878.

[182] R.J. Madon, M. Boudart, *Ind Eng Chem Fundam* 21 (1982) 438-447.

[183] Z.B. Wei, Q. Xin, P. Grange, B. Delmon, *J Catal* 168 (1997) 176-182.

[184] J. Światowska-Mrowiecka, S.d. Diesbach, V. Maurice, S. Zanna, L. Klein, E. Briand, I. Vickridge, P. Marcus, *J Phys Chem C* 112 (2008) 11050-11058.

[185] Z. Li, L. Gao, S. Zheng, *Mater Lett* 57 (2003) 4605-4610.

[186] L. Volpe, S.T. Oyama, M. Boudart, *Preparation of Catalysis III*, Elsevier, Amsterdam, 1983.

[187] J.G. Choi, J.R. Brenner, C.W. Colling, B.G. Demczyk, J.L. Dunning, L.T. Thompson, *Catal Today* 15 (1992) 201-222.

[188] J.R. Regalbuto, J.W. Ha, *Catal Lett* 29 (1994) 189-207.

[189] P. Ettmayer, *Mon Chem* 101 (1970) 127-140.

[190] M. Saito, R.B. Anderson, *J Catal* 63 (1980) 438-446.

[191] Y.J. Zhang, Y.X. Li, C. Li, Q. Xin, *"Adsorption and Migration of Hydrogen on Different Surface sites of γ-*Mo_2N *Catalyst" in Spillover and Migration of Surface Species on Catalysts*, Elsevier, Amsterdam, 1997.

[192] I. Pettiti, S. Colonna, S. De Rossi, M. Faticanti, G. Minelli, P. Porta, *PCCP* 6 (2004) 1350-1358.

[193] E. Elaloui, A.C. Pierre, G.M. Pajonk, *J Catal* 166 (1997) 340-346.

[194] J.E. Benson, H.S. Hwang, M. Boudart, *J Catal* 30 (1973) 146-153.

[195] S. Gómez-Quero, F. Cárdenas-Lizana, M.A. Keane, *Ind Eng Chem Res* 47 (2008) 6841-6853.

[196] C. Amorim, M.A. Keane, *J Chem Technol Biotechnol* 83 (2008) 662.

[197] M. Boudart, H.S. Hwang, *J Catal* 39 (1975) 44-52.

[198] M.A. Aramendía, V. Boráu, I.M. García, C. Jiménez, F. Lafont, A. Marinas, J.M. Marinas, F.J. Urbano, *J Catal* 187 (1999) 392-399.

[199] G.M. Tonetto, D.E. Damiani, *J Mol Catal a-Chem* 202 (2003) 289-303.

[200] T. Janiak, J. Okal, *Appl. Catal. B-Environ.* 92 (2009) 384.

[201] V. Kratky, M. Kralik, M. Mecarova, M. Stolcova, L. Zalibera, M. Hronec, *Appl Catal A-Gen* 235 (2002) 225-231.

[202] X.-X. Han, R.-X. Zhou, G.-H. Lai, X.-M. Zheng, *React Kinet Catal Lett* 83 (2004) 55-61.

[203] Z. Yu, S. Liao, Y. Xu, B. Yang, D. Yu, *J Mol Catal a-Chem* 120 (1997) 247-255.

[204] X.-X. Han, R.-X. Zhou, G.-H. Lai, X.-M. Zheng, *Catal Today* 93-95 (2004) 433-437.

[205] G. Konnecker, A. Boehncke, S. Schmidt, *Fresen Environ Bull* 12 (2003) 589-593.

[206] V.L. Khilnani, S.B. Chandalia, *Org Process Res Dev* 5 (2001) 263-266.

[207] Q. Xu, X.-M. Liu, J.-R. Chen, R.-X. Li, X.-J. Li, *J Mol Catal a-Chem* 260 (2006) 299-305.

[208] H. Liu, M. Liang, C. Xiao, N. Zheng, X. Feng, Y. Liu, J. Xie, Y. Wang, *J. Mol. Catal. A-Chem.* 308 (2009) 79-86.

[209] G.A. Somorjai, C.J. Kliewer, *React Kinet Catal Lett* 96 (2009) 191.

[210] L.P. Hammett, *JACS* 59 (1937) 96-103.

[211] M. Alamé, M. Jahjah, S. Pellet-Rostaing, M. Lemaire, V. Meille, C.d. Bellefon, *J Mol Catal a-Chem* 271 (2007) 18-24.

[212] H.H. Jaffé, *Chem rev* 53 (1953) 191-261.

[213] C.D. Johnson, *The Hammett Equation*, Cambridge University Press, Cambridge, 1973.

[214] J. Shorter, *Chem Lysty* 94 (2000) 210-214.

[215] T. Kamitanaka, T. Matsuda, T. Harada, *Tetrahedron Lett* 44 (2003) 4551-4553.

[216] Y. Himeda, N. Onozawa-Komatsuzaki, H. Sugihara, K. Kasuga, *J Photoch Photobio A-Chem* 182 (2006) 306-309.

[217] T. Yoneda, T. Takido, K. Konuma, *J Mol Catal a-Chem* 265 (2007) 80-89.

[218] J.R. Ruiz, C. Jiménez-Sanchidrián, J.M. Hidalgo, *Catal Commun* 8 (2007) 1036-1040.

[219] M.A.A. Lopidana, V.B. Bolos, C.J. Sanchidrian, J.M.M. Rubio, F.R. Luque, *Bull Chem Soc Jpn* 60 (1987) 3415-3419.

[220] V.M. Belousov, T.A. Palchevskaya, L.V. Bogutskaya, *React Kinet Catal L* 36 (1988) 369-374.

[221] B. Coq, F. Figuéras, *Coord Chem Rev* 178-180 (1998) 1753-1783.

[222] M. Lauwiner, P. Rys, J. Wissmann, *Appl Catal A-Gen* 172 (1998) 141-148.

[223] F. Cárdenas-Lizana, Z.M. de Pedro, S. Gómez-Quero, M.A. Keane, *J Mol Catal a-Chem* 326 (2010) 48-54.

[224] R.A. Sheldon, *Green Chem* 9 (2007) 1273-1283.

[225] F. Cárdenas-Lizana, S. Gómez-Quero, M.A. Keane, *Catal Commun* 9 (2008) 475-481.

[226] A. Corma, M. Boronat, S. Gonzalez, F. Illas, *Chem Commun* 32 (2007) 3371-3373.

[227] C. Jiménez-González, P. Poechlauer, Q.B. Broxterman, B.-S. Yang, D. am Ende, J. Baird, C. Bertsch, R.E. Hannah, P. Dell'Orco, H. Noorman, S. Yee, R. Reintjens, A. Wells, V. Massonneau, J. Manley, *Org Process Res Dev* 15 (2011) 900-911.

[228] F. Cárdenas-Lizana, S. Gómez-Quero, H. Idriss, M.A. Keane, *J Catal* 268 (2009) 223-234.

[229] F. Cárdenas-Lizana, S. Gómez-Quero, A. Hugon, L. Delannoy, C. Louis, M.A. Keane, *J Catal* 262 (2009) 235-243.

[230] B. Hammer, J.K. Nørskov, *Nature* 376 (1995) 238-240.

[231] C. Kartusch, J.A.v. Bokhoven, *Gold Bull* 42 (2009) 343.

[232] J. Li, X.-Y. Shi, Y.-Y. Bi, J.-F. Wei, Z.-G. Chen, *ACS Catal* 1 (2011) 657-664.

[233] G. Xie, Z. Jiang, *Chin. Sci. Bull.* 45 (2000) 1562.

[234] N. Perret, F. Cárdenas-Lizana, M.A. Keane, *Catal Commun* 16 (2011) 159-164.

[235] Y.H. Wang, W. Li, M.H. Zhang, N.J. Guan, K.Y. Tao, *Appl Catal A-Gen* 215 (2001) 39-45.

[236] P. Claus, *Appl Catal A-Gen* 291 (2005) 222-229.

[237] D.-Q. Xu, Z.-Y. Hu, W.-W. Li, S.-P. Luo, Z.-Y. Xu, *J Mol Catal a-Chem* 235 (2005) 137-142.

[238] I.W.C.E. Arends, R.A. Sheldon, *Appl Catal A-Gen* 212 (2001) 175-187.

[239] S. Tembe, G. Patrick, M. Scurrell, *Gold Bull* 42 (2009) 321-327.

[240] Y. Zhang, Y. Li, R. Raval, C. Li, R. Zhai, Q. Xin, *J Mol Catal a-Chem* 132 (1998) 241-253.

[241] M. Boronat, P. Concepción, A. Corma, S. González, F. Illas, P. Serna, *JACS* 129 (2007) 16230-16237.

[242] A.-M. Alexander, J.S.J. Hargreaves, *Chem Soc Rev* 39 (2010) 4388-4401.

[243] Z.L. Wu, S.W. Yang, Q. Xin, C. Li, *Catal Surv Asia* 7 (2003) 103-119.

[244] M.E. Eberhart, J.M. MacLaren, *The origins of the similarities between late transition metals and early transition metal monocarbides*, in: S.T. Oyama (Ed.), *The Chemistry of Transition Metal Carbides and Nitrides*, Springer Netherlands, 1996, pp. 107-120.

[245] F. Cárdenas-Lizana, D. Lamey, N. Perret, S. Gómez-Quero, L. Kiwi-Minsker, M.A. Keane, *Catal Commun* 21 (2012) 46-51.

[246] F. Cárdenas-Lizana, D. Lamey, S. Gómez-Quero, N. Perret, L. Kiwi-Minsker, M.A. Keane, *Catal Today* 173 (2011) 53-61.

[247] M.A. Keane, *J Catal* 166 (1997) 347-355.

[248] S.Z. Li, W.B. Kim, J.S. Lee, *Chem Mater* 10 (1998) 1853-1862.

[249] Z.B.Z. Wei, P. Grange, B. Delmon, *Appl Surf Sci* 135 (1998) 107-114.

[250] R. Marchand, F. Tessier, F.J. DiSalvo, *J Mater Chem* 9 (1999) 297-304.

[251] C.H. Jaggers, J.N. Michaels, A.M. Stacy, *Chem Mater* 2 (1990) 150-157.

[252] R.C.V. McGee, S.K. Bej, L.T. Thompson, *Appl Catal A-Gen* 284 (2005) 139-146.

[253] W. Setthapun, S. Bej, L. Thompson, *Top Catal* 49 (2008) 73-80.

[254] J. Logan, J. Heiser, K. McCrea, B. Gates, M. Bussell, *Catal Lett* 56 (1998) 165-171.

[255] G. Xie, Z. Jiang, *Chin Sci Bull* 45 (2000) 1562-1564.

[256] J.A. Peck, C.D. Tait, B.I. Swanson, G.E. Brown, *Geochim Cosmochim Ac* 55 (1991) 671-676.

[257] I. Dobrosz, K. Jiratova, V. Pitchon, J.M. Rynkowski, *J Mol Catal a-Chem* 234 (2005) 187-197.

[258] H.S. Oh, J.H. Yang, C.K. Costello, Y.M. Wang, S.R. Bare, H.H. Kung, M.C. Kung, *J Catal* 210 (2002) 375-386.

[259] R. Zanella, C. Louis, *Catal Today* 107-08 (2005) 768-777.

[260] A.D. Consuegra, P.M. Patterson, M.A. Keane, *Appl Catal B-Environ* 65 (2006) 227-239.

[261] J. Słoczyński, W. Bobiński, *J Solid State Chem* 92 (1991) 436-448.

[262] S. Aouadi, Y. Paudel, B. Luster, S. Stadler, P. Kohli, C. Muratore, C. Hager, A. Voevodin, *Tribol Lett* 29 (2008) 95-103.

[263] S. Gong, H. Chen, W. Li, B. Li, *Catal Commun* 5 (2004) 621-624.

[264] Y. Zhang, Q. Xin, I. Rodriguez-Ramos, A. Guerrero-Ruiz, *Mater Res Bull* 34 (1999) 145-156.

[265] K. Dewangan, S.S. Patil, D.S. Joag, M.A. More, N.S. Gajbhiye, *J Phys Chem C* 114 (2010) 14710-14715.

[266] C. Shi, A.M. Zhu, X.F. Yang, C.T. Au, *Catal Lett* 97 (2004) 9-16.

[267] J. Qi, L. Jiang, Q. Jiang, S. Wang, G. Sun, *J Phys Chem C* 114 (2010) 18159-18166.

[268] X.S. Li, S.S. Sheng, H.R. Chen, C.X. Ji, Y.J. Zhang, Q. Xin, *Acta Phys Chim Sin* 11 (1995) 678-680.

[269] M. Nagai, S. Omi, *J Jpn Petrol Inst* 38 (1995) 363-373.

[270] A. Corma, C. González-Arellano, M. Iglesias, F. Sánchez, *Appl Catal A-Gen* 356 (2009) 99-102.

[271] S.R. Kanth, G.V. Reddy, V.V.V.N.S.R. Rao, D. Maitraie, B. Narsaiah, P.S. Rao, *Synthetic Commun* 32 (2002) 2849-2853.

[272] S.U. Sonavane, M.B. Gawande, S.S. Deshpande, A. Venkataraman, R.V. Jayaram, *Catal Commun* 8 (2007) 1803-1806.

[273] F. Cárdenas-Lizana, S. Gómez-Quero, N. Perret, M.A. Keane, *Catal Sci Technol* 1 (2011) 652-661.

[274] Y.Z. Chen, Y.C. Chen, *Appl Catal A-Gen* 115 (1994) 45-57.

[275] A. Tijani, B. Coq, F. Figueras, *Appl Catal* 76 (1991) 255-266.

[276] J. Ren, J. Wang, C.-F. Huo, X.-D. Wen, Z. Cao, S. Yuan, Y. Li, H. Jiao, *Surf Sci* 601 (2007) 1599-1607.

[277] L.J. Deiner, D.H. Kang, C.M. Friend, *J Phys Chem B* 109 (2005) 12826-12831.

[278] M. Kosmulski, *Chemical Properties of Material Surfaces, in Surfactant Science Series Vol. 102, (Ed. M. Kosmulski), Marcel Dekker, New York*, 2001, pp.65-222.

[279] J.W. Geus, A.J. van Dillen, *Preparation of Supported Catalysts by Deposition-Precipitation* in Preparation of Solid Catalysts, (Eds. G. Ertl, H. Knözinger and J. Weitkamp), Wiley-VCH, Weinheim, 1999, pp. 460-486.

[280] F. Moreau, G.C. Bond, *Catal Today* 122 (2007) 260-265.

[281] M. Kosmulski, *Adv Colloid Interface Sci* 152 (2009) 14-25.

[282] F. Moreau, G.C. Bond, A.O. Taylor, *J Catal* 231 (2005) 105-114.

[283] F. Somodi, I. Borbáth, M. Hegedűs, A. Tompos, I.E. Sajó, Á. Szegedi, S. Rojas, J.L.G. Fierro, J.L. Margitfalvi, *Appl Catal A-Gen* 347 (2008) 216-222.

[284] G. Postole, A. Gervasini, C. Guimon, A. Auroux, B. Bonnetot, *J Phys Chem B* 110 (2006) 12572-12580.

[285] B. Silberova, G. Mul, M. Makkee, J. Moulijn, *J Catal* 243 (2006) 171-182.

[286] S.E. Collins, J.M. Cíes, E.d. Río, M. López-Haro, S. Trasobares, J.J. Calvino, J.M. Pintado, S. Bernal, *J Phys Chem C* 111 (2007) 14371-14379.

[287] N.A. Hodge, C.J. Kiely, R. Whyman, M.R.H. Siddiqui, G.J. Hutchings, Q.A. Pankhurst, F.E. Wagner, R.R. Rajaram, S.E. Golunski, *Catal Today* 72 (2002) 133-144.

[288] N.N. Greenwood, A. Earnshaw, *Chemistry of the Elements, 2nd edition, Butterworth-Heinemann, Oxford*, 1997.

[289] L. McEwan, M. Julius, S. Roberts, J.C.Q. Fletcher, *Gold Bull* 43 (2010) 298-306.

[290] P. Claus, H. Hofmeister, C. Mohr, *Gold Bull* 37 (2004) 181-186.

[291] G. Bond, C. Louis, D.T. Thompson, *Catalysis by Gold in Catalytic Science Series-Vol.6, (Ed. G. J. Hutchings), Imperial College Press, London, 2006, pp. 150-153*.

[292] A. Corma, P. Serna, *Nature protocols* 1 (2006) 2590-2595.

[293] A. Corma, P. Serna, *Science* 313 (2006) 332-334.

[294] F. Cárdenas-Lizana, S. Gómez-Quero, N. Perret, M.A. Keane, *Gold Bull* 42 (2009) 124-132.

[295] A. Corma, H. Garcia, *Chem Soc Rev* 37 (2008) 2096-2126.

[296] F. Cardenas-Lizana, S. Gomez-Quero, M.A. Keane, *ChemSusChem* 1 (2008) 215-221.

[297] D.J. Sajkowski, S.T. Oyama, *Appl Catal A-Gen* 134 (1996) 339-349.

[298] J.C. Schlatter, S.T. Oyama, J.E. Metcalfe, J.M. Lambert, *Ind Eng Chem Res* 27 (1988) 1648.

[299] N. Perret, F. Cárdenas-Lizana, D. Lamey, V. Laporte, L. Kiwi-Minsker, M. Keane, *Top Catal* 55 (2012) 955-968.

[300] I.T. Ghampson, C. Sepulveda, R. Garcia, B.G. Frederick, M.C. Wheeler, N. Escalona, W.J. DeSisto, *Appl Catal A-Gen* 413 (2012) 78-84.

[301] D.-W. Kim, D.-K. Lee, S.-K. Ihm, *Korean J Chem Eng* 19 (2002) 587-592.

[302] S.W. Gong, H.K. Chen, W. Li, B.Q. Li, T.D. Hu, *J Mol Catal A-Chem* 225 (2005) 213-216.

[303] J.G. Choi, *J Ind Eng Chem* 8 (2002) 1-11.

[304] Y.Z. Li, G.F. Luo, Y.N. Fan, Y. Chen, *Mater Res Bull* 39 (2004) 195-203.

[305] H. Ishii, M. Kiyoshi, M. Nagai, *Top Catal* 52 (2009) 1525-1534.

[306] K. Miga, K. Stanczyk, C. Sayag, D. Brodzki, G. Djéga-Mariadassou, *J Catal* 183 (1999) 63-68.

[307] M. Yamada, J. Yasumaru, M. Houalla, D.M. Hercules, *J Phys Chem* 95 (1991) 7037-7042.

[308] H. Al-Kandari, F. Al-Kharafi, A. Katrib, *J Mol Catal a-Chem* 287 (2008) 128-134.

[309] F. Al-Kharafi, H. Al-Kandari, A. Katrib, *Catal Lett* 123 (2008) 269-275.

[310] P. Uvdal, B.C. Wiegand, J.G. Serafin, C.M. Friend, *J Chem Phys* 97 (1992) 8727-8735.

[311] F. Cárdenas-Lizana, D. Lamey, N. Perret, S. Gómez-Quero, L. Kiwi-Minsker, M.A. Keane, *Catal Commun* 21 (2012) 46-51.

[312] R. Yuvakkumar, V. Elango, V. Rajendran, N. Kannan, *Synth React Inorg M* 41 (2011) 309-314.

[313] B.G. Demczyk, J.G. Choi, L.T. Thompson, *Appl Surf Sci* 78 (1994) 63-69.

[314] P.A. Spevack, N.S. McIntyre, *J Phys Chem-Us* 97 (1993) 11031-11036.

[315] M. Yamada, J. Yasumaru, M. Houalla, D.M. Hercules, *P Phys Chem* 95 (1991) 7037-7042.

[316] H.K. Park, J.K. Lee, J.K. Yoo, E.S. Ko, D.S. Kim, K.L. Kim, *Appl Catal A-Gen* 150 (1997) 21-35.

[317] M.W. Roberts, L. Whalley, *T Faraday Soc* 65 (1969) 1377-1385.

[318] K. Jeong, *J Vac Sci Technol A-Vac Surf Films* 7 (1989) 2199-2202.

[319] M. Arnold, S. Sologub, W. Frie, L. Hammer, K. Heinz, *J Phys-Condens Mat* 9 (1997) 6481-6491.

[320] S.W. Yang, C. Li, J. Xu, Q. Xin, *J Phys Chem B* 102 (1998) 6986-6993.

[321] Z. Wu, C. Li, P. Ying, Z. Wei, Q. Xin, *J Phys Chem B* 105 (2001) 9183-9190.

[322] J.F. Zhu, J.C. Guo, R.S. Zhai, X. Bao, X.Y. Zhang, S. Zhuang, *Appl Surf Sci* 161 (2000) 86-93.

[323] M. Nguyen, Z. Rappoport, *The Chemistry of Anilines. Part 1: "General and Theoretical Aspects of Anilines"*, in: Z. Rappopport (Ed.), *Partai Series: The Chemistry of Functional Groups*, Wiley, Chichester, 2007, pp. 75-165.

[324] S. Meijers, V. Ponec, *J Catal* 149 (1994) 307-316.

[325] E.A. Gelder, *The Hydrogenation of Nitrobenzene over Metal Catalysts*, in: *Department of Chemistry*, University of Glasgow, Glasgow, 2005, pp. 320.

[326] S. Huang, D. Fischer, J. Gland, *Catal Lett* 34 (1995) 365-374.

[327] I. Amer, T. Bravdo, J. Blum, K. Peter, C. Vollhardt, *Tetrahedron Lett* 28 (1987) 1321-1322.

[328] N. Perret, X.D. Wang, L. Delannoy, C. Potvin, C. Louis, M.A. Keane, *J Catal* 286 (2012) 172-183.

[329] P. Sangeetha, P. Seetharamulu, K. Shanthi, S. Narayanan, K.S.R. Rao, *J Mol Catal a-Chem* 273 (2007) 244-249.

[330] D. Procházková, P. Zámostný, M. Bejblová, L. Červený, J. Čejka, *Appl Catal A-Gen* 332 (2007) 56-64.

[331] D. Divakar, D. Manikandan, G. Kalidoss, T. Sivakumar, *Catal Lett* 125 (2008) 277-282.

[332] F. Pinna, F. Menegazzo, M. Signoretto, P. Canton, G. Fagherazzi, N. Pernicone, *Appl Catal A-Gen* 219 (2001) 195-200.

[333] P. Kluson, L. Cerveny, *J Mol Catal a-Chem* 108 (1996) 107-112.

[334] A. Saadi, Z. Rassoul, M.M. Bettahar, *J Mol Catal a-Chem* 164 (2000) 205-216.

[335] A. Saadi, R. Merabiti, Z. Rassoul, M.M. Bettahar, *J Mol Catal a-Chem* 253 (2006) 79-85.

[336] M.A. Vannice, D. Poondi, *J Catal* 169 (1997) 166-175.

[337] K. Lanasri, A. Saadi, K. Bachari, D. Halliche, O. Cherifi, *Gas phase hydrogenation of benzaldehyde over supported copper catalysts. Effect of copper loading*, in: P.M. Antoine Gédéon, B. Florence (Eds.), *Stud Surf Sci Catal*, Elsevier, 2008, pp. 1279-1282.

[338] R. Merabti, K. Bachari, D. Halliche, Z. Rassoul, A. Saadi, *Reac Kinet Mech Cat* 101 (2010) 195-208.

[339] M.A. Peralta, T. Sooknoi, T. Danuthai, D.E. Resasco, *J Mol Catal a-Chem* 312 (2009) 78-86.

[340] L. Červený, Z. Bělohlav, M.H. Hamed, *Res Chem Intermed* 22 (1996) 15-22.

[341] M. Siaj, C. Reed, S.T. Oyama, S.L. Scott, P.H. McBreen, *JACS* 126 (2004) 9514-9515.

[342] G. Frapper, M. Pélissier, J. Hafner, *J Phys Chem B* 104 (2000) 11972-11976.

[343] F. Zaera, *Catal Lett* 142 (2012) 501-516.

[344] G.C. Bond, *Surf Sci* 156 (1985) 966-981.

[345] H.U. Blaser, C. Malan, B. Pugin, F. Spindler, H. Steiner, M. Studer, *Adv Synth Catal* 345 (2003) 103-151.

[346] H. Borchert, D. Fenske, J. Kolny-Olesiak, J. Parisi, K. Al-Shamery, M. Bäumer, *Angewandte Chemie* 46 (2007) 2923-2926.

[347] K.M. Bratlie, H. Lee, K. Komvopoulos, P. Yang, G.A. Somorjai, *Nano Lett* 7 (2007) 3097-3101.

[348] H.R. Choi, H. Woo, S. Jang, J.Y. Cheon, C. Kim, J. Park, K.H. Park, S.H. Joo, *Chemcatchem* 4 (2012) 1587-1594.

[349] P.S. Roy, J. Bagchi, S.K. Bhattacharya, *Colloid Surface A* 359 (2010) 45-52.

[350] A.B.R. Mayer, J.E. Mark, *Polym Bull* 37 (1996) 683-690.

[351] N.J.S. Costa, L.M. Rossi, *Nanoscale* 4 (2012) 5826-5834.

[352] S.A. Nikolaev, L.N. Zanaveskin, V.V. Smirnov, V.A. Averyanov, K.L. Zanaveskin, *Russ Chem Rev* 78 (2009) 231-247.

[353] M. Ruta, N. Semagina, L. Kiwi-Minsker, *J Phys Chem C* 112 (2008) 13635-13641.

[354] N. Semagina, A. Renken, D. Laub, L. Kiwi-Minsker, *J Catal* 246 (2007) 308-314.

[355] M. Jin, H. Liu, H. Zhang, Z. Xie, J. Liu, Y. Xia, *Nano Res* 4 (2011) 83-91.

[356] T. Teranishi, M. Miyake, *Chem Mater* 10 (1998) 594-600.

[357] M. Crespo-Quesada, J.M. Andanson, A. Yarulin, B. Lim, Y. Xia, L. Kiwi-Minsker, *Langmuir* 27 (2011) 7909-7916.

[358] Z.-Y. Shih, C.-W. Wang, G. Xu, H.-T. Chang, *J Mater Chem A* 1 (2013) 4773-4478.

[359] N. Mishra, G. Das, A. Ansaldo, A. Genovese, M. Malerba, M. Povia, D. Ricci, E. Di Fabrizio, E. Di Zitti, M. Sharon, M. Sharon, *J Anal Appl Pyrol* 94 (2012) 91-98.

[360] H.P. Klug, L.E. Alexander, *X-ray Diffraction Procedures for Polycrystaline and Amorphous Materials*, Wiley, New York, 1974.

[361] W.-x. Tu, X.-b. Zuo, H.-f. Liu, *Chinese J Polym Sci* 26 (2008) 23-29.

[362] G.C. Bond, *Appl Catal A-Gen* 149 (1997) 3-25.

[363] R.T.K. Baker, R.J. Waite, *J Catal* 37 (1975) 101-105.

[364] M. Kumar, Y. Ando, *J Nanosci Nanotechnol* 10 (2010) 3739-3758.

[365] C. Park, M.A. Keane, *Chem Eng Commun* 191 (2004) 1456-1472.

[366] S. Lim, S.-H. Yoon, Y. Korai, I. Mochida, *Carbon* 42 (2004) 1765-1781.

[367] Y. Wang, Q.S. Zhu, H.G. Zhang, *J Mater Chem* 16 (2006) 1212-1214.

[368] H. Borchert, E.V. Shevchenko, A. Robert, I. Mekis, A. Kornowski, G. Grübel, H. Weller, *Langmuir* 21 (2005) 1931-1936.

[369] K.P.D. Jong, J.W. Geus, *Catal. Rev.-Sci. Eng.* 42 (2000) 481.

[370] S.B. Sinnott, R. Andrews, D. Qian, A.M. Rao, Z. Mao, E.C. Dickey, F. Derbyshire, *Chem Phys Lett* 315 (1999) 25-30.

[371] G. Berhault, L. Bisson, C. Thomazeau, C. Verdon, D. Uzio, *Appl Catal A-Gen* 327 (2007) 32-43.

[372] Y.L. Hsin, K.C. Hwang, C.T. Yeh, *JACS* 129 (2007) 9999-10010.

[373] Y. Bai, Z.H. Huang, Z.X. Zhang, F. Kang, *J Colloid Interf Sci* 394 (2013) 177-182.

[374] M.H. Seo, E.J. Lim, S.M. Choi, S.H. Nam, H.J. Kim, W.B. Kim, *Int J Hydrogen Energ* 36 (2011) 11545-11553.

[375] K.S. Kim, A.F. Gossmann, N. Winograd, *Anal Chem* 46 (1974) 197-200.

[376] C. Evangelisti, N. Panziera, P. Pertici, G. Vitulli, P. Salvadori, C. Battocchio, G. Polzonetti, *J Catal* 262 (2009) 287-293.

[377] Q.W. Zhang, J. Li, X.X. Liu, Q.M. Zhu, *Appl Catal A-Gen* 197 (2000) 221-228.

[378] J.H. Kang, E.W. Shin, W.J. Kim, J.D. Park, S.H. Moon, *Catal Today* 63 (2000) 183-188.

[379] J. Panpranot, K. Kontapakdee, P. Praserthdam, *Appl Catal A-Gen* 314 (2006) 128-133.

[380] P. Albers, J. Pietsch, S.F. Parker, *J Mol Catal A-Chem* 173 (2001) 275.

[381] M. Ruta, G. Laurenczy, P.J. Dyson, L. Kiwi-Minsker, *J Phys Chem C* 112 (2008) 17814-17819.

[382] R. Kosydar, M. Góral, J. Gurgul, A. Drelinkiewicz, *Catal Commun* 22 (2012) 58-67.

[383] M. Sinisi, F.P. Intini, G. Natile, *Inorg chem* 51 (2012) 9694-9704.

[384] L. Kiwi-Minsker, M. Crespo-Quesada, *Top Catal* 55 (2012) 486-491.

[385] E. Schmidt, W. Kleist, F. Krumeich, T. Mallat, A. Baiker, *Chem-Eur J* 16 (2010) 2181-2192.

[386] B.L. Cushing, V.L. Kolesnichenko, C.J. O'Connor, *Chem Rev* 104 (2004) 3893-3946.

[387] B.C. Ward, J.L. Templeton, *JACS* 102 (1980) 1532-1538.

[388] C. Kim, H. Lee, *Catal Commun* 10 (2009) 1305-1309.

[389] Y. Li, M.A. El-Sayed, *J Phys Chem B* 105 (2001) 8938-8943.

[390] Y. Borodko, S.E. Habas, M. Koebel, P. Yang, H. Frei, G.A. Somorjai, *J Phys Chem B* 110 (2006) 23052-23059.

[391] J.N. Li, M. Pu, C.-C. Ma, Y. Tian, J. He, D.G. Evans, *J Mol Catal A-Chem* 359 (2012) 14-20.

[392] A.J.D. Hartog, M. Deng, F. Jongerius, V. Ponec, *J Mol Catal* 60 (1990) 99-108.

[393] C.P. Vinod, G.U. Kulkarni, C.N.R. Rao, *Chem Phys Lett* 289 (1998) 329-333.

[394] F.C. Loh, K.L. Tan, E.T. Kang, *Polymer* 34 (1993) 5000-5002.

[395] K.F. Weyts, E.J. Goethals, *Polym Bull* 19 (1988) 13-19.

[396] A.N.R. Bos, E.S. Bootsma, F. Foeth, H.W.J. Sleyster, K.R. Westerterp, *Chem Eng Process* 32 (1993) 53-63.

[397] V. Polshettiwar, R.S. Varma, *Green Chem* 12 (2010) 743-754.

[398] K. Lee, M. Kim, H. Kim, *J Mater Chem* 20 (2010) 3791-3798.

[399] P. Claus, A. Bruckner, C. Mohr, H. Hofmeister, *J Am Chem Soc* 122 (2000) 11430-11439.

[400] C.O. Bennett, M. Che, *J Catal* 120 (1989) 293-302.

[401] R.S. Downing, P.J. Kunkeler, H. vanBekkum, *Catal Today* 37 (1997) 121-136.

[402] G.J. Hutchings, *J Mater Chem* 19 (2009) 1222-1235.

[403] S.A. Regenhardt, C.I. Meyer, T.F. Garetto, A.J. Marchi, *Appl Catal A-Gen* 449 (2012) 81-87.

[404] R.A. Rajadhyaksha, S.L. Karwa, *Chem Eng Sci* 41 (1986) 1765-1770.

[405] C. Exner, A. Pfaltz, M. Studer, H.U. Blaser, *Adv Synth Catal* 345 (2003) 1253-1260.

[406] V.L. Khilnani, S.B. Chandalia, *Org Process Res Dev* 5 (2001) 257-262.

[407] H. Rojas, G. Borda, P. Reyes, M. Brijaldo, J. Valencia, *J Chil Chem Soc* 56 (2011) 793-798.

[408] S.L. Zhao, H.D. Liang, Y.F. Zhou, *Catal Commun* 8 (2007) 1305-1309.

[409] Y.X. Liu, Z.J. Wei, S.G. Deng, J.Y. Zhang, *J Chem Technol Biot* 84 (2009) 1381-1389.

[410] M.M. Telkar, J.M. Nadgeri, C.V. Rode, R.V. Chaudhari, *Appl Catal A-Gen* 295 (2005) 23-30.

[411] J.H. Wang, Z.L. Yuan, R.F. Nie, Z.Y. Hou, X.M. Zheng, *Ind Eng Chem Res* 49 (2010) 4664-4669.

[412] K.J.A. Raj, M.G. Prakash, R. Mahalakshmy, T. Elangovan, B. Viswanathan, *Chin J Catal* 33 (2012) 1299-1305.

[413] R. Chen, Y. Du, W. Xing, N. Xu, *J Chem Technol Biotechnol* 15 (2008) 884-888.

[414] R.J. Kalbasi, A.A. Nourbakhsh, F. Babaknezhad, *Catal Commun* 12 (2011) 955-960.

[415] Y.X. Liu, J.X. Chen, J.Y. Zhang, *Chinese J Chem Eng* 15 (2007) 63-67.

[416] L. Kiwi-Minsker, E. Joannet, A. Renken, *Ind Eng Chem Res* 44 (2005) 6148-6153.

[417] J. Kimling, M. Maier, B. Okenve, V. Kotaidis, H. Ballot, A. Plech, *J Phys Chem B* 110 (2006) 15700-15707.

[418] U.K. Singh, M.A. Vannice, *Appl Catal A-Gen* 213 (2001) 1-24.

[419] N.M. Bertero, A.F. Trasarti, C.R. Apesteguia, A.J. Marchi, *Appl Catal A-Gen* 394 (2011) 228-238.

[420] R.L. Augustine, R.W. Warner, M.J. Melnick, *J Org Chem* 49 (1984) 4853-4856.

[421] A. Drelinkiewicza, A. Waksmundzka, W. Makowski, J.W. Sobczak, A. Król, A. Zieba, *Catal Lett* 94 (2004) 143-156.

[422] L. Ma, C. Lu, J. Lu, Q. Zhang, X. Li, *Adv Mat Res* 396-398 (2011) 2379-2383.

[423] S. Hub, L. Hilaire, R. Touroude, *Appl Catal* 36 (1988) 307-322.

[424] A. Quintanilla, V.C.L. Butselaar-Orthlieb, C. Kwakernaak, W.G. Sloof, M.T. Kreutzer, F. Kapteijn, *J Catal* 271 (2010) 104-114.

[425] J. Sehested, *J Catal* 217 (2003) 417-426.

[426] Y. Lu, Y. Mei, M. Ballauff, M. Drechsler, *J Phys Chem B* 110 (2006) 3930-3937.

[427] J.A. Johnson, J.J. Makis, K.A. Marvin, S.E. Rodenbusch, K.J. Stevenson, *J Phys Chem C* 117 (2013) 22644-22651.

[428] Y. Li, Y. Zhang, R. Raval, C. Li, R. Zhai, Q. Xin, *Catal Lett* 48 (1997) 239-245.

[429] M. Pang, C. Liu, W. Xia, M. Muhler, C. Liang, *Green Chem* 14 (2012) 1272-1276.

[430] M.L. Frauwallner, F. Lopez-Linares, J. Lara-Romero, C.E. Scott, V. Ali, E. Hernandez, P. Pereira-Almao, *Appl Catal A-Gen* 394 (2011) 62-70.

Curriculum Vitae

Education

- **2010 – 2015** **PhD in Chemical Engineering.**
  Group of Catalytic Reaction Engineering (Prof. L. Kiwi-Minsker),
  Swiss Federal Institute of Technology, Lausanne (EPFL).
- **2007 – 2009** **MSc in chemistry.**
  University of Geneva, department of Chemistry, Science-II.
- **2003 – 2006** **Engineer diploma in industrial and applied chemistry.**
  College of Engineering and Architecture of Fribourg (EIA-FR), chemistry department.
  Awarded for "*excellence of the results*" from the Industry Grouping of Fribourg.
- **2001 – 2003** **University and Technological Diploma, chemistry speciality.**
  University Institute of Technology of Strasbourg, chemistry department.

Work Experience

- **2010 – 2015** **Doctoral Assistant -** Group of Catalytic Reaction Engineering, EPFL.
  - I designed new catalyst formulations with a nano-sized active phase and tailored morphology leading to increased performance for the production of aromatic anilines and alkenes in a three-phase hydrogenation.
  - Teaching assistance for "*Chemical Engineering of Heterogeneous Reactions*" and "*Théorie des Réacteurs*" courses as well as "*Chemical Engineering Project and Lab*" by Prof. L. Kiwi-Minsker .
  - Supervision of master students for their diploma work (11 months overall).
- **06.2003 – 08.2003** **Trainee -** Rhodia Polyamide Intermediates, Chalampé.

  Analysis of production samples (HPLC, GC, UV-Vis, AAS-ICP, X-fluorescence) as part of the development of a manufacturing process for a Nylon 6-6.
- **06.2002 – 08.2002** **Trainee -** Peugeot Citroën laboratories, Mulhouse (PSA).

  Production monitoring by analysis (UV-Vis, AAS, X-fluorescence) of automotive elements.

Internships and Projects

- **02.2010 – 06.2010** Swiss Federal Institute of Technology, Lausanne (EPFL).
  Master thesis internship. Title: "*β-Mo Nitride as a Novel Catalyst for the Selective Hydrogenation of Chloronitrobenzene: the Promoting Effects of Mo and Au*".

  Development and characterization of novel nitride-based catalyst for selective gas and liquid phase hydrogenation of nitro-aromatic compounds.

- **09.2006 – 11.2006** Syngenta Crop Protection, Münchwilen AG.
  Diploma work in chemical engineering

  Production of an agrochemical intermediate by development of a semi-batch to continuous process.

- **05.2006** Institute for Value-based Enterprise (IVE)
  Enterprise economy workshop.

- **02.2006 – 06.2006** College of Engineering and Architecture of Fribourg (EIA-FR)
  Semester project in organic chemistry.

  Recovery of malic acid resulting from a wine demalication process.

Publications

- D. Lamey, F. Cárdenas-Lizana, L. Kiwi-Minsker. *Alkyne Hydrogenation over Molybdenum Nitrides: A Consideration of Pd-promoting Effect*. (In preparation).
- N. Perret, F. Cárdenas-Lizana, D. Lamey, L. Kiwi-Minsker, M.A. Keane. *New Insights into the Effect of Nitrogen Incorporation in Mo: Catalytic Hydrogenation vs. Hydrogenolysis.* (In preparation).
- D. Lamey, S. Moya-Pascual, F. Cárdenas-Lizana, L. Kiwi-Minsker. *When the Smallest are the Most Efficient: Colloidal Methods for Development of Ni-based Catalyst Selective in m-Dinitrobenzene Hydrogenation*. Current Topics in Catalysis, 2015 (Submitted).
- F. Cárdenas-Lizana, X. Wang, D. Lamey, M. Li, M.A. Keane, L. Kiwi-Minsker. *An Examination of Catalyst Deactivation in p-chloronitrobenzene Hydrogenation over Supported Gold*. Chemical Engineering Journal 255, 2014, 695-704.
- D. Lamey, I. Prokopyeva, F. Cárdenas-Lizana, L. Kiwi-Minsker. *Impact of organic-ligand shell on catalytic performance of colloidal Pd nanoparticles for alkyne gas-phase hydrogenation.* Catalysis Today 235, 2014, 79-89.
- N. Perret, F. Cárdenas-Lizana, D. Lamey, V. Laporte, L. Kiwi-Minsker, M. Keane. *Effect of Crystallographic Phase (beta vs. gamma) and Surface Area on Gas Phase Nitroarene Hydrogenation over* Mo_2N *and* Au/Mo_2N. Topics in Catalysis 55, 2012, 955-968.

- F. Cárdenas-Lizana, D. Lamey, N. Perret, S. Gómez-Quero, L. Kiwi-Minsker, M.A. Keane. *Au/Mo_2N as a New Catalyst Formulation for the Hydrogenation of p-chloronitrobenzene in Both Liquid and Gas Phases.* Catalysis Communications 21, 2012, 46-51.
- F. Cárdenas-Lizana, D. Lamey, S. Gómez-Quero, N. Perret, L. Kiwi-Minsker, M.A. Keane. *Selective Three-phase Hydrogenation of Aromatic Nitro-compounds over β-molybdenum Nitride.* Catalysis Today 173, 2011, 53-61.

Conferences

- June 1-6 2014, The Seventh Tokyo Conference on Advanced Catalytic Science and Technology, Kyoto, Japan.
  Nitroarene Liquid-Phase Hydrogenation: Enhanced Catalytic Performance of Nickel Nanoparticles supported on Activated Carbon Fibers (Oral Presentation).
- September 6 2013, SCS Fall Meeting, Lausanne, Switzerland.
  Tailoring Pd-nanoparticles selectivity via Colloidal Techniques (Poster).
- September 1-6 2013, 11th European Congress on Catalysis – EuropaCat-XI, Lyon, France.
  Modifying-Pd Colloid Agents for Tailoring Surface Properties: Acetylene Hydrogenation as a Case Study (Oral Presentation).
- June 16-19 2013, 10th Congress on Catalysis Applied to Fine Chemicals, Turku/Åbo, Finland.
  Nickel Supported on Structured Activated Carbon Fibers for the Selective Liquid-Phase Semi-Hydrogenation of 1,3-Dinitrobenzene (Oral Presentation).
- September 13 2012, SCS Fall Meeting, Zürich, Switzerland.
  Catalytic Hydrogenation over Mo_2N: a Consideration of Crystal Phase (β- vs. γ-) and Surface Area (Poster).
- June 16-17 2011, 1st Swiss Heterogeneous Catalysis Meeting, Grindelwald, Switzerland.
  Molybdenum Nitrides for the Selective Catalytic Hydrogenation of para-Chloronitrobenzene (Poster).

Languages

- **French:** Mother tongue.
- **German:** Good skills.
  ZMP: Zentrale Mittelstufenprüfung (C1)
- **English:** Good skills (C1)
- **Alsatian:** Beginner.